THE UNIVERSITY *of* EDINBURGH

Domain Growth in Alloys

Thesis submitted by

Kenneth Arthur Hawick

for the degree of
Doctor of Philosophy

The University of Edinburgh
April 1991

To my parents and my brother.

Acknowledgements

I wish to thank Stuart Pawley and Colin Windsor for their constant encouragement and inspiration throughout the course of this project. It is also a pleasure to thank A.D.Bruce, J.E.Epperson and R.D.Kenway for much advice and many helpful suggestions.

I am grateful to V.S.Rainey (AEA Harwell) and D.Wozniak (IPNS Argonne) for invaluable technical assistance, and to D.J.Wallace and M.W.Brown for providing and supporting my ridiculously large computing resource requirements.

I am pleased to acknowledge financial support from The Materials Science and Metallurgy Division of AEA Technology Harwell, the Intense Pulsed Neutron Source Division of Argonne National Laboratory, the Computer Simulation group of British Telecom Research Laboratories, the Edinburgh Parallel Computing Centre and the Science and Engineering Research Council.

Finally, I thank S.P.Booth, H.W.Yau, B.J.N.Wylie and S.F.B.Tett for making Edinburgh such an interesting place to work with computers.

I really hate this damn machine,
I wish that they would sell it.
It never does just what I want,
but only what I tell it.

Anon.

Whom computers would destroy, they must first drive mad.

Fortune Program, UNIX[1].

[1] UNIX is a trademark of AT&T Bell Laboratories

Abstract

This thesis describes Monte-Carlo computer simulations of binary alloys, with comparisons between small angle neutron scattering (SANS) data, and numerically integrated solutions to the Cahn-Hilliard-Cook (CHC) equation. Elementary theories for droplet growth are also compared with computer simulated data.

Monte-Carlo dynamical algorithms are investigated in detail, with special regard for universal dynamical times. The computer simulated systems are Fourier transformed to yield partial structure functions which are compared with SANS data for the binary Iron-Chromium system. A relation between real time and simulation time is found. Cluster statistics are measured in the simulated systems, and compared to droplet formation in the Copper-Cobalt system. Some scattering data for the complex steel PE16 is also discussed.

The characterisation of domain size and its growth with time are investigated, and scaling laws fitted to real and simulated data. The simple scaling law of Lifshitz and Slyozov is found to be inadequate, and corrections such as those suggested by Huse, are necessary. Scaling behaviour is studied for the low-concentration nucleation regime and the high-concentration spinodal-decomposition regime. The need for multi-scaling is also considered.

The effect of noise and fluctuations in the simulations is considered in the Monte-Carlo model, a cellular-automaton (CA) model and in the Cahn-Hilliard-Cook equation. The Cook noise term in the CHC equation is found to be important for correct growth scaling properties.

Contents

List of Figures

List of Tables

Chapter 1

Introduction

1.1 Overview of Alloys

Almost all the metallic materials used in engineering applications today are alloys. These are mixtures of two or more metallic elements and perhaps additional quantities of non-metallic elements. Alloys may vary in complexity from the familiar binary combinations of copper and zinc forming brass, and of lead and tin forming solder, to the highly complex combinations of iron, chromium, nickel, molybdenum, manganese, carbon and silicon which are some of the ingredients of modern steels. Alloy combinations are tailored for their mechanical, thermal and chemical properties and typically these properties are highly dependent on sample history such as the ageing process and heat treatment as well as composition. The desired properties may be high strength, flexibility, ductility, wide working temperature range, chemical resistance, electrical or magnetic characteristics.

Often the useful properties of alloys, in contradistinction to pure materials, can be linked to the formation and growth of domains within the solid material. These domains may be defined as regions with an identifiable parameter which deviates from its value in the bulk of the material. This may be a physical characteristic such as the magnetic moment of the domains which can form in steels, or a purely chemical or compositional one such as the local concentration of some solvent material such as a carbide. A number of common alloys owe their high strength

or hardness to the formation of small particulate domains which trap defects and prevent crack formation by relieving stress. However, it is important to control the size of these domains. If they are not allowed to grow large enough they may have no effect, whereas if too large they may have a detrimental effect by forcing the alloy apart.

In general an alloy will be treated or worked after it is manufactured so that its atoms form a regular atomic lattice at least on scales of a few tens or maybe hundreds of inter-atomic spacings. A piece of bulk material will probably consist of a large number of such crystalline composites forming a polycrystal. It is possible to treat or work such polycrystalline samples so that very large regions of near perfect lattice structure are formed and indeed macroscopic single crystal samples are becoming commercially viable. Typically a real alloy in the solid state will not have a perfect crystal structure but will have defects and distortions and a complicated microstructure. In addition, even those regions of the material that are close to regularity will have a lattice structure that depends on the composition and prevailing thermodynamic environment of temperature and pressure. Even compositionally simple alloys can have highly complex phase diagrams and may have a number of stable or metastable structural and compositional phases.

In spite of this wide variation of structures it is possible to identify some *common* features of alloys, in particular the domain growth and dissolution behaviour which take place, however slowly, in any alloy at a finite temperature. The length and temperature scales on which such phenomena occur are clearly material-specific, but the driving mechanisms and scaling behaviour appear to be more universal and allow a more general approach to understanding the microstructure.

Figure 1.1 taken from [1] shows the different regimes of concentration and ageing time and their effects on the morphology of inhomogeneities in an aluminium alloy. The low concentration alloys show a nucleation growth mechanism whereby spherical domains form and grow. Increased concentration leads to the wave-like structure characteristic of the spinodal decomposition growth mechanism. Further increase in the aluminium concentration means that the growing aluminium-enriched domains are percolated almost instantly upon quenching.

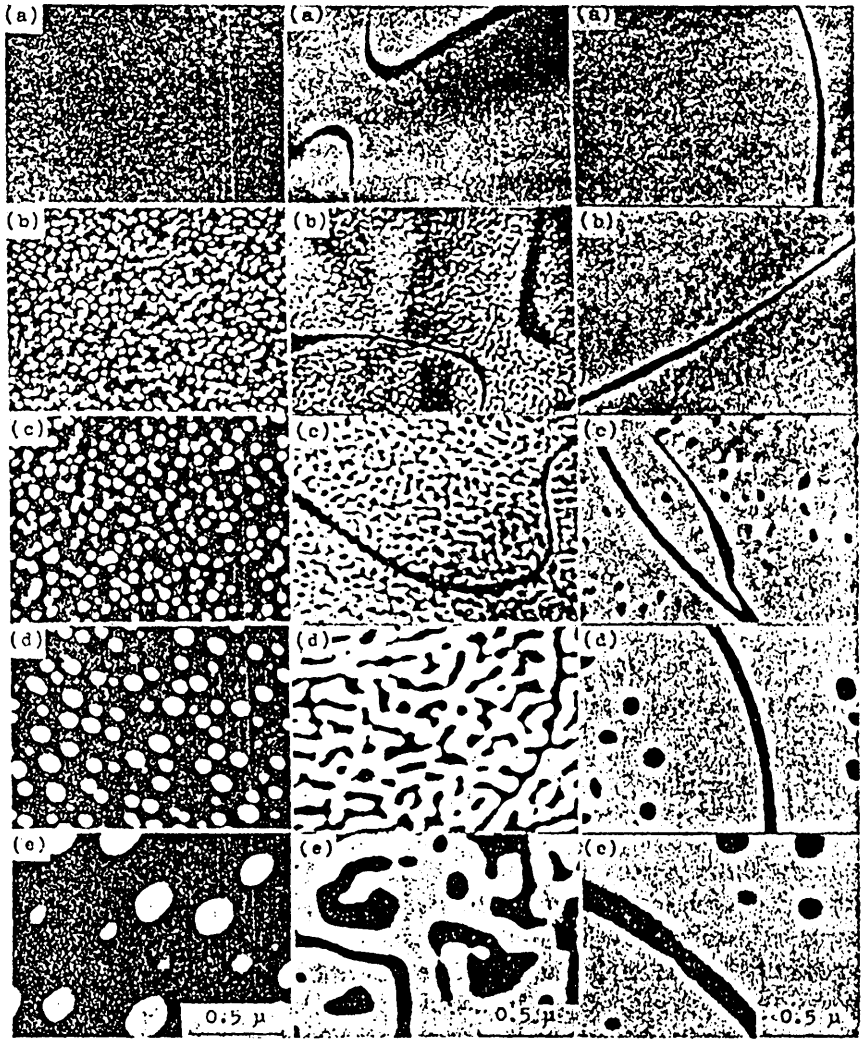

Figure 1.1: Domain structures in 23.0, 24.7 and 24.9 at% Al alloys, from left to right. The samples are quenched from 630C and annealed at 570C in the case of the 23.0 and 24.7 at% Al alloys and at 568C in the case of the 24.9 at% Al alloy. a) as quenched; b) annealed for 15 min in 23.0 and 24.9 at% Al and for 10 min in 24.7 at% Al alloy; c) 100 min; d) 1000 min; e) 10000 min. After Gunton et al. [1]

The remainder of this chapter reviews some of the existing experimental and theoretical work on alloy systems (section 1.3). The binary alloy model is introduced as a starting point for theory and for direct computer simulation in section 1.2 and is used as a common framework within which to discuss the phenomenology of domain growth in alloys.

1.2 The Binary Alloy Model

Consider a two component substitutional alloy consisting of a single crystallite of material. There are only two chemical species present and they occupy the sites of a regular lattice. They may be imagined as oscillating about some mean positions, but the bulk material retains its structure and the mean positions do not change, and there are no interstitial atoms permitted in the structure. Suppose that there are some N atoms on the lattice and they are subdivided by chemical species into N_A of species A and N_B of species B so that $N = N_A + N_B$. Consider the possible arrangements of the two species of atoms on the lattice. Focussing attention on species A the number of possible arrangements W of the N_A atoms of species A is simply given by:

$$W = \frac{N!}{N_A!(N - N_A)!} = \frac{N!}{N_A!(N_B)!} \tag{1.1}$$

given that the A-species atoms are indistinguishable. The microstructure produced by the set of atomic arrangements constitutes a microstate of the model alloy and to make the model able to simulate the dynamics of an alloy, it is necessary to impose a dynamical scheme whereby the system can explore its microstates.

1.2.1 The Model Hamiltonian

It is first necessary to consider the interactions between the species on the lattice. The simplest model Hamiltonian ($\mathcal{H}$) consists of an assignment of pair-wise interactions or bonds between neighbouring atoms. Consider a local concentration variable c_i for each lattice site which has the value 1 for A-sites and value 0 for

B-sites. The Hamiltonian may then be written in terms of coupling constants $V_{ij}^{c_i-c_j}$ between sites i and j.

$$\begin{aligned}\mathcal{H}_{\text{Alloy}} = \mathcal{H}^0 + \quad & \textstyle\sum_{i\neq j} \quad V_{ij}^{\mathbf{A-A}} c_i c_j + \\ & V_{ij}^{\mathbf{A-B}} c_i(1-c_j) + \\ & V_{ij}^{\mathbf{B-A}} (1-c_i) c_j + \\ & V_{ij}^{\mathbf{B-B}} (1-c_i)(1-c_j) + \\ & \textstyle\sum_i \quad \triangle\mu^{\mathbf{A-B}} c_i \end{aligned} \tag{1.2}$$

The first sum gives the pair-wise interactions and the second sum gives the relative chemical potential of the A-B mixture, it being more energetically favourable for the alloy to have more or less A-atom constituents. In practice, the interaction sum would not be over all pairs but over a restricted number of distance shells around individual atomic sites. The assumption is that long range electrostatic atomic interactions are screened in consequence of the overall neutral charge of the material and so the interactions are relatively short range.

This form of Hamiltonian can be shown to be isomorphic to that of the Ising model for a spin-$\frac{1}{2}$ magnet in a magnetic field [2] and was first employed by Bragg and Williams to study order-disorder processes in alloys [3], and by Cernuschi and Eyring as a model for lattice gases [4]. A review of more recent work using the model is given below in section 1.3. The chemical potential is directly related to the Ising model magnetic field and providing the interactions $V_{ij}^{c_i-c_j}$ are chosen so that the A-species and B-species are treated on an equal footing then the Hamiltonian can be written in the form:

$$\mathcal{H}_{Ising} = -\sum_{i\neq j} \mathcal{J}_{ij} s_i s_j + H \sum_i s_i \tag{1.3}$$

where the Ising spins s_i take the values $s_i = \pm 1$ and are given by the transformation:

$$s_i = 2c_i - 1 \tag{1.4}$$

$$c_i = \frac{s_i + 1}{2} \tag{1.5}$$

It is useful to consider the simplest case of this, where the interactions are very short range, isotropic, and are restricted to nearest neighbouring sites on the lattice. For this purpose, the Ising coupling parameter $\mathcal{J}_{ij}$ can be written as a

single value $\mathcal{J}$ and taken outside of the summation. This allows the Ising coupling $\mathcal{J}$ and magnetic field strength H to be written as:

$$\mathcal{J}_{ij} = \frac{1}{4}\{(V^{\mathbf{A-A}} + V^{\mathbf{B-B}}) - (V^{\mathbf{A-B}} + V^{\mathbf{B-A}})\} \tag{1.6}$$

$$H = -\frac{1}{2}\triangle\mu^{\mathbf{A-B}} \tag{1.7}$$

Since this only leaves two free parameters, the alloy Hamiltonian can be expressed in terms of just $V^{\mathbf{A-A}}$ and $\triangle\mu^{\mathbf{A-B}}$, giving a form where it is easier to generalise to a ternary alloy with less parameter redundancy. The binary alloy can be thought of as just the A-species in a background of B. The lattice gas picture merely involves treating the B sites as "vacancies". It is possible to reduce the parameters involved to one, by operating with zero chemical potential, as described in the dynamical scheme below.

1.2.2 Dynamics

Both the alloy and Ising Hamiltonians as expressed above do not give rise to a dynamical equation so it is necessary to introduce a stochastic mechanism whereby the system can explore its microstates. Focussing attention on the A-particles, there are two dynamical processes that need to be considered. Firstly, a mechanism for the particles to change position and explore the lattice but keeping the number of particles present (N_A) constant. Secondly, a means of operating with constant chemical potential $\mu^{\mathbf{A-B}}$ and increasing or decreasing the particle population. The first mechanism is know as 'spin-exchange' or Kawasaki dynamics [5] and is used for a canonical thermodynamical simulation of the alloy model where neighbouring site variables c_i and $c_{i\pm1}$ are exchanged. The second is the conventional 'spin-flip' dynamics where the site variable is inverted. In fact the exchanges or flips must be performed with a carefully specified probability if the system is to have valid thermodynamic properties.

It is interesting to consider the considerable differences between two apparently similar models as the spin-flip Ising model and the spin-exchange alloy model. The spin-flip model allows access to many more microstates than the spin-exchange

model. This number of states is given by:

$$W = 2^N \tag{1.8}$$

This grows with N much more rapidly than for the spin-exchange case as given in equation 1.1; even for $N = 10$ and $N_A = N_B = \frac{N}{2}$ this gives $W_{Ising} = 1024$ and $W_{Alloy} = 252$.

The aim in using the mechanisms described above is to drive the alloy system towards a well defined thermodynamic equilibrium for the given interaction and field parameters. A detailed description of the proper choices for transition probabilities is left to section 2.3.1.

1.2.3 Related Models

The model Hamiltonians given above involve a large number of degrees of freedom, the spins or site concentration variables, which naturally suggests a set of atoms located on a lattice. A number of similar models have been reviewed in [6] and a general nomenclature set up. The spin-exchange *alloy* model described above is generally known as 'Model B'. The spin-flip *Ising* model is 'Model A'. Other more sophisticated models involve decoration of the lattice with a vector- rather than a scalar-field, to allow consideration of anisotropic effects that result in ferromagnetic alloys. To date no attempts have been made to perform serious computer simulations on any of the models other than 'A' and 'B'.

1.3 Previous Work

The *alloy* model is not a recent one, and attempts have been made in the past to explain its fundamental properties [7, 8]. Success has been limited by a lack of theoretical tools for non-equilibrium thermodynamics, insufficient computer power for realistic simulations, and lack of appropriate experimental data for comparison.

This section reviews some of the important work on the theory of domain growth,

experimental studies of particular alloys and most recently some of the existing computer simulation work.

1.3.1 Alloy Characterisation

An important feature of any theory describing growth is its ability to predict quantitatively some parameter that can be measured in real alloys and also in computer simulations. Indeed the greatest use of the simulations is often in identifying the meaning of a measurement from an experiment and providing a bridge for comparison between theory and experiment. What general information can be inferred about a particular alloy after a certain treatment process ?

It is usually possible to determine the bulk chemical composition from a chemical assay. Electron microscopy of a sample cross-section can yield an accurate particle size distribution function. This can be misleading as the sample must be made very thin, must be flat and after preparation may quite likely be unrepresentative of the bulk alloy. Such a particle size-distribution can under certain circumstances be compared with the predictions of a droplet theory such as described below.

Another useful comparison is the structure factor as measured (at least as a partial structure factor) in a scattering experiment. This is derived for small-angle neutron scattering in chapter 4. It is easily defined for a binary alloy with spatial site variables c_i as follows:

$$S(\mathbf{q},t) = \frac{1}{N}\sum_{\mathbf{r}} e^{i\mathbf{q}.\mathbf{r}} \sum_{i} \langle [c_i(\mathbf{r_i},t) - \overline{c}][c_i(\mathbf{r_i}+\mathbf{r},t) - \overline{c}] \rangle \qquad (1.9)$$

This is discussed in more detail in chapter 2, but is just a spatial Fourier transform of the excess concentration field $(c_i - \overline{c})$, where $\overline{c}$ is the bulk concentration. The time t is defined as the time since the phase separation process started, this typically being the time since the alloy was quenched from a high temperature to one below the first order phase transition temperature. A typical form for $S(\mathbf{q},t)$ is shown in figure 1.2, showing the time evolution of a peak which shifts towards *lower* wavevector $\mathbf{q}$ values, which are indicative of *larger* domain sizes, with time. The system in figure 1.2 is of size $128 \times 128 \times 128 = 2097152$ sites, with $\overline{c} = 0.5$.

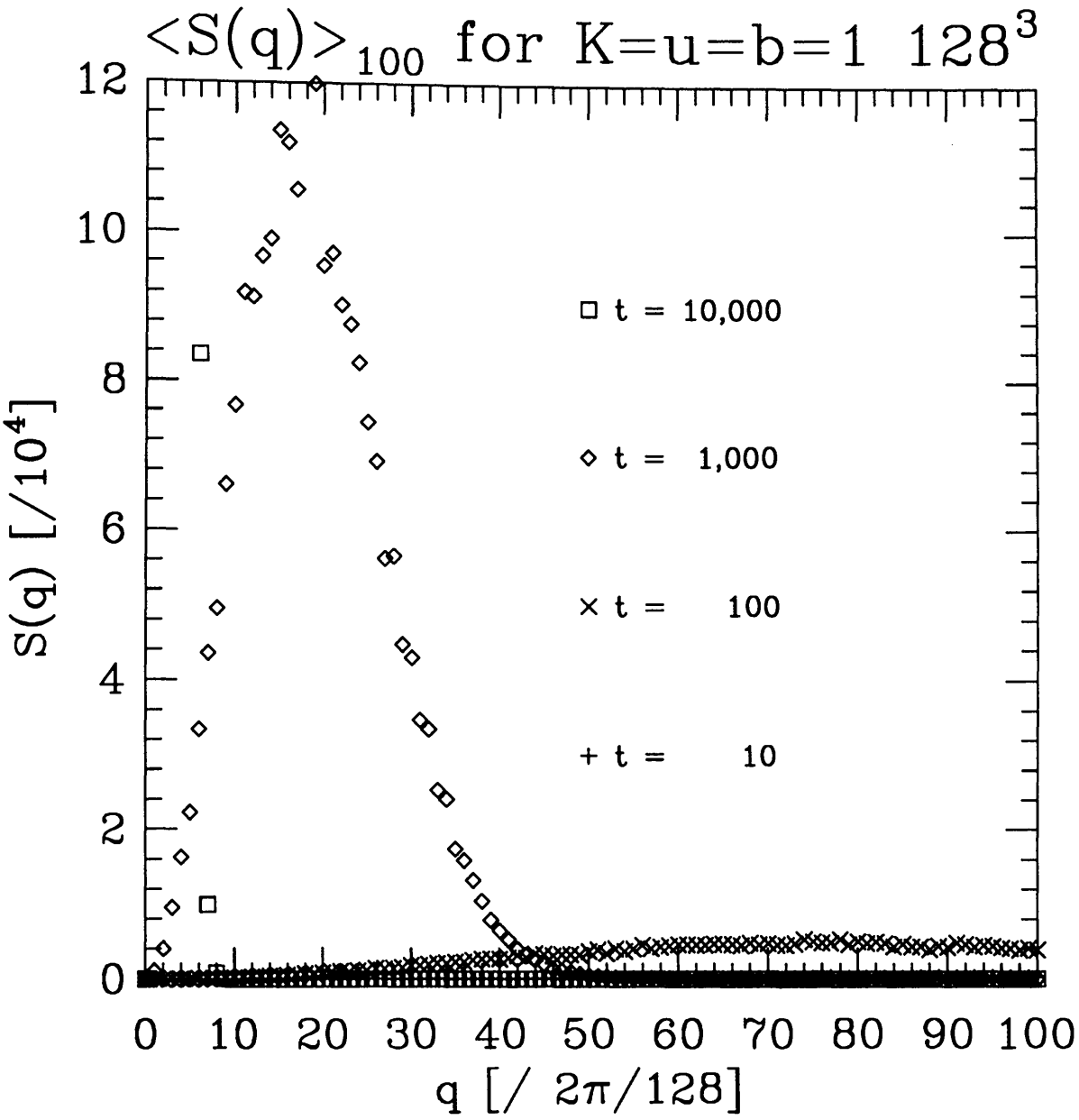

Figure 1.2: Structure factors computed from spatial Fourier transforms of 100 independent samples of Cahn-Hilliard trajectories on a cubic mesh of $128 \times 128 \times 128$ grid points.

The structure function calculations or measurements yield information about the characteristic domain size and how much these domains scatter. If the precise values of the domain compositions are known (ie from direct observation in the computer simulation, or by chemical analysis in the experiment) it is also possible to infer the volume fractions of the scattering domains. Unfortunately real systems are rarely purely binary and it is difficult to attribute a particular scattering contribution to growth of a single phase. In such cases it is useful to compute *partial* structure factors from each phase present and attempt to fit the particular combination to the observed total structure factor.

A useful parameter to characterise the growth is some measure of the 'typical' or 'dominant' domain size. In general this is just a scalar unless there are anisotropic directions in which growth is favoured. There are a number of ways of defining this quantity depending on the systems studied and the properties of interest. Some of the methods are as follows:

- The peak in the structure factor locates Q_{peak} from which the corresponding size R_S is given by: $R_S = \frac{2\pi}{Q_{peak}}$. This measure is used extensively for the experimental SANS data as well as for computer simulated systems of high concentration.

- The pair correlation function $g(\mathbf{r}, t)$ has a zero corresponding to the characteristic domain size R_P. This can be fitted by interpolating about the zero. This is only feasible for very small computer simulated systems.

- If the equilibrium energy E_0 per site is known for temperature T, then it is possible to compute $R_E = \frac{2K}{E(t)-E_0}$, where K is the bond coupling parameter J in units of kT. This is essentially an inverse perimeter density and was originally suggested by [9]. It is readily applied using Onsager's solution to the 2d Ising model, but for other systems where the equilibrium energy is unknown, measured values for E_0 must be used.

- If the configuration is small enough it is possible to compute an explicit radius of gyration for each cluster and identify the mean of the distribution. Alternatively the maximum radius value may be taken as the 'characteristic' value for R_C. Unfortunately this algorithm is time-consuming to apply and

will be unhelpful in the case of a percolated cluster with no clearly defined size. This is used extensively for computer simulations of low concentration systems.

- Other moments of the structure factor S can be employed to give variations of R_S [10].

Some of the above are described in more detail in [10], and are used in the discussion of scaling in chapter 5, where they are applied to experimental and computer simulated data.

After defining the characteristic size of the growing domains, it has proved interesting to consider how these sizes behave as a function of time and of quenching temperature and other model parameters. It is the form of this dynamical function that classifies the type of growth mechanism that dominate alloys' behaviour.

There has been much speculation and several attempts have been made to predict this functional form. The two most popular forms are a truncated power series in the time variable [11] and logarithmic behaviour [12]. The former is a derivation of the classic prediction of Lifshitz and Slyozov [13] and is currently favoured in the literature. The latter is losing credibility but this is still controversial.

The original Lifshitz-Slyozov (LS) theory claims that the characteristic domain size can be written as:

$$R(t) \sim t^n \tag{1.10}$$

This simply states that the dominant term in the power expansion in t is of power n, and does *not* imply a simple proportionality relationship. This idea of dynamic scaling is considered in [14]. There is considerable disagreement in the literature as to the value of n, and even whether equation (1.10) is adequate. It is widely believed that for many alloy systems $n \simeq \frac{1}{3}$ in the long time limit with a probable crossover from other values after a short time. For two-dimensional systems this long time limit is thought to be $n \simeq \frac{1}{2}$. This very naturally suggests that generally $n = \frac{1}{d}$; unfortunately there is as yet insufficient evidence that n is a reciprocal integer with many experimentalists reporting precise values away from $n = \frac{1}{3}, \frac{1}{2}$. Computer simulation evidence has also been somewhat inconclusive.

The exponent n also depends on the dimension of the order parameter, that is whether it is a scalar or a vector property. For this work the order parameter is a scalar but for more sophisticated vector models, this extra dependence needs to be considered [6].

Attempts have been made to associate dynamic universality classes with the different growth kinetics and different values for n [15] but there still appears to be considerable disagreement between computer experiments and experimental data and even amongst theoretical predictions. This controversy makes this a competitive and interesting field for study.

1.3.2 Theoretical Advances

There have been a number of theoretical attempts to describe the kinetic behaviour of phase separation in materials which are quenched from a homogeneous composition. There have been two main approaches which theoretical development has taken, a macroscopic free energy field equation scheme, and a microscopic physical cluster enumeration method. A rough outline of work in these areas is given below, with fuller details of the free energy approach deferred to chapter 3 where a derivation is needed to describe numerical integration work. The most recent review of these advances is somewhat dated now [1] but some more recent work has been discussed in [16, 17] and [7, 8]. Older works taking a wider viewpoint are [18, 19].

In general the free energy model is more successful in correctly describing phase separation in binary systems with near 50 percent concentration, ie quenches into the unstable regime of the phase diagram. The droplet approach is more successful when there are identifiable domains or clusters of a clearly defined minority phase, as is the case for concentrations below the percolation limit.

The essence of this method is to define continuous quantities, a free energy density and a concentration field, defined over the volume of the alloy system. It is then possible to set up a non-linear Langevin equation which governs the dynamical behaviour.[1] It is not possible to solve the resulting equation analytically, however it may be linearised around the 50 percent concentration point resulting in an approximate mean-field-like theory. The equations required for this have been employed by a number of authors. In the metallurgy field Cahn and Hilliard are given credit for the first application[20]. This theory has recently been reviewed by Binder [21]. A different approach is given in [22, 23], where the equations are treated directly as time-dependent Ginzburg-Landau theory.

Fourier transformation of the linearised equation allows a solution as a superposition of spatial concentration waves. This is qualitatively helpful in that it does correctly indicate the occurrence of phase separation. However it predicts an unbounded exponential growth in the structure factor with time.

In its simplest form this theory is only adequate to account for the earliest stages of growth. Binder lists a number of reasons why the Cahn-Hilliard theory is inadequate [21]. Foremost are that thermal fluctuations play an important role in the dynamics, and that non-linear effects *are* important in *even* the *earliest* stages of growth.

Some improvement to the Cahn-Hilliard theory was made by Cook [24] by addition of thermal fluctuations in the composition auto-correlation. This crucial addition to the theory allows the model alloy to climb over energy minima. The full consequences of this are reviewed in [25] but the most important is that the structure factor still grows exponentially. However, the position of the peak in the structure is predicted to shift at early times, giving some quantitatively correct behaviour at early times, and qualitatively correct predictions for the long time

[1] Alternative conceptual starting points give essentially the same equation. The theory can be set up using a Langevin equation, a Time-dependent Ginzburg-Landau (TDGL) equation or a Fokker-Planck (FP) equation as a conceptual starting point. See [1]. The resulting descriptive equation is the same.

limit. Nevertheless the Cahn-Hilliard-Cook theory is still a *linearised* theory and to model the kinetics of decomposition correctly the higher order terms of the Taylor series for the free energy density are required.

The higher order terms make the resulting equation impossible to solve in closed form, although an attempt to approximate the higher order fluctuations has been made by Langer, Bar-On and Miller (LBM) [26]. This theory assumes isotropic phase separation and is formulated in terms of the structure factor. It predicts slower than exponential growth and a correct shift in the structure factor peak position, and the correct Ornstein-Zernike (wavevector-squared) tail behaviour.

This theory is the best *complete* theory developed to date to describe spinodal decomposition. However, a number of objections have been raised, regarding the treatment of fluctuations in it [27, 1] and attempts are still being made to improve on it [28, 29]. Another main difficulty with the LBM theory is in relating theoretical parameters to measurable quantities. In particular it is difficult to measure the coarse-grained free energy either in real alloys or in computer simulations [30, 31].

The Cahn-Hilliard theory is discussed in detail in chapter 3, where the linearisation approximation is avoided by resorting to numerical solutions.

Cluster or Droplet Theories

The alternative approach to predicting the domain growth behaviour is to consider the effects of minority phase clusters against a background of majority phase material. This approach owes its origins to Becker and Doring [32] and has recently been revived and considerably developed by Binder [33, 34]. It has also been successfully applied to other systems [35].

The principle is to define the cluster mass distribution function as a histogram $n_l(t)$ of the size (l) population of minority phase clusters and follow it in time (t). The objective is to set up and solve a set of rate equations giving $\frac{dn_l}{dt}$ as a function of $n_l(t)$, l and t. Binder showed that these equations may be written in terms of a coagulation term which dominates at the early stages of decomposition, and an

evaporation-condensation term dominating at later times. The coagulation mechanism does not change the $n_l(t)$ but merely allows existing clusters to compactify. The evaporation-condensation mechanism describes the addition or subtraction of single particles to or from existing clusters. Since a cluster's mobility goes inversely with its size, at early times when the clusters are small, the coagulation mechanism *must* dominate.

This approach is very attractive for direct comparisons with computer simulation. Using speed-optimised algorithms for parallel computers it is possible to determine cluster distributions directly from simulated alloy configurations [2]. The algorithms are described in appendix A and the results discussed in chapter 5. Attempts to establish explicit solutions to the rate equations for small clusters on regular lattices are currently being attempted [3].

The main predictions of Binder's theory are that the structure factor will have a well-defined peak position giving the characteristic cluster size, and that this will evolve in time according to a simple power law and will *not* grow exponentially without bound. It also allows parameters of the model, namely the diffusion coefficients, to be directly related to measured values in real systems. It is also possible to calibrate the computer simulation time in terms of these [36].

A major disadvantage of this theory is its inability to cope with very large clusters and in particular with percolated clusters. This means that for systems in the unstable regime, the theory is inapplicable due to difficulties in defining yet alone handling a percolating cluster. Recent work [37] in studying the percolation transition has helped considerably in identifying the problem without solving it as yet.

This theoretical approach is discussed in chapter 3 and its weaknesses illustrated by comparison with computer simulated data.

[2]This is a computationally demanding calculation and parallel computers are needed to obtain statistically meaningful results in useful times

[3]Private communication. C.G.Windsor, 1990

1.3.3 Scaling, Multiscaling and Renormalisation Group studies

Following on from the classic work on dynamical scaling by Lifshitz and Slyozov [13] several authors have tried to construct more elaborate and general theories explaining scaling behaviour over all time regimes [11, 38, 39, 40]. These have led on naturally to the ideas of block scaling and renormalisation group calculations using self similarity transforms to capture growth behaviour. The renormalisation technique is well described for the spin-flip Ising model in [41] but the best attempt to appear so far for the spin-exchange model is [42]. The coarse-graining method involves elimination of the 'hard' modes in the Langevin equation for the alloy, leaving only the 'soft' modes of low wavevectors. A change of scale reinstates the ultraviolet cutoff for the soft modes to its original value while simultaneously rescaling the time variable as required by scale invariance.

The resulting rescaled Langevin equation is interpreted in terms of a rescaled transport coefficient, temperature and Hamiltonian. Scale invariant behaviour is associated with the fixed points of this transformation and the zero temperature fixed point describes the scaling at least for the symmetric case of spinodal decomposition. This work suggests that $n = d + 2 - y$ where $y = d - 1$ for a scalar order parameter giving $n = \frac{1}{3}$ precisely for $d = 3$ and $y = d - 2$ for a vector order parameter. At present there are no results available for the non-symmetric quench involving nucleation.

1.3.4 Other Simulation Work

Realistic computer simulations have only become viable within the last 5 years or so, and it is now possible to simulate systems big enough that finite size and specifically surface effects are negligible compared to bulk behaviour. A number of early computer experiments were attempted on simple regular lattices with only nearest neighbour interactions considered [43] and references within.

To date, computer simulations, while giving a good qualitative insight into growth

processes, have merely added to the confusion in the hunt for forms of the dynamical scaling function and dynamical exponent n. It is likely that this is due to uncertainty in what constitutes the asymptotic time regime where the LS result is expected to hold.

Due to the length of the computer times that are required to obtain statistically relevant results from simulations, most work to date has concentrated on two-dimensional systems with only a single nearest-neighbour interaction shell. Such three-dimensional data as *is* available is typically on very small simple cubic lattices where the effects are dominated by finite size effects. Some of the problems associated with extrapolating from such small lattices are considered in [44]. Most work has also been restricted to the simple binary alloy model in the symmetric concentration case. This is the model most easily compared to known results for the conventional spin-flip Ising model.

Some of the earliest work was on the case of ordering in binary alloys [45, 46]. This model yields a structure not unlike the AB ordering that occurs in β-brass with a well-defined ground state. The anti-ferromagnetic or anti-clustering growth that occurs in such materials is relatively well understood compared with the clustering or ferromagnetic domain growth that is considered here. Some recent work in this area of ordering systems is reported in [47], where the short and long range ordering in nickel-molybdenum alloys were simulated.

One of the earliest computer simulations of the clustering binary alloy model was [48]. This work was done before the search for dynamical scaling became widespread, and considered the wavevector-squared tail of the structure factor in a comparison with LBM theory for a two-dimensional system, with symmetric quenches to above and below the corresponding critical Ising temperature. Further work and corresponding results followed for a three-dimensional system [49]. This work well illustrates the need for very long computer simulation times. Work on the non-symmetric quench was done in [50] (2d) and [43] (3d), where with medium concentrations on square and simple cubic lattices these authors were unable to investigate fully the nucleation regime as they were working too close to the percolation limit.

The first serious attempt to study scaling in the nucleation regime was [51] where values for n of between 0.2 and 0.28 were reported for low concentration quenches on a simple cubic lattice. These low values are almost certainly attributable to insufficient ageing time, and to the simulated alloy not being in the asymptotic time regime. The lattice size of 25×25 was probably beyond the capabilities of the computers of that time.

There have been few attempts to simulate more complicated systems. One paper described work on exchange dynamics with the Q-state Potts model for various low Q values in two-dimensions [52]. Qualitatively interesting results regarding pinning effects and kinetic slowing down resulted but no scaling measurements. The corresponding model in three-dimensions would prove interesting for ternary and four-species alloys.

The most ambitious simulations to date have been for realistic structures such as the FCC lattice with first and second neighbour interactions [53, 54]. A good attempt at enumerating the ground states has been made but there are few scaling behaviour results.

Very few authors have attempted to make any direct comparison between their own simulated and experimental data. A recent work [55] obtained good qualitative agreement between growth of small clusters in an aluminium-chromium-iron alloy and a small computer simulated system. The simulation explained the changing slope seen in structure factors measured with small angle neutron scattering. These were due to a change in cluster shape during the early stages of growth.

1.3.5 Other Experimental Work

The main difficulty in obtaining useful comparisons with experimental data lies in the complexity of real materials. Real systems are not single crystals, are not simple binary or even necessarily ternary in composition and are not necessarily isotropic even along the crystal axes. Nevertheless, a body of experimental small-angle scattering (both X-ray and neutron) data exists for nearly pure polycrystalline and specially grown single crystals of certain alloys [56, 57].

A popular form of experiment to test for scaling is to solution-treat an alloy at high temperature in an attempt to remove all domains and obtain a highly homogeneous state. The alloy is then quenched either directly or as a two stage process to some temperature just below or around the miscibility gap. The experiment is then to observe the formation and growth of phase separated domains. The techniques are either some form of scattering experiment or electron microscopy. Another technique less common now is to measure the electrical resistivity of an alloy sample, inferring domain growth from the scattering effect on conduction electrons, and hence increased resistivity.

The most common experimental technique is probably small-angle scattering either by neutrons or by x-rays, to obtain the domain sizes from the measured structure factor. For example [58, 59] report detection of small Ni_3Al particles in a quenched nickel-aluminium alloy using a number of the techniques mentioned above. The early stages of phase separation in $FeCr$ and $AlZn$ alloys is described in [60, 57] where the shape of the structure factor tail is used to infer the domain sizes. These authors report that dynamical scaling as predicted by the LBM theory, fits their data.

Some attempts to measure the diffusion parameters necessary to match a computer simulation to experiments on iron-nickel alloys are reported in [61].

1.4 Aims

It is the aim of this thesis to explore some of the mechanisms whereby domains grow in solid alloy materials and to determine how this behaviour may be measured and characterised. In summary the aim is to explain the behaviour illustrated in figure 1.1. Figure 1.3 shows the structure of this thesis.

This introduction splits into three parallel routes to discuss the simulation, theory and experimental measurement of domain growth in alloys. The resulting three chapters each describe the methodology for each approach before presenting and selected results. The three routes are cross linked to the low and high concentra-

tion regimes which categorise domain growth in alloys. The three parallel threads are brought together for common discussion and conclusions in chapter 5.

The approach taken is to discuss theoretically an idealised model for the configurational dynamics of an alloy and consider how this can be taken beyond the limitations of current theories by use of computer simulation. Chapter 2 describes work on a Monte Carlo model for binary substitutional alloys. In chapter 3 a theoretical model for describing binary alloys in the high concentration regime is given and the resulting non-linear Langevin equation is numerically integrated to provide some theoretical predictions of alloy growth behaviour.

The low concentration regime is considered using the Becker-Doring droplet theory for comparisons with cluster size distributions in a computer simulated system.

Several real metallic alloys are studied, and methods for investigating their domain-growth behaviour are discussed in chapter 4. The experimental data is compared with the theoretical and computer-simulated results in chapter 5.

The simulation and numerical integration work described in chapters 2 and 3 made heavy use of parallel computers and parallel computation techniques and details of these are relegated to appendix A.

Additional appendices describe the maximum entropy parameter fitting code developed to aid in fitting structure factors to experimental SANS data, and also the derivation of the form factor for SANS from spherical particles.

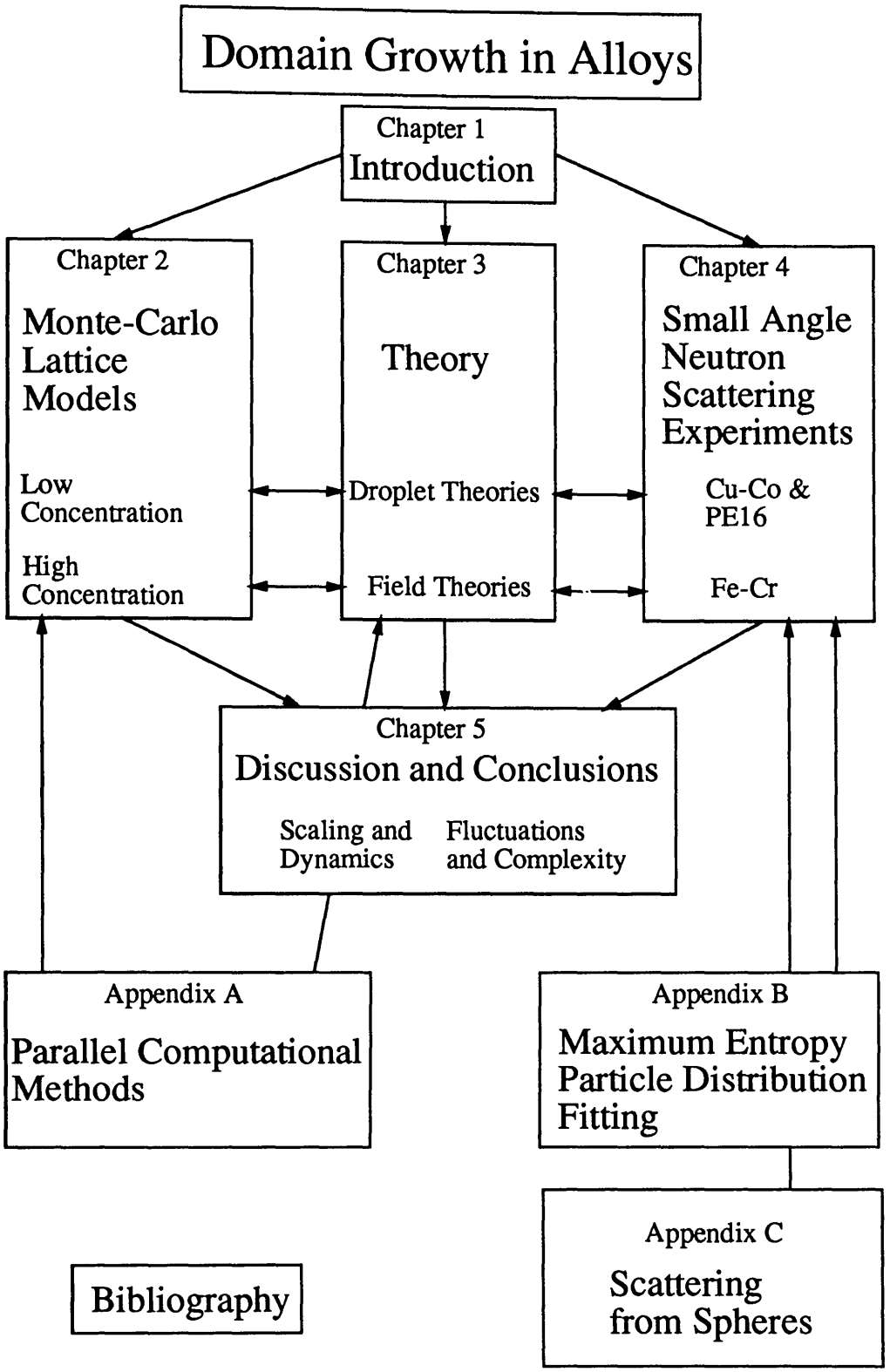

Figure 1.3: Chapter outline of this thesis.

Chapter 2

Computer Simulations

2.1 Introduction

This chapter is concerned with choosing a suitable model to explore the phenomenology of domain growth in alloys, and to make some quantitative comparisons between the dynamical properties of simulated and real alloy systems. What is required, is a simple model that can be set up for a purely *binary* alloy system, that will allow exploration of the configurational thermodynamics of growth in a substitutional alloy, and that will be computationally fast enough to allow very long simulation times, comparable with the ageing times applied to real alloys.

A natural point to start looking for a simple model that can be related directly to real time is in the technique of molecular dynamics, and this is dealt with in the next section. Unfortunately this method transpires to be too slow computationally, to cope with simulated ageing times of many hours. The remainder of the chapter describes work using a Monte Carlo lattice model. The dynamical algorithm is described, and the resulting model is used to discuss the phase diagram of a binary alloy. A series of numerical experiments on the binary alloy model is presented, and some of the time dependent properties are discussed. A full discussion of dynamical scaling results is deferred to chapter 5, where results for the computer simulated systems are compared with those for theoretical predictions, and from real scattering experiments.

2.2 Molecular Dynamics

The molecular dynamics (MD) technique involves a numerical integration of the classical equations of motion for a number of particles, or molecules, given a model Hamiltonian [62]. The resulting numerical trajectory through phase space, can be used to make a number of useful measurements of the dynamical properties of a system [63].

There are several difficulties involved in applying this technique to the simulation of an alloy, even a purely binary one. Primarily, the first requirement is for a suitable model Hamiltonian for the system. While this is not easy to obtain exactly, it *is* possible to construct an approximate one with the basic properties, using pair-wise potentials. For example one very simple model would be to assume a system of soft spherical atoms in a box, with two atomic species present, and atoms of each species preferentially attracting atoms of its own species. A model Hamiltonian of the Lennard-Jones form [62] can be constructed using:

$$U(R) = 4\epsilon \left[\left(\frac{\sigma}{R}\right)^{12} - x^{i,j} \left(\frac{\sigma}{R}\right)^{6} \right] \tag{2.11}$$

This gives the potential energy U due to the pair-wise interaction of two atoms of species i, j, separated by some radial distance $R = \left|\mathbf{r}_i - \mathbf{r}_j\right|$, given two atom specific parameters in the form of an energy ϵ and a length scale σ, and a cross term coupling fraction $x^{i,j}$ which is greater for interactions between like species i, j than for opposite species. The use of such a primitive model Hamiltonian is illustrated in figure 2.1 where a number of two dimensional disk-like atoms are placed in a perfectly reflecting box and allowed to relax. This simulation used parameters appropriate for two species of pseudo-Argon atoms with $x = 2$ for like-like atoms, and $x = 1$ for unlike pairs, and a time step of 0.1 picoseconds. Figure 2.1 shows the system initialised randomly with an equal mix of the two species, and a snapshot of the system after some 10^7 integration time steps, using the Beeman integration algorithm [62]. This calculation took some $48 \times 64 = 3072$ transputer-hours using the Edinburgh Concurrent Supercomputer, as described in appendix A. It reveals a number of the limitations of the MD technique for phase separation in a solid alloy.

It was necessary to allow the system in figure 2.1 to remain a liquid to achieve

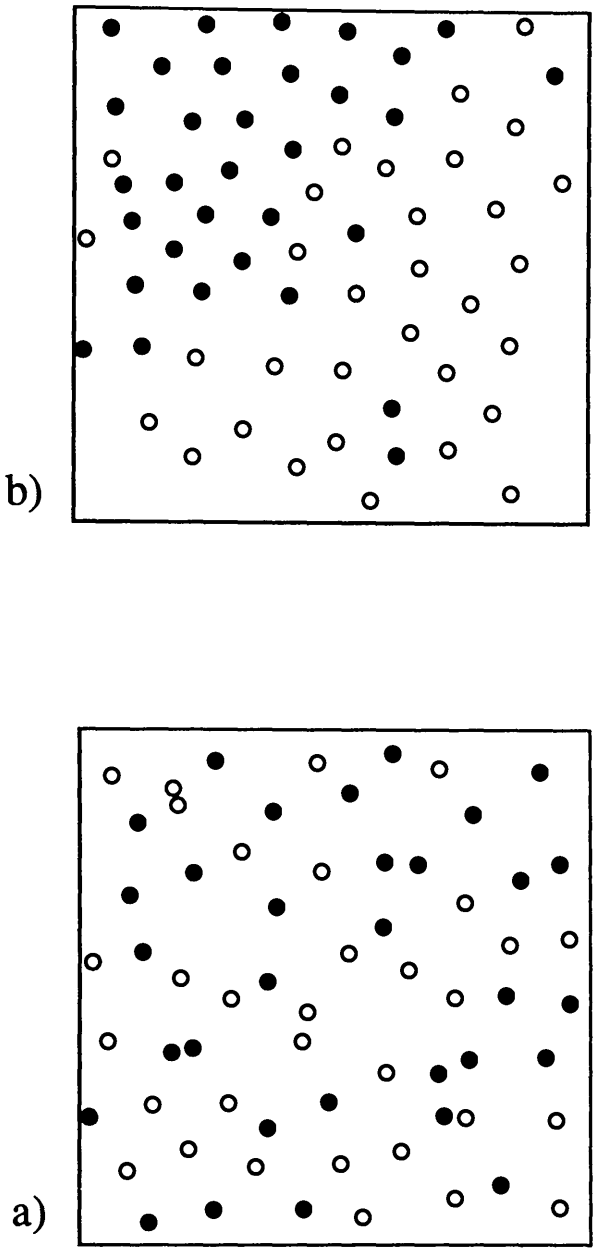

Figure 2.1: Phase separation in liquid two dimensional Lennard-Jonesium. a) shows the initial random configuration, b) shows the system after 1000 nanoseconds of evolution. Dark circles represent A-type atoms, and open circles B-type. Like-like atoms are attractive.

phase separation. Constraining it as a solid lattice meant the numerical integration routine would become unstable too rapidly. It was difficult to quench the system to a low temperature, by running a canonical simulation, and still achieve phase separation. There are time scales inherent in the MD algorithm, that quite correctly require that phase separation will occur only very slowly in a quenched system, due to insufficient thermal activity. The simulated time that can be achieved is of the order of $100 - 1000$ nano seconds, whereas real alloys are quenched in seconds, and are aged for anything from minutes to years of real time. There is no obvious way to re-scale the MD simulation time to achieve phase separation in a solid.

Existing computer technology is not capable of simulating large enough solid systems using the MD technique, for phase separation effects, probably not even for the two dimensional liquid system shown in figure 2.1, which has only 64 atoms in it. Even using the known computational 'tricks' to cut-down on the interaction calculations [62], MD is not appropriate for this work.

2.3 Monte-Carlo Dynamics

In this section, the Monte-Carlo lattice model outlined in the introduction is discussed in detail, and is proposed as an alternative to an MD approach.

Recall the model Hamiltonian, introduced in chapter 1, for the alloy model:

$$\begin{aligned} \mathcal{H}_{\text{Alloy}} = \mathcal{H}^0 + \sum_{i \neq j} & V_{ij}^{\mathbf{A-A}} c_i c_j + \\ & V_{ij}^{\mathbf{A-B}} c_i (1 - c_j) + \\ & V_{ij}^{\mathbf{B-A}} (1 - c_i) c_j + \\ & V_{ij}^{\mathbf{B-B}} (1 - c_i)(1 - c_j) \end{aligned} \tag{2.12}$$

where the chemical potential term has been omitted, as we wish to operate at a *fixed* value of the global concentration $< c >$. All the parameters used in this Hamiltonian can be specified explicitly, or we can limit the model to nearest neighbour isotropic interactions, so that only one parameter V^{A-A} is not redundant. By expressing this one parameter in units of $k_b T$, we are actually specifying the

temperature T of the system, and a quench experiment is possible. As stated in chapter 1, this Hamiltonian has no explicit dynamical scheme associated with it, and so one must be imposed artificially.

2.3.1 Transition Probabilities

In this section a derivation is given of the appropriate transition probabilities for the Monte-Carlo dynamics.

Recall that each microstate of the alloy system is completely specified by the set of site variables $\{c_i\}$ given the coupling and chemical potential parameters. Let the probability functional $P(\mathbf{X}, t)$ be associated with the microstate $\mathbf{X} \equiv \{c_i\}$ at time t and consider the transition probability $W_{\mathbf{X}\to\mathbf{X}'}$ giving the likelihood of a change of microstate $\mathbf{X}$ to $\mathbf{X}'$. The following master equation can immediately be set up, requiring that the rate of change of probability of microstate $\mathbf{X}$ at time t be given by considering all transitions from $\mathbf{X}$ and all transitions to $\mathbf{X}$:

$$\frac{dP(\mathbf{X})}{dt} = -\sum_{\mathbf{X}'} W_{\mathbf{X}\to\mathbf{X}'} P(\mathbf{X}) + \sum_{\mathbf{X}'} W_{\mathbf{X}'\to\mathbf{X}} P(\mathbf{X}') \tag{2.13}$$

By requiring the algorithm to yield $P(\mathbf{X}) \to P_{eq}(\mathbf{X})$, the thermodynamic equilibrium probability of microstate $\mathbf{X}$ as $t \to \infty$ a solution of 2.13 with $\frac{dP(\mathbf{X})}{dt} = 0$ so that:

$$\sum_{\mathbf{X}'} W_{\mathbf{X}\to\mathbf{X}'} P(\mathbf{X}) = \sum_{\mathbf{X}'} W_{\mathbf{X}'\to\mathbf{X}} P(\mathbf{X}') \tag{2.14}$$

This is the condition of detailed balance. It is common to use the stronger (but tractable) condition that:

$$\frac{W_{\mathbf{X}'\to\mathbf{X}}}{W_{\mathbf{X}\to\mathbf{X}'}} = \frac{P(\mathbf{X})}{P(\mathbf{X}')} \tag{2.15}$$

So that the probability of the system moving to microstate $\mathbf{X}$ is increased for highly probable microstates $\mathbf{X}$, and decreased for unlikely ones. It is then necessary to recognize that for a Boltzmann statistical weighting of the microstates, the probabilities $P(\mathbf{X}$ can be expressed in terms of the Hamiltonians $\mathcal{H}(\mathbf{X})$.

$$P(\mathbf{X}) = Ae^{-\frac{\mathcal{H}(\mathbf{X})}{k_b T}} \tag{2.16}$$

Where A is a normalising constant, k_b is Boltzmann's constant and T the temperature. Substituting 2.16 in 2.15 gives:

$$\frac{W_{\mathbf{X}'\to\mathbf{X}}}{W_{\mathbf{X}\to\mathbf{X}'}} = e^{-\frac{\{\mathcal{H}(\mathbf{X})-\mathcal{H}(\mathbf{X}')\}}{k_b T}} \tag{2.17}$$

This does not have a unique solution. The two most commonly used are [64, 65]:

$$W_{\mathbf{X}\to\mathbf{X}'} = \begin{array}{ll} \frac{1}{\tau}e^{-\frac{\Delta\mathcal{H}}{k_b T}}, & \Delta\mathcal{H} > 0 \\ \frac{1}{\tau}, & \Delta\mathcal{H} \leq 0 \end{array} \tag{2.18}$$

$$W_{\mathbf{X}\to\mathbf{X}'} = \frac{1}{\tau}\left(\frac{e^{-\frac{\Delta\mathcal{H}}{k_b T}}}{1+e^{-\frac{\Delta\mathcal{H}}{k_b T}}}\right) \tag{2.19}$$

These are illustrated in figure 2.2. It may be seen that the Metropolis function has the greatest area under it and is non-symmetric about the change in Hamiltonian. It *always* accepts configuration changes which lower the total energy. The Glauber function *is* anti-symmetric about $d\mathcal{H} \equiv 0$. The parameter τ controls the units of time and is conventionally set equal to unity.

It remains to decide which of these two schemes produces the more realistic dynamics. Older works in the literature such as [65] have used the Glauber scheme for dynamical work, relegating the Metropolis algorithm to work where a thermodynamically equilibrated configuration is required and the dynamics is unimportant. Figure 2.3 illustrates the difference between the two algorithms for a simulation of a spin-flip simulation of the Ising Hamiltonian on a square lattice of size 128^2 sites. Three measurements were made dynamically on the system: the bonds per site or energy; the magnetisation; and the correlation with the initial configuration. The Glauber algorithm is systematically slower to reach an equilibrated configuration, than the Metropolis algorithm. They do produce qualitatively similar configurations, as the convergence of the energy and correlation curves shows. It appears that for computational purposes, the Metropolis algorithm is better, since it involves one less floating point operation — a division, it produces a faster dynamics but similar equilibrium results, and a qualitatively similar trajectory through phase space.

The simulation time can then be defined in units of 'an average of one Metropolis update attempt per site'. It is important to include every site in this definition

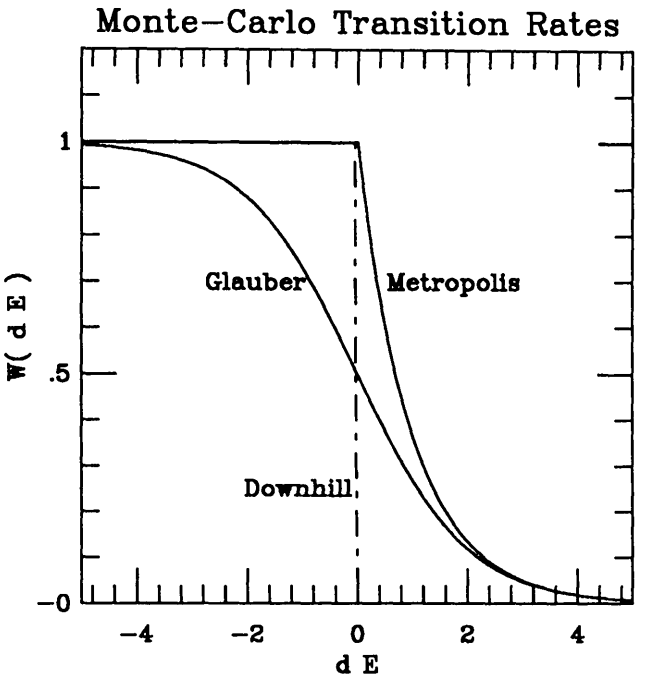

Figure 2.2: Metropolis and Glauber transition rate functions for importance sampling Monte-Carlo.

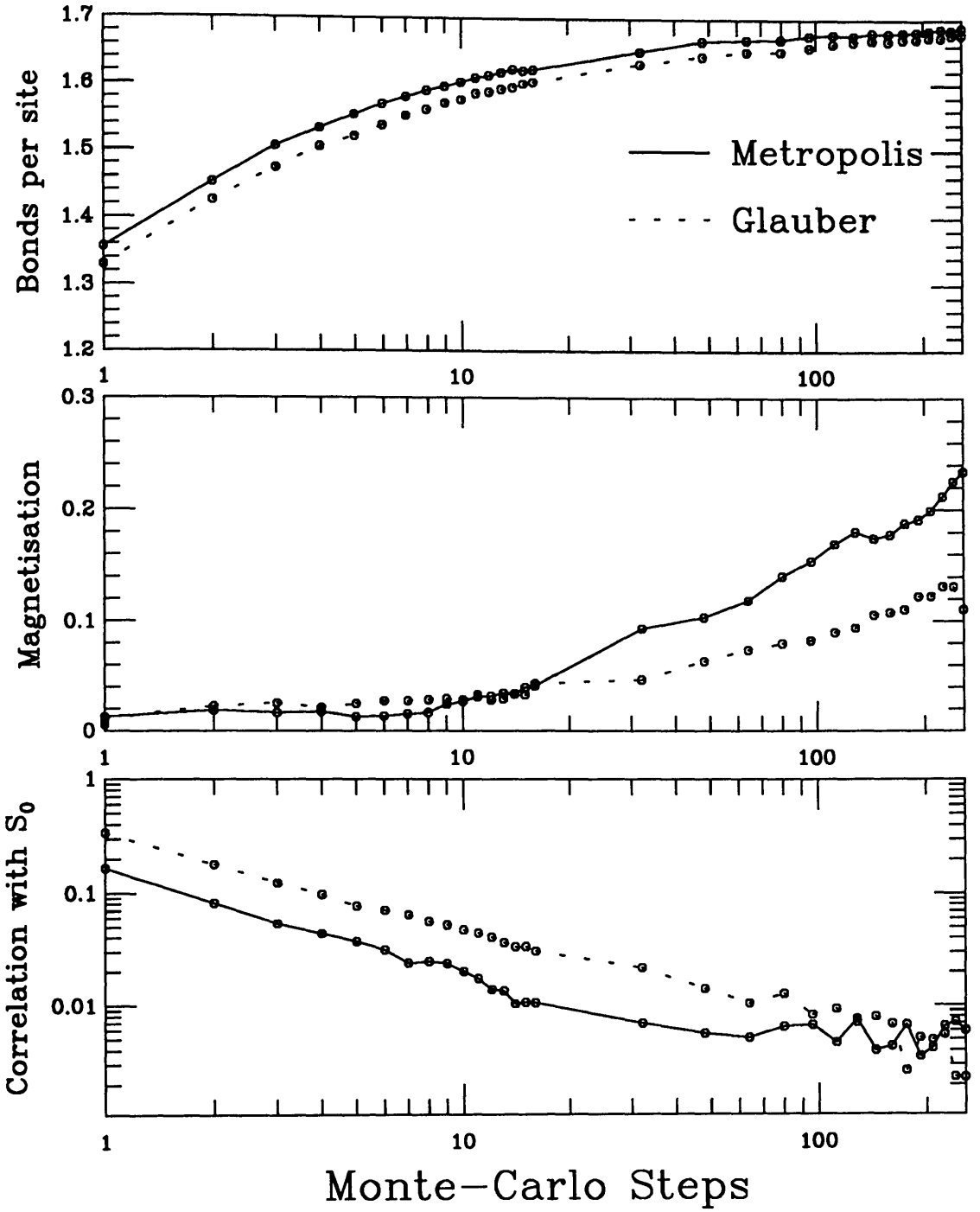

Figure 2.3: The energy, magnetisation and auto-correlation dynamical measurements on a two dimensional Ising model using Metropolis and Glauber transition rate functions.

of the time-step. Without such a universal definition, it becomes impossible to compare other works in the literature and on slightly different models, in terms of their dynamical properties. The problem remains that this is only an artificially constructed time. It is also noticeable that for deep quench experiments, there is little thermal activity below the phase transition temperature and the system evolves very slowly. This effect is known as hydro-dynamic slowing down.

The subject of whether the stochastic time variable in a Monte-Carlo simulation bears any resemblance to a *real* time is still controversial [7, 66]. In general it does not, but it is thought that for certain models it can be scaled to a real time, at least in the long-time limit. There is strong evidence that the Monte-Carlo time *is* scaleable to real ageing time for some of the experimental alloy data presented in chapter 4.

2.4 Other Monte Carlo Algorithms

A number of new Monte Carlo algorithms have appeared recently in the literature, purporting to speed up the dynamics and reduce the effect of the hydro-dynamic slowing down. Some of these are [67], [68], [69], and are reviewed in [70]. In general, they are all short-cuts to finding the most thermodynamically probable region of phase space, and thus are excellent for obtaining thermally equilibrated configurations. Unfortunately the paths through phase space are not necessarily the ones that a real system with short range interactions between atoms, would take, and these algorithms are therefore unsuited to a study of the dynamics. They do find use, however, in [71] for computing equilibrium properties of the three dimensional Ising model.

One particular limiting case of the Metropolis algorithm described above is the downhill or decreasing energy dynamical scheme. This ignores all fluctuations in the energy and as a result generates a very restricted trajectory through phase space, that can easily become stuck. Surprisingly, such a dynamical scheme does allow some phase separation but only if the system is well above the percolation limit and surface tension effects allow domains to coarsen. This *cellular automata*

[72] approach is described in [73, 74] and [75]. It has some interesting properties, but is *not* a good model for universal growth, since the system does inevitably become stuck, when the smaller isolated domains can coarsen no more, and are unable to evaporate.

The Metropolis algorithm is therefore the best compromise between a computationally efficient and a physically realistic one, although it should be emphasised that it has no physical basis and is is still only an artificially constructed means of generating phase space trajectories. It is used in all the simulation work described in this thesis.

2.5 Mean Field Theory and the Phase Diagram

This section considers the phenomenology of growth in alloys, making reference to the alloy model described above, and to the mean field theory approximation to the model. What is of interest are the different regimes of concentration $< c >$ and temperature T that can be explored during a quench experiment on an alloy. It is useful to discuss these in the context of the phase diagram for the alloy. Establishing the phase diagram numerically is non-trivial, even for the relatively simple alloy model set up above. It is useful to resort to the mean field approximation to the model, and this is easist to set up for the spin-flip Ising model.

2.5.1 Mean Field Approximation

The treatment below is loosely based on that of Stanley [14]. Consider the nearest-neighbour Ising model Hamiltonian for a system of spin variables σ_j. The mean field approximation is to assume that each spin variable interacts with all the other spins as though they were fixed at their mean values. That is to say, all fluctuations are ignored. This means that the mean field energy ϵ^{MF} of a given spin σ_j can be defined as:

$$\epsilon^{MF}(\sigma_j) = \mathcal{H}_{\text{ising}}(\{\sigma_j\})\Big|_{\sigma_j=<\sigma_k>} \quad \forall k \neq j \tag{2.20}$$

so that:

$$\epsilon^{MF}(\sigma_j) = -H\sigma_j - \mathcal{J}\sigma_j \sum_{k}^{nn} < \sigma_k > + \mathcal{H}_0 \tag{2.21}$$

where the summation is over the nearest neighbouring spins of σ_j and H is the magnetic field. This can be rewritten as:

$$\epsilon^{MF}(\sigma_j) = -H^{MF}\sigma_j + \mathcal{H}_0 \tag{2.22}$$

with the mean field defined as:

$$H^{MF} = H + \mathcal{J} \sum_{k}^{nn} < \sigma_k >= H + \mathcal{J}qM \tag{2.23}$$

where q is the lattice co-ordination number and $q = 4$ for the square lattice and $q = 6$ for the cubic lattice. M is the order parameter, the total magnetisation and is defined by $M \equiv < \sigma_j >$, so that:

$$M = \frac{\sum_{\sigma_j=\pm 1} \sigma_j e^{\frac{-\epsilon^{MF}(\sigma_j)}{k_b T}}}{\sum_{\sigma_j=\pm 1} e^{-\frac{\epsilon^{MF}(\sigma_j)}{k_b T}}} \tag{2.24}$$

This leads to the well known mean field result [14]:

$$M = \tanh(\frac{H^{MF}}{k_b T}) = \tanh(\frac{H + q\mathcal{J}M}{k_b T}) \tag{2.25}$$

For the case of the alloy model, although the Hamiltonian is the same form as above, we are working with a fixed order parameter or concentration, and therefore constrain the field H or analogously the chemical potential, to be zero. This yields the equation:

$$M = \tanh(\frac{T_c^{MF}}{T} M) \tag{2.26}$$

where the mean field transition temperature $T_c^{MF} = \frac{q\mathcal{J}}{k_b}$. Above this temperature, there is only one solution to equation 2.26 at $M \equiv 0$, but below it there is an additional solution, at a non-zero M value. Where this non-zero solution vanishes defines the transition temperature. Equation 2.26 is a transcendental equation with no analytic solution, but it is easily solved numerically, by the bisection method [76], to obtain the mean field temperature T^{MF} as a function of the order parameter M. This forms the mean field phase diagram for the alloy model and is illustrated in figure 2.4. Note that this mean field phase diagram is independent of the lattice as yet. The implications of figure 2.4 are that the

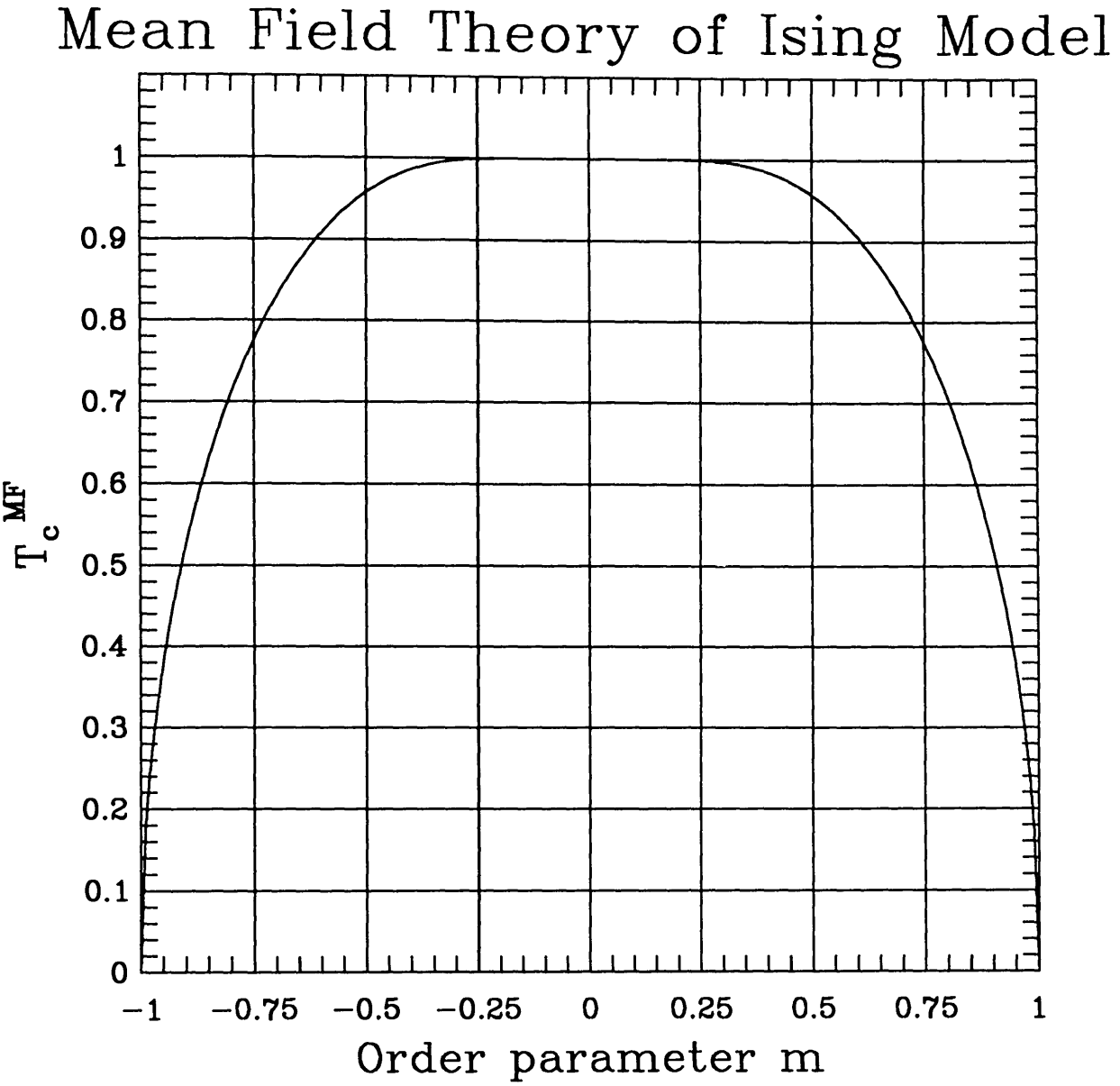

Figure 2.4: Mean field prediction for the Ising phase diagram, showing the transition temperature as a function of the order parameter or global concentration, $k_b T$ is set to unity here. Numerical values were obtained using the bisection method.

square alloy model should have a transition temperature at a critical coupling value of $K_c \equiv \frac{\mathcal{J}}{k_b T_c} = \frac{1}{4}$ and the cubic system at $K_c = \frac{1}{6}$, for the symmetric case of 50% concentration. Although the essential shape of figure 2.4 is thought to be correct, the transition temperature is known to be too high, the actual values of the critical coupling being $K_c^{square} \sim 0.440686$ from the Onsager solution to the square Ising lattice [77], and approximately $K_c^{cubic} \sim 0.221654$ from the most recent Monte-Carlo Renormalisation Group calculation on the Ising model [71]. It is therefore convenient to use these *known* values as reference values for the simulation work. They are correct for the critical concentration value of 50%, and although the exact values for the non-symmetric case are unknown, their ratios to the 50% value are probably given to within a factor of two by the corresponding mean field ratios given in table 2.1.

Concentration in alloy model $\% < c >$	Magnetisation in spin model $< M >$	Mean Field temperature T_c^{MF}
0	1.0	0
5	0.9	0.525431
10	0.8	0.710413
15	0.7	0.828635
20	0.6	0.907333
25	0.5	0.957504
30	0.4	0.985624
35	0.3	0.997414
40	0.2	0.999909
45	0.1	1.000000
50	0.0	1

Table 2.1: Values of the mean field temperature in units of $k_b T$, for various values of the order parameter. These were obtained using a bisection method and are accurate to 6 decimal places.

Table 2.1 shows that there is only a strong variation in transition temperature well away from the symmetric case of 50%. Throughout this work, the numerical values used for the quench temperatures are expressed as fractions of the accu-

rately known Onsager or MCRG values. It is more convenient for the purposes of computer simulation codes to express these as $A - A$ coupling values for the interaction between A-type atoms. Equation 1.6 shows that that the pair-wise interaction can be written in terms of the Ising coupling parameter as $V^{A-A} = 4\mathcal{J}$, with $V^{A-B} \equiv V^{B-B} \equiv 0$ for the case of nearest neighbour interactions. Table 2.2 gives the numerical values of V^{A-A} used for the simulations on square and cubic lattices and the corresponding fractions of the Onsager or MCRG temperatures.

Temperature Number	Fraction of Onsager or MCRG temperature	V^{A-A} for Square lattice	V^{A-A} for Cubic lattice
1	$\frac{1}{4}$	7.050976	3.546464
2	$\frac{1}{2}$	3.525488	1.773232
3	$\frac{3}{4}$	2.350325	1.182155
4	1	1.762744	0.886616
5	$\frac{5}{4}$	1.410195	0.709293
6	$\frac{3}{2}$	1.175163	0.591077
7	$\frac{7}{4}$	1.007282	0.506638
8	2	0.881372	0.443308

Table 2.2: Values of the A-A coupling used for computer simulations on square and cubic lattices and the corresponding Onsager or MCRG temperatures

These values were chosen to cover the range of interesting phenomena in the model systems. Although most of the simulation work was done using the 3-dimensional cubic lattice, it is illustrative to examine snap-shot configurations of the 2-dimensional square lattice. Figure 2.5 shows a typical sample for each of the temperatures listed above, at each of the fixed concentration values of A-type atoms, 10, 20, 30, 40 and 50%. The A-atoms are shown as black blocks, the B-atoms as white. The layout of this diagram is similar to that of the phase diagram in 2.4, and shows the phase separation effect.

Each configuration has evolved for some 2048 Monte-Carlo time steps or update attempts per site. This is roughly long enough to have achieved equilibrium for such a small lattice size as $64^2 = 4096$ sites.

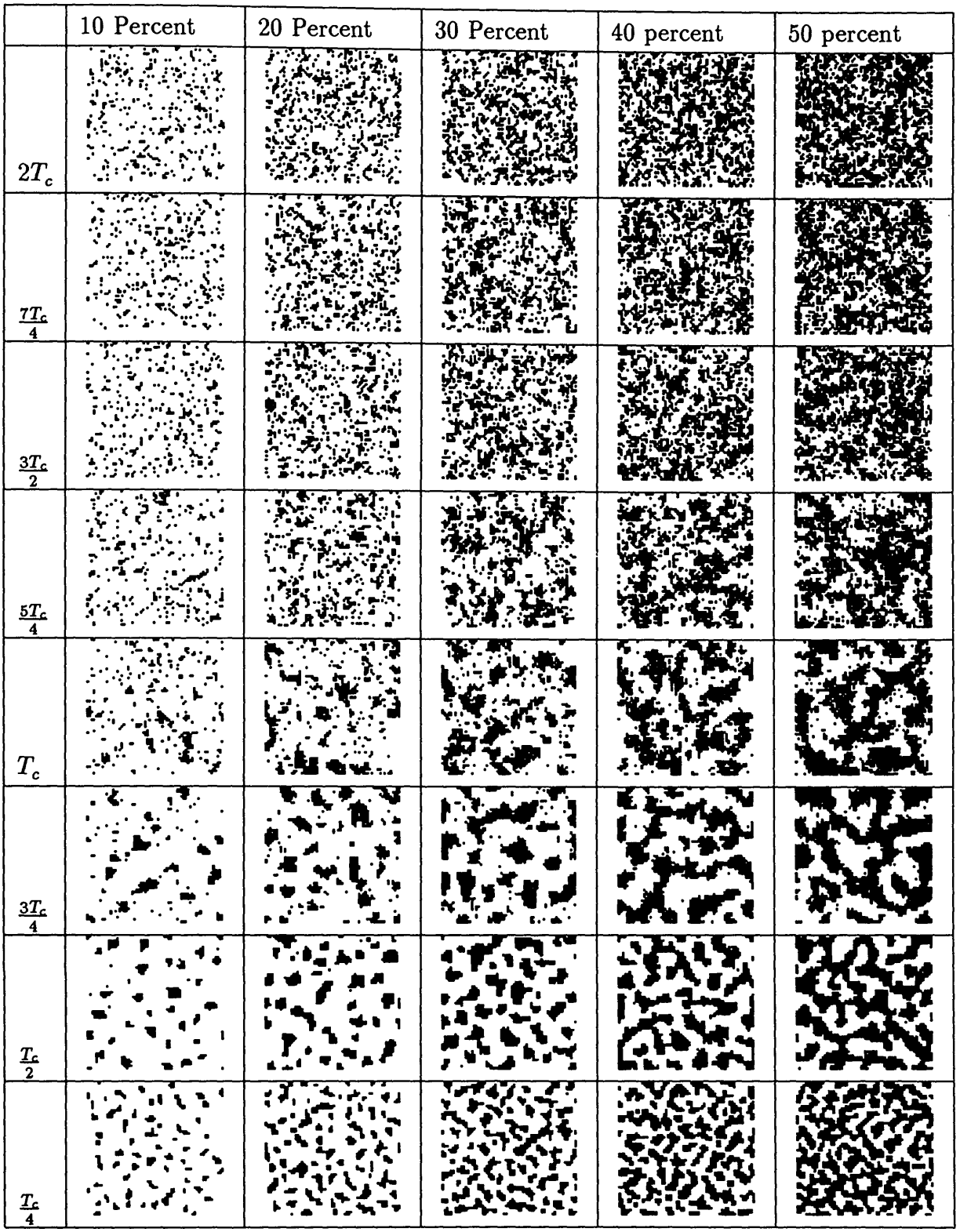

Figure 2.5: Binary alloy phase diagram showing snapshots of a 64×64 site alloy model at various fractions of the Onsager T_c after 2048 Monte-Carlo time steps following a quench from an initially random configuration.

Figure 2.5 shows that for temperatures well above T_c, there is little phase separation with time, and the configuration is qualitatively similar to that of the nearly infinite temperature, as represented by a completely random start. At the the higher concentrations, however, the A-atoms are forced to interact more and there *is* some significant domain formation. This increases dramatically below the transition temperature and the greatest characteristic domain size is for the 50% system just below T_c. In this system there is enough thermal energy for growth to occur quickly, and the process is rapidly dominated by a surface tension driven coarsening mechanism. At lower temperatures, there is insufficient thermal energy available, and while large length scale percolated structures still form, they coarsen much more slowly. The percolation transition is not a fixed property of the lattice, and has been shown to depend on the quench temperature [37]. At high temperatures, it is not significantly modified from 0.59275 [78] for site percolation on the square lattice. This is lowered considerably at temperatures below T_c and percolated structures exist in the 40% configuration, just below T_c.

On further cooling however, the domains coarsen so quickly that they do not percolate. Furthermore, at very low temperatures, the monomer population drops considerably, and since the monomers are the only means of concentration transport, the domains remain smaller and more compact. At such low temperatures, the only mechanism for re-arrangement is that of surface tension, whereby atoms can move along the surface of a domain, without the need for any thermal excitation to break a bond.

At low concentrations, growth is even more limited by the size of the monomer populations. Monomer have to travel further between the growing domains, and at low temperatures are much less likely to be able to escape capture by the domains. The diagram shows that the domains at $\frac{T_c}{2}$ are much more compact and symmetric than those at $\frac{T_c}{4}$.

Figure 2.5 give a qualitative feel for the phase diagram of the binary alloy. There is no evidence to suggest that the mechanisms in a three dimensional system are different from that of the two dimensional system, although the numerical values of the transition temperature and percolation limit are altered.

2.6 Monte-Carlo Simulated Data

This section discusses a number of computer simulation experiments on the binary alloy system and presents a number of measurements that can be made on the generated configurations. The aim is to characterise the length scales present in the system in a quantitative manner, to summarise the phenomena exhibited in figure 2.5. The following sections describe various measurements on the computer simulated system, how they were made, and the results.

The work is divided into studies of quench experiments with a cubic lattice of $32^3 = 32,768$ sites, at concentrations of between 10% and 19% of A-Atoms, and on a lattice of $128^3 = 2,097,152$ sites with a concentration of 50%. In each case, the configuration was initialised randomly, and evolved for a number of Monte-Carlo update steps at a fixed quench temperature. A number of parallel computational techniques were used to speed up these experiments and the measurements. Details of these techniques can be found in appendix A.

2.6.1 Relaxing Energy

One of the simplest measurements to make on the configuration is that of the energy. It is of interest to know the bulk energy of the system held by the number of like-like bonds, and the surface or interface energy held by the number of broken bonds. Figure 2.6 illustrates the growth of the number of A-A bonds with time for a number of quench temperatures. Two curves are shown for each temperature, representing experiments with an A-atom concentration of 10% and 19%. The 10% system always has fewer A-A bonds, even if the data were presented as mean numbers per A-atom. This reflects the surface tension coarsening mechanism available to the higher concentration system. The curves reach a steady value within approximately 100 time steps, indicating that the systems are close to equilibrium. The deep quench curves can be fitted by a power law in time, of the form $N^{A-A} \sim t^x$, where x is close to $\frac{1}{3}$. This scaling behaviour is discussed in chapter 5.

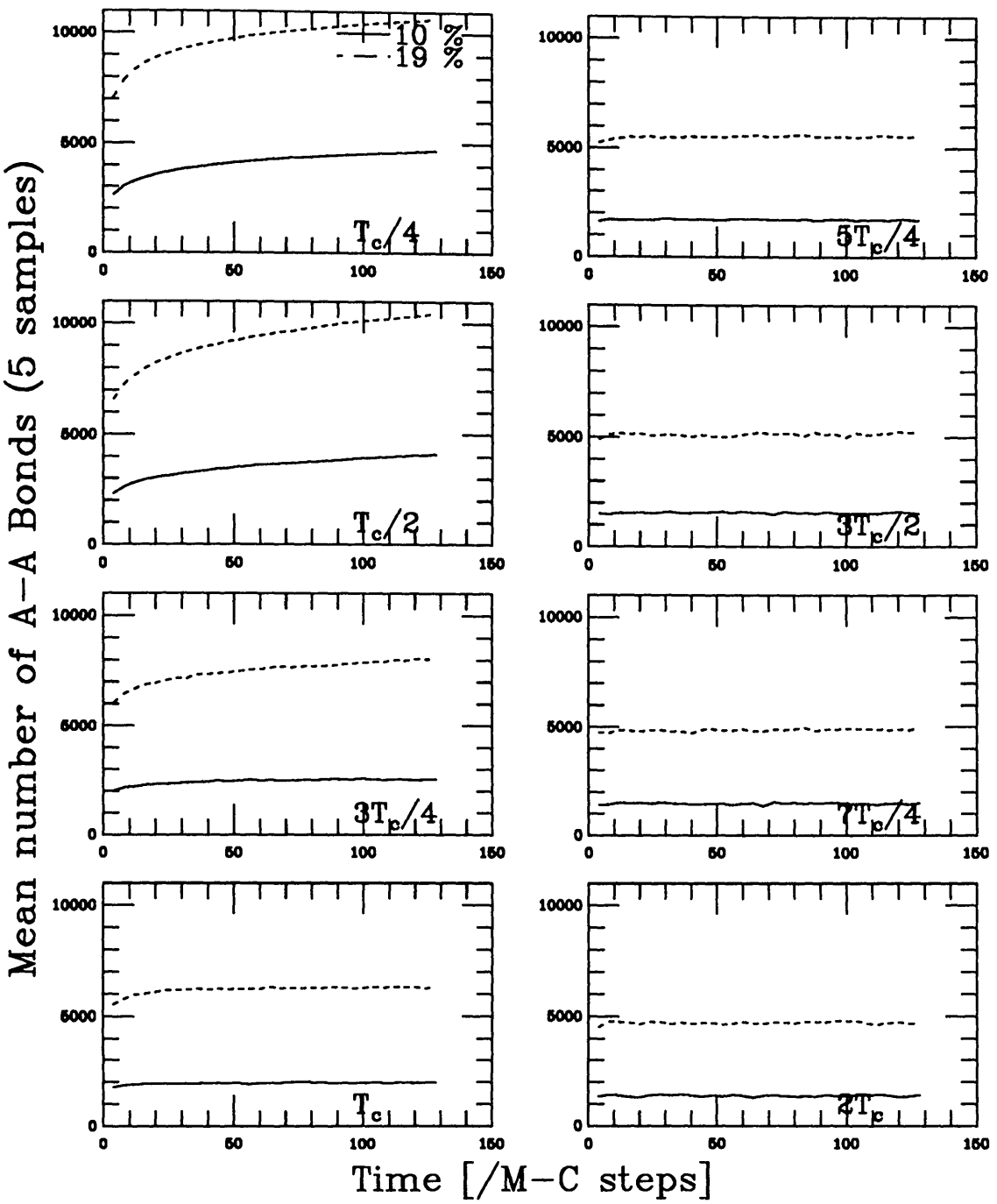

Figure 2.6: The number of A-A bonds present in a simulation of a cubic lattice, with 10% and 19% A-atom concentrations. This is representative of the bulk energy in the system. Evolution was for 128 Monte-Carlo time steps following a quench to the stated temperatures from a pseudo infinite temperature. The curves represent an average over 5 independent samples.

Figure 2.7 shows the surface energy given by the number of $A-B$ bonds. It is not surprising that this relaxes in the opposite direction to the number of like-like bonds, since the total number of bonds available in the system is fixed. There need not always be a trivial relationship between the number of like-like and unlike bonds, since the total number of bonds in the system can be diluted to simulate the presense of defects [79].

A similar measurement to the total energy is that of the mean co-ordination number. This gives a measure of the ratio between the bulk and surface energy per site. It is not discussed here where we are primarily concerned with characterising the length scales present in the system. This measurement can be useful in determining the compactness of forming domains, and to an extent their shape if not symmetric. It is discussed in [80].

2.6.2 Cluster population

A more demanding measurement to make involves the cluster statistics of the simulated system. The size distribution and various moments of it are useful in characterising the domain growth. The computational work to obtain the cluster size distribution is quite large, and algorithms for this are discussed in appendix A. Ideally, what is required is a grouping of all A-atoms in the configuration into clusters, from which information all other cluster information can be calculated.

Figure 2.8 shows the cluster mass distribution function for three different concentrations after a quench to $\frac{T_c}{4}$. Note the drop in monomer and dimer populations, and a general shifting of the distribution to higher mean cluster mass, with increased concentration. These diagrams contain too much information and it is useful to examine some features in more detail.

Figure 2.9 shows the evolution of the number of separate clusters. The 10% system always has *more* or the same number of clusters than the 19% system. For deep quenches, the form of the curves is that of an exponential and a flat background.

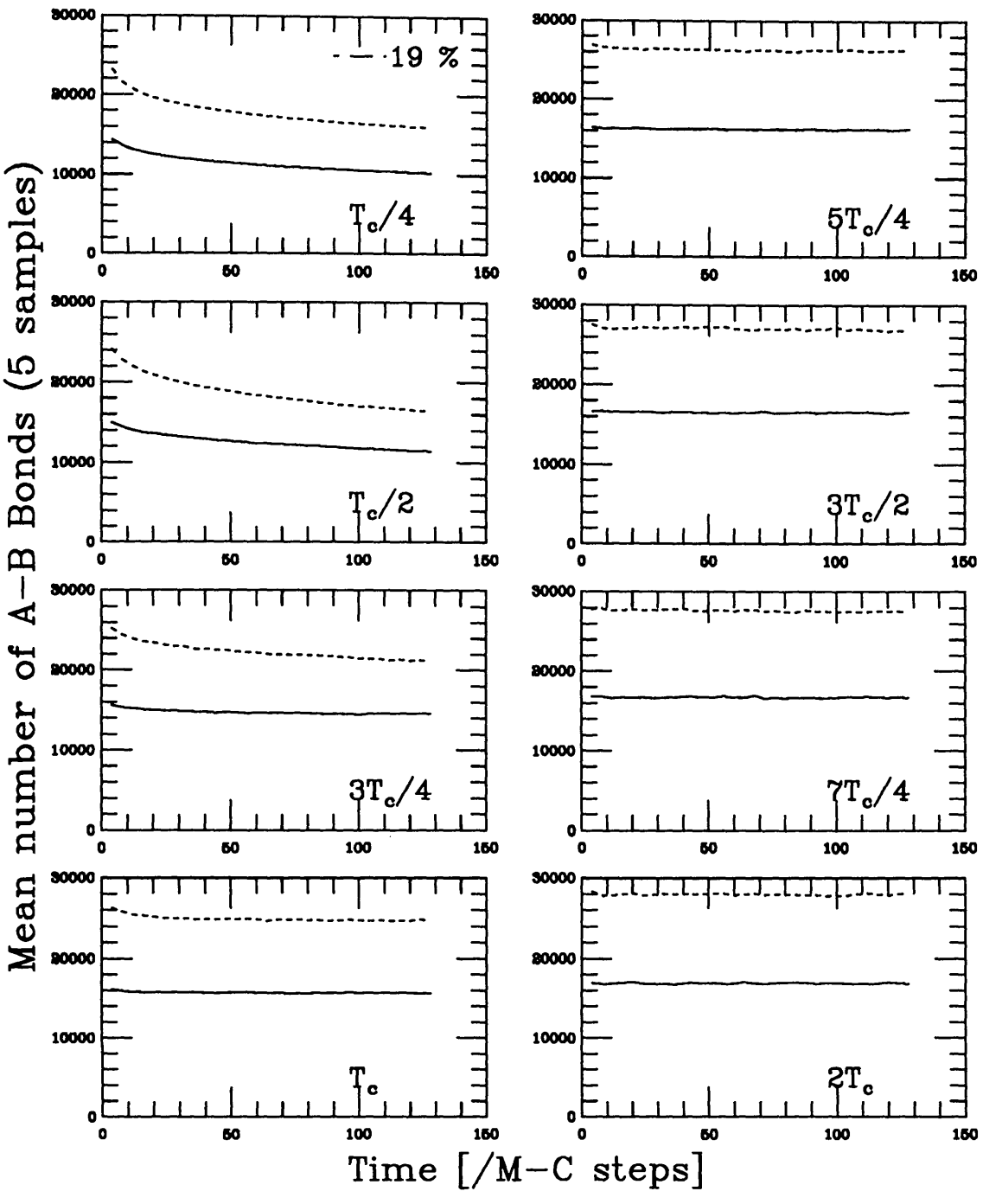

Figure 2.7: The number of A-B bonds present in a simulation of a cubic lattice, with 10% and 19% A-atom concentrations. This is representative of the surface energy in the system. Evolution was for 128 Monte-Carlo time steps following a quench to the stated temperatures from a pseudo infinite temperature. The curves represent an average over 5 independent samples.

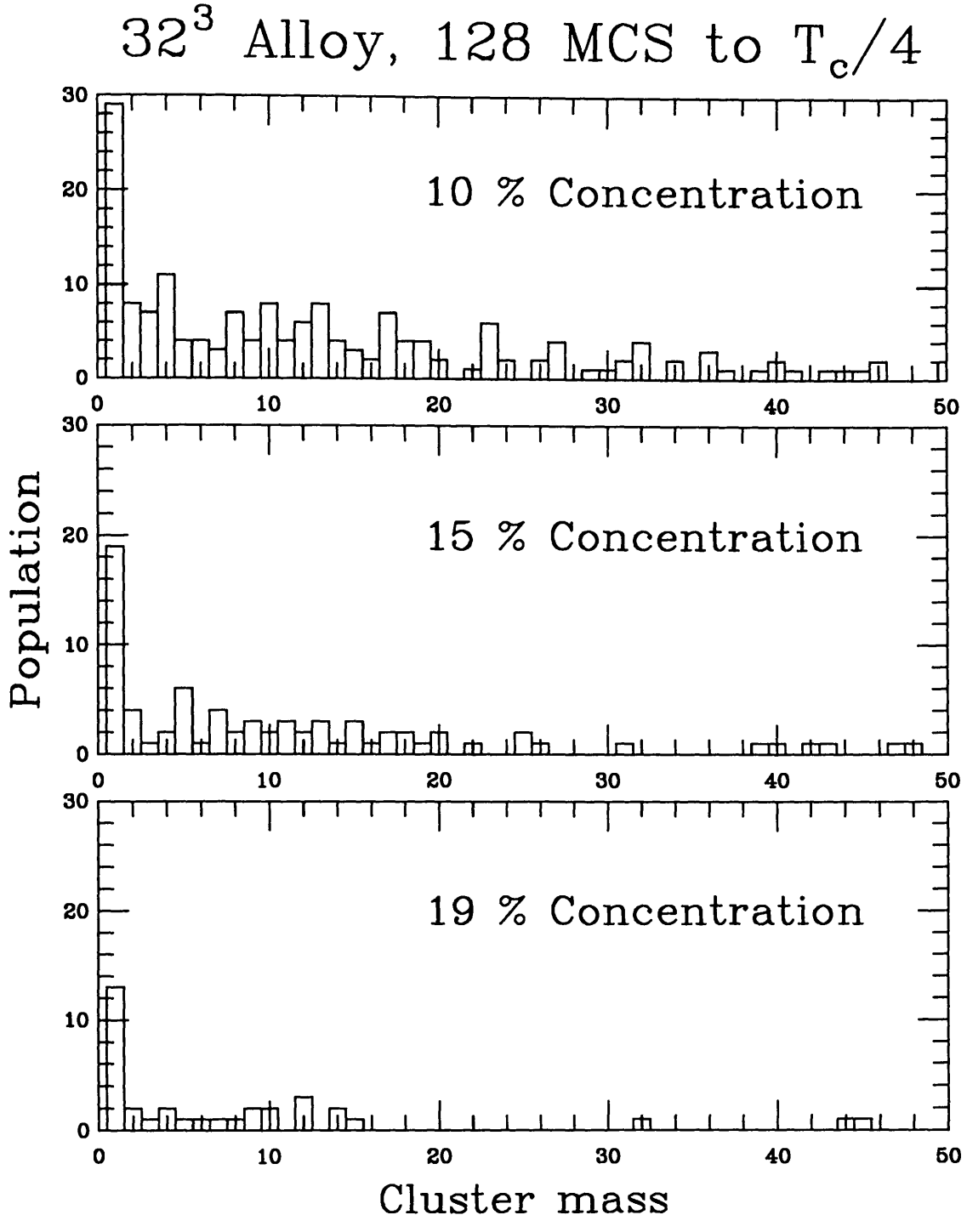

Figure 2.8: The A-Cluster size distribution function in a simulation of a cubic lattice with 10%, 15% and 19% A-atom concentrations. Evolution was for 128 Monte-Carlo time steps following a quench to $\frac{T_c^{MCRG}}{4}$ from a pseudo infinite temperature.

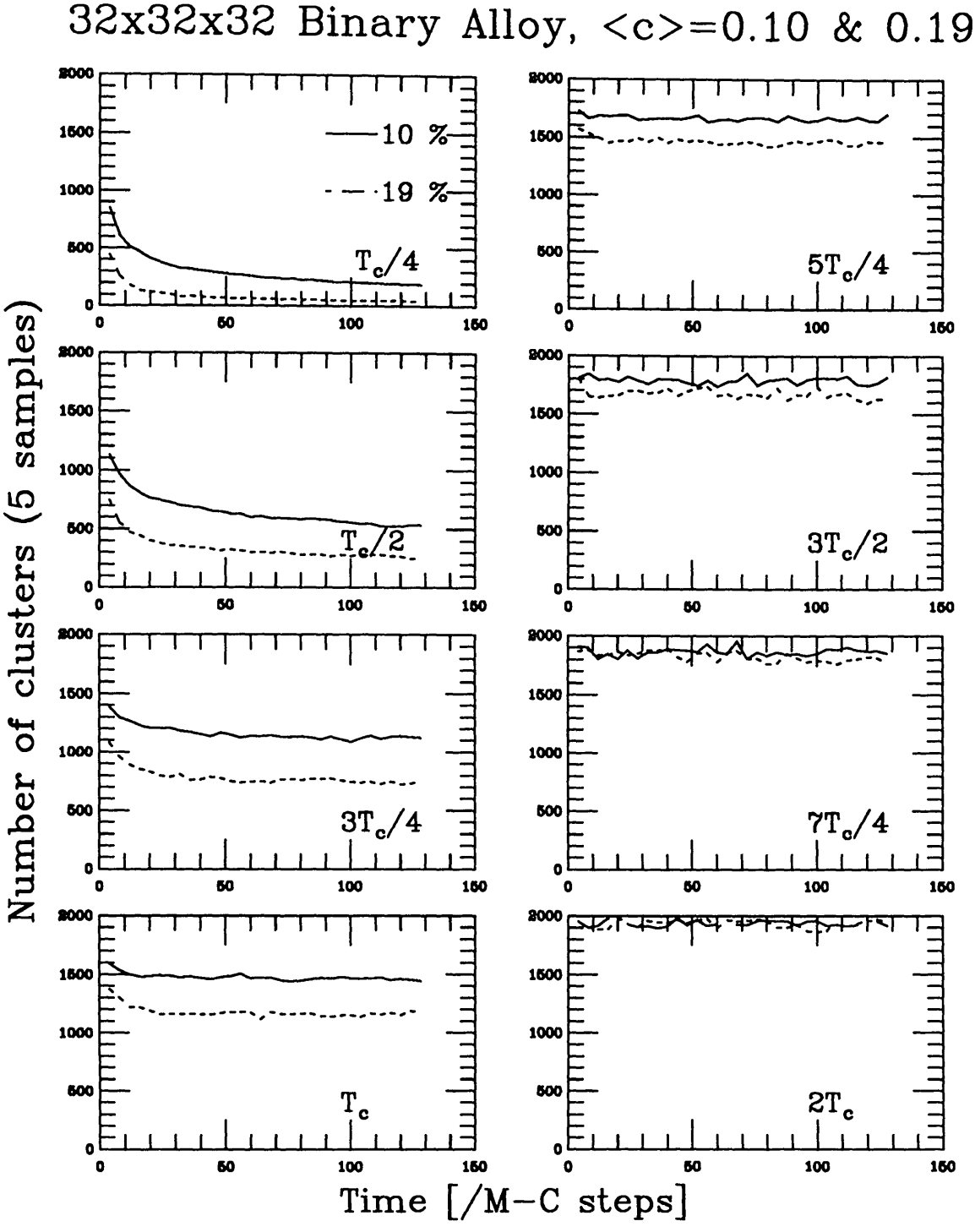

Figure 2.9: The number of A-Clusters in a simulation of a cubic lattice, with 10% and 19% A-atom concentrations. Evolution was for 128 Monte-Carlo time steps following a quench to the stated temperatures from a pseudo infinite temperature. The curves represent an average over 5 independent samples.

Figure 2.10 shows the mass of the largest cluster present in the system. The 19% configuration is above the percolation threshold, and consequently its behaviour is rapidly dominated by one large percolated cluster.

2.6.3 Transport Carriers

It is useful to focus attention on the population of small clusters, namely the A-monomers of mass one and A-dimers of mass two. The monomers are the most mobile of all clusters and their migration constitutes the main transport mechanism in the model alloy. The dimers can only break up to form monomers if there is sufficient energy to break their single bond. This can occur fairly easily at finite temperatures, and the dimer population is also a useful clue to thermal activity in the alloy. Figure 2.11 and 2.12 show the monomer and dimer population evolutions respectively for the 32^3 site cubic system.

The monomer and dimer populations both exhibit the effect of the percolation transition whereby the 10% concentration system has a *higher* population of such small clusters, since they have not been captured by dominant percolating cluster as in the case of the 19% system. The dimer population is less susceptible to the percolation transition than that for the monomers. In the case of dimers, the curves have converged within the size of fluctuations present, at a temperature of $2T_c$.

2.6.4 Particle Size Characterisation

While the cluster masses are a good general indicator of the characteristic length scale of the growing domains, it is better to compute actual lengths, in the form of radii of gyration of the A-clusters. This is defined for each cluster i as:

$$(R_i^g)^2 = \sum_j (r_j - R_i^{CM})^2 \tag{2.27}$$

where R_i^{CM} is the centre of mass of cluster i. These curves are noisy, but are a good measure of the characteristic length present in the unpercolated system. The

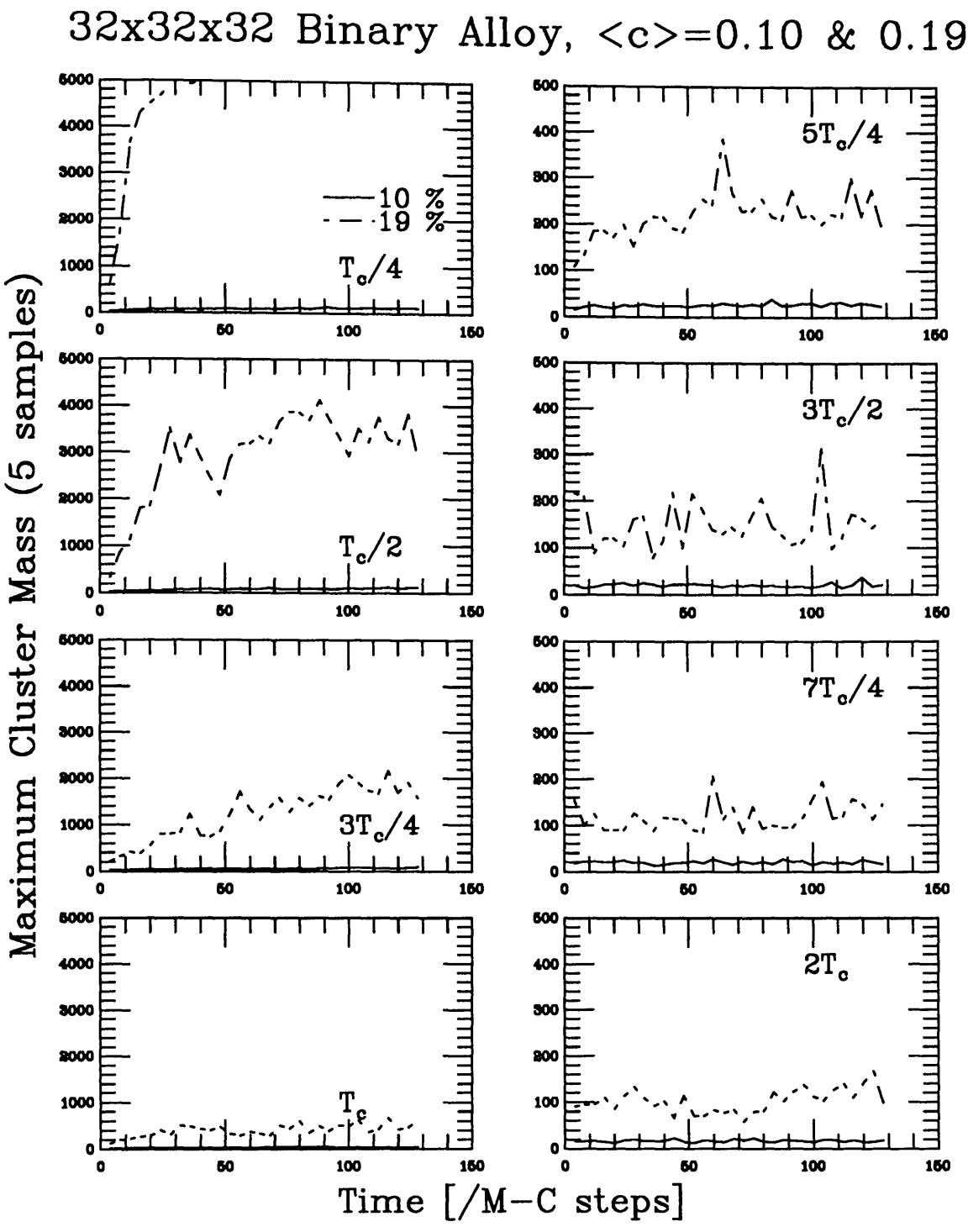

Figure 2.10: The mass of the largest A-Cluster in a simulation of a cubic lattice, with 10% and 19% A-atom concentrations. Evolution was for 128 Monte-Carlo time steps following a quench to the stated temperatures from a pseudo infinite temperature. The curves represent an average over 5 independent samples. Note the different scales on the left and right.

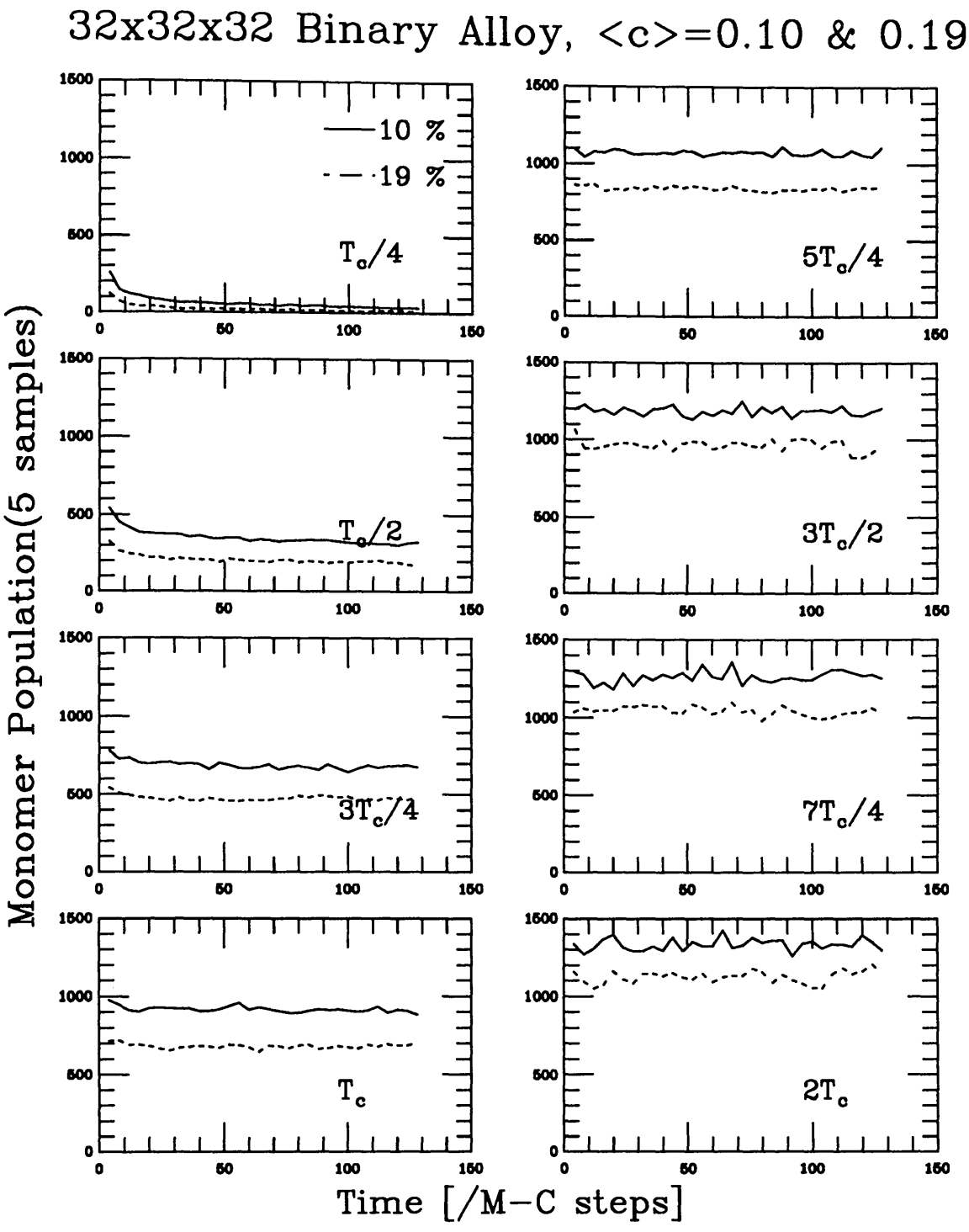

Figure 2.11: The population of A-monomers present in a simulation of a cubic lattice, with 10% and 19% A-atom concentrations. Evolution was for 128 Monte-Carlo time steps following a quench to the stated temperatures from a pseudo infinite temperature. The curves represent an average over 5 independent samples.

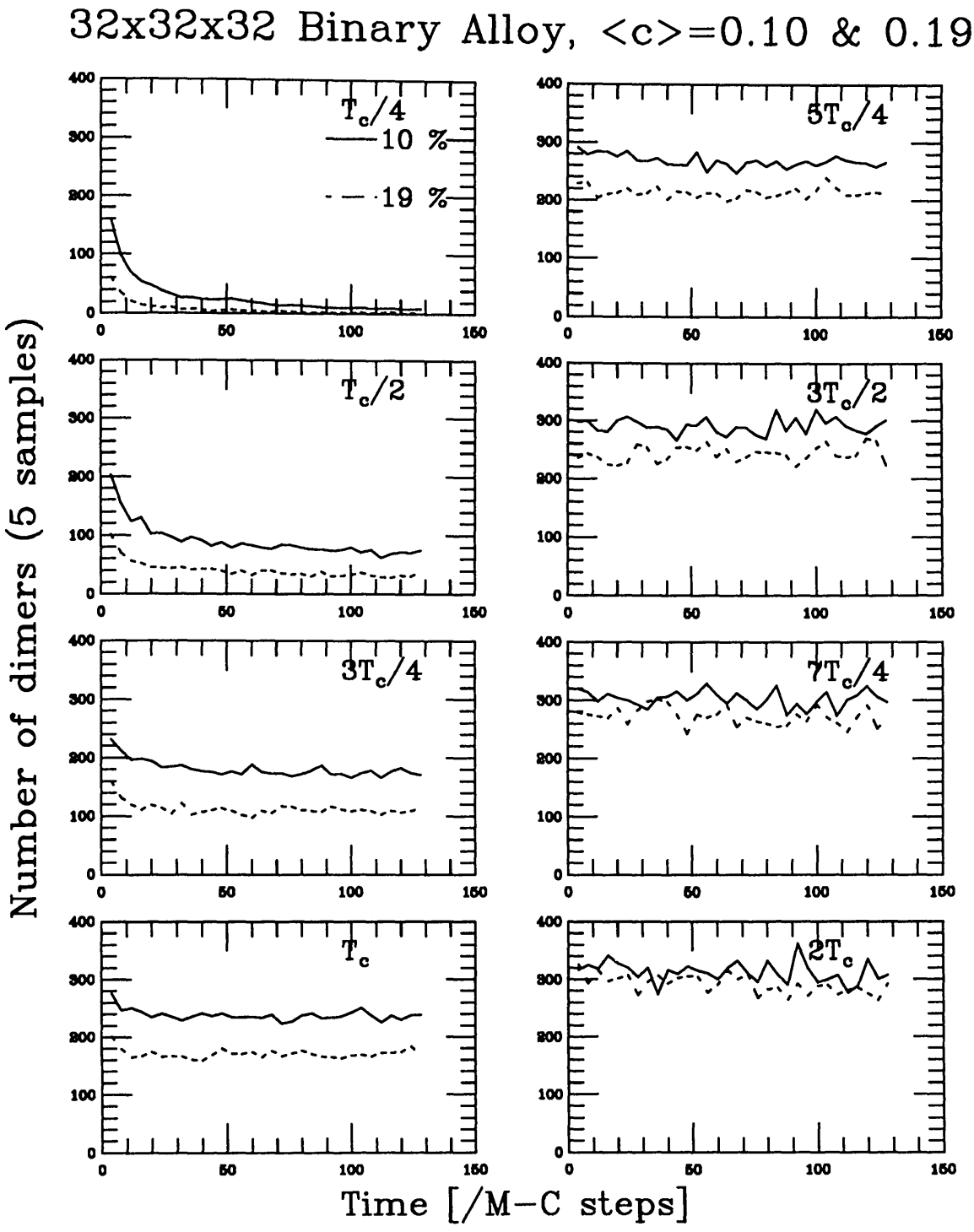

Figure 2.12: The population of A-dimers present in a simulation of a cubic lattice, with 10% and 19% A-atom concentrations. Evolution was for 128 Monte-Carlo time steps following a quench to the stated temperatures from a pseudo infinite temperature. The curves represent an average over 5 independent samples.

curves are roughly of the form $R(t) \sim t^x$, the exact value of x is discussed in chapter 5. Above percolation, the algorithm fails and returns too large a characteristic length as shown. For a percolated system it is not really meaningful to refer to a radius of gyration. The only means of determining a sensible length scale involves the scattering experiments described in the next section.

2.6.5 Simulated Scattering

It is possible to carry out a numerical scattering experiment on the simulated configurations, using a Fourier transformation of the concentration distribution. This is expressed by:

$$S(\mathbf{q},t) = \frac{1}{N}\sum_{\mathbf{r}} e^{i\mathbf{q}.\mathbf{r}} \sum_{i} \langle [c_i(\mathbf{r_i},t) - \overline{c}][c_i(\mathbf{r_i}+\mathbf{r},t) - \overline{c}] \rangle \qquad (2.28)$$

where q is the wavevector in reciprocal space and is given by $q = \frac{2\pi}{r}$ if r is a distance in the position space of the configuration. The c_i are the concentration variables and $\overline{c} =< c >$ is the global mean concentration and is equal to 0.5 for a 50% system. $S(\mathbf{q},t)$ is effectively a structure function characterising the domains in the system. It is most useful if it is averaged spherically to give $S(q,t)$. A discussion on the best algorithms for obtaining $S(q)$ is given in appendix A. Figure 2.14 shows this structure function computed for a simulation of a 50% system on a 128^3 site cubic lattice. A large number of averages and a large lattice size are necessary to obtain cleanly defined curves. Figure 2.14 shows that the 'scattering' from the configuration is in the form of a low intensity peak in q space, that intensifies and shifts to lower peak positions with ageing time, following a quench experiment. This behaviour was is discussed for a two dimensional system in [10], and is qualitatively similar to that of the three dimensional system here.

The position of the peak defines a characteristic size or length scale R_{Max} in the evolving alloy. Figure 2.15 shows this length scale plotted against simulation time since the quench. The curve is dominated by a power law of the form $R_{Max} \sim t^x$. The fact that x is less than unity illustrates the hydro-dynamic slowing down effect. The growing domains in the alloy are using up the available solvent, and thus growth slows down with time.

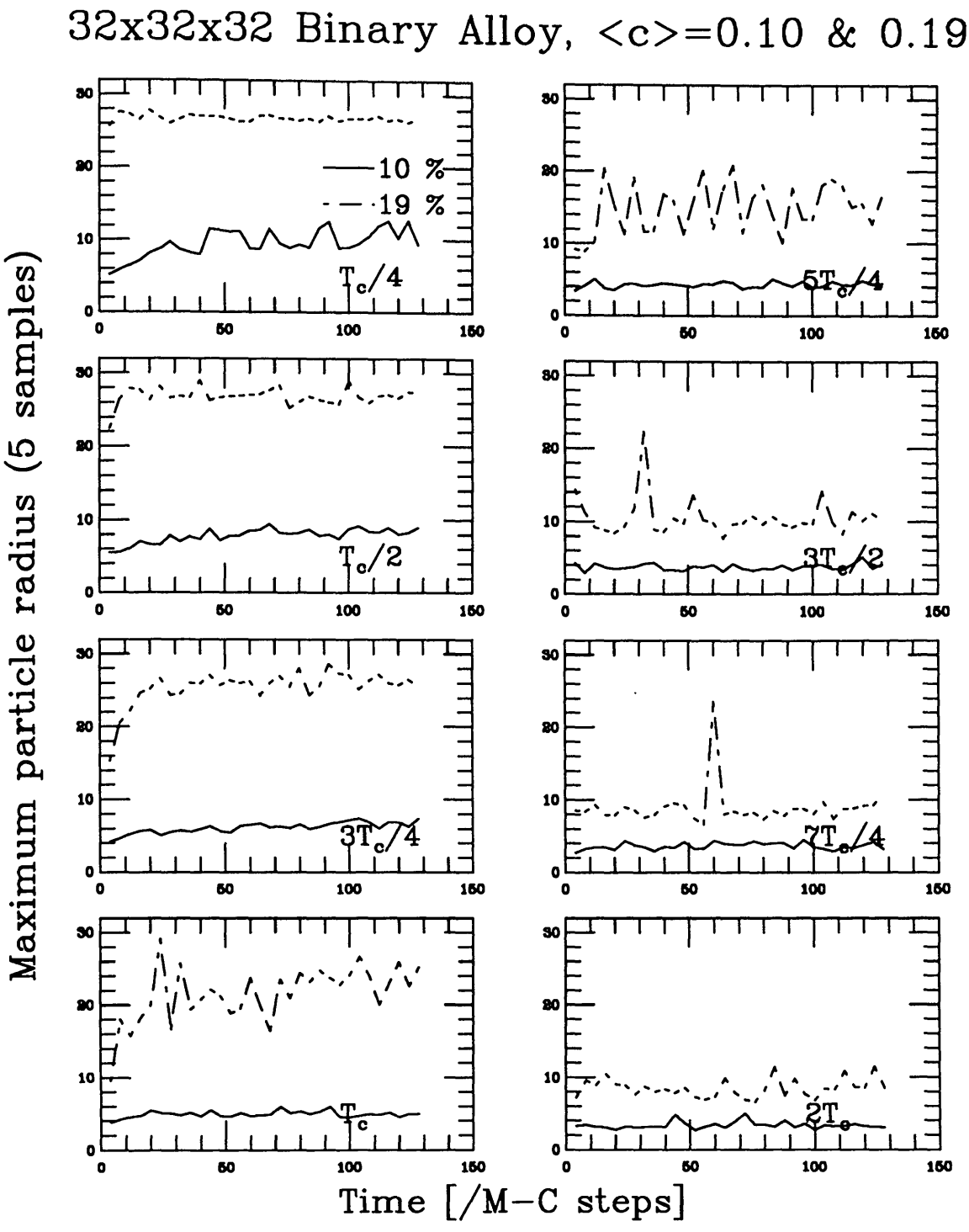

Figure 2.13: The radius of gyration of the largest particle present in a simulation of a cubic lattice, with 10% and 19% A-atom concentrations. This is representative of the surface energy in the system. Evolution was for 128 Monte-Carlo time steps following a quench to the stated temperatures from a pseudo infinite temperature. The curves represent an average over 5 independent samples.

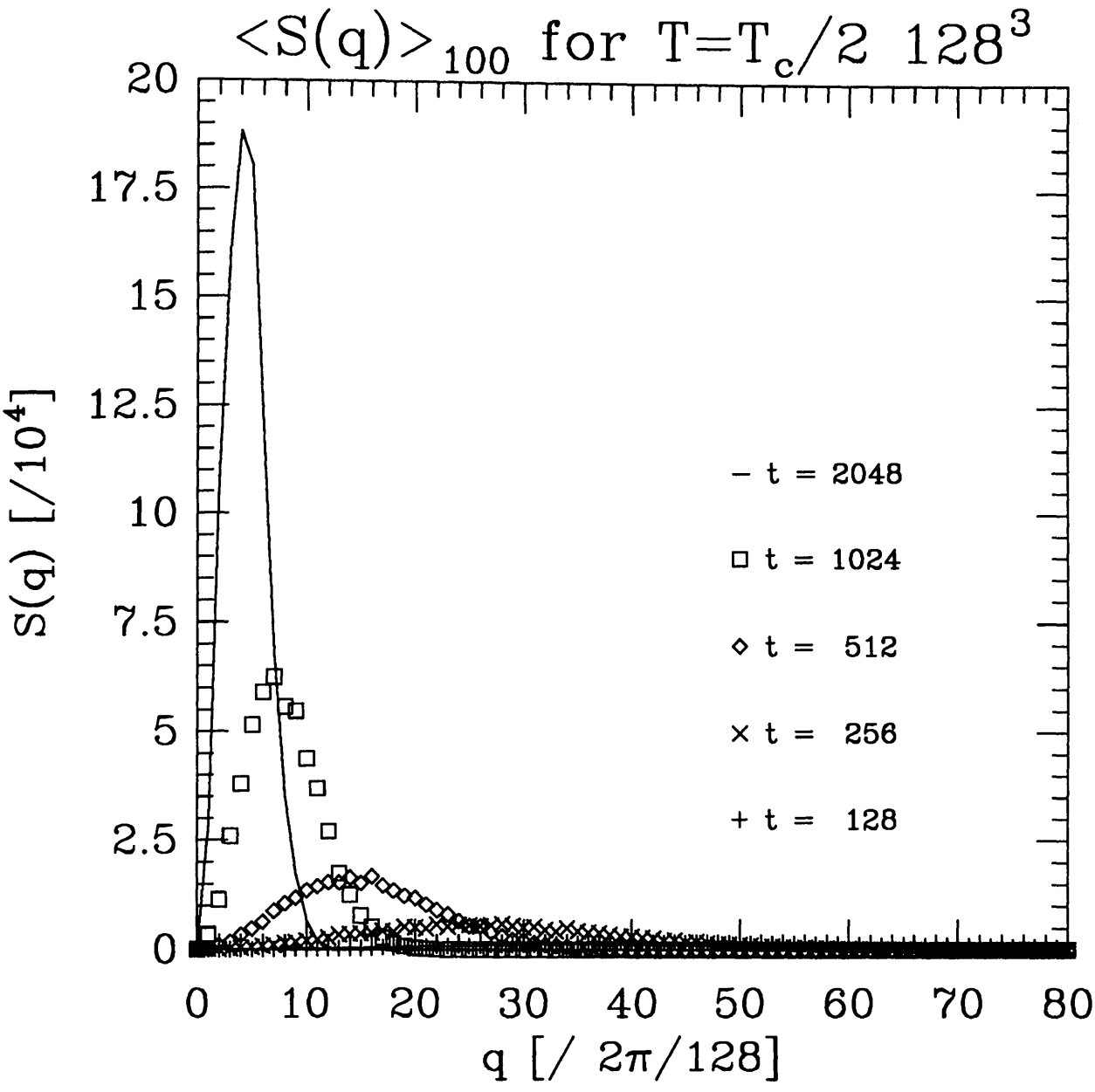

Figure 2.14: The structure function computed from an average of the Fast Fourier transforms from 100 independent samples each of size 128^3, all at $T = \frac{T_c}{2}$ at the number of time steps indicated. The system has a concentration of 50% of A-atoms.

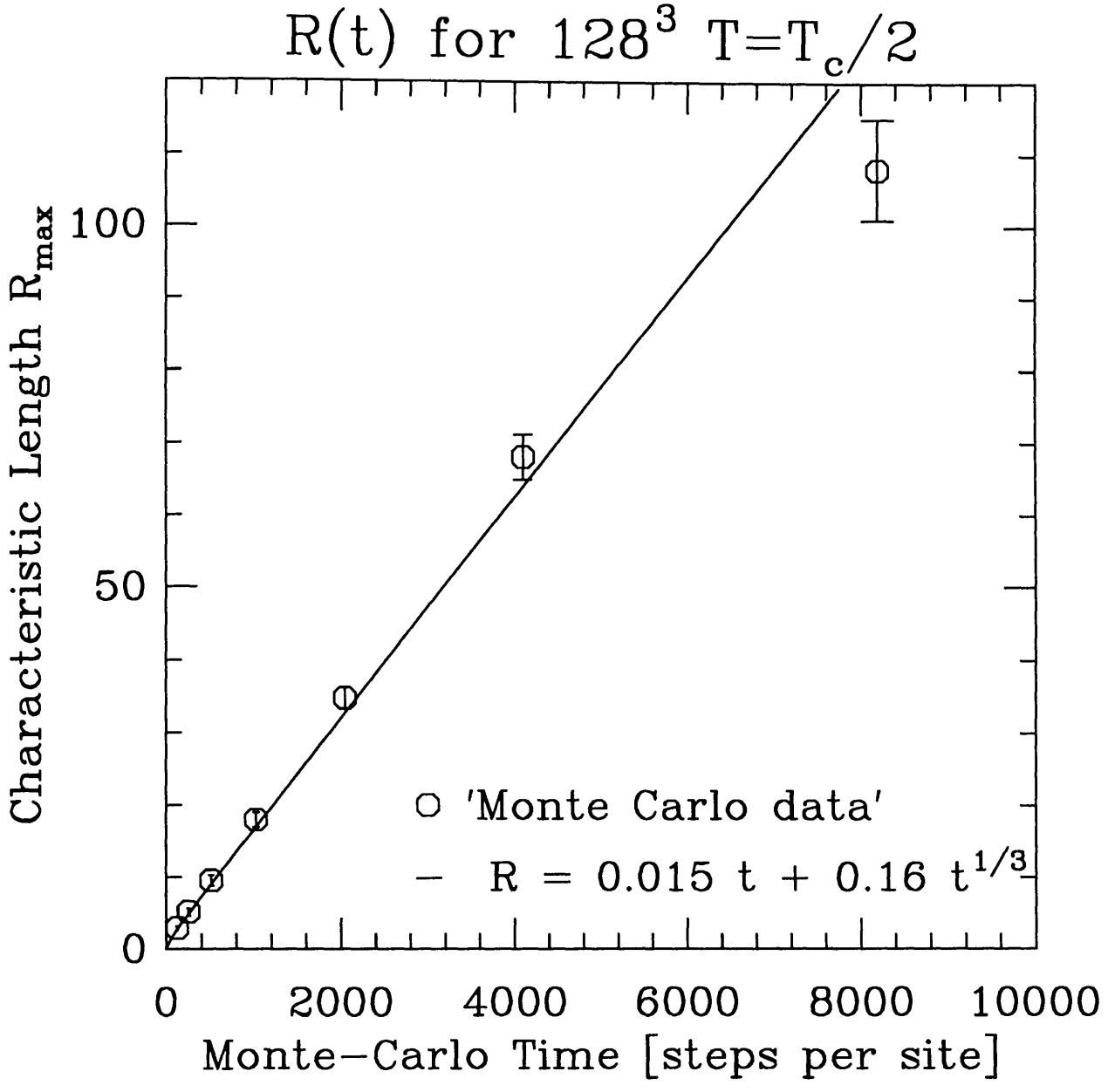

Figure 2.15: Fitted characteristic size from the peaks in the structure factor for the Fourier transformation of a 50% concentration system on a cubic lattice of 128^3 sites.

The volume fraction of the cubic system that is occupied by the growing domains of A-enriched phase is also of interest. An approximate measure of this is the integrated scattering intensity. This is shown in figure 2.16 and as seen it increases monotonically but slows down with time as the available solvent is used up.

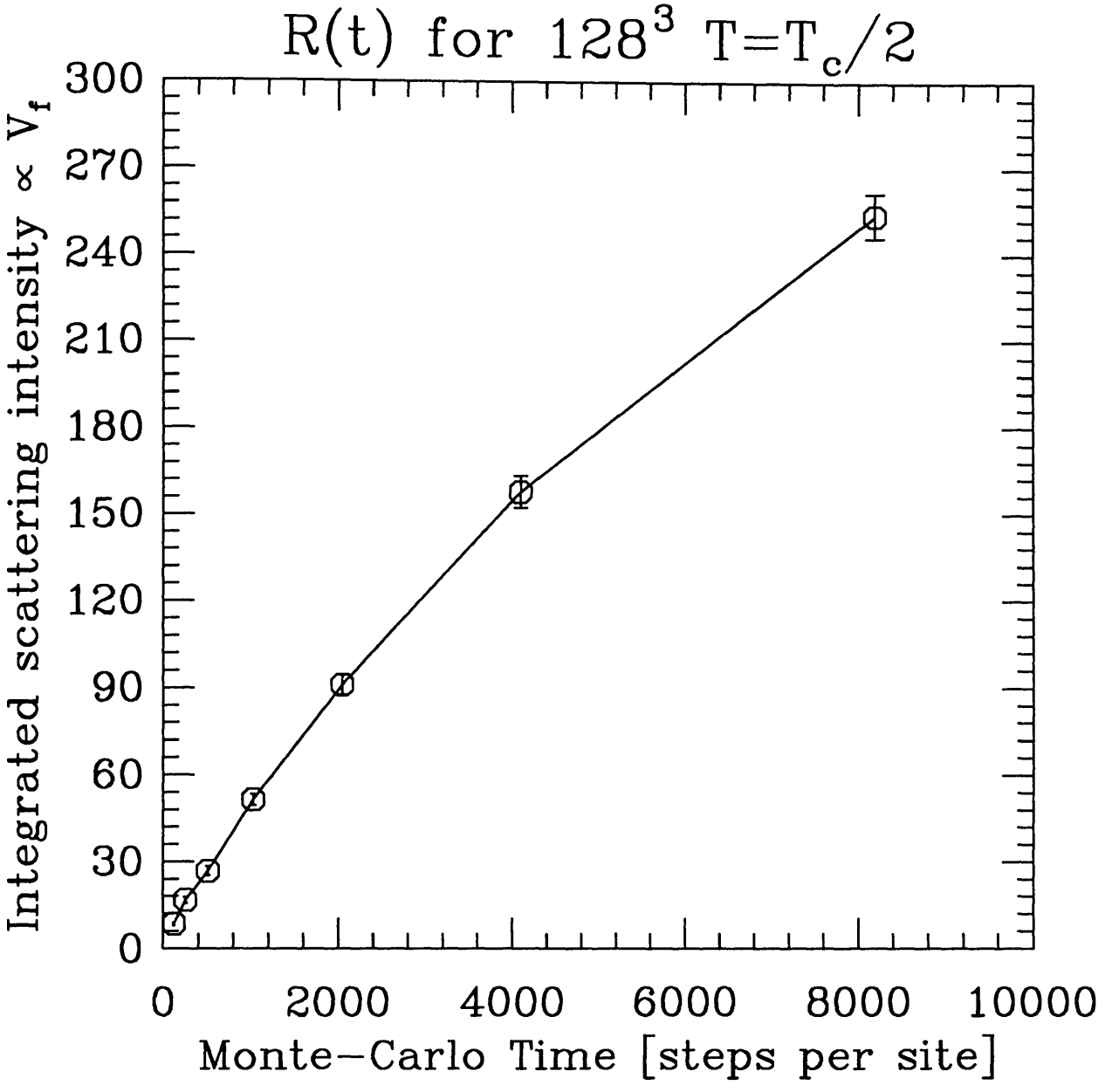

Figure 2.16: Integrated total intensity of the structure factor from the Fourier transformation of the configurations generated during a simulation of a 50% concentration system on a 128^3 site lattice. This is proportional to the total volume fraction of the precipitate phase.

Chapter 3

Theories for Binary Phase Separation

This chapter describes an investigation of the theory of phase separation in a binary system. The Cahn-Hilliard-Cook (CHC) *equation* is derived and is shown to give a reasonable representation of phase separation and decomposition in a binary system, providing one accepts that it cannot be applied successfully without resorting to numerical methods. The Cahn-Hilliard-Cook *theory* is essentially a mean field approximation to the time-dependent Ginzburg-Landau equation for the free energy of a binary system. The differential equation that describes the phase separation cannot be solved analytically, and requires further approximation. Alternatively it can be solved numerically for a particular set of parameters.

An elementary droplet theory is also discussed in the context of predicting the particle size distribution for an ageing alloy, following a quench. The Becker-Doring formulation is used to obtain a crude prediction of the droplet distribution. The weaknesses of the Becker-Doring theory and and possible extensions to this theory are also discussed.

3.1 Derivation of Cahn-Hilliard-Cook Theory

This section provides a brief overview of the Cahn-Hilliard-Cook (CHC) theory and outlines its shortcomings. The main idea behind the theory is that the rapidly varying atomic concentration variables $\{c_i\}$ can be replaced by a more smoothly

varying continuous field variable $\phi(\mathbf{r})$ which represents an average value of the excess concentration of A-atoms over a macroscopic spatial cell. The field variable is a scalar defined to lie on $[-1, 1]$, with the extremum values representing an excess of B-atoms (-1) and an excess of A-atoms $(+1)$ respectively.

3.1.1 Helmholtz Free Energy of a Binary Solution

Consider the Helmholtz free energy for an isotropic binary solid in solution and having a non-uniform composition. A convenient form for this is the Ginzberg-Landau functional [20]:

$$\frac{\mathcal{F}\{\phi(\mathbf{r})\}}{k_b T} = \frac{F_0}{k_b T} + \int_V \left\{ f\{\phi(\mathbf{r})\} - \frac{H}{k_b T}\phi(\mathbf{r}) + \frac{1}{2d}[R\nabla\phi(\mathbf{r})]^2 \right\} d\mathbf{r} \qquad (3.29)$$

The scalar field $\phi(\mathbf{r})$ describes the composition as a function of position $\mathbf{r}$. The interaction range is described by $\frac{R}{d}$ and the applied field is H. For this work, the atomic concentration is fixed, so that the applied field H is set identically to zero for an equal concentration of A-type and B-type atoms.

The phase separating alloy may be thought of as a set of macroscopic cells, each containing a volume of space and a number of atomic sites. These cells must be large enough for a local instantaneous free energy function $f(\mathbf{r})$ to be defined, but small enough that the effect of 'relevant' short length scale composition fluctuations are not integrated out. It is convenient to write this local free energy density function $f\{\phi(\mathbf{r}, t)\}$ in the Landau form:

$$f\{\phi(\mathbf{r}, t)\} = f_0 - \frac{1}{2}b(\phi(\mathbf{r}, t))^2 + \frac{1}{4}u(\phi(\mathbf{r}, t))^4 + \cdots \qquad (3.30)$$

where $b, u > 0$. The form of the local free energy for one cell is shown in figure 3.1. It has a double minimum for the homogeneous case and relaxes towards a single minimum after the quench. A distinction is usually drawn between different regions of the phase diagram from points on this double well functional. The central local maximum in the free energy is separated from the two minima by points of inflection where $f'' \equiv \frac{d^2 f}{d\phi^2} = 0$. These points mark the division between the metastable $f'' > 0$ and unstable $f'' < 0$ regimes. The locus of points where $f'' = 0$ defines the spinodal curve in the temperature-composition phase diagram of figure 3.1.

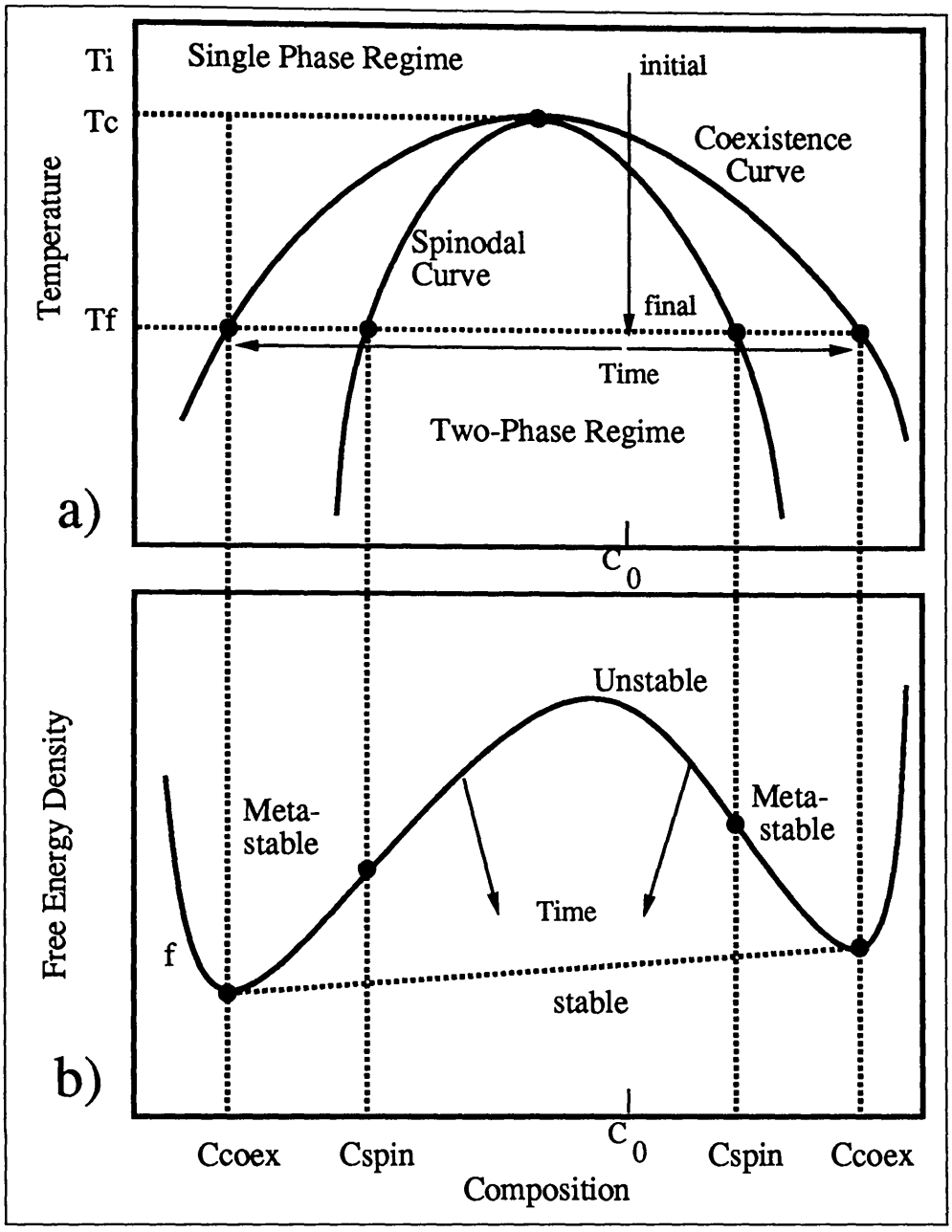

Figure 3.1: a) sketch of phase diagram for binary material, showing coexistence and spinodal curves. b) corresponding free energy curve showing stable, metastable and unstable regimes. We are typically interested in quench experiments, where the system is initially at some temperature T_i in the single-phase regime, and is quenched to an unstable point (T_f, c_0) in the two phase regime.

For a quench in a system of given composition c_0 between the spinodal points, f'' is negative and the curve is always convex-down causing a negative $\mathcal{F}$. In this case there is no barrier to a fluctuation of any amplitude and the kinetic process is governed solely by diffusion. For a c_0 lying outside the spinodal points only large amplitude composition fluctuations will lower the free energy of the system. This requires sufficient thermal energy in the system to overcome the barrier.

3.1.2 Conservation Law

In a real material the number of atoms of a given species is conserved and hence the concentration field must also be. This is expressed by:

$$\frac{1}{V}\int_V \phi(\mathbf{r},t)\,d\mathbf{r} = c_A \tag{3.31}$$

where V is the system volume, and c_A the concentration of atomic species A. This conservation law implies that the local concentration field obeys a continuity equation of the form:

$$\frac{d\phi(\mathbf{r},t)}{dt} + \nabla.\mathbf{j}(\mathbf{r},t) = 0 \tag{3.32}$$

Which defines a concentration current $\mathbf{j}(\mathbf{r},t)$, assumed to be proportional to the gradient of the *local* chemical potential difference [1] $\mu(\mathbf{r},t)$ with constant of proportionality m, the mobility.

$$\mathbf{j}(\mathbf{r},t) = -m\nabla\mu(\mathbf{r},t) \tag{3.33}$$

The chemical potential difference is, by definition:

$$\mu(\mathbf{r},t) = \frac{d\mathcal{F}\{\phi(\mathbf{r},t)\}}{d\phi(\mathbf{r},t)} \tag{3.34}$$

Where $\mathcal{F}$ is the Landau functional given above in equation 3.29. Differentiating this functional with respect to ϕ and assuming a scalar mobility yields the chemical potential difference as:

$$\mu(\mathbf{r},t) = \left.\frac{\partial f}{\partial\phi}\right|_T - \frac{R^2}{d}k_bT\nabla^2\phi(\mathbf{r},t) \tag{3.35}$$

[1] The global chemical potential is identified with the field term in the Ising Hamiltonian and is identically zero for a system of conserved concentration

which when substituted into the continuity equation 3.32 gives the Cahn-Hilliard equation [20] for the concentration field.

$$\frac{\partial\phi(\mathbf{r},t)}{\partial t} = m\nabla^2\left(\left.\frac{\partial f\left(\phi(\mathbf{r},t)\right)}{\partial\phi}\right|_T - K\nabla^2\phi(\mathbf{r},t)\right) \tag{3.36}$$

Where the parameter K is defined as:

$$K = \frac{R^2}{d}k_bT \tag{3.37}$$

Expanding equation 3.36 we obtain finally:

$$\frac{\partial\phi}{\partial t} = m\nabla^2\left(-b\phi + u\phi^3 - K\nabla^2\phi\right) \tag{3.38}$$

As indicated it is usual to truncate the series in the free energy at the ϕ^4 term, although some recent work has used up to the ϕ^6 term [81].

3.1.3 The Cahn-Hilliard Theory

Equation 3.36 is non-linear and therefore cannot be solved analytically, although a numerical approach is possible. As described in section 1.3.2 and [20], the Cahn-Hilliard theory proceeds by linearising the equation around $\phi = c_A$ to obtain:

$$\frac{\partial(\phi - c_A)}{\partial t} = m\nabla^2\left(\left.\frac{\partial f}{\partial\phi}\right|_{T,c_A} - K\nabla^2(\phi - c_A)\right) \tag{3.39}$$

This is Fourier-transformed using:

$$\Phi(\mathbf{q},t) = \int e^{i\mathbf{q}.\mathbf{r}}(\phi(\mathbf{r},t) - c_A)\,d\mathbf{r} \tag{3.40}$$

to yield:

$$\Phi(\mathbf{q},t) = \Phi(\mathbf{q},t{=}0)e^{B(\mathbf{q})t} \tag{3.41}$$

and the time amplification factor B is given by:

$$B(\mathbf{q}) = -m\mathbf{q}^2\left(\left.\frac{\partial f}{\partial\phi}\right|_{T,c_A} + K\mathbf{q}^2\right) \tag{3.42}$$

The structure function can be then obtained as an auto-correlation of the concentration field:

$$S(\mathbf{q},t) = \langle\,\Phi(-\mathbf{q},t)\,\Phi(\mathbf{q},t)\,\rangle|_T \tag{3.43}$$

Re-writing this in terms of the values just prior to the quench gives:

$$S(\mathbf{q},t) = \langle\, \Phi(-\mathbf{q},t=0)\,\Phi(\mathbf{q},t=0)\,\rangle|_T\, e^{2B(q)t} \tag{3.44}$$

The prefactor in 3.44 is the static structure factor of the initial state at T_0, just prior to the quench.

$$S_0(\mathbf{q}) = \langle\, \Phi(-\mathbf{q},t=0)\,\Phi(\mathbf{q},t=0)\,\rangle|_{T=T_0} \tag{3.45}$$

It is evident then that the linearised Cahn-Hilliard theory implies that fluctuations of $\mathbf{q}$ present in the initial state will grow exponentially with time following the quench if $B(\mathbf{q}) > 0$ but will decay to zero for $B(\mathbf{q}) < 0$. There is an implied critical wavevector $\mathbf{q}_c$ for which $B(\mathbf{q}) \equiv 0$. There has been recent controversy in the literature [21] about the validity of this linearised theory, but it seems clear that the theory is not valid for systems with short range interactions such as the alloy model used in this work. A full discussion of the failings of the theory is left to [21].

3.1.4 Cook's Extension to Cahn-Hilliard Theory

The Cahn-Hilliard theory as described above is essentially a mean field theory. That is, it approximates the interactions between the concentration variables by a mean value and ignores thermal fluctuations. It might be expected that consequently it will incorrectly predict the dynamical behaviour of the system. A simple extension to equation 3.36 was considered by Cook [24] in which an additional random force term ζ is added to give:

$$\frac{\partial\phi(\mathbf{r},t)}{\partial t} = m\nabla^2\left(\left.\frac{\partial f\,(\phi(\mathbf{r},t))}{\partial\phi}\right|_T - K\nabla^2\phi(\mathbf{r},t)\right) + \zeta(\mathbf{r},t) \tag{3.46}$$

This noise term is assumed to come from the very short time scale phonon modes of the alloy and is required to have the following properties:

$$\langle\zeta(\mathbf{r},t)\rangle = 0 \tag{3.47}$$

$$\langle\zeta(\mathbf{r},t)\zeta(\mathbf{r}',t')\rangle = -2k_bTm\nabla^2\delta(\mathbf{r}-\mathbf{r}')\delta(\mathbf{t}-\mathbf{t}') \tag{3.48}$$

Equations 3.47 and 3.48 express two things. Namely that there is no overall drift force and that the noise is uncorrelated in time, but partially correlated in

space such that there are no long wavelength components in the noise spectrum. The magnitude of the noise is set by k_bT and mobility m. More specifically, the ∇^2 in equation 3.48 expresses the conservation law for the field. A random force component which 'piles up' matter at one site must be exactly balanced by force contributions at neighbouring sites which deplete those sites of matter. The form of equation 3.48 ensures this is so.

The Cook noise term does not rescue the linearised theory from invalidity, but it does have important implications for numerical work. To date there have been no attempts to numerically solve equation 3.46, and is it still controversial whether the Cook noise term plays much importance in the long time dynamics of the alloy [82]. Evidence is presented below for the importance of the noise term, as a source of vital fluctuations in the early stages of decomposition.

3.2 Numerical Solutions

Although equations 3.36 and 3.46 are highly non-linear in nature, it is nevertheless possible to numerically integrate them in time to follow the structure evolution. Two numerical methods suggest themselves for equations of this type, namely the well known finite differencing method and a lesser known spectral method such as the Fourier analysis and cyclic reduction algorithm (FACR) [83]. The former is relatively easy to set up and has been considered by other authors for very simple cases [82, 84]. Unfortunately it is fairly demanding of computational power to perform the time and spatial integrals of realistic systems. The FACR algorithm is more complicated to implement and while in general a spectral method is more suited to a studying a theory formulated in terms of waves in Fourier space, this algorithm is not suitable for comparison with the Monte Carlo simulations in position space since it does not yield a real space representation of the concentration field.

Subsection 3.2.1 discusses suitable finite differencing schemes for solving the Cahn-Hilliard equation and subsection 3.2.3 describes the analysis of the integrated trajectories.

3.2.1 Finite differencing Schemes

Consider equation 3.46 that we wish to integrate numerically: This can be re-cast as:

$$\frac{\partial \phi(\mathbf{r},t)}{\partial t} = P(\mathbf{r}) \tag{3.49}$$

All the spatial dependence is now contained in the functional P, which can be discretised using a centred space representation. The scheme is illustrated below, initially only for a one dimensional system.

$$\begin{aligned} P_j^{(n)} = \; & \tfrac{M}{\Delta x^2}(\; -b\phi_{j-1}^{(n)} + 2b\phi_j^{(n)} - b\phi_{j+1}^{(n)} \\ & \quad +u\phi_{j-1}^{(n)3} - 2u\phi_j^{(n)3} + u\phi_{j+1}^{(n)3} \\ & + \tfrac{1}{\Delta x^2}[\; -K\phi_{j-2}^{(n)} + 4K\phi_{j-1}^{(n)} - 6K\phi_j^{(n)} \\ & \quad +4K\phi_{j+1}^{(n)} - K\phi_{j+2}^{(n)}]) \\ & + \zeta_j^{(n)} \end{aligned} \tag{3.50}$$

where the spatial mesh of N points is indexed by $1 < j < N$, and the time discretisation mesh in indicated by $0 < n < \infty$ This centred space finite difference scheme is second order accurate in the spatial mesh size $\triangle x$ and is optimal for a diffusional equation like the Cahn-Hilliard equation. Higher order accuracy in space is likely to be inherently unstable, and lower order is too limiting in terms of numerical accuracy [85]. This scheme was indeed found the best and can readily be extended to two and three dimensions.

It now remains to choose a discretisation scheme for the time domain. This is considerably more difficult. The obvious choice is the Forward-Time or Euler scheme and is only first order accurate in time. It is easily implemented as:

$$\phi_j^{(n+1)} = \phi_j^{(n)} + P_j^{(n)}.\triangle t \tag{3.51}$$

In this scheme, each new grid point value of ϕ depends only on its previous value. This method requires a small time-step but was only found to be sufficiently stable for the one dimensional system. A better scheme is required for higher dimensions. There are a number of widely used reliable schemes available [85], but the computational demands of such schemes prohibit their use, particularly in the present case where the computer technology is already being stretched to its limits in terms of speed.

The problem with the forward differencing scheme described above can be identified with the non-symmetric way it uses available data to perform each time step. Figure 3.2 illustrates the three methods considered here for evaluating the ∇^2 operator in the Cahn-Hilliard equation. The $\nabla^2.\nabla^2 = \nabla^4$ contributes no new problem, it merely compounds the old one.

The staggered-leapfrog scheme is a well known method that is second order in time. It requires information from the two previous time steps to compute the next value and can be written as:

$$\phi_j^{(n+1)} = \phi_j^{(n-1)} + P^n.\triangle t \tag{3.52}$$

This additional storage requirement is a disadvantage over the simpler forward differencing scheme, particularly for the large grids required. The staggered-leapfrog is surprisingly no improvement and indeed is considerably less stable for certain values of K, u, b and M. This anomaly can be understood by considering the effect of the alternating mesh used by this scheme. The two alternating meshes are in fact decoupled, so that drift instabilities can arise between the two meshes. This leads to rapid divergence of the field in opposing directions for each mesh.

This decoupling problem can be partially alleviated using the Lax scheme, whereby grid points used in the time-step calculation are replaced by interpolated values at half grid points $\phi_{j+\frac{1}{2}}^n$. This method uses a small *numerical viscosity* term obtained by adding a small fraction f of the value on the alternate grid to the grid calculation. This is somewhat unphysical and furthermore tends to damp out high frequency components in the evolving field. For this reason a better scheme is the two-step Lax-Wendroff method. In this scheme, the first operation is to evaluate the interpolated half-step points in time *and* space according to the Lax scheme, and then to use these intermediate values (which are discarded afterwards) to make a single time step movement. See figure 3.2.

$$\begin{aligned}
\phi_{j+\frac{1}{2}}^{(n+\frac{1}{2})} &= \frac{1}{2}\left(\phi_{j+1}^{(n)} + \phi_j^{(n)}\right) + \frac{\triangle t}{2\times 2}\left(P_{j+1}^{(n)} + P_j^{(n)}\right) \\
\phi_j^{(n+1)} &= \phi_j^{(n)} + \frac{\triangle t}{2}\left(P_{j-\frac{1}{2}}^{(n+\frac{1}{2})} + P_{j+\frac{1}{2}}^{(n+\frac{1}{2})}\right)
\end{aligned} \tag{3.53}$$

This is the best *explicit* scheme found. It allows quite large time steps, and therefore relatively fast computation times for a given evolution time and very low mesh drifting despite low numerical viscosity.

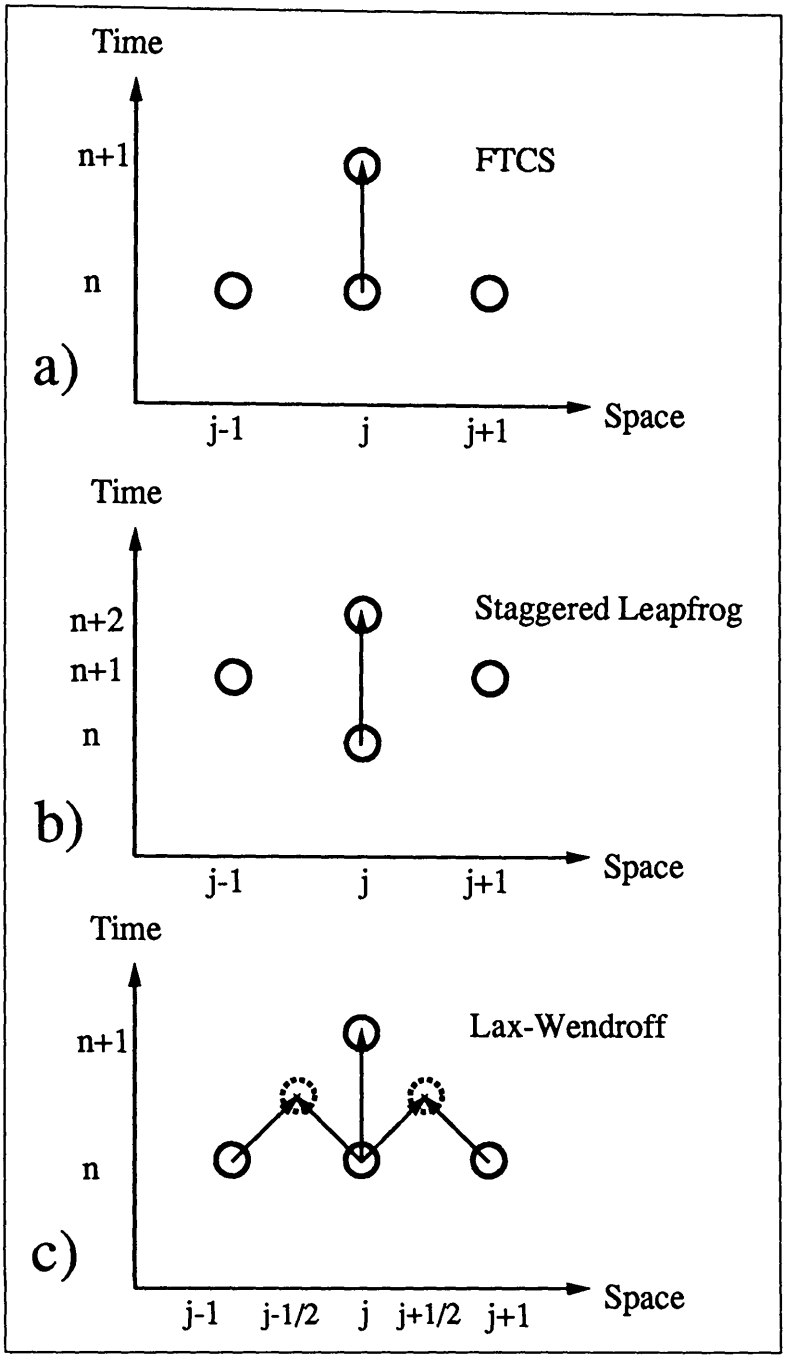

Figure 3.2: Finite difference time step algorithms for the ∇^2 operator in one space dimension. a) The Forward time centred space (FTCS) method is second order in space but only first order in time. b) The staggered leapfrog algorithm computes the update from the two previous time steps of spatial information and is second order in time. It involves two decoupled overlapping grids, and is unstable. c) The two-step Lax Wendroff scheme computes intermediate values at $t = n+\frac{1}{2}, x = j \pm \frac{1}{2}$ before performing a stable update from the previous time step.

The schemes are summarised in table 3.1, they are described in [62, 85]. The

Scheme	Range of Stability in Δt	Storage Requirements	Efficiency	Comment
FTCS (Euler)	0.01 – 0.00001	Low	Poor	Physical but inaccurate
Staggered-leapfrog	0.001 – 0.00001	Medium	Medium	Unreliable
Lax	0.05 – 0.00001	Medium	Good	Unphysical viscosity
Lax-Wendroff	0.1 – 0.00001	High	Very Good	Physical and reliable

Table 3.1: Finite Difference Schemes as applied to the Cahn-Hilliard-Cook Equation. Note that computational efficiency also takes account of how high the time step may be, since it is possible to integrate to longer simulated times much faster with an algorithm which allows large time steps.

upper limits on stability are determined from the highest value of Δt that will converge for all reasonable parameter values *and* gives the *same* results with a 10% variation in Δt. The lower limit of stability is quoted as 0.00001, this resulting from the 32-bit real number precision employed in the calculations. This can be reduced at the expense of computational time, by resorting to 64-bit arithmetic.

3.2.2 Meaning of the CHC parameters

The Cahn-Hilliard-Cook equation is derived with parameters that are not obviously related to experimentally measurable properties of an alloy. The parameters u, b, m, and K that appear in equation 3.38 *can* be related to the microscopic parameters in the lattice gas model described in chapter 2, by a comparison with mean field theory.

The mobility m appears only as a multiplicative constant and effectively controls the time scale. In numerical work it can be absorbed into the time-step of inte-

gration. The parameter $K = \frac{R^2}{d} k_b T$ reduces to $K = \frac{k_b T}{d}$ for the nearest neighbour interaction model, since:

$$R^2 = \frac{\sum_{i,j}(r_i - r_j)^2 (V_{i,j}^{A-A} + V_{i,j}^{B-B} - 2V_{i,J}^{A-B})}{\sum_{i,j}(V_{i,j}^{A-A} + V_{i,j}^{B-B} - 2V_{i,j}^{A-B})} \tag{3.54}$$

where the $V_{i,j}^{c_i - c_j}$ are the Ising coupling parameters discussed in chapter 2 and d is the spatial dimension.

This means K, like u and b have units of free energy density, and all contain a factor of $k_b T$ which can also be absorbed into the mobility or time scale. Standard mean field theory for the Ising model [86] shows that the parameter b controls the quench temperature for the model through the relation $b = \frac{T}{T_c^{MF}} - 1$, where T_c^{MF} is the mean field critical temperature discussed in chapter 2. This leaves the parameter u undetermined, but for numerical work it is convenient to set it to unity and employ the ratio $\frac{b}{u}$ to determine the interaction strength J^{A-A}. The combination of parameters $b = u = M = K = 1$, then corresponds to an infinite quench for an unknown linear time scale.

Increasing K corresponds to increasing the range of the model interactions, while changing the sign of K changes the ground state of the model to that of an ordered system, the exact nature of which will depend on the global concentration of A-atoms [81]. This present work considers only positive values of K.

Specific values of the Cook noise term appear less important than the fact of its mere presence. The correct magnitude is set by equation 3.48 and a convenient form is that of a Gaussian distribution centred on zero with $\sigma^2 = 2k_b T m$ in the units of the simulation, and with the properties dictated by equations 3.47 and 3.48.

3.2.3 The CHC Equation in One Dimension

A natural place to begin investigations is a symmetric quench as shown in figure 3.1, from a temperature T_0 well above the two-phase coexistence curve to one below it T_1. A completely random starting configuration is a good approximation to the case $T_0 \to \infty$.

A simple illustration of the important properties of the Cahn-Hilliard-Cook equation is given in figures 3.3, 3.4 and 3.5. A one dimensional system of 4096 sites was initialised randomly with $\phi_j \in [-0.25, 0.25], \sum_j \phi_j = 0$, and numerically integrated with the parameter values $K = m = b = u = 1$ using a spatial mesh of $\triangle x = 1$ and a time step of $\triangle t = 0.01$ with the FTCS scheme. The initially homogeneous mix separates out into two well defined phases. The real space evolution is shown in figure 3.3 as an intensity plot for the composition field ϕ as a function of time vertically and space horizontally. The initial grey mix separated into a spatially modulated two phase structure. This can also be tracked for a longer time by examining the composition population as shown in figure 3.4.

The 'scattering intensity' is obtained from a fourier transform of the composition field, and is shown in figure 3.5. The modulus of the transform is shown, averaged over all 100 independent samples. The spectrum is initially flat and extends to all frequencies. As the system evolves, a peak forms at the characteristic domain length scale and this peak increases in intensity and lowers its reciprocal position with time as the system coarsens and domains grow. The position and size of this peak can be determined by fitting a Gaussian curve to it [2]. The size of the peak determines the amount of each phase present and contains no more information than the composition population shown in figure 3.4, but the characteristic length R_{max} as determined from the position of the peak is more interesting.

Figure 3.6 shows the evolution of the characteristic size in integration time, for three values of the temperature parameter b. It appears that for an pseudo-infinite quench, growth occurs, but slowly. The Cook noise term is zero for a quench to zero temperatures, and this is reflected in the similarity between the two lowest curves. At a temperature of $\frac{T_c}{4}$, the Cook noise term clearly accelerates the initial growth process substantially, although at later times, the curves converge. At a higher still temperature of $\frac{T_c}{2}$, there is sufficient thermal energy in the model system that the Cook term appears to have a less dramatic effect, although it still accelerates growth.

[2]Strictly a Maxwellian is better, but more difficult numerically. No significant difference in position and area results from using a Gaussian fit.

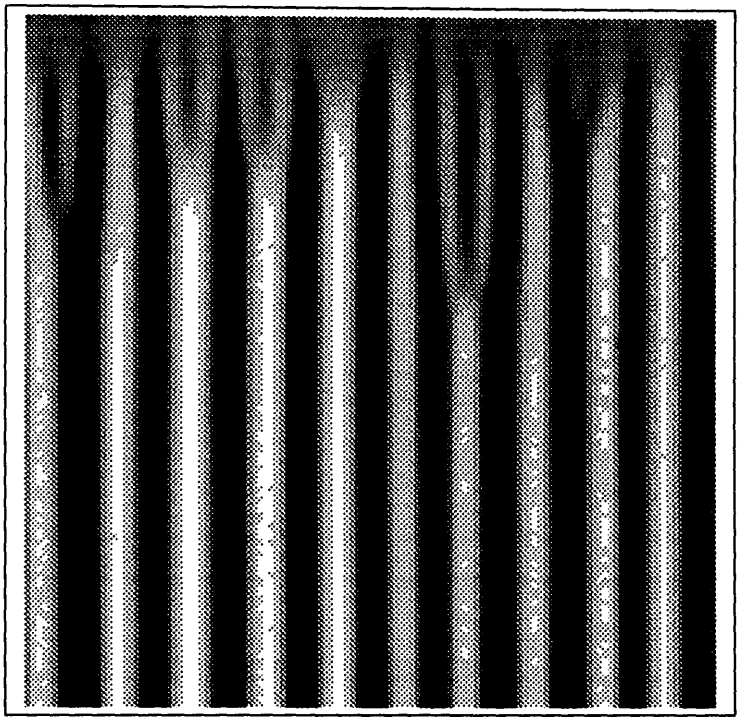

Figure 3.3: Real space evolution of a 128-point periodic mesh, showing the phase separation of the initial homogeneous single phase (grey) into two separated phases with $\phi \rightarrow -1$ (black) and $\phi \rightarrow 1$ (white). The system was evolved for 12800 steps with $\triangle t = 0.01$, time being from top to bottom, with position being horizontal.

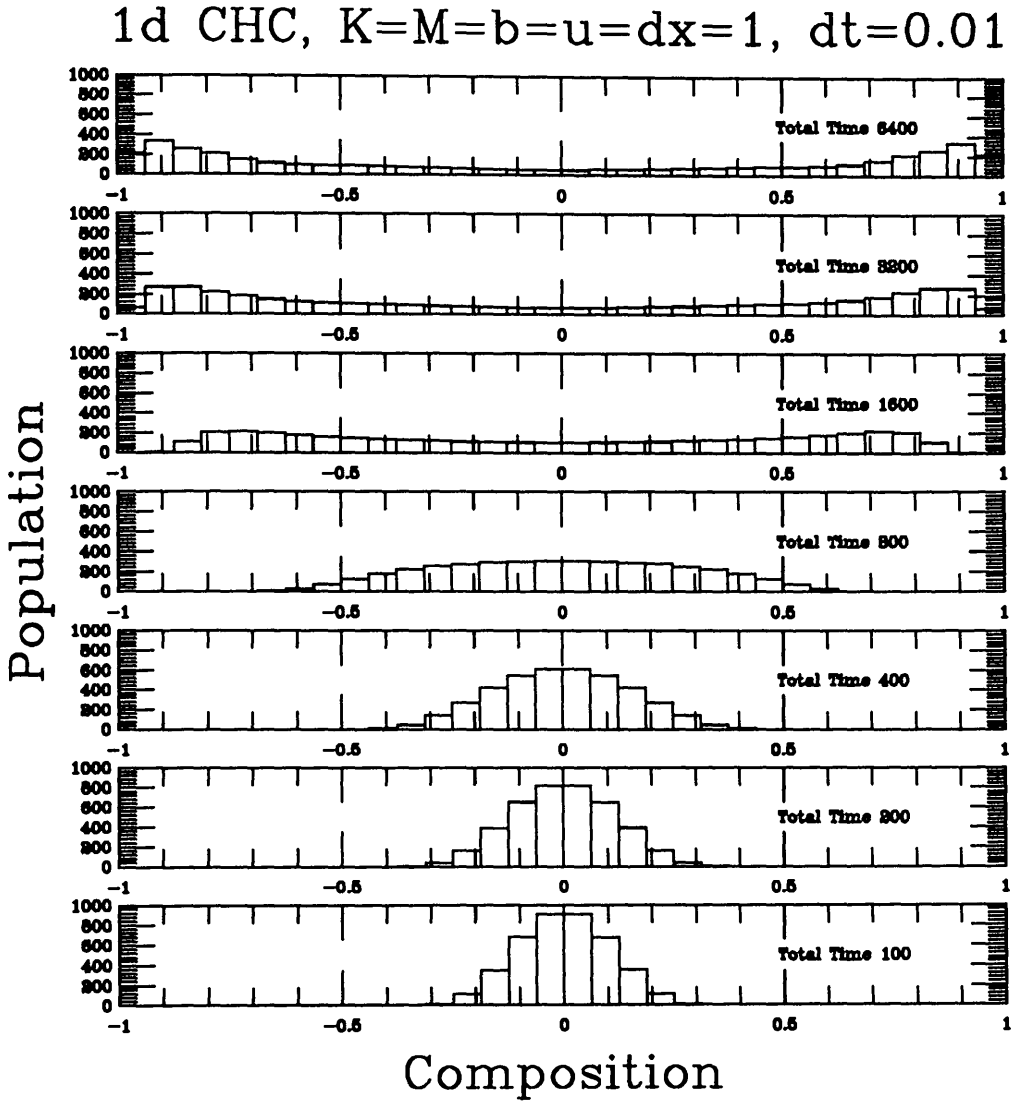

Figure 3.4: The composition population as a function of evolution time. The initial condition was a narrow uniformly random profile with $\phi \in [-0.25, 0.25]$. Times shown are as powers of 2, with the parameter values of $K = b = u = m = 1$, with integration spacings $\triangle x = 1.0$, $\triangle t = 0.01$, for the FTCS scheme.

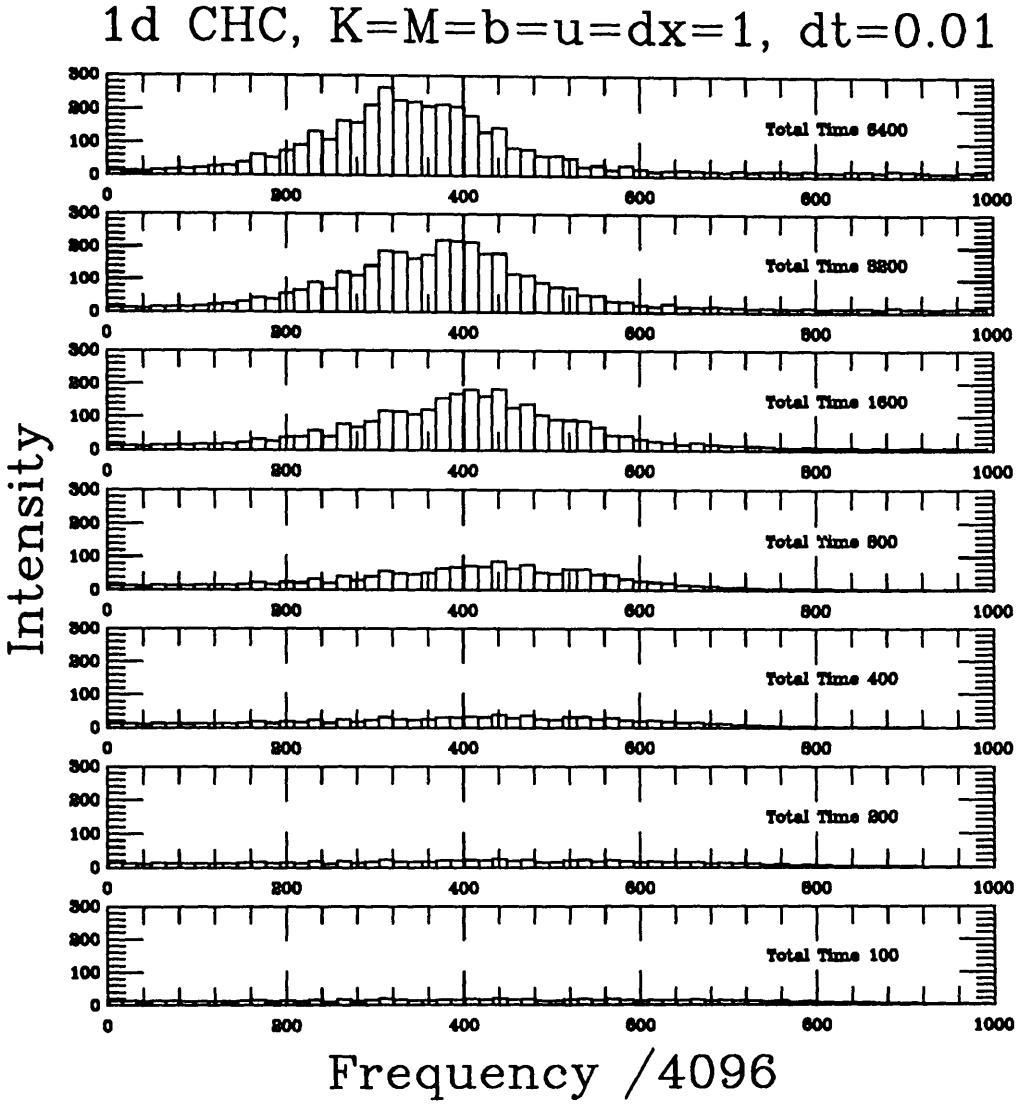

Figure 3.5: The Fourier spectrum as a function of evolution time. The initial condition was a narrow uniformly random profile with $\phi \in [-0.25, 0.25]$. Times shown are as powers of 2, with the parameter values of $K = b = u = m = 1$, with integration spacings $\Delta x = 1.0$, $\Delta t = 0.01$, for the FTCS scheme.

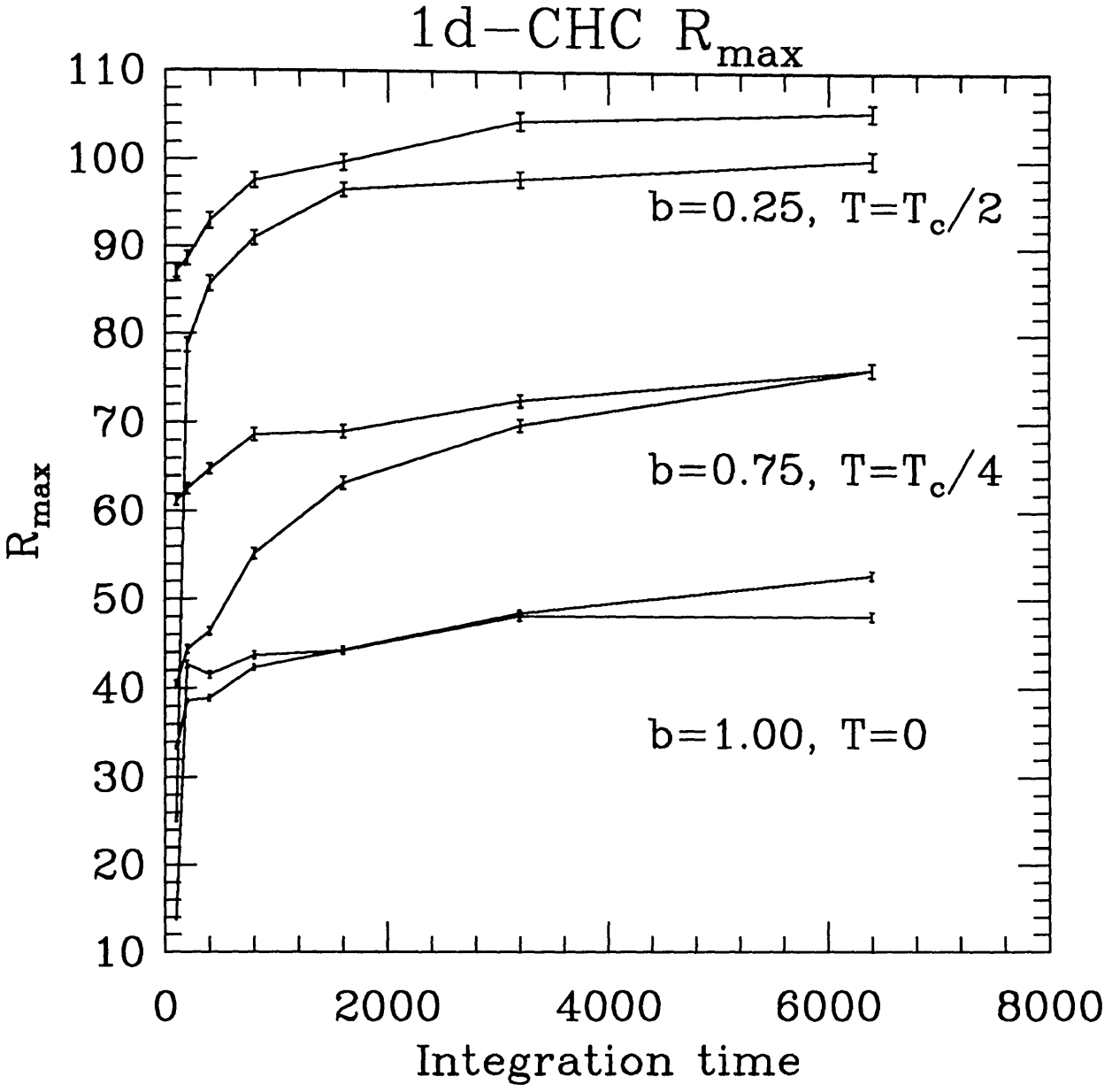

Figure 3.6: Characteristic size evolution in the 1-d Cahn-Hilliard Cook equation showing the effect of lowering the temperature, on the size. At $T = \frac{T_c}{2}$ and $T = \frac{T_c}{4}$ the Cook noise speeds up the initial formation of the minority phase, but does not significantly change the coarsening behaviour of the growth. The lower curve at each temperature has had the noise term applied, the upper curve has not. These represent averages over some 100 samples. A suitable scaling form for these curves is discussed in chapter 5.

3.2.4 The CHC Equation in Two Dimensions

A great deal of insight into the typical processes taking place can be obtained by visual examination of the time evolution of the concentration field and its Fourier transform. Figures 3.7 and 3.8 show snapshots of a two dimensional system on a square mesh of $128 \times 128 = 16384$ grid points, as it evolves in time. Also shown are two dimensional Fourier transforms of the concentration field. These latter are to be compared with the scattering images of chapter 4 and show the collapsing halo which characterises the domain growth. The field pattern eventually coarsens to one or two single domains of A-atom enrichment, at which point the intensity has shrunk almost to a point. It is interesting to note the initial Fourier pattern is featureless, as is the initially random configuration. In the numerical transform of a periodic mesh, aliasing or non-matching causes there to be scattering outwith the first Brillouin zone. This persists until sufficient integration time has elapsed that this scattering from very small fluctuations is dominated by the much brighter scattering from the coarsening interconnected structure.

The system is initialised to $-0.5 \leq c_i \leq 0.5$ in a uniform distribution. This narrow peaked single phase decomposes into a double peaked distribution denoting two distinct phases of predominantly positive and negative field respectively.

Note that the greyscale intensities are from white to black representing $\phi \in [-1, 1]$ for the concentration field pictures, but that they are scaled arbitrarily from minimum to maximum value for the Fourier intensities. In consequence, the Fourier intensity increases by approximately an order of magnitude from top to bottom, and this can not be shown using only 16 grey levels of display. The Fourier images are show as inverse, with black representing intense scattering and white representing low intensity.

Figure 3.9 summarises some of this information by showing the time evolution of the composition population. The initial state is seen to rapidly change to a normal distribution. At this point the configuration remains for an 'incubation period' before coarsening into the distinctive two-phase structure.

Pair correlation functions may be obtained directly from the concentration field

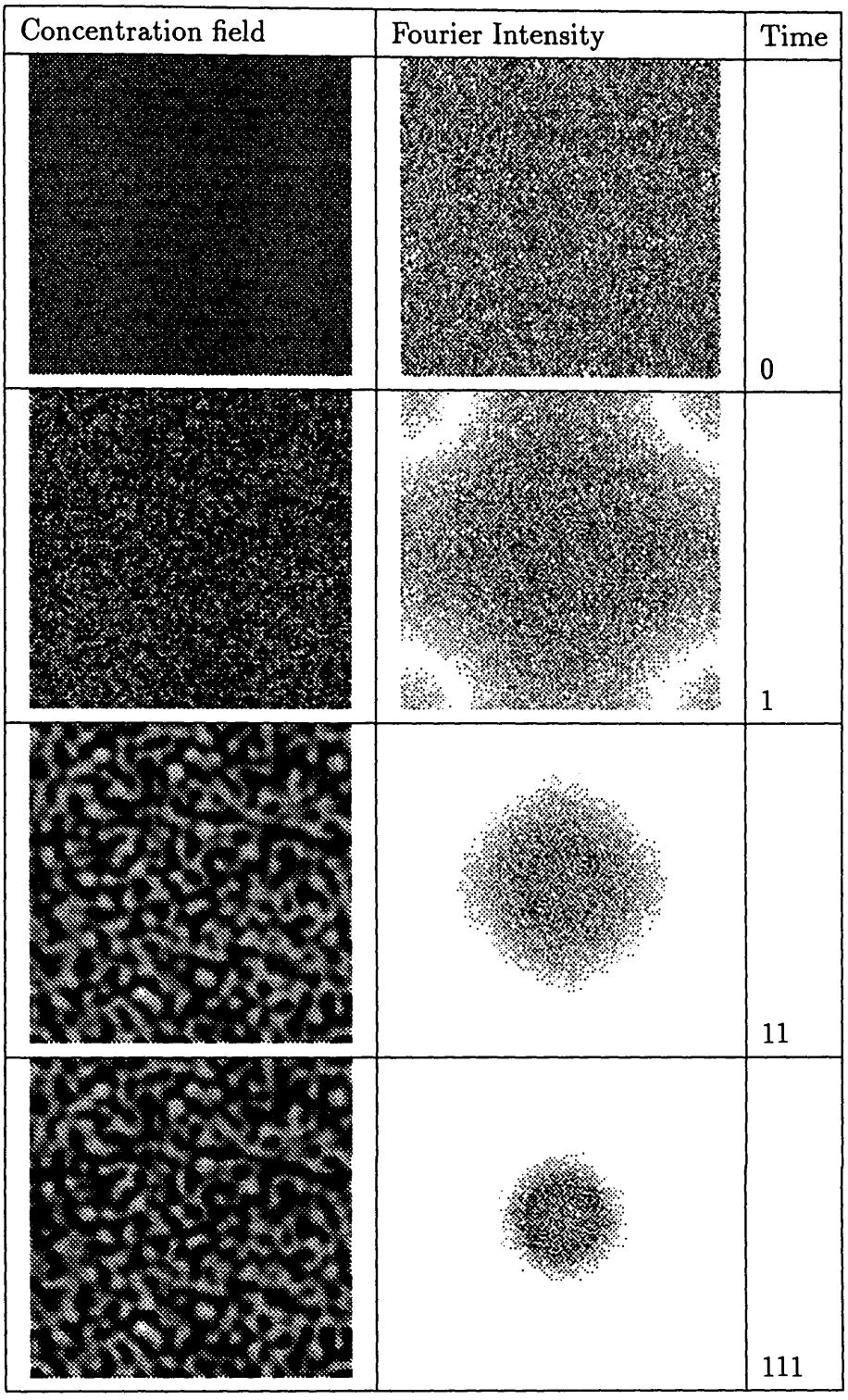

Figure 3.7: Snapshots in time of the concentration field and it spatial Fourier transform during time evolution of the Cahn-Hilliard equation on a square mesh. Times shown are t=0, 1, 11, 111 steps, with $\delta t = 0.1$

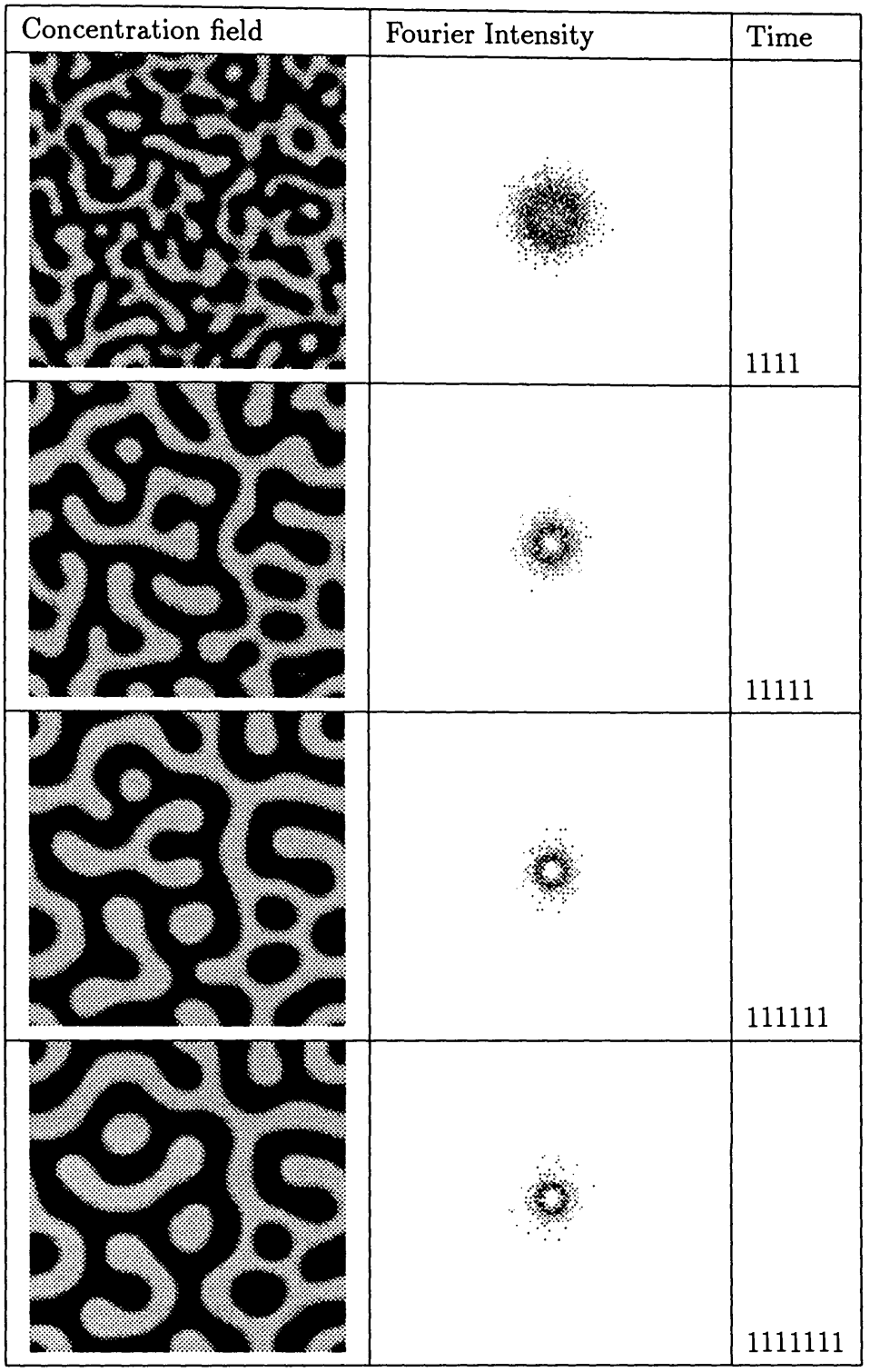

Figure 3.8: Snapshots in time of the concentration field and it spatial Fourier transform during time evolution of the Cahn-Hilliard equation on a square mesh. Times shown are t=1111, 11111, 111111 and 1111111 steps, with $\delta t = 0.1$

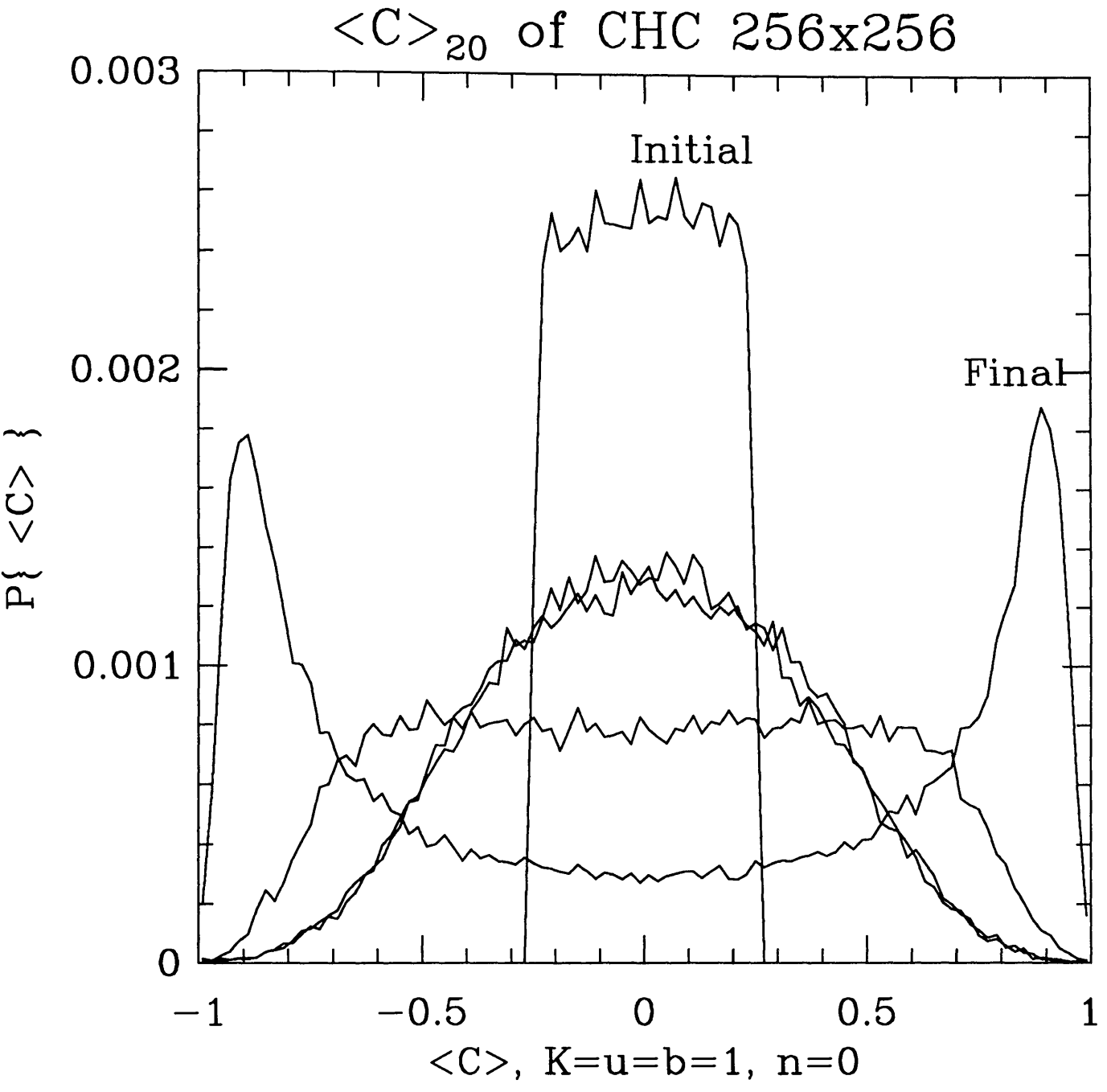

Figure 3.9: Composition population of the Cahn-Hilliard integrated solutions on a square mesh of 256 × 256 grid points, as a function of time.

as described in 2, however this calculation requires of order N^2 operations for a mesh of N gridpoints. With the large meshes used here, this is impractical and the Fourier transform technique (see 2) is the only practical method of obtaining the characteristic domain size. The two dimensional transforms in figures 3.7 and 3.8 are too noisy to obtain this directly and the two dimensional transforms shown in figure 3.10 were obtained by averaging over 20 samples prior to the circular binning. From these the location of the peak in q gives a measure of the characteristic domain size as a function of time.

3.2.5 Three Dimensional CHC Solutions

It is more difficult to track a three dimensional system visually and more reliance must be placed on the size characterisation of the separating phases by averaged Fourier transforms. Figure 3.11 shows the usual peak formation and evolution in time of the spherically averaged scattering intensity. The peaks vary considerably in magnitude, but the peak positions can be well determined, and mapped to characteristic sizes. The time evolution of these sizes is shown in figure 3.12 to which a power law has been well fitted — not entirely surprising with only four data points.

A very significant computational resource is required to integrate a mesh that is large enough to achieve a useful three dimensional Fourier transform when spherically averaged. Appendix A describes some of the parallel computational methods employed in implementing the integration schemes described in this chapter.

Chapter 5 draws together the characteristic size scaling data from the numerical solutions presented here, as well as for the Monte Carlo simulations presented in chapter 2 and for some real experimental scattering data discussed in chapter 4.

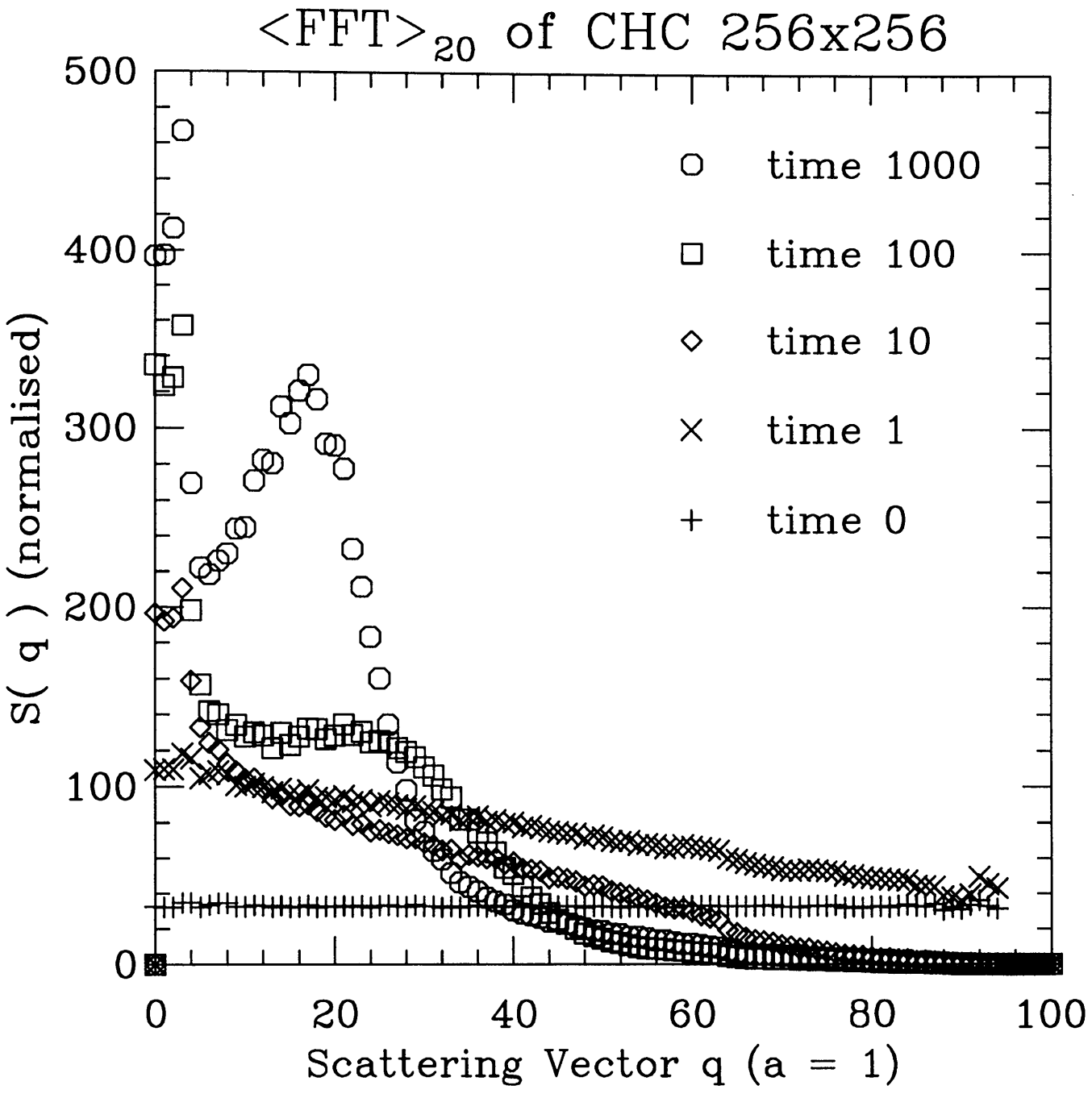

Figure 3.10: Partial structure factors computed from spatial Fourier transforms of 20 samples of Cahn-Hilliard trajectories on a square mesh of 256 × 256 grid points.

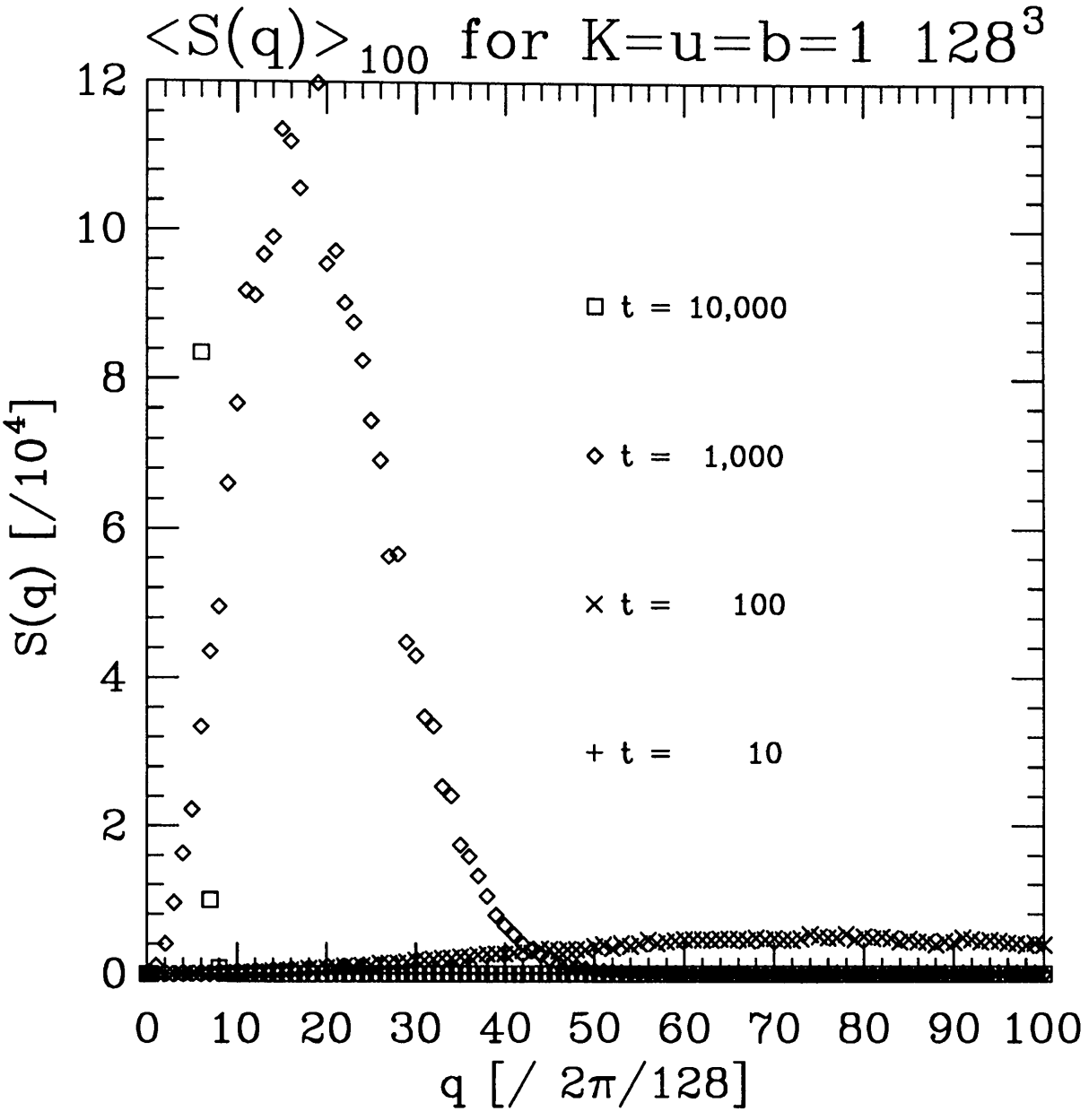

Figure 3.11: Partial structure factors computed from spatial Fourier transforms of 100 samples of Cahn-Hilliard trajectories on a cubic mesh of $128 \times 128 \times 128$ grid points.

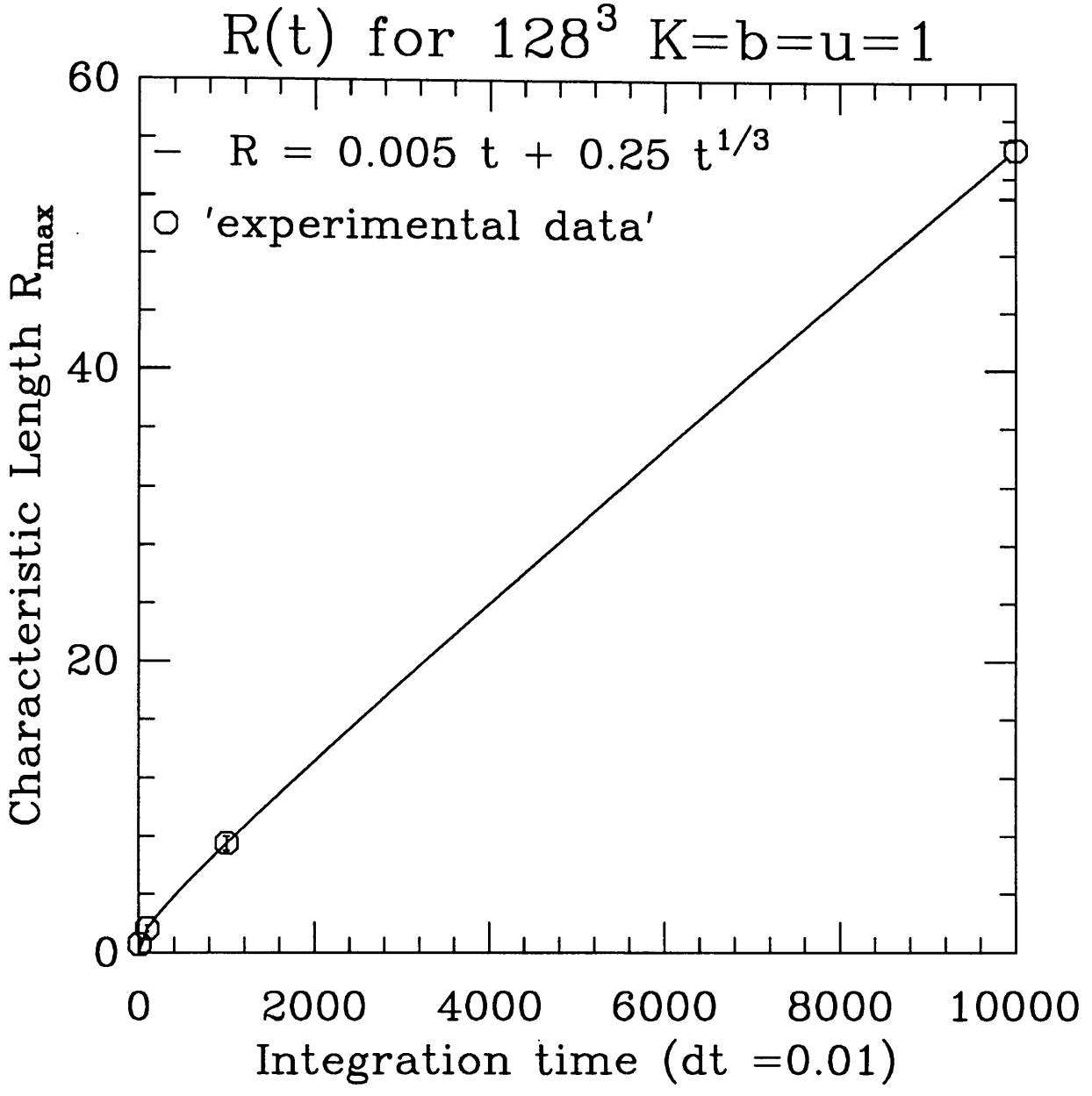

Figure 3.12: Time evolution of the characteristic size for 3d Cahn Hilliard integrated solutions with a fitted growth law.

3.3 Nucleation Theory

The central assumption behind droplet and cluster theories of growth in binary solutions, is that it is the heterophase or droplet fluctuations which lead to the decay of metastable states. These theories are generally formulated in the dilute limit, where a small volume fraction of solute material is uniformly distributed in the solvent as a single phase state. Following a quench, droplet fluctuations start the nucleation process, and these droplets then grow or shrink in size according to the condensation and evaporation mechanisms available.

A convenient starting point for this approach is that of [32], whereby a rate equation can be set up to describe changes in the cluster distribution function.

Let the number of the minority-phase clusters with a mass of l A-atoms be denoted by $n_l(t)$ per unit volume at time t. The rate equation for condensation and evaporation processes can be written as:

$$\frac{dn_l(t)}{dt} = C^+_{l-1}n_{l-1}(t) - C^+_l n_l(t) + C^-_{l+1}n_{l+1}(t) - C^-_l n_l(t) \quad l \geq 2$$
$$\frac{dn_l(t)}{dt} = C^+_1 n_1(t) + C^-_2 n_2(t) \quad l = 1 \qquad (3.55)$$

The coefficients for condensation or growth of an l-cluster, C^+_l and for evaporation or decay of an l-cluster, C^-_l are themselves functions of time. Their values must reflect the facts that we are only considering monomer activated processes, that is processes where a cluster increases or decreases its mass by a single atom, and that in a canonical simulation, the monomer population is finite. As clusters grow, the monomer population is depleted, and so C^+_l will necessarily decease with time. Equation 3.55 can be rewritten using the detailed balance condition for growth and decay that states:

$$C^+_l n^{eq}_l = C^-_{l+1}n^{eq}_{l+l} = W(l, l' = 1) \qquad (3.56)$$

Where $l' = 1$ denotes that we are only considering monomer activated processes, and W is the combined rate factor, and is strictly speaking time dependent itself,

although it is treated here as constant in time. The rate equation is now parameterised by n_l^{eq}, the equilibrium or most probable cluster size distribution. The main task for a nucleation theory is to predict a form for this equilibrium cluster size distribution, by some approximation [87, 77]. It is sufficient here to suppose that the equilibrium cluster distribution can be written as

$$n_l^{eq} = n_0 e^{-\Delta F_l k_b T} \tag{3.57}$$

after Fisher, in which n_0 is a constant, and ΔF_l is the non-classical droplet free energy. This approach is essentially that of an ideal gas law for a non-interacting assembly of droplets, and is correct in the dilute limit[87].

Following [86], the rate equation can now be recast as:

$$\frac{dn_l(t)}{dt} = W(l-1,1)\left[\frac{n_{l-1}(t)}{n_{l-1}^{eq}} - \frac{n_l(t)}{n_l^{eq}}\right] + W(l+1,1)\left[\frac{n_{l+1}(t)}{n_{l+1}^{eq}} - \frac{n_l(t)}{n_l^{eq}}\right] \tag{3.58}$$

Valid for $l \geq 2$

and expanding about l using:

$$\begin{aligned} \frac{n_{l\pm1}(t)}{n_{l\pm1}^{eq}} &= \frac{n_l}{n_l^{eq}} \pm \frac{\partial}{\partial l}\frac{n_l}{n_l^{eq}} + \frac{1}{2}\frac{\partial^2}{\partial l^2}\frac{n_l}{n_l^{eq}} + \cdots \\ W(l-1,1) &= W(l,1) - \frac{\partial}{\partial l}W(l,1) \end{aligned} \tag{3.59}$$

to yield:

$$\frac{\partial n_l(t)}{\partial t} = \frac{\partial}{\partial l}\left[W(l,1)\frac{\partial}{\partial l}\frac{n_l(t)}{n_l^{eq}}\right] \tag{3.60}$$

which may be used to define a *cluster current* J_l:

$$\frac{\partial n_l(t)}{\partial t} = -\frac{\partial}{\partial l}J_l \tag{3.61}$$

since this is a continuity equation in cluster-size space $\{l\}$. This can be generalised for the cases where clusters grow and decay by addition and subtraction of more than one atom at a time, by allowing the case $l' \geq 1$.

$$J_l = -\sum_{l'} l'^2 W(l,l')\frac{\partial}{\partial l}\frac{n_l(t)}{n_l^{eq}} \tag{3.62}$$

This is instructive, but it is expected that the rate coefficients $W(l,l')$ are very small for high values of l', and furthermore such processes are difficult to simulate using lattice models, since each cluster requires storage, over and above the

efficient storage requirements for the lattice sites. This latter point is discussed in greater detail in appendix A.

It is convenient to define a cluster reaction rate R_l for processes involving $l \rightleftharpoons l'$ as

$$R_l = \frac{1}{n_l^{eq}} \sum_{l'} l'^2 W(l, l') \tag{3.63}$$

and expanding the derivative in J_l and assuming Fisher's form for n_l^{eq} in equation 3.57 above we obtain:

$$J_l = -\left[R_l \frac{\partial}{\partial l} n_l(t) - \frac{\partial}{\partial l} \frac{\triangle F_l}{k_n T} R_l n_l(t) \right] \tag{3.64}$$

This illustrates that J_l contains two terms: a diffusive term

$$-R_l \frac{\partial}{\partial l} n_l(t) \tag{3.65}$$

and a drift term

$$\frac{\partial}{\partial l} \frac{\triangle F_l}{k_b T} R_l n_l(t) \tag{3.66}$$

Only the drift term contains explicit dependence on the *form* of the equilibrium distribution. These two terms are of opposite sign, and it is supposed in cluster theories that there is a critical droplet size l^* at which the two terms are equal. For $l < l^*$ the drift term acts against the diffusion so that if a large droplet *does* form, it is likely to *decay* again. However, for the case when $l > l^*$ the drift term acts with the diffusion and hence super-critical droplets can grow steadily.

Following a quench to a metastable state, there is a transient time during which the cluster concentration $n_l(t)$ grows for clusters less than the critical cluster size $l \lesssim l^*$, until clusters saturate weakly at their equilibrium sizes. After this time lag, the nucleation current J_{l^*} around the maximum cluster size, has almost reached a steady state value known as *the* nucleation rate J.

So far the formulation of nucleation theory has only relied on the approximation of taking a specific form for the *unknown* droplet free energy function. Further progress can not be made without building in the restrictions mentioned earlier, of having a large *dilute* system, with a *fixed* monomer population density, and the additional constraint, that large droplets once formed, are removed from the system. This latter prevents all the solute material from precipitating out of

solution and allows us to solve the steady state condition for the dilute system. Following Becker and Doring [86], these constraints can be expressed by:

$$\lim_{l\to 0}\frac{n_l(t)}{n_l^{eq}} = 1 \tag{3.67}$$

for the requirement that the monomer population density is fixed, and

$$\lim_{l\to\infty} = \frac{n_l(t)}{n_l^{eq}} = 0 \tag{3.68}$$

for the removal of large droplets. The steady state cluster concentration n_l^{ss} can be obtained using :

$$\frac{\partial n_l^{ss}}{\partial t} = 0 \tag{3.69}$$

requiring that $J_l \equiv J$ independent of l. Hence:

$$J = n_l^{eq} R_l \frac{d}{dl}\frac{n_l^{ss}}{n_l^{eq}} \tag{3.70}$$

which gives:

$$\frac{n_l^{ss}}{n_l^{eq}} = J\int_l^{\infty}\frac{dl'}{R_{l'}n_{l'}^{eq}} \tag{3.71}$$

with

$$J = \frac{1}{\int_0^{\infty}\frac{dl}{R_l n_l^{eq}}} \tag{3.72}$$

using the boundary equations 3.67 and 3.68. If l^* is large, the free energy term in R_l can be expanded as a quadratic around l^* as:

$$\triangle F_l \approx R_{l^*} - \frac{1}{2}gk_bT(l-l^*)^2 \tag{3.73}$$

where g is a constant. Equation 3.71 can be recast as:

$$\frac{n_l^{ss}}{n_l^{eq}} = \frac{1}{2}\{1 - \mathrm{erf}\left(\frac{l-l^*}{\sqrt{\frac{g}{2}}}\right)\} \tag{3.74}$$

The meaning of the parameter g is then to control the width of the region in which the ratio $\frac{n_l^{ss}}{n_l^{eq}}$ changes from unity to zero. This parameter is known as the Zeldovitch parameter [88]. The ratio in equation 3.74 is illustrated for various values of the Zeldovitch parameter g in figure 3.13.

This implies that $\frac{n_l^{ss}}{n_l^{eq}}$ is close to unity around $l \lesssim l^*$ and goes to zero rapidly, for cluster sizes greater than l^*. This justifies the idea that the critical cluster size is a useful concept and can be employed as a cutoff on the full distribution.

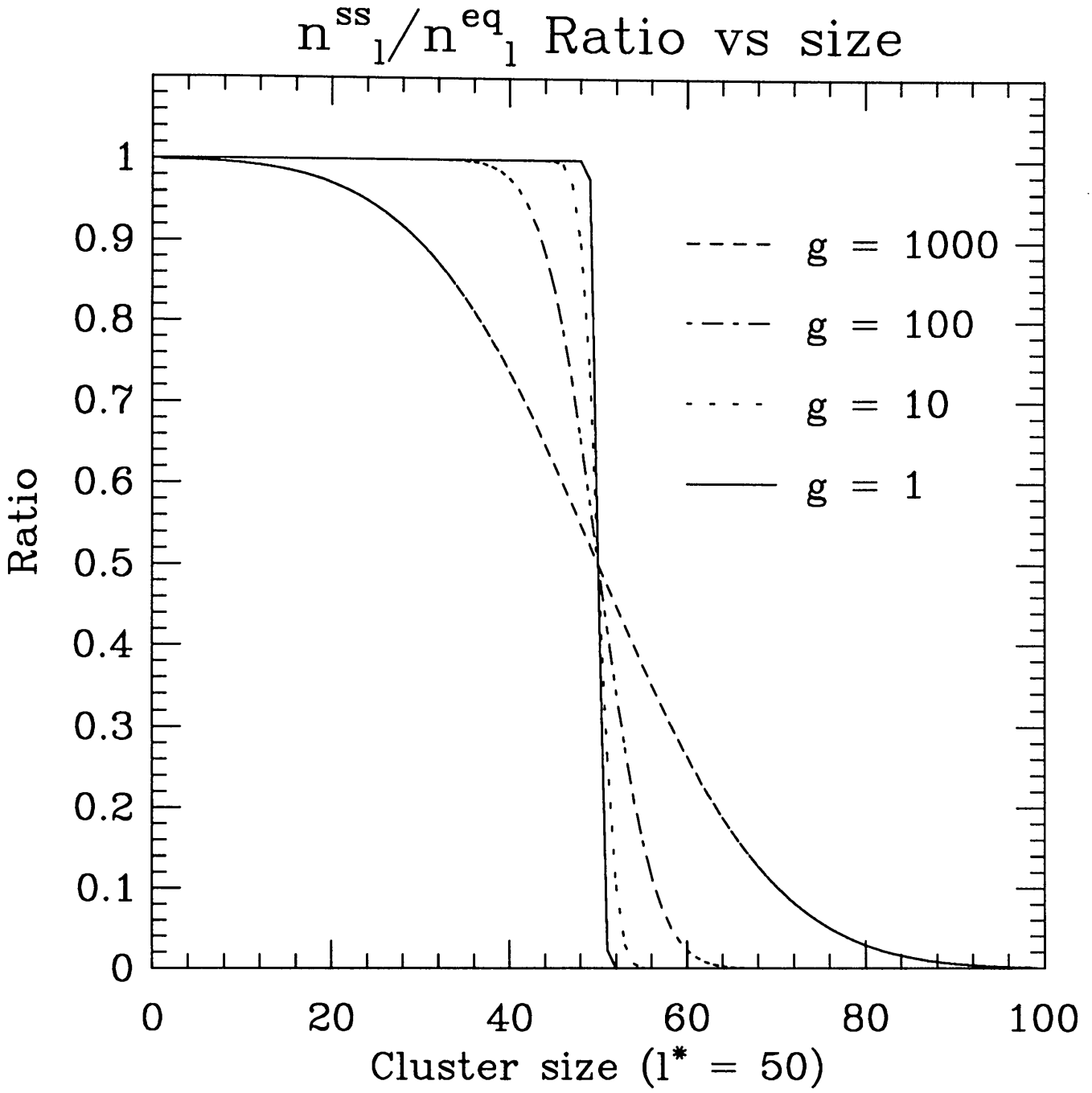

Figure 3.13: The value of the ratio $\frac{n_l^{ss}}{n_l^{eq}}$ for various values of the Zeldovitch parameter g.

3.3.1 Cluster size distributions in Lattice Models

It is possible to look for nucleative behaviour in the lattice models simulations described in chapter 2. Consider figures 3.14 and 3.15.

These illustrate that although Fisher's exponential form for the free energy is useful at high temperatures, it breaks down for quenches to temperatures below the critical temperature. This is attributable to the depletion of the crucial monomers in the simulation, although this would in principle extend to other small mobile clusters, in a real alloy system. There are clearly other deficiencies with the Becker-Doring theory, as it fails to take proper account of the particle interactions, but this problem with particle depletion is perhaps a more fundamental restriction to the theory's applicability.

3.3.2 Extensions to Becker-Doring

Some progress has been made recently in improving the range validity of the Becker-Doring theory. Most notably Binder's cluster theory generalises the cluster distribution to more than one co-ordinate. Other cluster properties such as the cluster surface area and other characterisation of its deviation from sphericity can be employed as additional co-ordinates in cluster space. The problem then becomes one of determining the *vector* nucleation rate, and the critical nucleation co-ordinates in this vector space [89]. This goes some way towards better approximating the interactions amongs sites and clusters, but there is still a need for a more applicable model for the free energy of a droplet than 3.57. Explicit account needs to be taken of the diminishing population of monomers and other mobile clusters, during the quench.

3.4 Summary

This chapter has discussed the two basic theories for describing phase separation, the Cahn-Hilliard theory and its derivatives, and the Becker-Doring cluster ap-

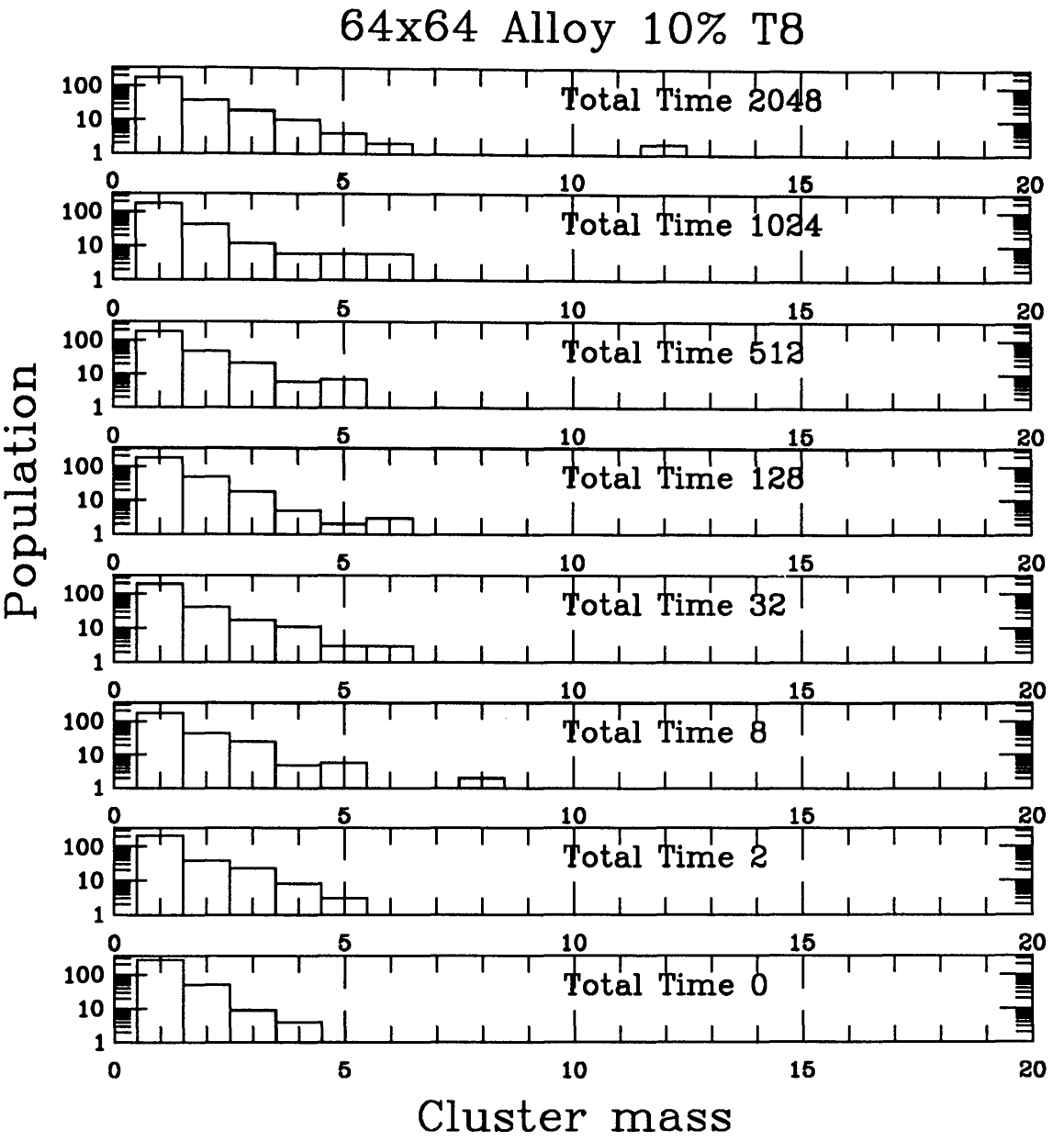

Figure 3.14: Cluster mass distribution in a simulation of a 64×64 binary alloy with minority phase concentration of 10% and at temperature $T = \frac{T_c}{4}$. The distribution remains well approximated by Fisher's exponential form.

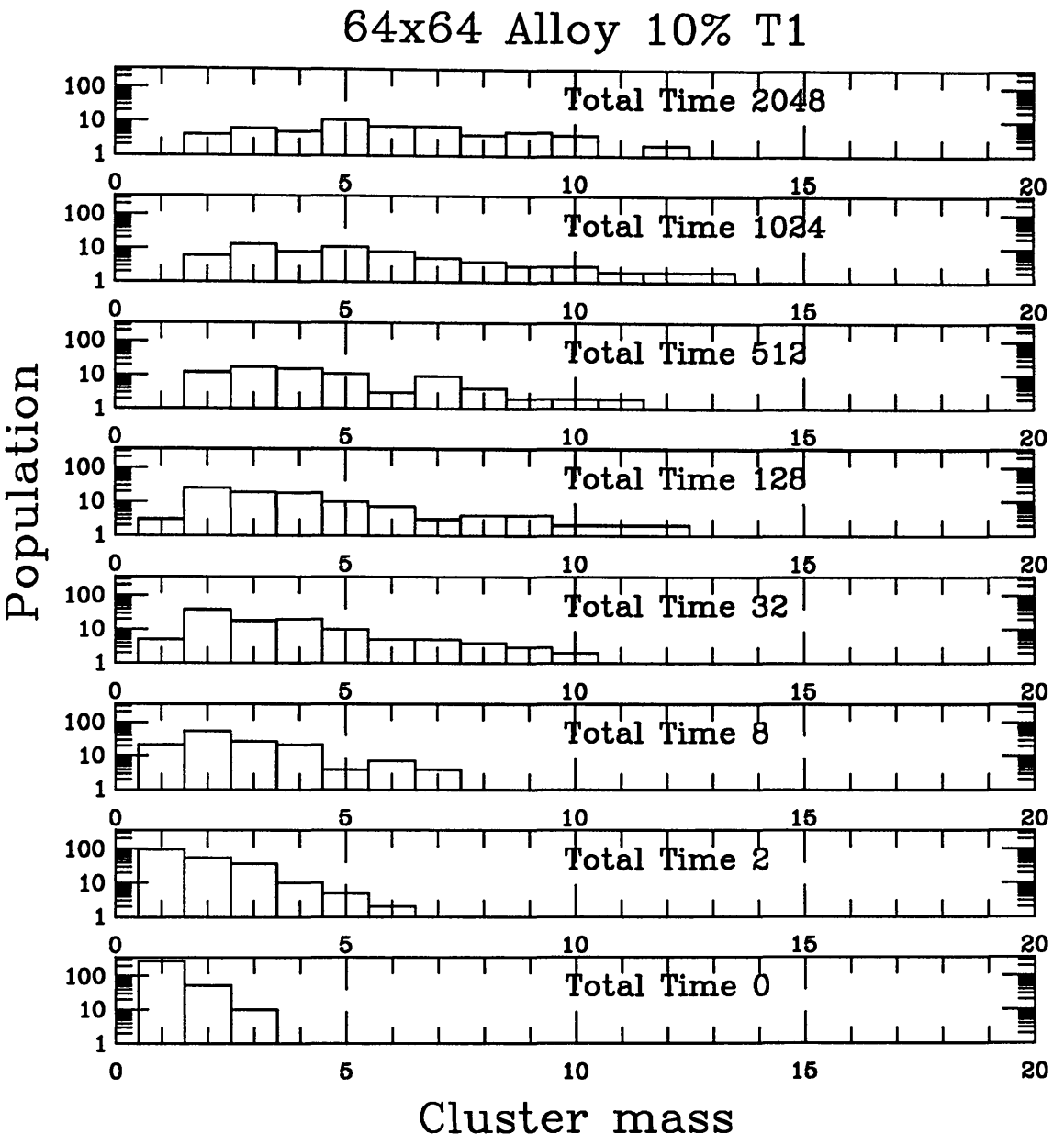

Figure 3.15: Cluster mass distribution in a simulation of a 64×64 binary alloy with minority phase concentration of 10% and at temperature $T = 2T_c$. The monomer population is depleted and the distribution is no longer approximated by Fisher's exponential form. It is better described by a log-normal distribution or a Maxwellian distribution.

proach. These are good starting approximations in the regimes of high and low concentration respectively.

Numerical methods have been employed to make use of the Cahn-Hilliard equation, where the linearised approximation breaks down, and can produce useful pseudo-experimental data in a purely binary model system. There is clearly scope for further numerical integration work of the Cahn-Hilliard equation, on large systems, and for a greater range of quench temperatures than could be done here due to insufficient computational resource.

Numerical data has been used to illustrate the shortcomings of both field and cluster theories, and has provided quantitative evidence for the importance of the Cook noise term in the Cahn-Hilliard-Cook equation. The transport function performed by the monomers and other small clusters is also apparent and suggests that a successful theory for droplet growth must take these into account.

Chapter 4

Small Angle Neutron Scattering Experiments

4.1 Introduction

This chapter describes the theory and methods of small angle neutron scattering (SANS) used to collect the data described in section 4.6. There are a number of detailed texts on neutron scattering available [90, 91], most recently the multi-volume tome by Price and Skold [92]. These give much more theoretical detail than is required here to set up a common formalism for comparing the SANS data and computer simulated data of chapters 2 and 3. Section 4.2, below, gives a sufficient overview for analysing the SANS data.

Section 4.3 aims to summarise the SANS technique citing two typical small angle diffractometers (SAD) as examples, namely the small angle scattering instrument (SAS) on the PLUTO Reactor at Harwell Laboratory and the SAD instrument on the Intense Pulsed Neutron Source (IPNS) at Argonne National Laboratory (ANL). These instruments are each typical of their classes — steady and pulsed neutron source instruments, respectively, and the IPNS SAD is arguably the best pulsed instrument of its kind in the world. The PLUTO reactor is sadly decommissioned now, but its SANS instrument was of similar design to the better known D11 instrument at the Institute Laue-Langevin (ILL). All the experimental data cited in this work were collected at either the PLUTO or IPNS instruments. A fuller description of neutron scattering terminology and methods is given in [93].

A major part of the effort involved in this present work has been in the development of data processing and analysis software for SANS, most of which is now available to users at Harwell and IPNS. A description of the methodology is given in section 4.3.3. Some justification for the techniques involved in interpreting the processed small angle signals is given in section 4.5.

The data presented in section 4.6 are chosen as representative of three regimes. Data for the binary system iron-chromium is used to illustrate phase separation in a *concentrated* system, well *above* the percolation threshold. The copper-cobalt system studied was for a very *low* elemental concentration of cobalt at two weight percent, although the nucleating domains formed are not necessarily pure cobalt. Finally some data for the formation of the γ' phase in the complex steel PE16, demonstrates that even in a complex many component system, it is still possible to treat the system as though it had only two relevant phases.

4.1.1 SANS as a Materials Probe

Small angle neutron scattering has become a widely used method for studying microstructure in metallic and organic materials, particularly alloys and polymers. This work concentrates on studies of metallic alloys, but the methodology is similar for other materials. The SANS technique has a number of significant advantages over other methods such as electron microscopy (EM) [94, 95, 96]. The sample used in SANS is typically a disk of material, approximately 10mm in diameter and a few mm thick. The SANS measurements effectively probe all the sample giving bulk properties rather than local inhomogeneities as done using EM. Sample preparation is generally much easier than for EM, with only minimal sample surface cleaning being required.

Since SANS is essentially a non-destructive probe, it is possible to examine samples in a variety of special environments without disturbing the processes under study. For example, it is possible to use SANS on metallic alloys where the sample is held at high temperature in a furnace and in a magnetic field, and the probing neutron beam has a negligible effect. Such measurements allows detailed study of ageing effects in alloys, over periods of time up to several days.

4.2 Scattering Theory

The following describes the formalism necessary to discuss small angle neutron scattering in terms of the interaction of a neutron beam with a fixed scattering sample. The treatment here is loosely based on [90] and [97]. A more simplified discussion is given in [98], and [99]. The aim here is to link the scattering interaction theory to what is measured, and what can be calculated from a computer simulated sample.

Consider the interaction between a single incoming neutron and a single scattering atom. The neutron is described by its wave-vector $\mathbf{k}$ and mass m_n. The energies and speeds of the thermal neutrons used in SANS experiments are sufficiently low such that the neutron may be considered a non-relativistic particle, with its energy E given by $E = \frac{1}{2}m_n v_n^2 = \hbar^2\mathbf{k}^2/(2m_n)$, where v_n is the neutron's speed. The incoming neutron at position $\mathbf{r}$ is now described as a plane wave $e^{i\mathbf{k}.\mathbf{r}}$ and the scattering atom as a spherically symmetric potential $V(|\mathbf{r}|)$. The solution to the Schrödinger wave equation for such a potential is known to be (see chapter 24 of [100]) of the approximate form at large distances $|\mathbf{r}-\mathbf{r}'|$:

$$\psi(\mathbf{r}) = e^{i\mathbf{k}.\mathbf{r}} - \frac{1}{4\pi}\int \frac{e^{i\mathbf{k}'.(\mathbf{r}-\mathbf{r}')}}{|\mathbf{r}-\mathbf{r}'|}\frac{2m_n}{\hbar^2}V(\mathbf{r}')\psi(\mathbf{r}')\,d\mathbf{r}' \tag{4.75}$$

This is illustrated in figure 4.1. The second term represents a superposition of all the spherical waves of wave-vector $\mathbf{k}'$ scattered from the atom at $\mathbf{r}'$. The well known Born approximation is to take the wave function $\psi(\mathbf{r}')$ to be of the same form as the incident wave. Writing $\mathbf{R}' = |\mathbf{r}-\mathbf{r}'|$ this equation can be re-cast as:

$$\psi(\mathbf{r}) = e^{i\mathbf{k}.\mathbf{r}} - \frac{1}{4\pi}\int \frac{e^{i\mathbf{k}'.(\mathbf{R}'+\mathbf{r}')}}{|R'|}e^{i(\mathbf{k}-\mathbf{k}').\mathbf{r}'}\frac{2m_n}{\hbar^2}V(\mathbf{r}')\,d\mathbf{r}' \tag{4.76}$$

Consider now not a single neutron, but a beam of neutrons incident on the scattering atom. If there are n neutrons incident per unit area per unit time then the number of them scattered into the differential solid angle $d\Omega$ will be proportional to n and to $d\Omega$ with constant of proportionality $\frac{d\sigma}{d\Omega}$, known as the differential cross section. Since the incident plane wave has unit density, n is just given by $\frac{\hbar k}{m_n}$. The spherically scattered wave $\frac{f e^{i\mathbf{k}'.\mathbf{R}'}}{\mathbf{R}'}$, represents a wave of density $\frac{|f|^2}{\mathbf{R}'^2}$ and speed $\frac{\hbar\mathbf{k}'}{m_n}$, where the amplitude f is given by:

$$f = -\frac{1}{4\pi}\int e^{i(\mathbf{k}-\mathbf{k}').\mathbf{r}'}\frac{2m_n}{\hbar^2}V(\mathbf{r}')\,d\mathbf{r}' \tag{4.77}$$

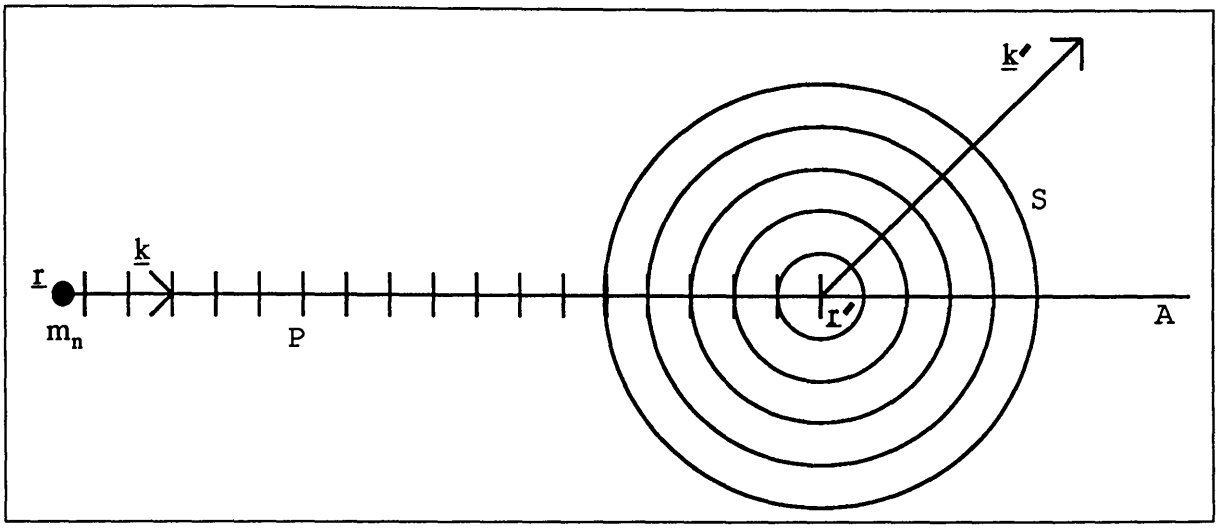

Figure 4.1: An incident neutron of mass m_n is represented as a plane wave P with wavevector $\mathbf{k}$ and scatters from an atom located at $\mathbf{r}'$ as spherical waves S with wavevector $\mathbf{k}'$.

The number of neutrons scattered into area $\mathbf{R}'^2 d\Omega$ per second is:

$$\frac{|f|^2}{\mathbf{R}'^2}\frac{\hbar \mathbf{k}'}{m_n}\mathbf{R}'^2\, d\Omega \tag{4.78}$$

Which gives the differential cross section as:

$$\frac{d\sigma}{d\Omega} = \frac{\mathbf{k}'}{\mathbf{k}}\left|\frac{1}{4\pi}\int e^{i(\mathbf{k}-\mathbf{k}').\mathbf{r}'}\frac{2m_n}{\hbar^2}V(\mathbf{r}')\,d\mathbf{r}'\right|^2 \tag{4.79}$$

Making the assumption that the scattering is elastic, ie that $|k| = \left|\mathbf{k}'\right|$ and writing $\mathbf{Q} = \mathbf{k} - \mathbf{k}'$ this becomes:

$$\frac{d\sigma}{d\Omega} = \left|\frac{1}{4\pi}\int e^{i\mathbf{Q}.\mathbf{r}'}\frac{2m_n}{\hbar^2}V(\mathbf{r}')\,d\mathbf{r}'\right|^2 \tag{4.80}$$

Where the scattering vector $\mathbf{Q}$ is easily seen on geometrical grounds (see figure 4.2) to be given by $\mathbf{Q} = 2\,k\sin(\theta) = \frac{4\pi\sin(\theta)}{\lambda}$. This then states that the differential cross section is essentially a Fourier transform of the nuclear scattering potential. For SANS, the details of $V(\mathbf{r})$ are generally not of direct importance since the relevant length scales are much greater than the neutron-nucleus interaction lengths. This means that the high frequency components of the Fourier transform are of no interest and the integral in 4.80 can be written using:

$$b = -f = \frac{1}{4\pi}\int \frac{2m_n}{\hbar^2}V(\mathbf{r}')\,d\mathbf{r}' \tag{4.81}$$

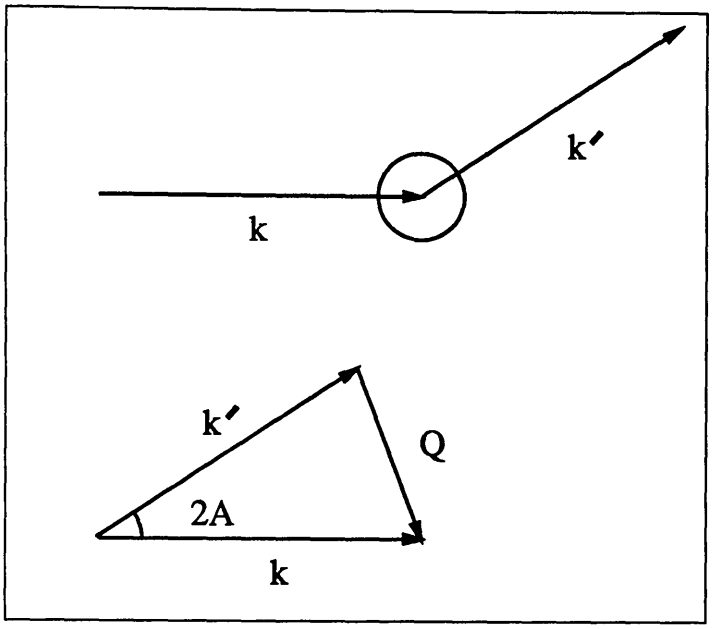

Figure 4.2: Effect of combining wavevectors $\mathbf{k}$ with $\mathbf{k}'$ to obtain the scattering vector $\mathbf{Q} = \mathbf{k} - \mathbf{k}'$ after a neutron has been scattered through angle $2A$

where b is known as the bound-atom scattering length and is well tabulated for most of the known isotopes. This gross approximation in characterising an isotope solely by one parameter, b is reflected in the observation that b varies considerably amongst isotopes, being complex in general. Experimental values for b, are tabulated in [92, 93, 101].

Consider a beam of incident neutrons impinging on a spatial distribution of scattering atoms as in a solid sample. If the atoms in the sample are labelled by j and are located at mean positions $\mathbf{r}_j$, then the total differential scattering cross-section may be written as:

$$\frac{d\sigma_t}{d\Omega} = \sum_{j,k} b_j b_k e^{i\mathbf{Q}.(\mathbf{r}_j - \mathbf{r}_k)} \tag{4.82}$$

It is often useful to separate this conceptually into a coherent component $\frac{d\sigma_{coh}}{d\Omega}$ which depends strongly on λ and hence on $\mathbf{Q}$, and an incoherent part $\frac{d\sigma_{inc}}{d\Omega}$ which varies only weakly with $\mathbf{Q}$, and can often be approximated by a flat constant value, over the range of $\mathbf{Q}$ values accessible in a small angle scattering experiment. Writing $\frac{d\sigma_t}{d\Omega}$ in the form:

$$\frac{d\sigma_t}{d\Omega} = \sum_j b_j^2 + \sum_{j,k,j\neq k} b_j b_k e^{i\mathbf{Q}.(\mathbf{r}_j - \mathbf{r}_k)} \tag{4.83}$$

allows this to be separated into:

$$\begin{aligned}\frac{d\sigma_t}{d\Omega} &= N < b^2 > -N < b >^2 \\ &\quad +N < b >^2 \sum_{j,k} e^{i\mathbf{Q}.(\mathbf{r}_j - \mathbf{r}_k)}\end{aligned} \tag{4.84}$$

This yields the approximations:

$$\begin{aligned}\frac{d\sigma_{inc}}{d\Omega} &= N < b^2 > -N < b >^2 \\ \frac{d\sigma_{coh}}{d\Omega} &= N < b >^2 \left| \sum_j e^{i\mathbf{Q}.\mathbf{r}_j} \right|^2\end{aligned} \tag{4.85}$$

It is convenient to use just:

$$\frac{d\sigma_{coh}}{d\Omega} = \left| \sum_j b_j e^{i\mathbf{Q}.\mathbf{r}_j} \right|^2 \tag{4.86}$$

which is recognizable as a discrete Fourier transform of the spatial distribution of the scattering length density. It can be recast into a continuous form by imagining a macroscopically smooth scattering length density function $\rho(\mathbf{r})$, defined over the total volume V of the sample to yield:

$$\frac{d\sigma}{d\Omega} = \frac{1}{V} \left| \int_V \rho(\mathbf{r})\, e^{i\mathbf{Q}.\mathbf{r}} d\mathbf{r} \right|^2 \tag{4.87}$$

This is related to the intensity $I(\mathbf{Q})$, which is *actually measured* in a small angle scattering experiment, by a simple proportionality due to the choice of units, *providing* the elastic scattering approximation ($|\mathbf{k}| = |\mathbf{k}'|$) holds. A number of other assumptions are involved, and contribute correction factors to this equation. These include multiple scattering effects and absorption in the scattering material. A detailed discussion of these corrective factors is given in [102].

The quantity of interest in small angle scattering experiments and indeed in the computer simulations, is a measure of the domain shapes and sizes, independent of the actual constituent atomic species. This function is the structure factor $S(\mathbf{Q})$ and is difficult to obtain directly from the measured intensity $I(\mathbf{Q})$ without further approximation. An common and useful approach is to assume a two-phase model description of the system. Following [98], the sample can be treated as a particulate phase on a background of matrix phase. The particulate or precipitating phase has scattering length density ρ_p and the matrix phase has ρ_m. The

integral in 4.80 can then be separated out into a uniform integral over the whole sample, and one with scattering length density given by $\rho = \rho_p - \rho_m$, the 'excess scattering length density' due to the precipitating phase. The important feature of this approximation is that the scattering length density is now represented as a single value, constant over the sample, and therefore *outside* the integral sign in 4.80.

$$\frac{d\sigma}{d\Omega} \approx \left(\rho_p - \rho_m\right)^2 \frac{1}{V} \left| \int_V e^{i\mathbf{Q}.\mathbf{r}} d\mathbf{r} \right|^2 \tag{4.88}$$

The term $\left(\rho_p - \rho_m\right)^2$ is known as the small angle scattering contrast, denoted as $\triangle\rho^2$. A large value of $\triangle\rho^2$ gives higher *relative* scattering intensity from the precipitate phase. Equation 4.88 can then be rewritten as:

$$\frac{d\sigma}{d\Omega} \approx \left(\rho_p - \rho_m\right)^2 \frac{1}{V} S(\mathbf{Q}) \tag{4.89}$$

which defines the structure function as

$$S(\mathbf{Q}) = \left| \int_V e^{i\mathbf{Q}.\mathbf{r}} d\mathbf{r} \right|^2 \tag{4.90}$$

which is strictly a dimensionless quantity, but is often incorrectly equated in the scattering literature with the differential cross section itself. The structure function is discussed further in the context of scattering from spherical particles in the two-phase approximation in appendix C.

If we do not wish to resort to the two-phase model approximation, it is necessary to consider *partial* structure functions, where a separate function is obtained for the relative structure of each pair of phases, giving three independent functions for a binary material and six for a ternary system. These must be measured separately using different sample compositions and the isotope substitution method as described in [103].

Equation 4.89 is a bridge equation connecting the SANS measurements, theoretical calculations of the structure factor, and calculated Fourier transforms of computer simulated sample configurations.

4.3 SANS Implementation

4.3.1 Instruments

Having shown how the small angle neutron scattering intensity gives a practical measurement of the idealised structure factor, how is the SANS experiment implemented ? A SANS instrument consists of a source of neutrons, a beam guide and sample environment equipment, and a detector system. The means of producing neutrons either by thermalising fast neutrons from a nuclear reactor or from a pulsed accelerator and target system is of considerable interest in its own right [104] . There is insufficient space to discuss it fully here, and this work will simply assume some distribution of neutron wavelengths with mean wavelength λ_{mean} and width $\Delta\lambda$, determined by the moderator temperature.

The beam must also be collimated before arriving at the sample. There are a number of techniques for this described in [105], all that need be considered here, is the signal smearing effect the collimation system has. If this is known and can be parameterised, it can be removed from the processed data, using deconvolution methods. This is discussed in section 4.3.5. Figure 4.3 shows the usual arrangement with a normalising counter (M_u) upstream from the sample (S), and scattered neutrons detected by an area detector (A). This diagram is used as the basis for discussing the measurement and data normalisation procedure to obtain the scattering intensity $I(\mathbf{Q})$ in standard units of cm^{-1} [1]. A second monitor, downstream (M_d) is sometimes employed for transmission measurements, although cells of the area detector itself can sometimes be used for this purpose. The instrument has the general characteristic that the relative scattering intensity or detector-counts can be measured as a function of cartesian co-ordinates (x, y) and hence transformed to polar angles θ and ϕ for a range of small θ values, but with very small values inseparable from the large count rates from the straight-through beam. If the neutron wavelength is known, the measured count rate gives a measure of $S(\mathbf{Q})$ where $\mathbf{Q}$ is determined uniquely from θ, ϕ and λ. Small angle scattering instruments are discussed generally in [106] and the PLUTO and IPNS

[1] This work consistently uses cm and $\AA$ units in describing scattering experiments, since this is consistent with the current literature, and what's in a few factors of 10 anyway ?

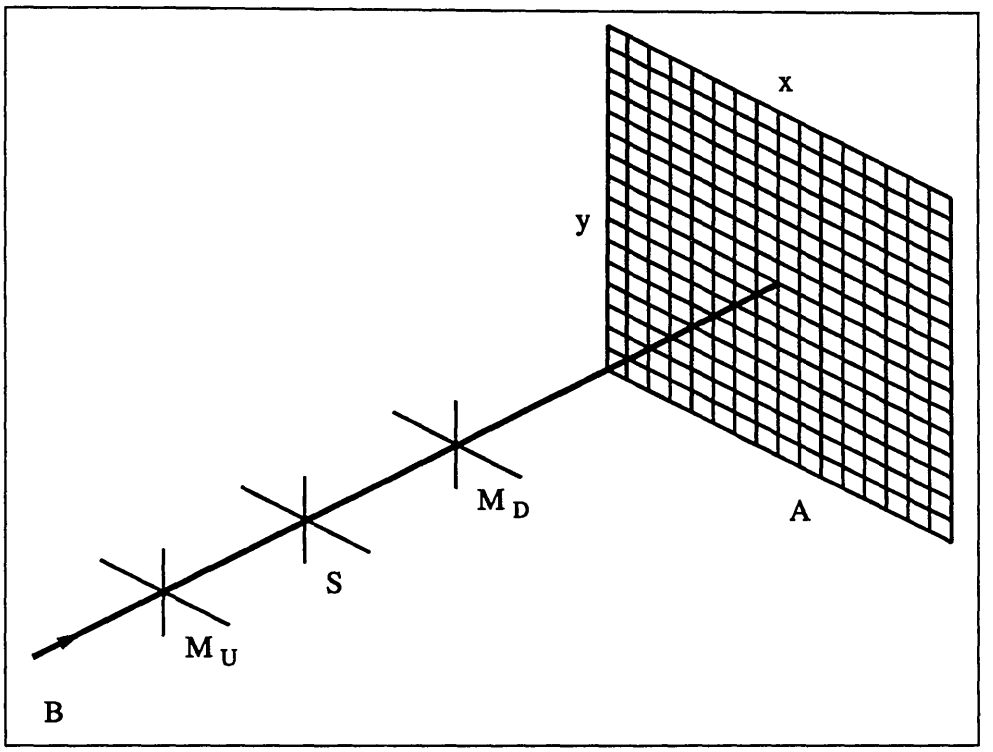

Figure 4.3: A generalised small angle neutron scattering instrument, showing a collimated beam of neutrons B, the normalising upstream monitor M_U, the scattering sample S, the (optional) downstream monitor M_D for transmission measurement, and the area detector consisting of a grid of position-event recording cells $A(x, y)$. The area detector is not necessarily centred on the beam and may be offset for anisotropic measurements.

instruments are described in detail in [107, 108] respectively.

4.3.2 Bragg Scattering

It is worth mentioning that for small angle scattering experiments it is important to *avoid* Bragg scattering occurring, or at least to avoid measuring its effects. A SANS sample must be macroscopically thick to obtain sufficient scattering signal, and is typically a few millimetres in thickness. In a polycrystalline sample, as used for all the data presented in this work, strong multiple scattering effects can occur if certain combinations of crystallographic orientations occur accidentally. The resulting very strongly Bragg scattered neutrons will have a high probability of being further scattered as they pass through the sample.

It is by no means trivial to correct for such multiple scattering effects [109]. It is usual to avoid the problem by choosing a neutron wavelength range so that the strong Bragg scattering does not occur. The Bragg relation:

$$n\lambda = 2d\sin\theta \tag{4.91}$$

will only be satisfied for neutrons with a low enough λ, given the d spacing in the polycrystalline sample material. If $\lambda > 2d$ is chosen, then no Bragg scattering can occur.

This choice is relatively simple at a steady state reactor neutron source, where the chopper can be adjusted to keep λ above the cutoff. At a pulsed source, it is not always possible to have the beam characteristics changed, and the only solution is to discard the channels with too low a wavelength. This often limits the resolution of the instrument.

4.3.3 SANS data Reduction

Using figure 4.3 as a reference, it is possible to describe how raw small angle scattering data is reduced to a structure factor like quantity $I(\mathbf{Q}) \propto S(\mathbf{Q})$. Consider

the expression for the scattering wavenumber $|\mathbf{Q}|$.

$$Q = |\mathbf{Q}| = \frac{4\pi}{\lambda} \sin(\frac{2\theta}{2}) \tag{4.92}$$

where the redundant factor of two is retained to emphasise that the neutron of wavelength λ is scattered through an angle of 2θ.

This indicates that a scattering experiment can measure intensity as a function of Q, by varying the neutron wavelength as well as by using a position-dependent and therefore θ-dependent detector. This is the method employed at a pulsed source instrument, and will be described first.

At the Intense Pulsed Neutron Source (IPNS) facility at Argonne, a pulsed proton beam impinges on an enriched uranium target to provide pulses of fast neutrons by fission. These are then moderated to provide beams of thermalised neutrons, and are made available as a collimated beam to the various instruments. This pulsed beam contains neutrons of wavelengths that vary with their time of arrival at the area detector in a known way. It is then possible to use an electronic gating system to obtain time sliced intensity readings for each spatial cell in the area detector. This allows the recording of position and time dependent intensity measurements $I(x, y, t)$. From knowledge of the geometry of the instrument and its relationship to the scattering smaple, it is possible to convert the (x, y) into a scattering angle 2θ for an isotropic scatterer, or to retain the azimuthal angle (ϕ) dependence about the beam axis for an anisotropic scatterer. Information about the time of arrival of the neutrons and knowledge of the pulsed beam properties allows determination of the appropriate wavelength in expression 4.92 above. It is then possible to bin the intensity measurements as required.

The raw intensity measurements must be calibrated in standard units, if they are to be compared usefully with measurements made on other samples, and perhaps at other instruments. It is also necessary to remove background intensity readings from the unscattered beam, and from any other spurious sources such as general background radioactivity or analogue electronic noise in the detector system.

Consider the general expression used to obtain calibrated intensity readings using

the IPNS SAD instrument.

$$I(x,y,t) = \frac{\mathrm{SF}}{\mathrm{DETSEN}(x,y) \times \mathrm{SPEC}(t)} \left[\frac{M_u^{SB}(t)}{T^S(t)} \left(\frac{I^S(x,y,t)}{M_u^S(t)} - \frac{I^C(x,y,t)}{M_u^C(t)} \right) - \frac{M_u^{SB}(t)}{T^B(t)} \left(\frac{I^B(x,y,t)}{M_u^B(t)} - \frac{I^C(x,y,t)}{M_u^C(t)} \right) \right] \quad (4.93)$$

Where the superscripts S, B, SB, C refer to measurements made with the sample, the sample background (ie the empty sample holder), a standard background, and a cadmium blank disk (which absorbs the neutrons and thus blocks the beam). The scale factor SF is obtained from measurements on a standard sample as described below. The detector sensitivity DETSEN can be obtained from measurements of the relative count rates for an known scattering sample. The upstream monitor counts M_U are required to allow the beam intensity to fluctuate without affecting the measurement calibration. The transmissivities (T)are determined using the down-stream monitor, or from the central cell(s) of the area detector itself, using the expression:

$$T = \frac{M_D^S - \frac{M_U^S}{M_U^E} M_U^C}{\frac{M_U^S}{M_U^E} M_D^E - \frac{M_U^S}{M_U^C} M_D^C} \quad (4.94)$$

This applies to each time channel t, with the superscripts S, E and C referring to sample, empty beam and cadmium runs, and the subscripts U and D referring to the upstream and downstream monitors. Finally the term SPEC refers to a determination of the relative populations of neutron wavelengths present in the beam. This is done by attenuating the beam with a disk of absorbing cadmium, with small holes in it, and by filtering out fast neutrons with a crystal of MgO. More detail is given in [108].

The calibration process for a pulsed source is complicated considerably by the need to keep track of the different wavelengths. Small angle instruments at a steady state or reactor neutron source, typically use one fixed neutron wavelength. This is typically done using a chopper, consisting of rotating helical channels through a cylinder of neutron absorbing material such as cadmium, that only allows neutrons of a restricted range of wavelengths to pass. See for example [107]. Equation 4.93 is then independent of time channel, but is otherwise unchanged.

A standard sample is required to calibrate the scattering data into known units. The choice of this sample is somewhat controversial. Generally, the standard

should be a strongly isotropic scattering substance, of precisely known composition, and generally available. It is also preferable that its scattering should be either independent of neutron wavelength over the usual SANS range of $3 - 10\mathring{A}$ or at least have scattering intensity well parameterised in terms of wavelength. The scattering Materials used in the past are vanadium, which is unfortunately a weak scatterer, water, which does have a wavelength dependence, or a calibrated secondary standard polymer which is less generally available. See [110] for a discussion of these materials and intercalibration methods. This work employed water as a calibration standard for experiments with iron chromium and PE16 steel performed at the Harwell PLUTO reactor, and used the secondary standard 'Bates polymer' [111], as calibrated by the Oak Ridge National Laboratory, for the experiments on copper-cobalt alloys performed at IPNS.

4.3.4 Binning Schemes

Equation 4.93 describes the measured intensity I as a function of $\mathbf{Q}$. This can be binned in a number of ways depending upon the properties of the sample, and how the scattering signal is to be interpreted. If the sample is an isotropic scatterer, it is sensible to reduce the statistical noise in the measurement by averaging the intensity around circles of constant $Q = |\mathbf{Q}|$. Figure 4.4 indicates how intensity measurements are binned this way. An example is given for the isotropic scattering pattern of iron chromium at a high temperature.

4.3.5 Data Filtering and De-Smearing

As indicated in figure 4.5 there can be considerable noise present in a two dimensional small angle scattering pattern. To a large extent this is less important when circular averaging about the beam centre is done, but even then, the signal to noise ratio may be too low at extreme Q values. Techniques for reducing the noise present in a systematic way involve Fourier filtering of the raw intensity data and are described in [112, 113]. Briefly, the scattering pattern is Fourier transformed in two dimensions, either in cartesian or polar co-ordinates. A filtering

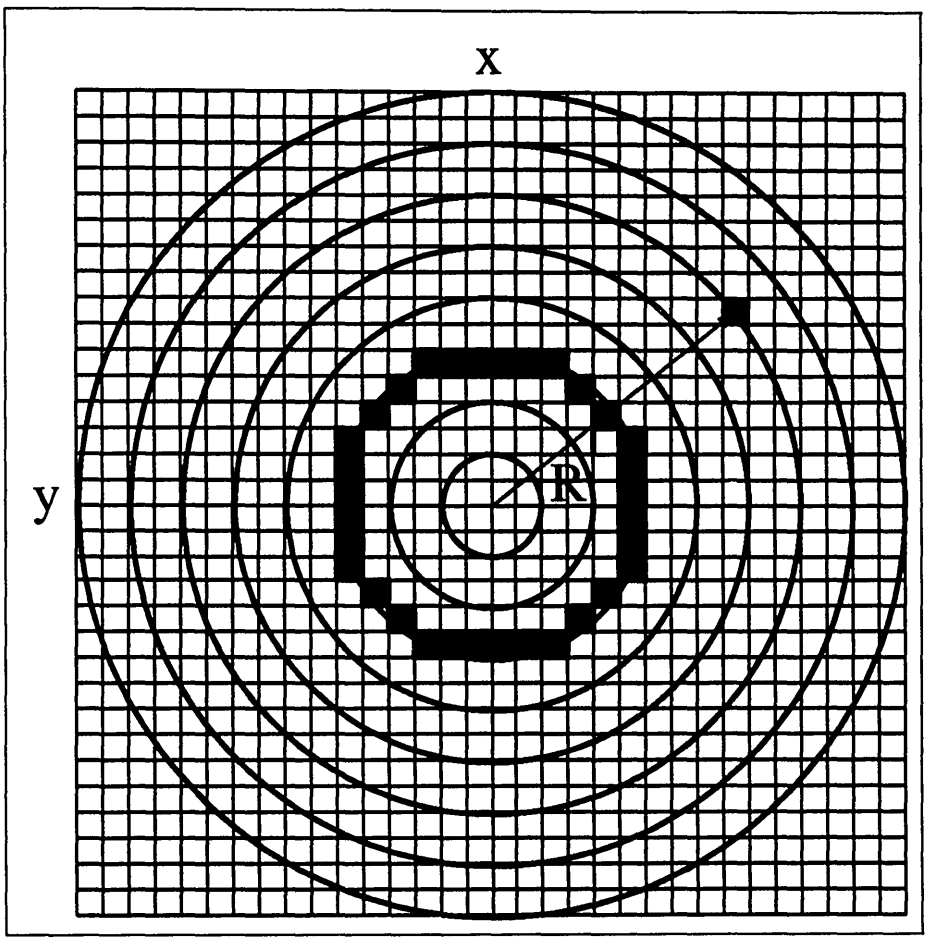

Figure 4.4: The circular binning scheme for the two dimensional scattering pattern. Values in Q-space are converted to radial average values, by binning around circles of constant $|Q|$. For an isotropic scattering sample this is adequate for a Q range of typically $|Q| > 0.005\mathring{A}$, although, as shown, resolution is limited at lower $|Q|$ values by the cartesian approximation to a circle.

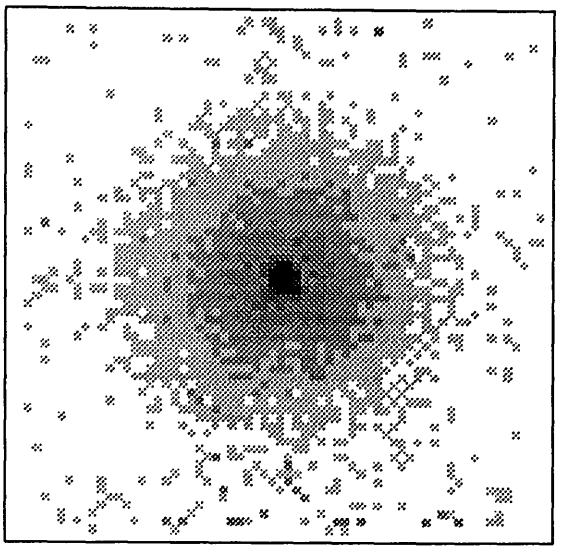

Figure 4.5: A typical isotropic scattering pattern, showing approximately circular pattern with a very high intensity from the unscattered neutrons in the straight through beam. The sample is a polycrystalline Iron - Chromium alloy at a temperature of 833K, and the scattering is from growing domains of chromium enriched material.

window is used to suppress or discard high spatial frequency components of the transform prior to applying an inverse transform to restore the pattern, which is then analysed in the usual way. These methods are useful when the scattering is so weak that the normalisation and background correction schemes can introduce negative values into the processed data, and cause the analysis codes to fail. Filtering inevitably causes some loss of information content in the scattering signal, and must be used with caution.

A related technique for pre-processing the scattering signal is de-convolution or desmearing. A consequence of the collimation system of the scattering instrument is that the signal is smeared and sharp features are blurred or convolved by the resolution function of the instrument. *If* the resolution function is known and can be parameterised, it is possible to Fourier de-convolve the measured signal, to restore any sharp features that were lost [114]. Good attempts at this parameterisation of SANS instruments at Los Alamos National Laboratory (LANL) and at Argonne National Laboratory (ANL) have been made [115, 116]. The present work has *not* employed these methods, since a serious systematic error is introduced if the resolution parametrisation is wrong. There is still scope for worthwhile work to

test this method with known scattering samples.

4.4 Magnetic SANS

This section describes a method for separating the scattering signals from the atomic nuclei, and from ferro-magnetic effects in the sample. This technique is a small subset of more general methodology needed for treating anisotropic small angle scattering signals. The aim is to separate the nuclear scattering signal that contains information about the spatial composition of an alloy, from the magnetic contribution that describes how the magnetic domains are aligned in spin direction. This method is used for interpreting the scattering data from a copper cobalt alloy, presented below.

Consider a binary alloy sample with a ferromagnetic component, held in a saturated magnetic field, in the horizontal direction. Following [117] the total scattering signal I_S is assumed to consist of nuclear I_N and magnetic I_M scattering contributions as follows:

$$I_T(Q) = I_N(Q) + I_M(Q) \tag{4.95}$$

with the nuclear part taken to be:

$$I_N(Q) = \left| \int_V \triangle\rho_N e^{i\mathbf{Q}.\mathbf{r}} d\mathbf{r} \right|^2 \tag{4.96}$$

ind the magnetic part as:

$$I_M(Q) = \left[1 - \left(\frac{\mathbf{Q}.\mathbf{M}}{QM} \right)^2 \right] \left| \int_V \triangle\rho_M e^{i\mathbf{Q}.\mathbf{r}} d\mathbf{r} \right|^2 \tag{4.97}$$

Note however, that modified values of the scattering length densities are required to take proper account of the nuclear and magnetic scattering. These values, ρ_N and ρ_M respectively can be calculated or measured as described below. In the presence of a saturated magnetic field, the magnetic signal will depend on the azimuthal angle but the nuclear component will not. Taking the azimuthal angle as a positive angle defined as the anti-clockwise angle with respect to the horizontal axis of the magnetic field as shown in figure 4.6 the scattering signal is

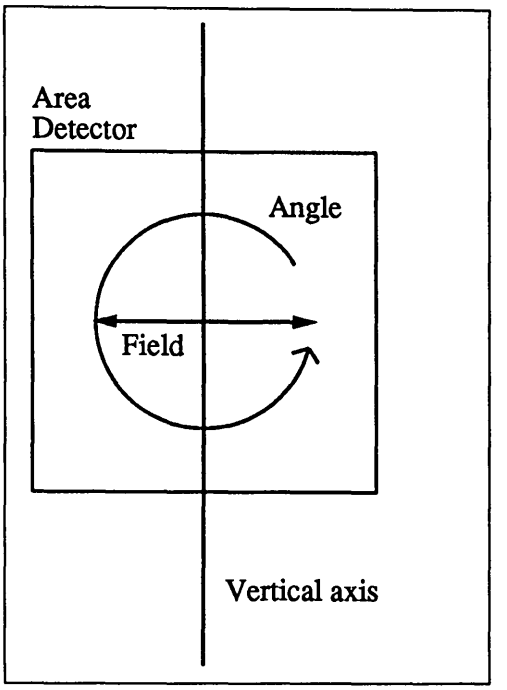

Figure 4.6: The relative orientation of the magnetic field as indicated by the arrow wrt the area detector and sample, with the neutron beam into the paper at the centre.

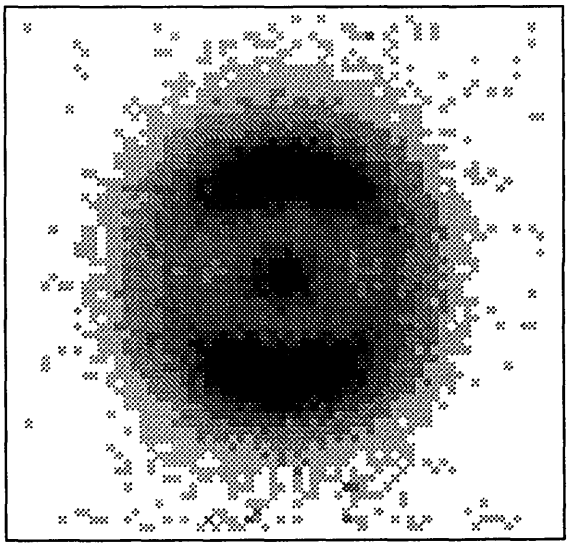

Figure 4.7: A typical magnetic scattering pattern, with high intensity 'wings' where the magnetic and nuclear scattering combine.

of the form shown in figure 4.7 with strong wings where the nuclear and magnetic scattering signals combine.

These can be separated by considering concentric rings of constant $Q = |\mathbf{Q}|$. The prefactor in equation 4.97 involves a dot product giving a ratio for the magnetic to nuclear components of $1 - \cos^2(\phi) = \sin^2(\phi)$. If there are N spatial cells contributing to a given Q ring, then by using the first and second moments of $\sin^2(\phi)$, the following matrix equation can be solved using Gaussian elimination, to determine the nuclear I_N and magnetic I_M scattering contributions from the total I_T scattering intensity.

$$\begin{bmatrix} N & \sum_j \sin^2(\phi_j) \\ \sum_j \sin^2(\phi_j) & \sum_j \sin^4(\phi_j) \end{bmatrix} \begin{pmatrix} < I_N > \\ < I_M > \end{pmatrix} = \begin{pmatrix} \sum_j I_{T,j} \\ \sum_j I_{T,j} \sin^2(\phi_j) \end{pmatrix} \tag{4.98}$$

where the angled brackets denote an average value for the circle of fixed Q. This system of equations was implemented in the program *ANLAN* for treating SANS data at the IPNS SAD instrument [113]. An example of processed data is given in section 4.6.1 for a copper cobalt alloy.

4.5 SANS data Interpretation

A wealth of *lore* surrounds the interpretation of small angle scattering data. The basic aims of SANS are to yield the shape and volume fraction of scattering features of a characteristic size of approximately $10 - 1000\mathring{A}$, in a bulk sample. If the sample contains a precipitating phase, the growing particles can be characterised from the SANS signal. Their shape comes from the shape of the scattering curve as a function of Q, while the volume fraction comes from the absolute values of the scattering intensity.

Generally SANS is inadequate to determine an accurate volume fraction unless the particle composition is known. Only then is it possible to compute the contrast $\Delta\rho^2$ for the precipitating phase. The problem of accurately characterising the particle shape and size distribution is especially difficult when there is more than two phases present or if there are many different shapes present. In such

cases, other experimental data is needed, such as accurate chemical analysis of the precipitates, or TEM micrographs giving the particle size distribution.

Even if the composition of the precipitating phase is unknown it is still possible to use SANS to obtain quantitative estimates for the relevant length scales. This is particularly useful in the case of a percolated domain structure, where there is no longer an unambiguous definition of particle size. The SANS signal can still give a good estimate of the correlation length of such a structure.

The following is a brief description of the scattering expected from a distribution of spherical particles. Form factors for other shapes are also quoted and the limiting forms for these factors, according to the Porod law, is discussed.

The well known Rayleigh formula for scattering from a single sphere of radius R can be readily derived from an integration of equation 4.87 in spherical co-ordinates, as done in appendix C, to yield:

$$F^2(QR) = \left| \frac{3\sin(QR) - QR\cos(QR)}{(QR)^3} \right|^2 \tag{4.99}$$

which gives the scattering intensity for a monodisperse system of spheres of radius R, as:

$$I_{\text{sph}}(Q) = \frac{4}{3}\pi R^3 \;\; V_f \;\; \Delta\rho^2 \;\; F^2(QR) \tag{4.100}$$

in the two-phase approximation, where V_f is the volume fraction of the sample taken up by the precipitating phase. The ideal scattering intensity for such a monodisperse system is illustrated in figure 4.8.

This form is unlikely to be seen in real experimental data for a number of reasons. A real sample is unlikely to be exactly monodisperse, and the interference troughs will be smeared out. Additional smearing arises from the resolution of the instrument. Finally, real particles in a polycrystalline alloy will form lattice approximations to spheres, also causing some smearing of the Rayleigh curve. In consequence, limiting forms of equation 4.99 are often used.

Taking $x = QR$, an expansion of equation 4.99 gives:

$$F^2(x) = 1 - \frac{x^2}{5} + \frac{x^4}{48} - \frac{4x^6}{4725} + \cdots \tag{4.101}$$

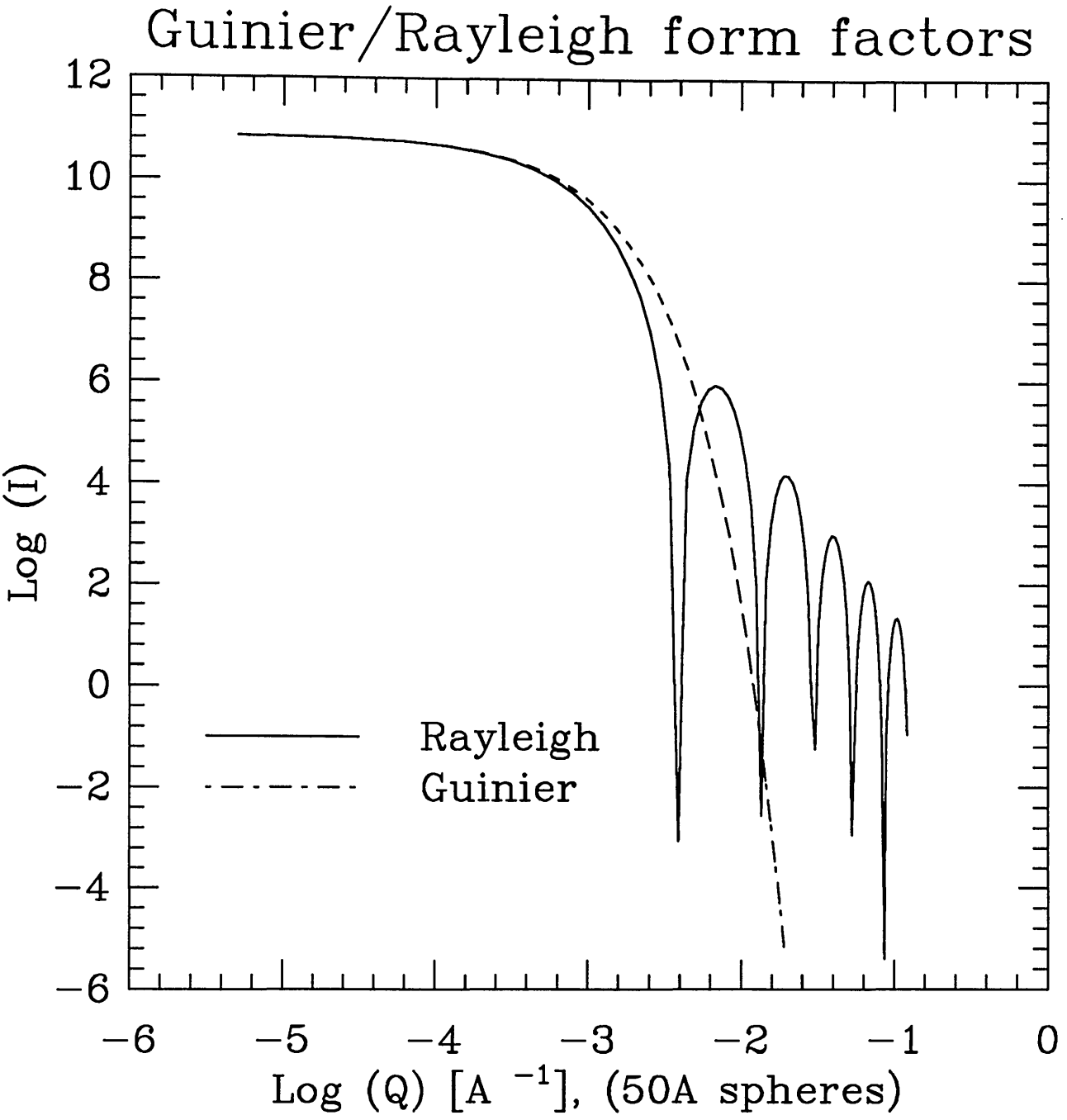

Figure 4.8: The Rayleigh form factor for a monodisperse system of spherical scatterers of radius $50\mathring{A}$, and the Guinier approximation to it, plotted for a typical SANS Q range of $0.005 - 0.4\mathring{A}^{-1}$. There is good agreement at low QR values.

A comparison between this and the expansion:

$$e^{\frac{-x^2}{5}} \simeq 1 - \frac{x^2}{5} + \frac{x^4}{50} - \frac{x^6}{750} + \cdots \tag{4.102}$$

shows that the Guinier approximation given by:

$$I_{\text{sph}}(Q) \simeq \frac{4}{3}\pi R_G^3 \;\; V_f \triangle\rho^2 \;\; e^{\frac{-(QR_G)^2}{5}} \tag{4.103}$$

is correct to second order in QR. Equation 4.103 defines a Guinier radius R_G as a characteristic length scale for the particulate phase. The range of agreement with the Rayleigh formula is shown in figure 4.8. A common method of analysis for SANS of spheres, is to take logs of the Guinier equation 4.103. This yields a linear equation that can easily be fitted to data, and determines the Guinier radius R_G and volume fraction V_f from the fitted gradient and intercept respectively. A more accurate and robust method employs the Maximum Entropy method, described in appendix B, to fit a distribution of spherical scatterers to the SANS data.

A number of other form factors are in general use to describe commonly occurring features in SANS signals [118, 119]. Two of particular interest are for long randomly oriented rods or needle-like precipitates, and for thin randomly oriented platelets. For needles or long rods of radius a the form factor is:

$$F^2(Q) = \frac{J_1^2(Qa)}{Q(Qa)^2} a^4 \tag{4.104}$$

for randomly oriented thin platelets of thickness $2a$:

$$F^2(Q) = \frac{J_{\frac{1}{2}}^2(Qa)}{Q^2(Qa)} a^2 \tag{4.105}$$

where J_ν denote Bessel functions of the first kind [120, 121]. in a similar notation, the Rayleigh formula becomes:

$$F^2(Q) = \frac{J_{\frac{3}{2}}^2(QR)}{(QR)^3} R^6 \tag{4.106}$$

It should be emphasised that these form factors are theoretical limiting forms that are never obtained in real resolution limited experiments.

Of particular interest is the low-Q limiting of these form factors. A plot of $\log I(Q)$ versus $\log Q$ yields the leading power of Q as a gradient, and is a common means

of determining the dominant particle shape present in the precipitating phase. This is the Porod law, that states $\log I(Q) \propto -4 \log Q$ for spherical scatterers, in the limit of low QR. Similarly a gradient of -1 indicates rods and -2 randomly oriented sheets [118]. These approximations are, unfortunately, not helpful when a number of different shapes are present.

4.6 SANS Alloy data

This section presents three sets of SANS data for three different alloys. These alloys were chosen as representative of the regimes of a low-concentration binary system, a high-concentration binary system, and a complex many component system, where the dominant precipitating phase is in fact a compound [2].

The system copper cobalt is used to illustrate the growth of roughly spherical particles of cobalt in a matrix phase of copper with two weight percent of cobalt. Since cobalt is ferromagnetic, it was necessary to use the magnetic/nuclear separative techniques, described above, to process this data.

Various concentrations of chromium in iron alloys were studied as an alloy system in the concentrated regime, where a long-range interconnected chromium rich phase forms. I am grateful to Drs J.E.Epperson and C.G.Windsor for access to this data, which was collected using the PLUTO SANS instrument. It was unfortunately not possible to use a saturated magnetic field for these experiments, and so the data presented is the total scattering intensity, containing both nuclear and magnetic contributions. This data was treated using the software described above, by the present author, and published in [122]. Work on the iron chromium system is still underway as a collaborative project between Drs Epperson and Windsor and the author. There is some very recent evidence that the effects seen in the PLUTO unseparated total scattering data are essentially unchanged in nuclear/magnetic separated data collected at the IPNS instrument.

[2] OK, they weren't chosen, they were all that was available!

4.6.1 Copper-Cobalt

The copper cobalt system is an interesting system where the lattice parameters of the matrix are almost unchanged by the introduction of a small amount of dissolved cobalt. In addition, there is no intermediate phase formed, and the precipitate is almost certainly pure cobalt. A phase diagram for the copper cobalt system is given in [123]. The low strain due to the similar lattice parameters of copper and cobalt in the face centred cubic phase, suggests that the precipitating phase will be in the form of near spherical particles. These cobalt particles may be surrounded by 'depletion zones' where the cobalt is absent from the matrix.

This system presents an opportunity to study the very early stages of precipitation, a previous study only reporting on phase formation after long ageing times of more than 100 hours [117].

Cobalt is ferromagnetic, so it is necessary to use the magnetic/nuclear scattering separation techniques described previously.

Several samples of an alloy of two weight percent cobalt were prepared using 99.999% pure components, and were solution treated at 1273 K for one hour to remove any precipitate phase formed during manufacture. The samples were subsequently quenched in iced brine.

The samples were then annealed for various times at 873 K prior to re-quenching in iced brine. This final quench process should be fast enough to halt the precipitation process, so that the SANS experiments can study the growth at very short times, where there would have been insufficient scattering intensity for in-situ experiments. The instrument response time is also too short to allow accurate experiments lasting less than about a minute. Sample treatment times at 873 K were: 30 seconds, 1, 2, 4, 8, 16, 32, 64 and 128 minutes.

The copper-cobalt alloy sample used in this work has the composition shown in table 4.1.

Element	Weight percentage W_i	Atomic percentage A_i	Atomic weight M_i	Scattering length b_i $(/10^{-12}cm)$
Cu	98.0	97.846	63.55	0.769
Co	2.00	2.154	58.93	0.270
C	$\ll 0.1$	$\ll 0.1$	12.01	0.665

Table 4.1: $Cu_{0.978} - Co_{0.022}$ composition and constituent properties

The scattering length densities can then be computed from the formula:

$$\rho = N_A \overline{d} \frac{\sum_i A_i b_i}{\sum_i A_i M_i} \tag{4.107}$$

Where $\overline{d}$ is the sample density. In the case of the matrix phase the density can be computed from the mean atomic weight and the mean atomic volume of an atom in an fcc lattice of unit cell length $a_0 \simeq 3.617\mathring{A}$. The scattering length densities are then: The small angle scattering contrast for pure cobalt domains in a matrix

Phase	ρ_m $[10^{-12}$ cm$^{-2}]$
Cu-Co(2wt%) matrix	0.0643
Pure Cu	0.0649
Pure Co	0.0246

Table 4.2: Scattering length density for the phases in copper cobalt

of Cu-Co(2wt%) is then 1.5755×10^{21} cm^{-4}.

A selection of data is shown for the two weight percent Cobalt sample, in figure 4.9. Figure 4.10 is a log-log plot emphasising the features.

The ratio between nuclear and magnetic scattering is shown for a sample heat treated for 128 minutes in figure 4.11 and is relatively flat. There are no substantial peaks at low Q values. This suggests that the large scattering feature that causes the peak at low Q does *not* appear to be magnetic in nature, since it

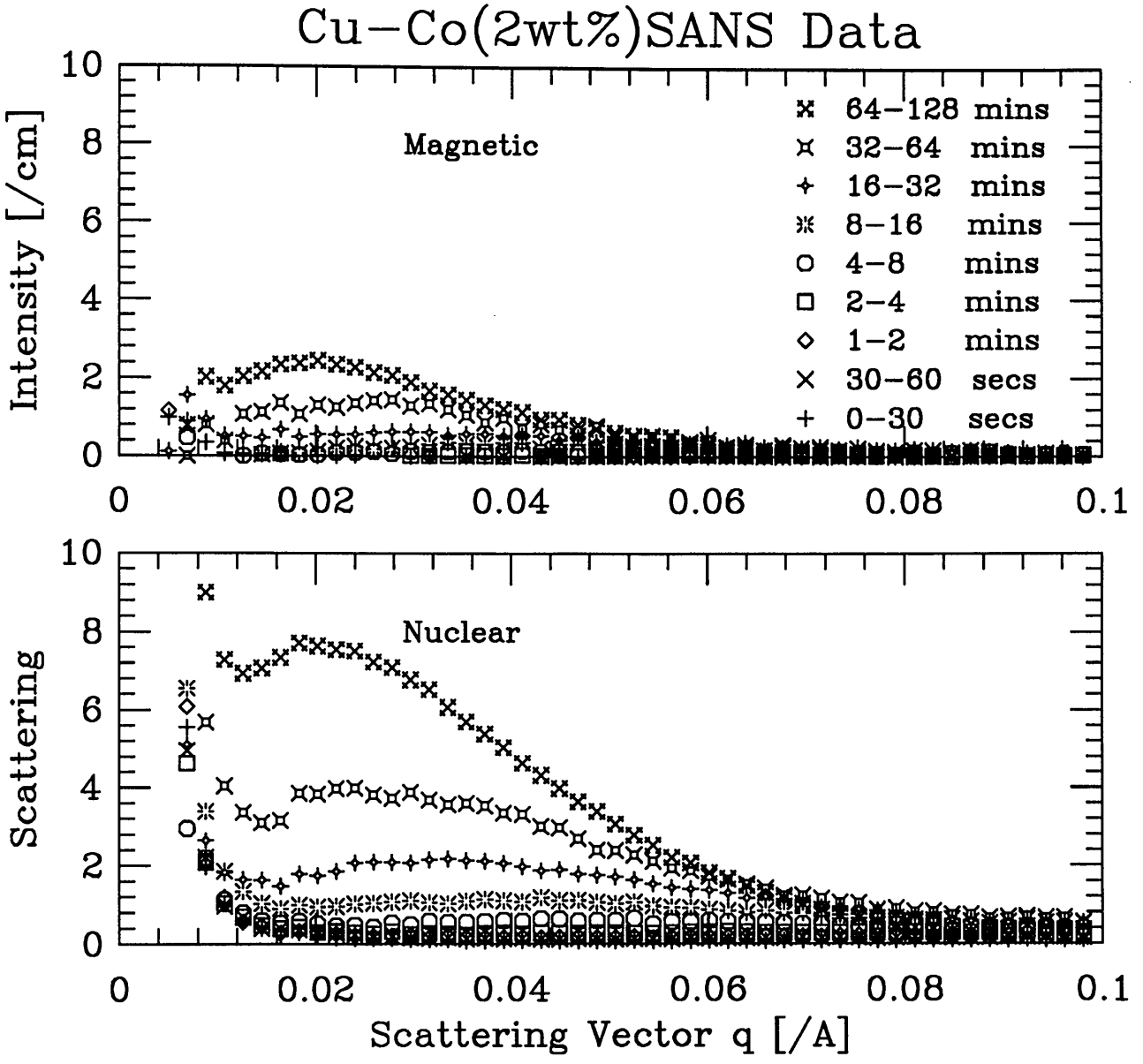

Figure 4.9: Copper-Cobalt scattering data with nuclear and magnetic scattering components separated using saturated magnetic field.

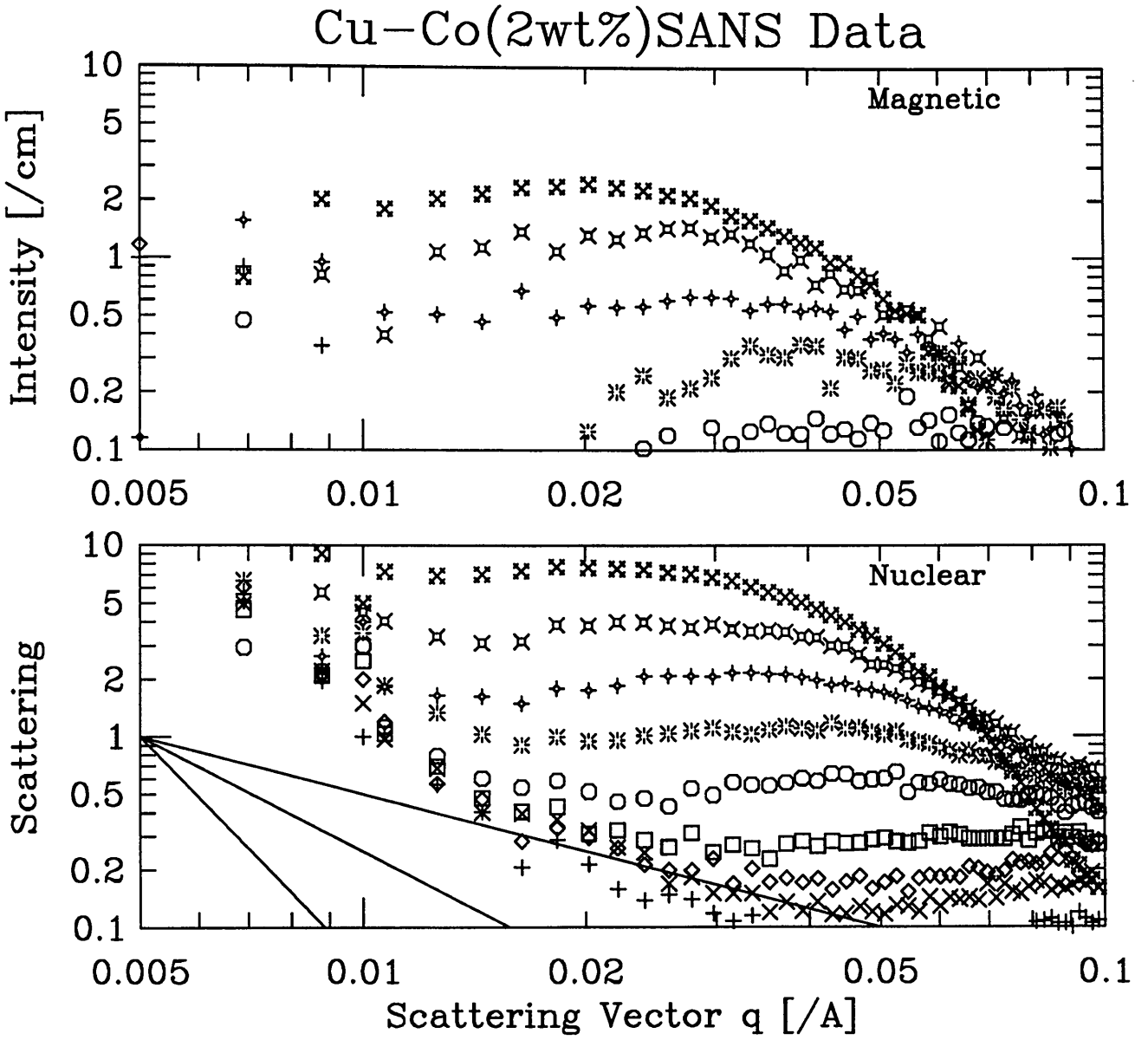

Figure 4.10: Copper-Cobalt scattering data on a log-log scale to emphasise the features.

appears predominantly in the nuclear component. It may be due to grain boundaries in the polycrystalline sample. It is possible to simply subtract this peak from those samples which have been heat treated for the longer times of $\gtrsim 8$ minutes, since there is sufficiently strong scattering from the precipitating phase. This is difficult and therefore of limited accuracy for the weaker scattering occurring in the those samples treated for shorter times.

The maximum entropy method described in appendix B is used to fit a distribution of spherical scatterers to the subtracted spectra. This gives an excellent and rapidly converging fit, and yields size distributions of fairly sharp Gaussian shape, as shown in figure 4.12. These distributions can be fitted to a Gaussian curve, to determine the volume fraction and mean particle size as a function of heat treatment time. Figure 4.13 shows the fitted particle radii as a function of heat treatment time and figure 4.14 the volume fractions. The radii and volume fractions are tabulated in table 4.3.

Time at 873 K minutes	Mean Particle radius [$\AA$]	Volume Fraction
1	33.7	0.016
2	33.6	0.042
4	32.0	0.17
8	34.3	0.48
16	38.9	0.68
32	38.2	1.01
64	44.0	1.07
128	45.3	1.73

Table 4.3: Fitted parameters to the Cu-Co(2wt%) alloy, following an effective quench to 873 K.

In general, the volume fractions can be obtained much more accurately than the the mean particle sizes, since they are less sensitive to the particle distribution shape.

Figures 4.15 and 4.16 indicate how well the assumed distribution of spherical

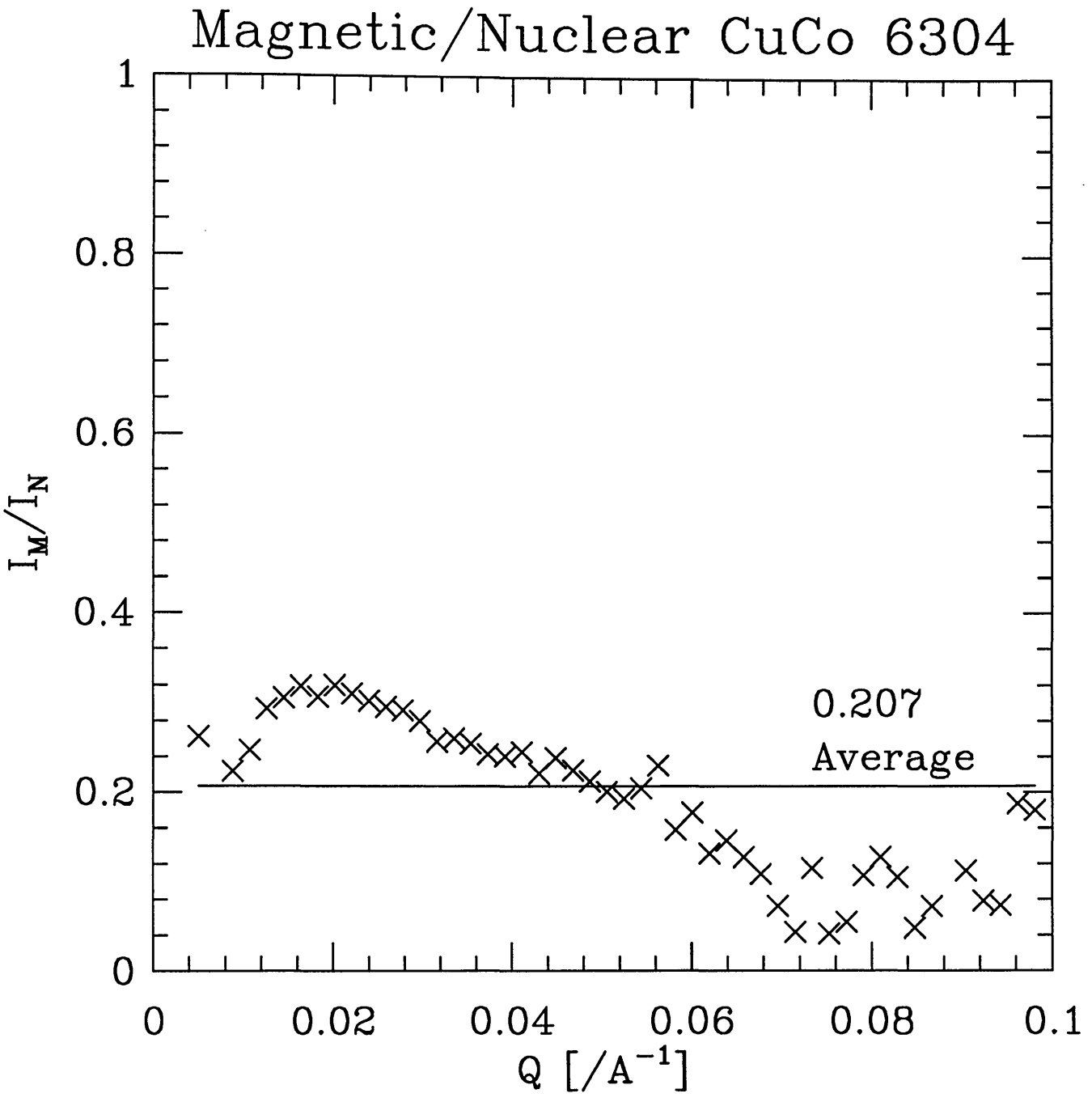

Figure 4.11: The ratio between magnetic and nuclear scattering in Cu-Co(2wt%) after 128 minutes at a temperature of 873 K.

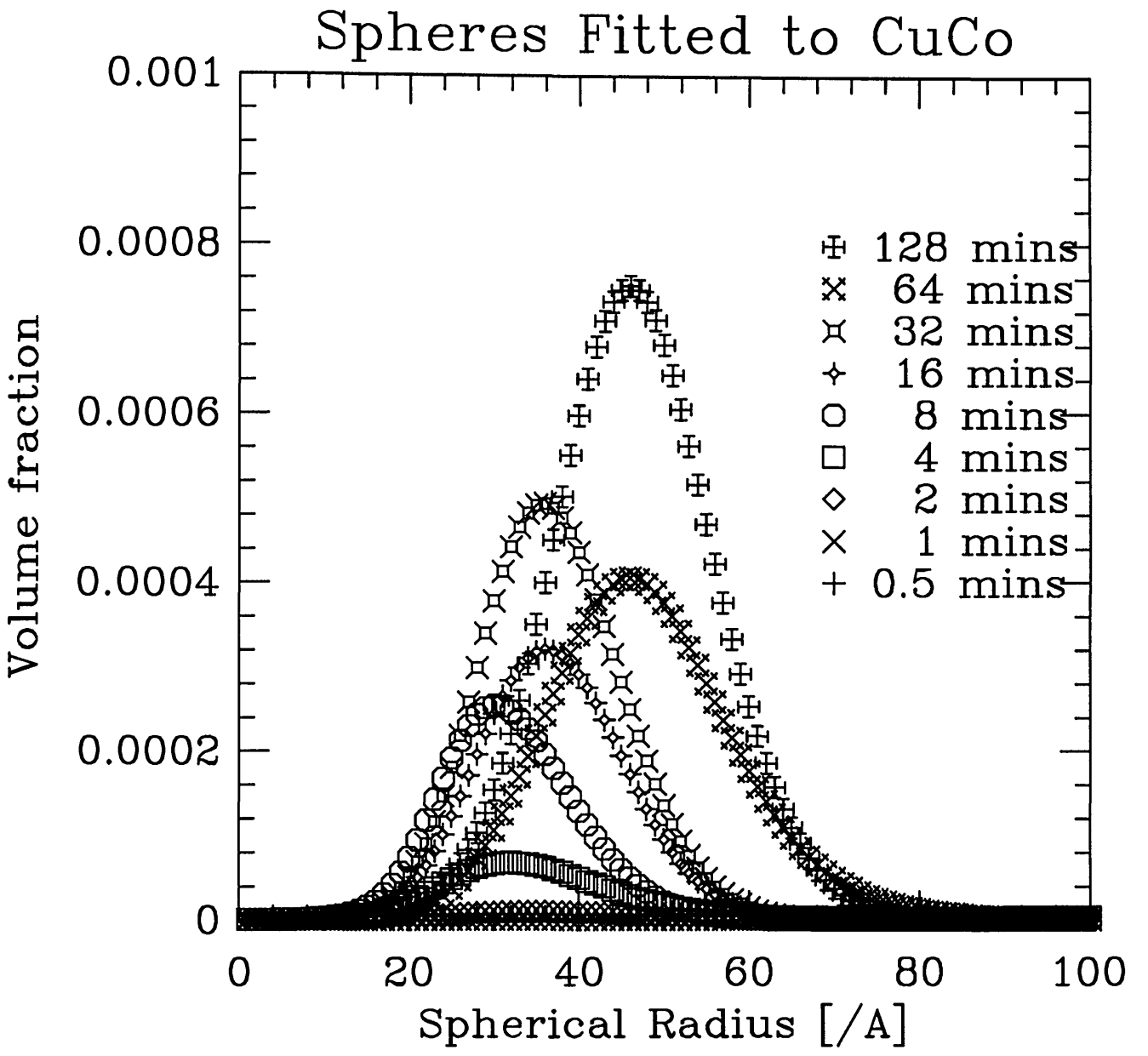

Figure 4.12: Fitted volume fractions to the Cu-Co(2wt%) heat treated data, for 0.5 minutes to 128 minutes at 873 K. These values assume pure cobalt particles. Note the anomalously high value at 32 minutes.

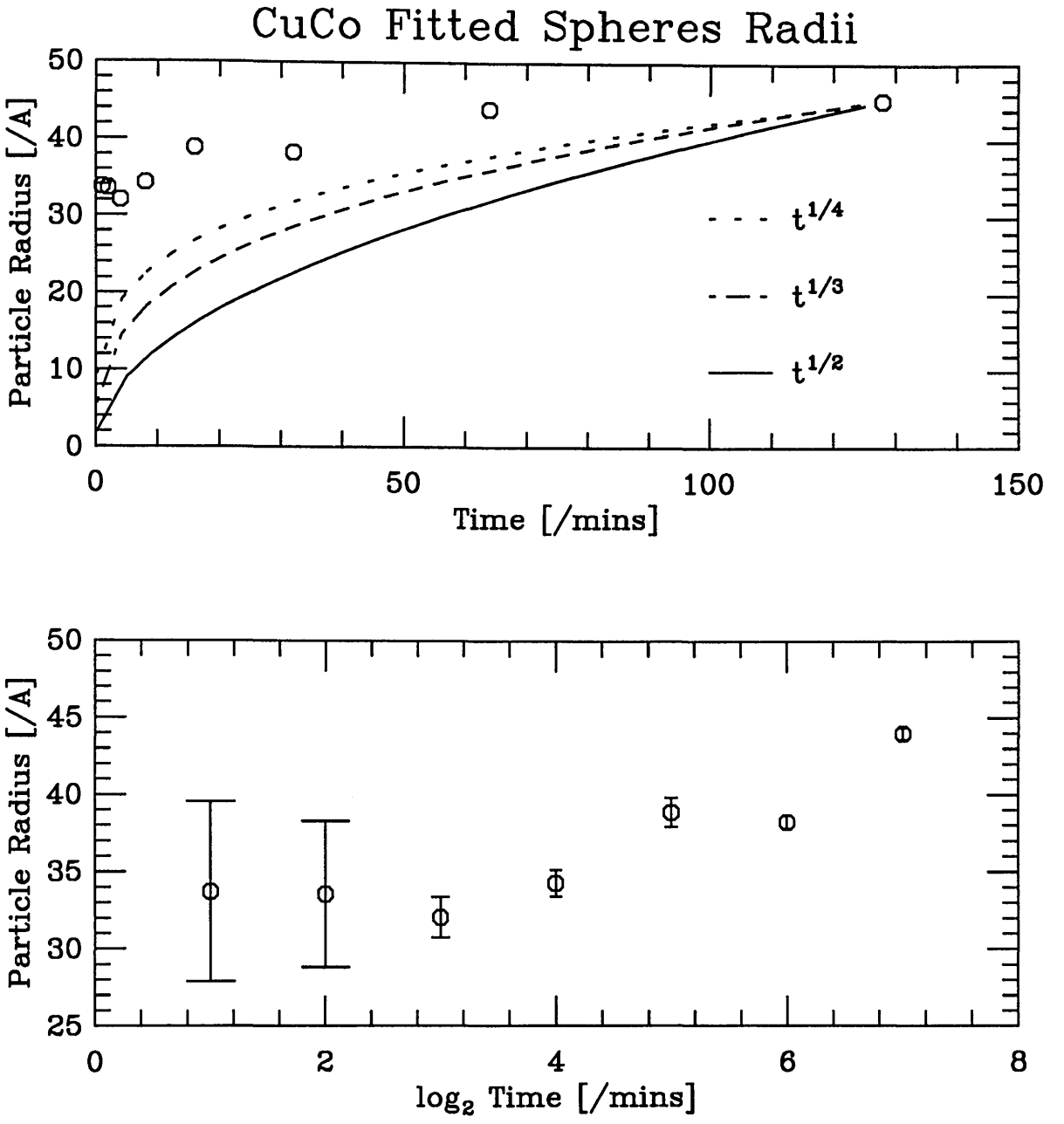

Figure 4.13: The mean particle radii for the heat treated Cu-Co(2wt%) samples from 0.5 to 128 minutes. The upper graph shows a comparison between various power laws, and the experimental data. The lower curve shows mean particle size against $\log_2$ time. None of the commonly employed growth laws fits the data over the whole range.

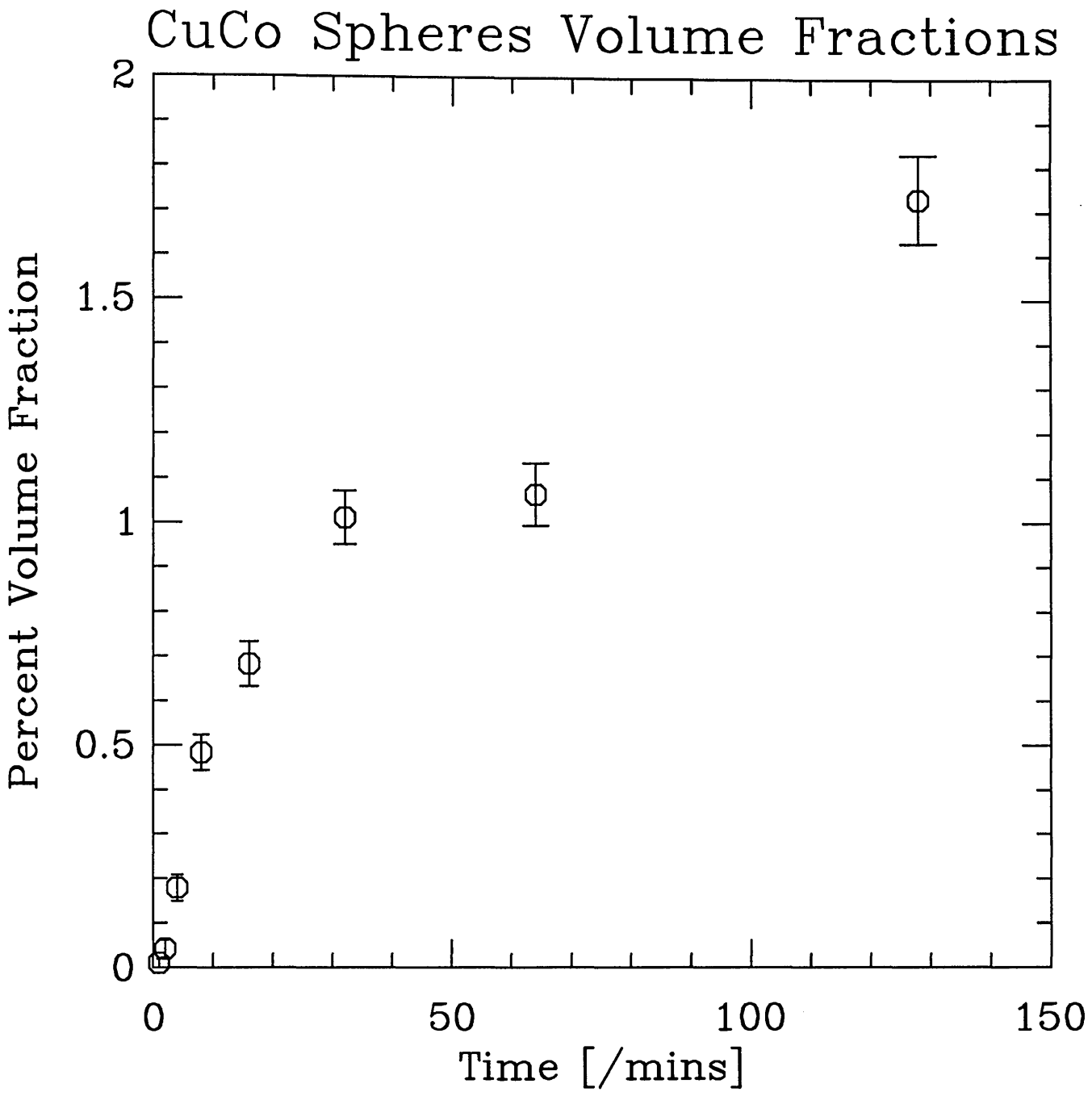

Figure 4.14: The particulate volume fraction for the heat treated Cu-Co(2wt%) samples from 0.5 to 128 minutes. Note the anomalously low value at 64 minutes of heat treatment

particles fits the scattering data.

This work has assumed that the growing particles are pure cobalt and that there is a sharp interface between the matrix phase of Cu-Co and the cobalt particles. This is almost certainly not true, as there will be a depletion zone formed around the growing cobalt particles where the available cobalt has been used up. This means that the two-phase approximation breaks down. A closer study of this effect is worthy of further study since its range imparts information on the diffusion coefficients of cobalt in copper. This work is already in progress [124].

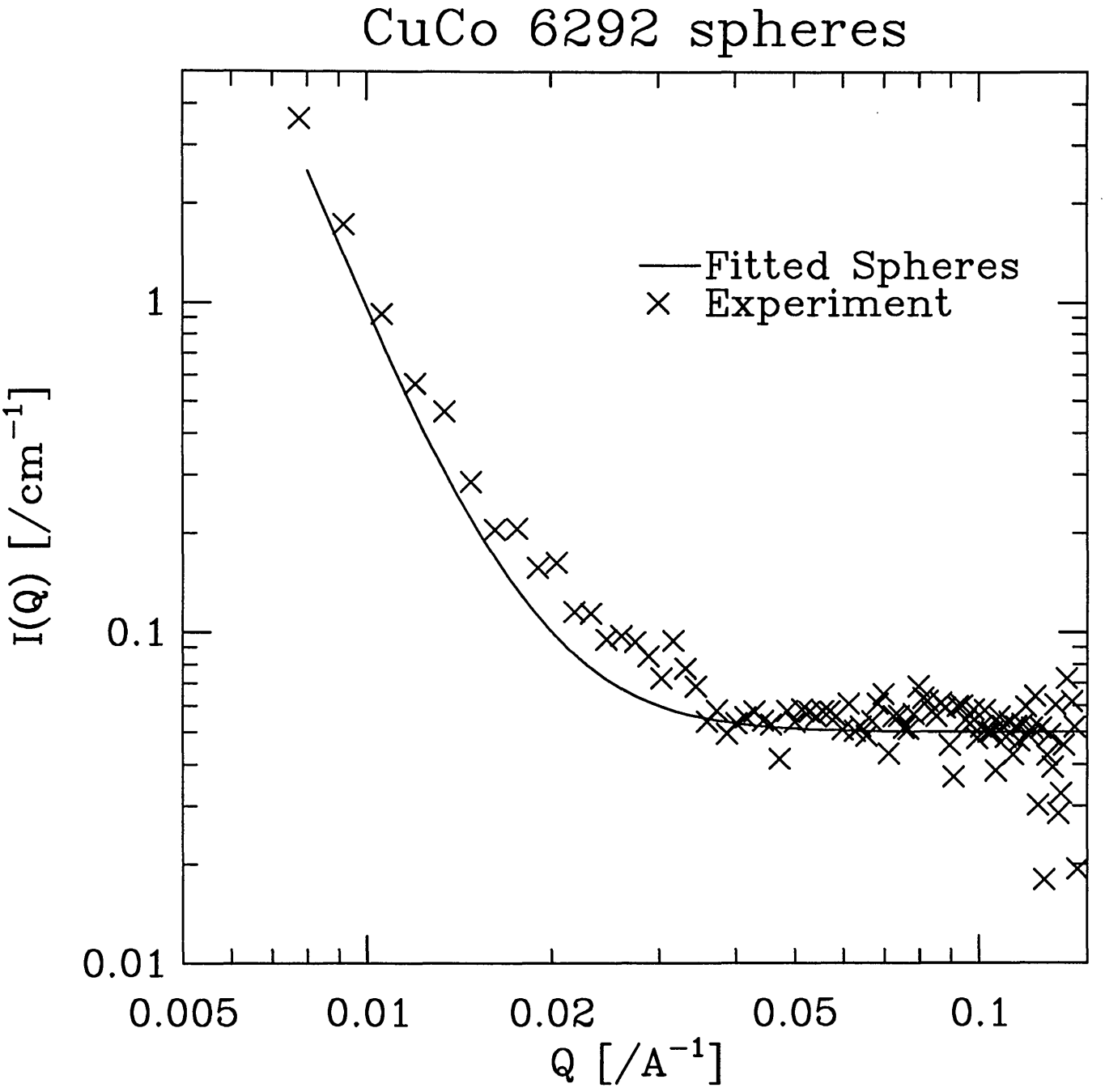

Figure 4.15: Fitted scattering intensity for Cu-Co(2wt%) after the initial quench into iced brine from 1273 K, using a distribution of spherical scatterers and an incoherent scattering background of 0.00877×10^{20} cm^{-4}

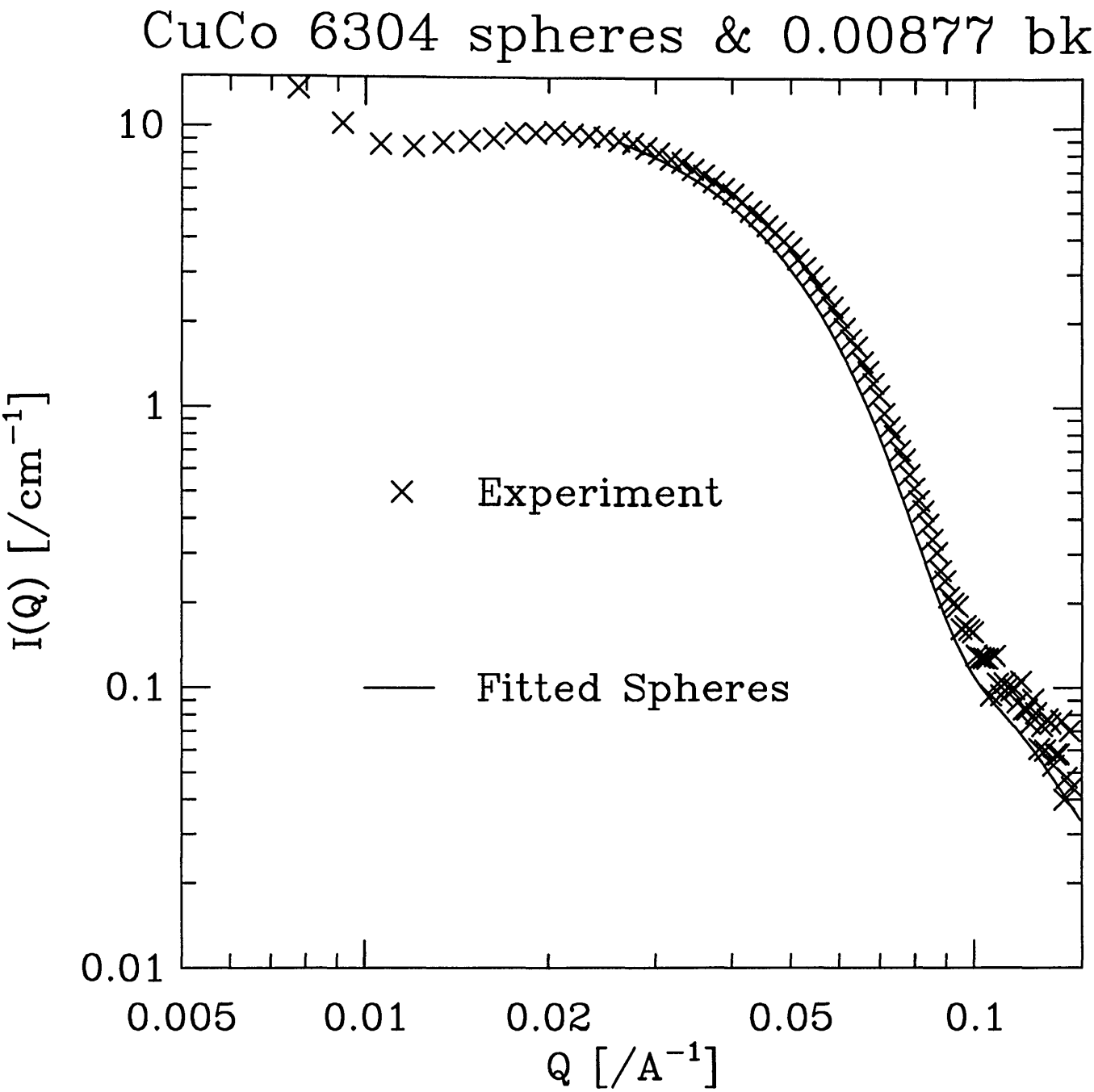

Figure 4.16: Fitted scattering intensity for Cu-Co(2wt%) after 128 minutes treatment at a temperature of 873 K, using a distribution of spherical scatterers and an incoherent scattering background of 0.00877×10^{20} cm^{-4}

4.6.2 Iron-Chromium

The binary iron-chromium system is particularly suitable for comparisons between simulation and experiments as it is possible to work with an almost purely binary system with real dynamics slow enough to be followed in an *in-situ* experiment. In addition there is already a body of experimental data available for this system [125, 57] which forms the *binary* alloys closest in composition to practical steels.

This section presents some temporal sequences of SANS data for binary iron-chromium alloys of 20, 30 and 40 at% Cr content, following quenches to below the miscibility gap. The work in this section has been published in [122]

Figure 4.17 shows an approximate phase diagram for the iron-chromium system, due to [57]. The exact positions of the curves are still controversial, but the layout is thought to be correct. Of particular relevance for these experiments is the intersection of the Curie curve and the miscibility gap.

Alloys of the compositions 20, 30 and 40 atomic percent Chromium were prepared from high purity materials: 99.999% Fe (Metalsmart) and 99.996% Cr (Materials Research Corporation). The constituent metals were melted and thoroughly mixed in an arc furnace equipped with a water cooled hearth. The homogenized alloys were rolled in steps with intermediate anneals, to plate stock 1mm in thickness. Flat coupons 19x19 mm^2 were stamped from this stock. The high purity materials were used to reduce the formation of carbides and other scattering features.

The platelets were encapsulated in a quartz ampoule, backfilled with just under one atmosphere of Helium and homogenized at 1000 C for over 100 hours. Sample quenching was done by immersing and breaking the ampoules in iced-brine. Finally the platelets were mechanically polished and etched for a few seconds in a solution of 15 parts (by volume) HCl, 4 parts H_2O_2 (30%) and 10 parts H_2O.

Table 4.4 shows the relevant properties of the iron-chromium system for computing the small angle scattering contrast of the separating phases.

The lattice spacing of iron chromium is approximately 2.86$\AA$, [126], at tempera-

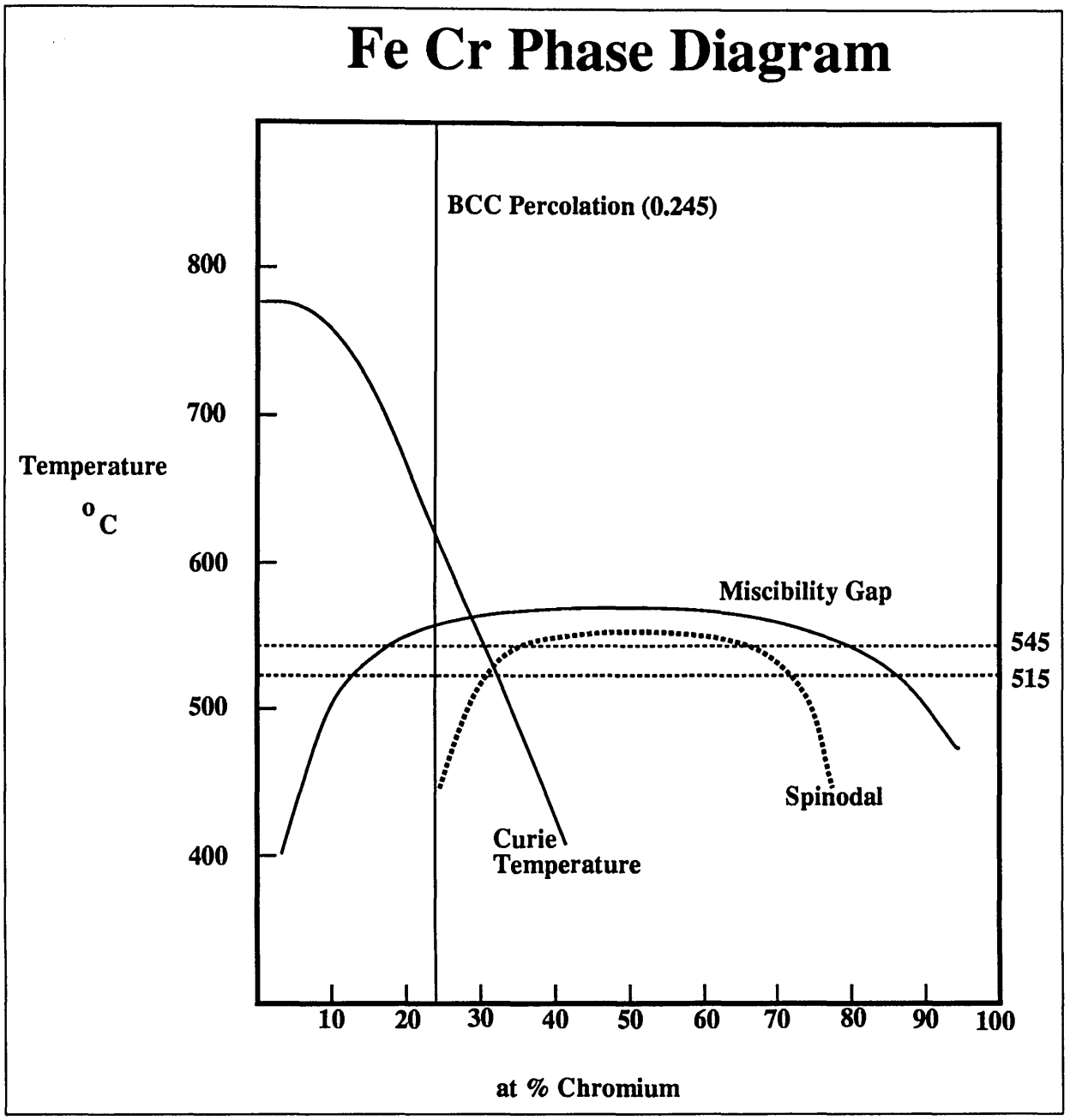

Figure 4.17: Fe-Cr Phase diagram, after Furusaka et Al. [57]

Element	Weight percentage W_i	Atomic percentage A_i	Atomic weight M_i	Scattering length b_i $(/10^{-12}cm)$
Fe	61.7	60.0	55.85	0.954
Cr	38.3	40.0	52.01	0.353
C	$\ll 0.1$	$\ll 0.1$	12.01	0.665

Table 4.4: $Fe_{0.6} - Cr_{0.4}$ composition and constituent properties

tures of $700 - 1000$ K. This allows calculation of the scattering length density ρ_m of the matrix phases for 20, 30 and 40 atomic percent of chromium as:

Phase	ρ_m $[10^{-12}$ cm$^{-2}]$
Fe-Cr(20at%) matrix	0.0713
Fe-Cr(30at%) matrix	0.0615
Fe-Cr(40at%) matrix	0.0610
Pure Fe	0.0810
Pure Cr	0.0294

Table 4.5: Scattering length density for the possible phases in iron-chromium

These experiments were performed with the PLUTO reactor at AEA Technology (Formerly Harwell Laboratory) and used the SAS instrument there. This instrument is described in [107]. A neutron beam of mean wavelength 0.5nm and a specially designed furnace for *in-situ* sample heat treatment were used. Each homogenised sample was rapidly heated to either 515°C, 530°C or 545°C and scattering signals collected in a time sequence of $\frac{1}{2}, 1, 2, 4, 8, 16, \ldots$ hours. The scattering intensities were normalised using a thin water sample using the procedure described in [107, 127]

Figure 4.18 shows a selection of scattering spectra for total scattering from iron-chromium.

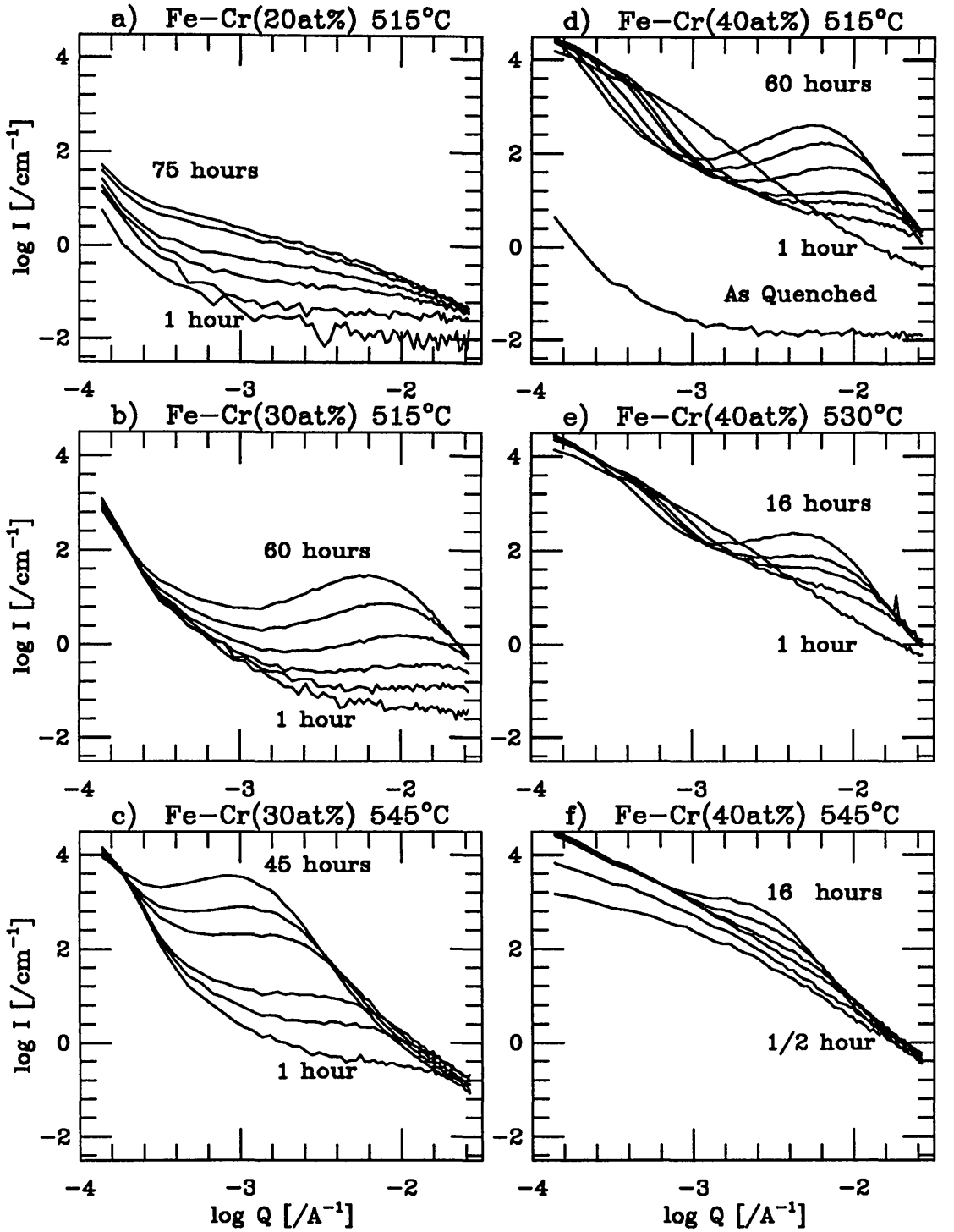

Figure 4.18: Iron-Chromium Scattering Data a) 20 at%Cr; b,c) 30at%Cr; d,e,f) 40at%Cr Time sequences as marked, in hours.

There are a number of regimes of interest in these curves. Firstly, the background scattering in the 40at%Cr sample (after it was quenched into iced-brine after its initial homogenisation at 1000°C) is relatively flat at high-q values but does show some scattering at lower Q (See figure 4.18d). This intensity at low-Q appears in the other curves and still requires a full explanation. It was not reported in an earlier work on iron-chromium scattering [57], possibly because that scattering instrument was unable to operate at such low-q values. Recent work on iron-chromium-nickel alloys [127] and further work on iron-chromium [125] show a similar result. This anomalous scattering *may* be attributed to needles and platelets seen in TEM micrographs of iron-chromium, but is probably *not* due to carbides nor to surface scattering effects.

The diffuse peaks seen in the 30at%Cr and 40at% Cr sample data (See figure 4.18b-f) are often considered as indications of the well known spinodal decomposition process. Their positions depend on time and the maxima evolve to lower q-values indicating an increase in the characteristic domain length scale. Note that at 545°C, the peaks develop faster and larger due to the increased thermal activity. Model studies of spinodal decomposition reveal that it corresponds to a percolated interconnected structure, of a time dependent thickness.

It is significant that in the 20at%Cr sample data (See figure 4.18a), there are no visible peaks. This suggests that for a system below the site percolation limit (p=0.245 for a bcc lattice) [78], there is no scattering from a percolated chromium enriched domain structure and furthermore such scattering as *is* present originates from the magnetic domain structure within the iron. A monotonic increase with time of scattering intensity for all q-values in the 20at%Cr sample data is consistent with this hypothesis.

Since the critical magnetic scattering is relatively constant in time, it is possible to separate out the spinodal curves by simply subtracting off the earliest measured curve from the rest. Ideally the measured scattering immediately after the homogenisation treatment would be subtracted. Unfortunately this measurement was not made for all the samples, since such a low intensity requires considerable beam time for the statistical reliability needed to subtract two signals.

The difficulty in interpreting the iron-chromium data in terms of absolute volume fractions is that the precise compositions of the precipitating phases are unknown. They can be said to be chromium enriched and iron enriched, compared to the matrix phase, but the two-phase approximation is not valid when the concentrations are so close to 50%. Another difficulty is that since only total scattering is available, and not that due to the nuclear scattering, it is not possible to deduce much from the absolute values of the scattering intensities. However, since all the data sets were collected in the same way, it *is* possible to make sensible comparisons between the relative scattering intensities at the different concentrations, quench temperatures and quench times.

The scattering data in figure 4.18 can be analysed in two ways, to yield characteristic sizes. For the samples with the low concentration of chromium of 20 atomic percent, it is possible to apply the maximum entropy fitting algorithm described in appendix B to fit a distribution of chromium particles. This can also be applied to the early stages of the data with 30 and even 40 atomic percent of chromium. At an early enough stage, the domains formed are not yet fully connected, and can be approximated by spheres.

Figure 4.19 shows the mean particle size obtained from a quench experiment on Fe-Cr(20at%). There is no single regime where the mean particle size follows a simple power law, although the limiting behaviour is that of $R \sim t^{\frac{1}{3}}$. Figure 4.20 shows the corresponding calculated volume fraction of the particulate chromium phase. There is an interesting unexplained phenomena after 20 hours, where the particle size and volume fraction diverge from the reasonably smooth curves. Note the rate of increase of the volume fraction decreases as the chromium available in the matrix phase is used up.

At later times in the concentrated systems, it is only possible to locate the characteristic length scale from the position of the peak in the scattering intensity. Since there remains some background scattering either from critical magnetic effects, or from impurities, it is necessary to subtract off the earliest available scattering curve, following the quench.

Figures 4.21 and 4.22 show the characteristic length obtained in this way for a

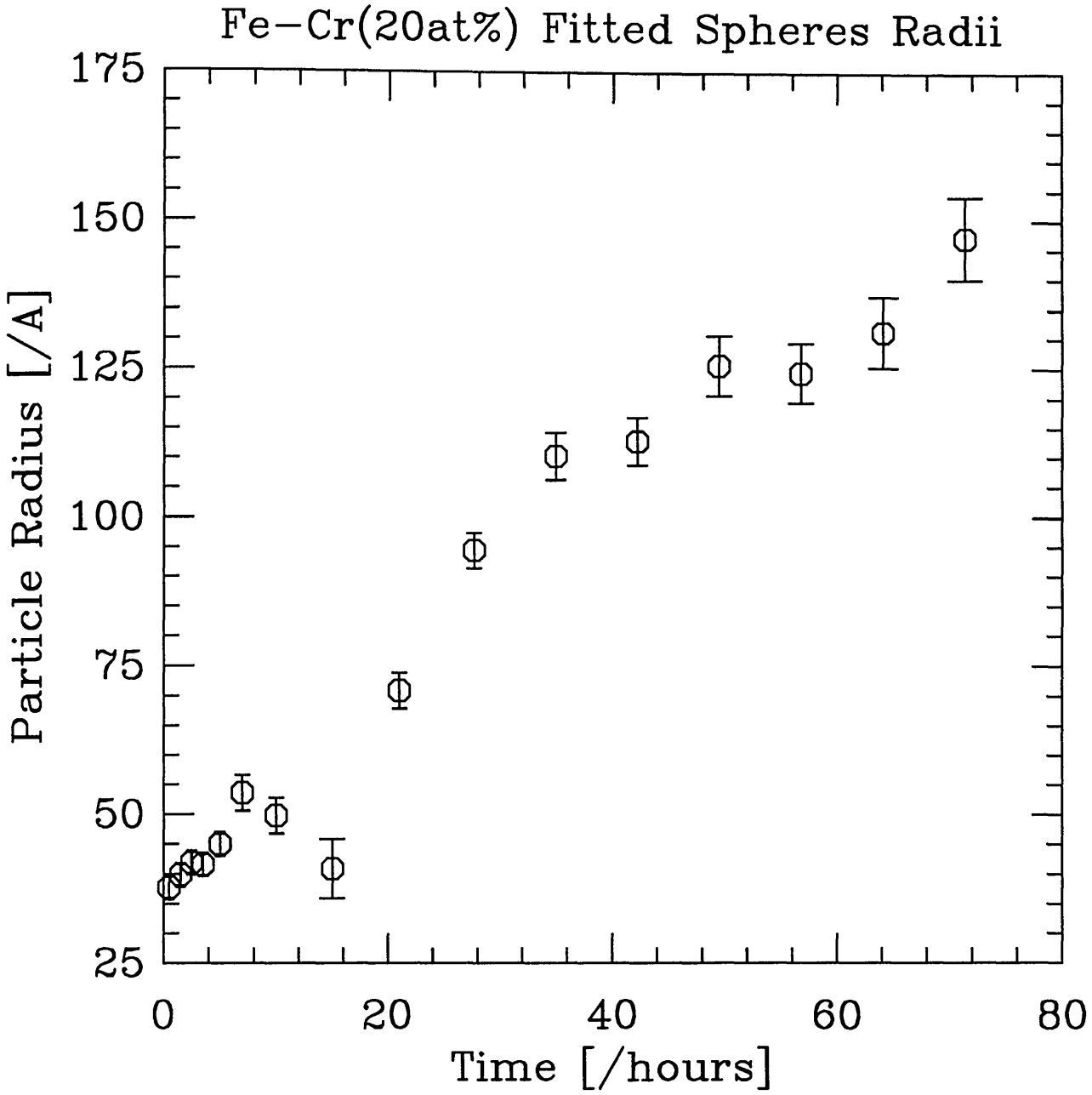

Figure 4.19: Fitted distribution of spherical scatterers to Fe-Cr(20at%), yielding mean particle size as a function of time, following a quench from 973 K to 788 K.

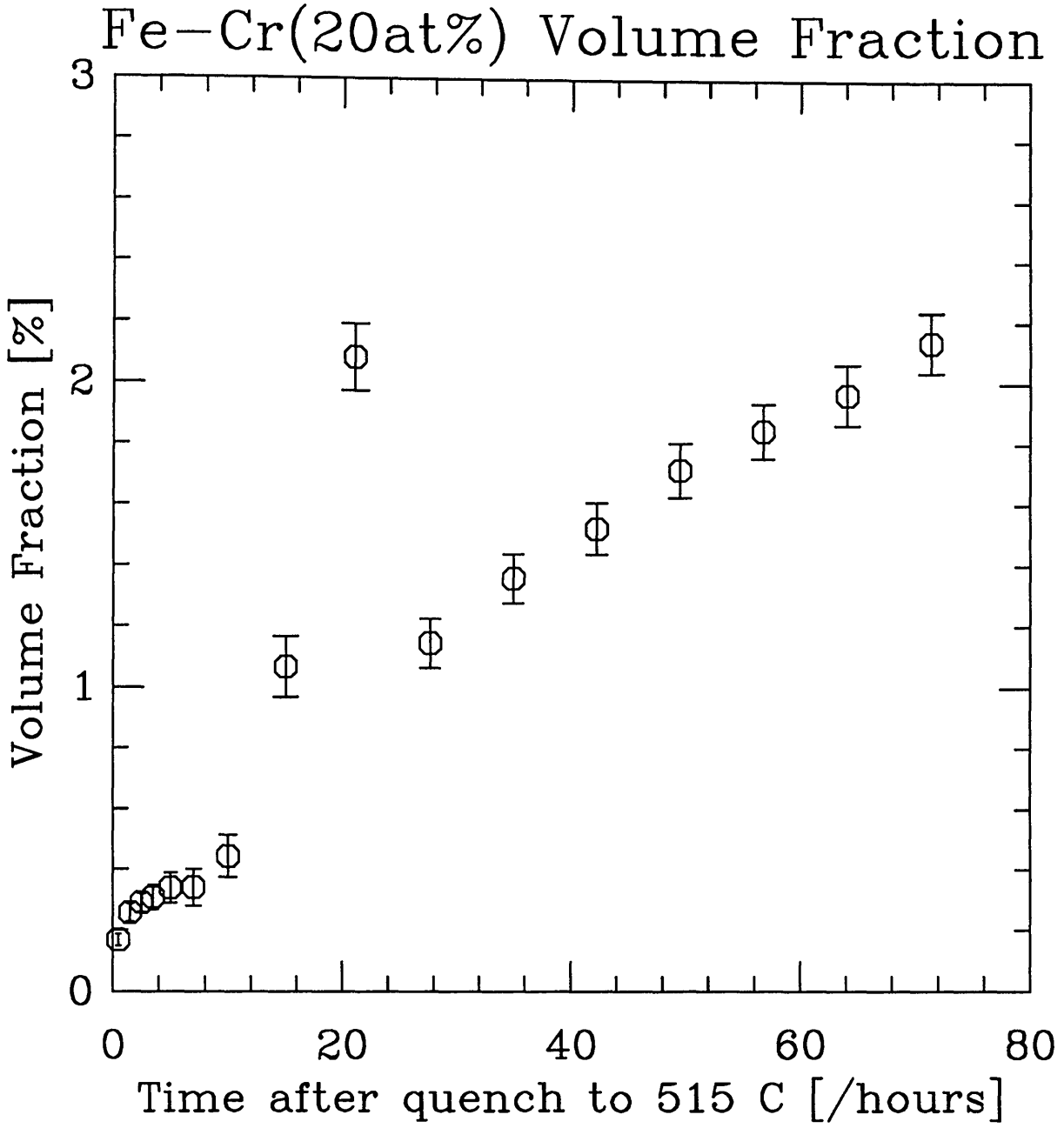

Figure 4.20: Fitted distribution of spherical scatterers to Fe-Cr(20at%), yielding particulate phase volume fraction as a function of time following a quench from 973 K to 788 K.

sample of Fe-Cr(30at%) quenched to 788 and 818 K respectively from an initial solution treatment temperature of 973 K.

Finally, figures 4.23 and 4.24 show the distribution of scattering features present in a sample of Fe-Cr(40at%) following a quench to room temperature after a long period above 1000 K. As indicated, there are a number of sizes of features present, prominently at particle radii of 10, 100, 150 and 350 $\AA$. The volume fractions of each of these have been computed as though they were all pure chromium, although this is almost certainly not the case. It is an ongoing piece of work to identify the exact nature of these initial features, as they probably control the subsequent dynamics of phase separation. Figure 4.24 illustrates how well the small angle scattering signal can be fitted using the un-normalised particle distribution in figure 4.23. This is not surprising, as there are over 100 adjustable parameters, and despite the ability of the maximum entropy algorithm not to overfit, extreme caution must be exersised in interpreting the fit.

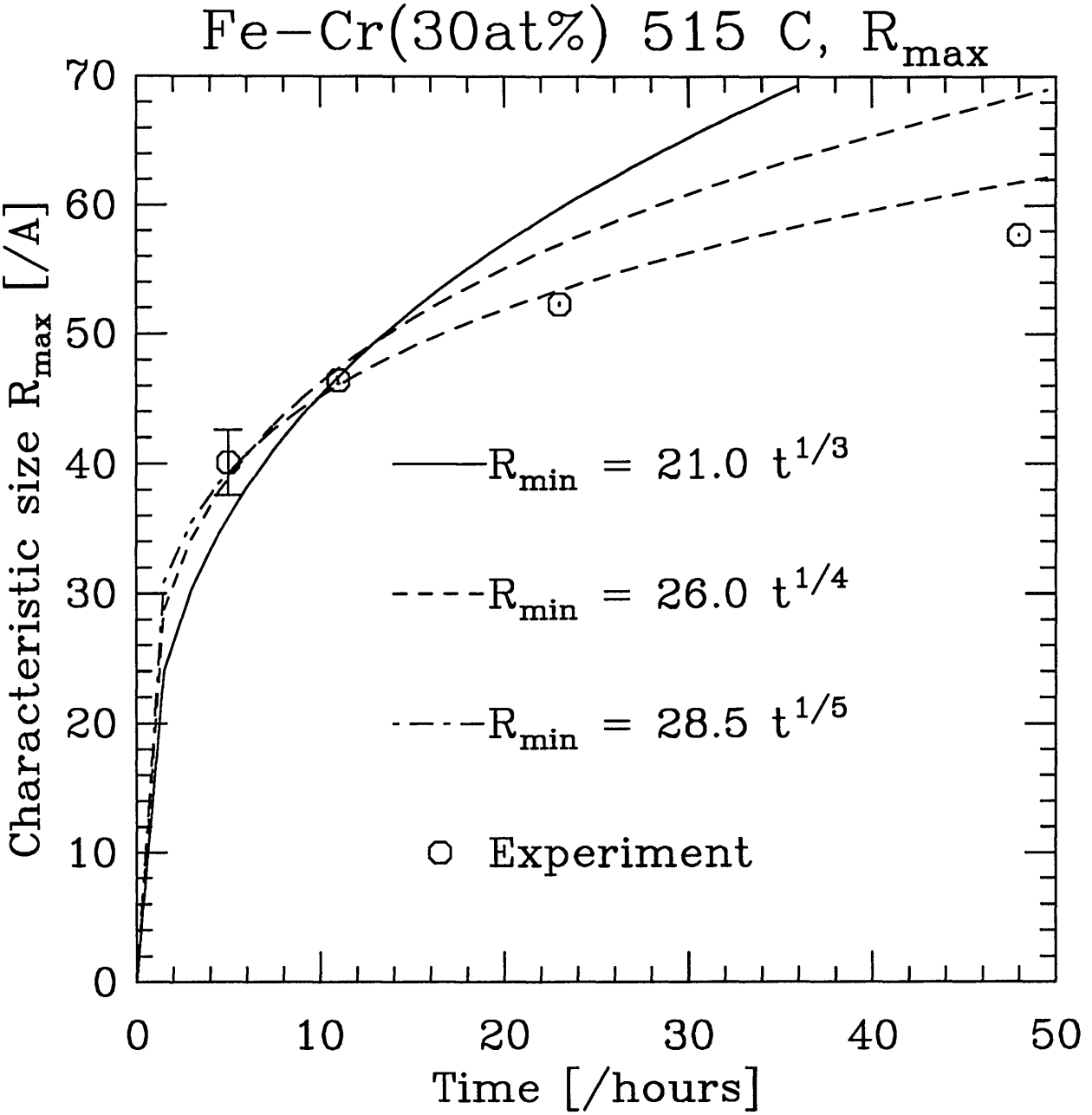

Figure 4.21: Characteristic size measured from position of peak in intensity spectra, after subtracting the earliest curve for Fe-Cr(30at%), following a quench from 973 K to 788 K.

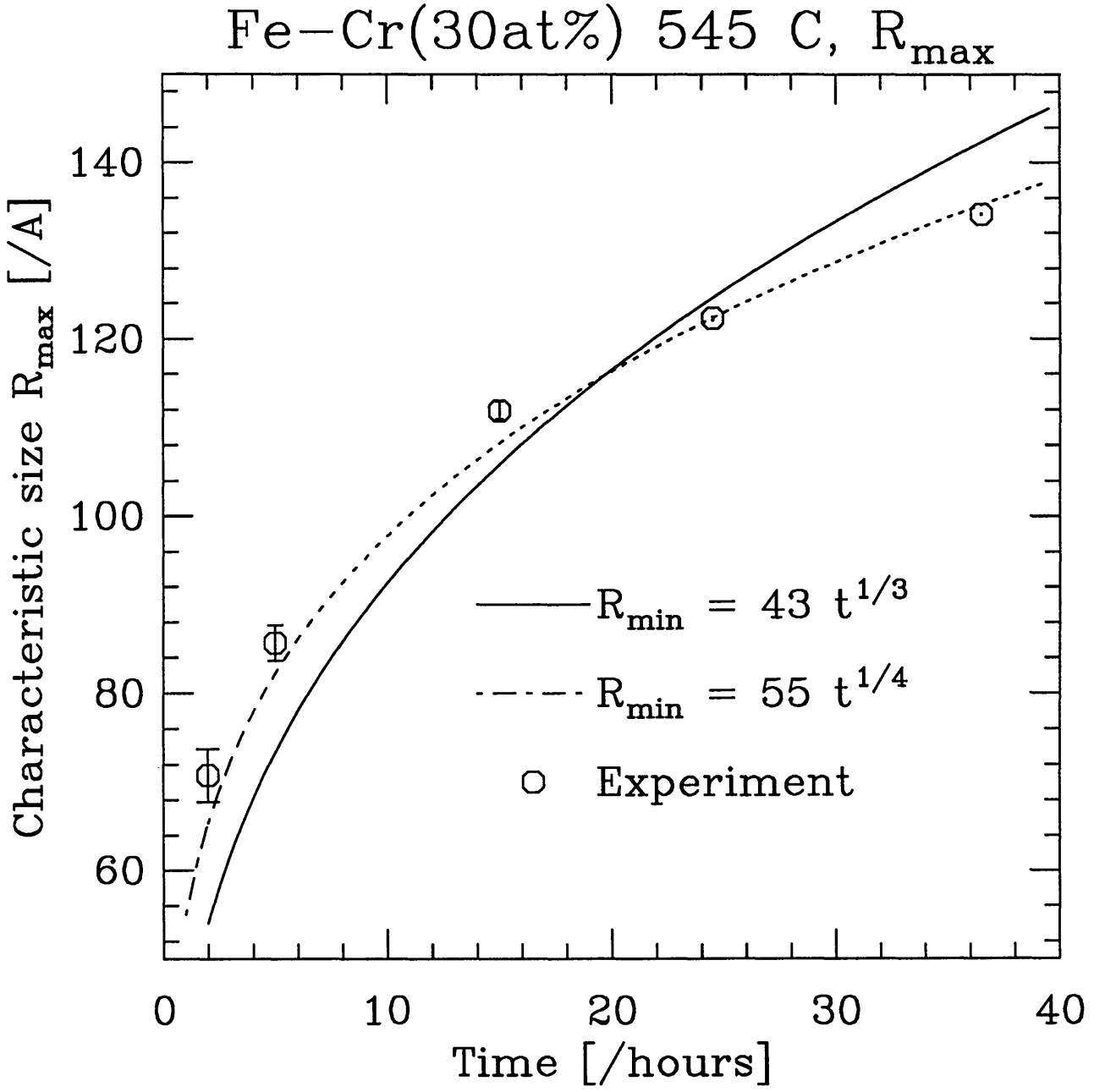

Figure 4.22: Characteristic size measured from position of peak in intensity spectra, after subtracting the earliest curve for Fe-Cr(30at%), following a quench from 973 K to 818 K.

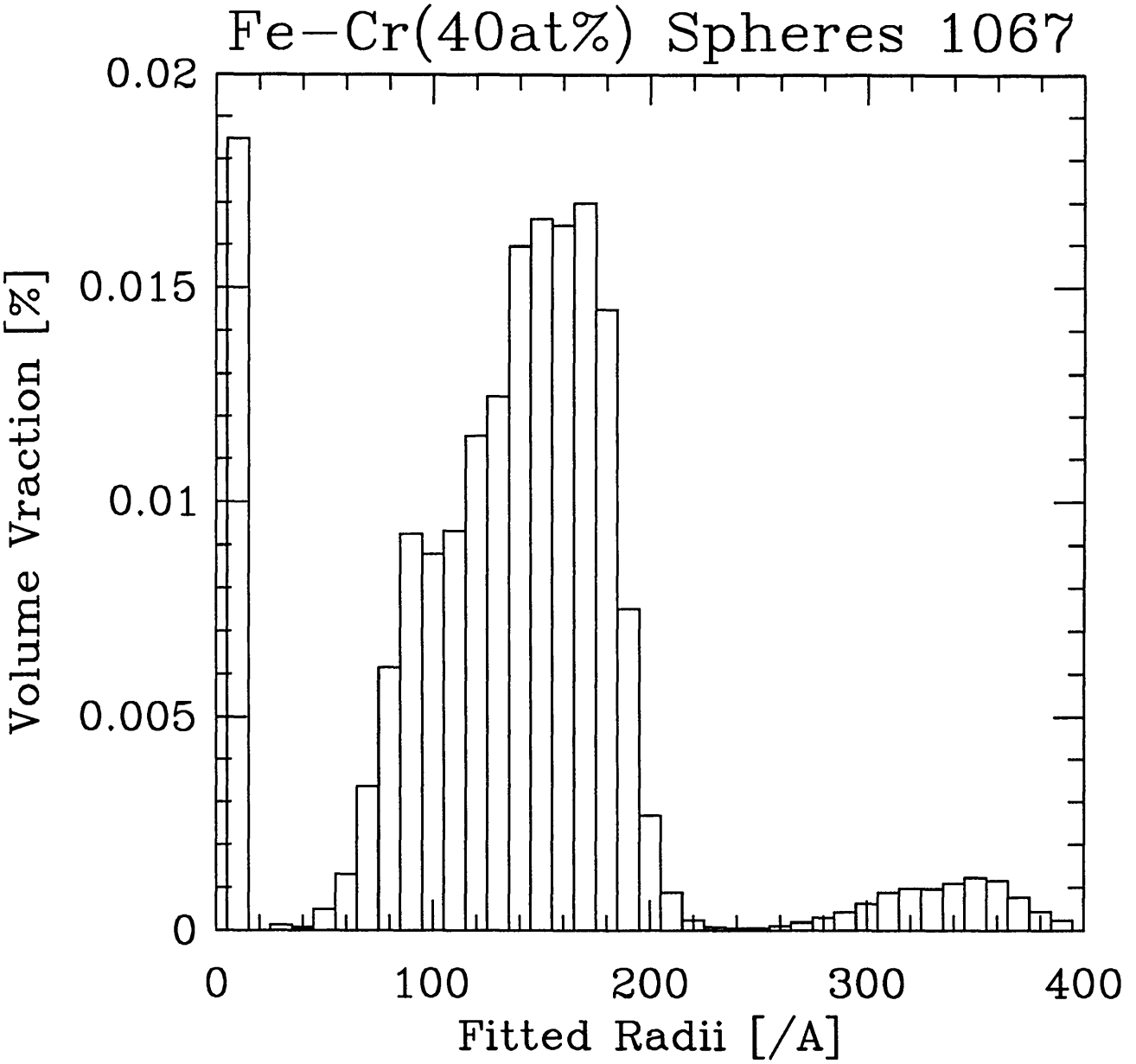

Figure 4.23: Distribution of spherical particles present in Fe-Cr(40at%), following a deep quench from 1273 K to 293 K.

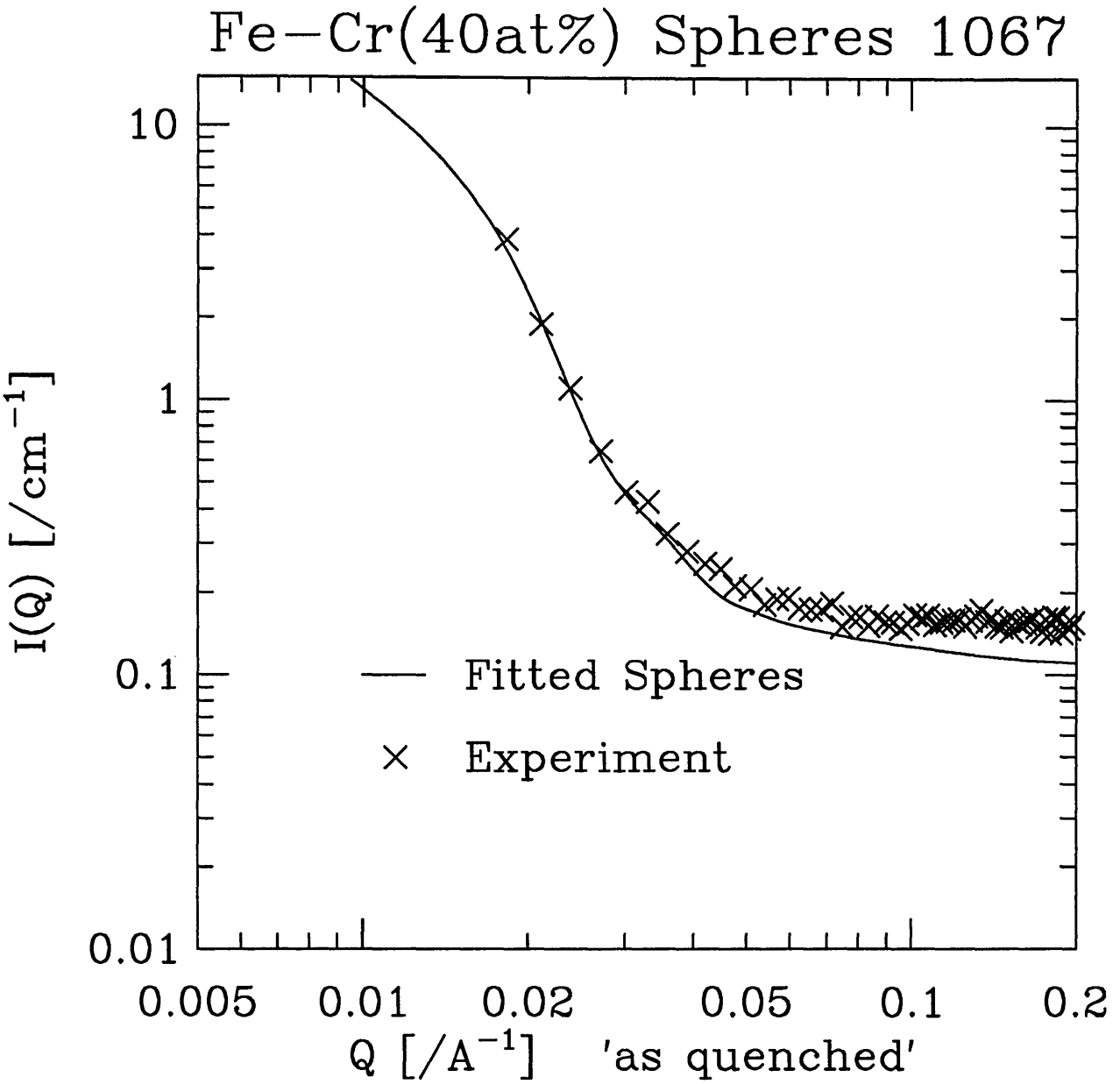

Figure 4.24: Fitted scattering intensity from distribution of spherical particles present in Fe-Cr(40at%), following a deep quench from 1273 K to 293 K.

4.6.3 PE16 Steel

Conventional iron-based steels can lose much of their strength at temperatures above 970 K, when dislocations are created and are mobile. Precipitate hardened superalloys such as PE16, are strengthened by the presence of particles which pin the dislocations and thus prevent plastic flow. It is important, however that the particles of the hardening phase are not allowed to grow beyond a certain size, since this will have the detrimental effects on making the alloy brittle, and can cause crack formation.

As a consequence of its superior strength, PE16 is used in a number of performance critical components in nuclear power stations and therefore studies of its ageing behaviour and response to extreme conditions of pressure, temperature and irradiation are of particular importance and current interest. It is especially important to determine the quantities of the hardening phase formed over long periods of time, when the components are in service.

A number of samples with various treatment histories were supplied to the materials Physics and Metallurgy Division of AEA Technology for non destructive examination by small angle neutron scattering on the PLUTO SAS instrument.

This section describes SANS data collected for these samples and analysed using the software described in appendix B.

Nimonic PE16 is nickel-based high temperature steel alloy. Its chemical composition is given in table 4.6. Several scattering features are known to occur in the samples [96]. The γ' hardening precipitate phase is thought to have the composition $Ni_3Fe_y(Ti_xAl_{1-x})$, which has the same cubic symmetry as the face centred cubic matrix. This phase forms an ordered structure with the nickel and iron atoms occupying the face centred positions in a cubic array of random titanium and aluminium atoms. The ordered structure of the γ' phase is not accessible to SANS experiments, and the precipitate is only observed as a distribution of approximately spherical particles.

The exact composition of the γ' phase is still controversial [96], but is approxi-

Element	Weight percentage W_i	Atomic percentage A_i	Atomic weight M_i	Scattering length b_i $(/10^{-12}cm)$
C	0.047	0.22	12.01	0.665
Si	0.22	0.44	29.08	0.42
Mn	0.06	0.06	54.94	-0.373
S	0.003	0.01	32.06	0.285
Cr	16.6	17.90	52.01	0.353
Mo	3.22	1.88	95.95	0.695
Ni	43.6	41.64	58.71	1.03
Al	1.19	2.47	26.98	0.345
B	0.002	0.01	10.81	0.535
Co	0.27	0.26	58.95	0.270
Ti	1.20	1.40	47.90	-0.337
Zr	0.035	0.02	91.22	0.70
Fe	33.553	33.69	55.85	0.954

Table 4.6: PE16 chemical composition and constituent properties

mately given by $Ni_{2.9}Fe_{0.1}(Ti_{0.4}Al_{0.6})$, which means that is has a SANS contrast of $0.150 \times 10^{20} cm^{-4}$ with the matrix phase.

In addition to the γ' phase there is almost certainly a number of carbide phases and for the particular samples described here, a distribution of irradiation induced voids, possibly filled by helium [128, 129]. This work concentrates solely on the γ' phase, since a useful discussion of the other phases cannot be made without more information on the sample treatment histories than can be stated here.

The eight samples and their designated labels and treatment temperatures are described in table 4.7. All samples are from the same original batch of material, and have had several years treatment at the specified temperatures. Samples A-J have been continually exposed to radiation of varying degrees of intensity, sample U was the control sample and has not.

Sample Label and Run Number	Treatment Temperature [K]	Volume Fraction of $0-20\AA$ particles	Volume Fraction of $20-60\AA$ particles	Volume Fraction of $60-1000\AA$ particles
A (7611)	588	1.08	0.222	0.0606
B (7617)	613	2.39	1.60	0.194
C (7601)	643	1.64	2.13	0.157
D (7609)	703	1.52	0.628	0.791
F (7593)	823	1.22	0.303	0.283
G (7615)	893	0.913	0.149	0.297
J (7613)	953	0.906	0.0725	0.296
U (7604)	293	0.954	0.295	0.0318

Table 4.7: PE16 Samples and treatment temperatures and measured volume fractions. Note the volume fractions have been determined for a contrast of $10^{20} cm^{-4}$, so for γ' phase, divide volume fractions by $\Delta\rho^2 = 0.150$ to obtain true percentages.

Figure 4.25 shows the fitted size distribution of spherical particles, assuming a flat contrast value of $10^{20} cm^{-4}$ for all the scattering features present. There are three distinct size groups of features present, from $0-20\AA$ radius, $20-60\AA$ radius and

above 60Å radius. These may be identified with voids, γ' and carbides respectively. The integrated volume fractions from these distributions are tabulated in table 4.7, but must be divided by the true contrast values to obtain true percentage volume fractions. The volume fractions have been deliberately left uncorrected by the precipitate contrast, since there is a possibility that the large precipitate are also γ' [130]. This cannot be determined without further electron microscope examination of the samples.

Figure 4.26 shows how the assumed distributions of spherical particles fits the scattering intensity measurements. There is a good fit except at high Q values. At these values, the form factor deviates from that of spherical particles. It has been postulated [131], that this may be due to the formation of rod like particles growing preferentially at grain boundaries in the samples, since these would give rise to the slope of -1 seen in the Porod plot shown in figure 4.26.

Figure 4.27 summarises the volume fraction data, showing the precipitate volume fractions as a function of temperature. The volume fraction is low at low temperatures and initially increases with temperature, reaching a maximum between 600 and 700 K. This is probably due to increased thermal activation and increased mobility of the γ' constituent atoms. Above this temperature range, the precipitate phase volume fractions decrease, presumably as the solute is dissolved back into the matrix.

In fact, the situation is more complex than indicated above, and irradiation effects are also most likely to influence those samples treated between 600 and 700 K.

The samples described here, form part of one mechanical structure, and the variation of volume fraction with temperature in the manner indicated has implications for the mechanical strength of the structure, and its weakest point.

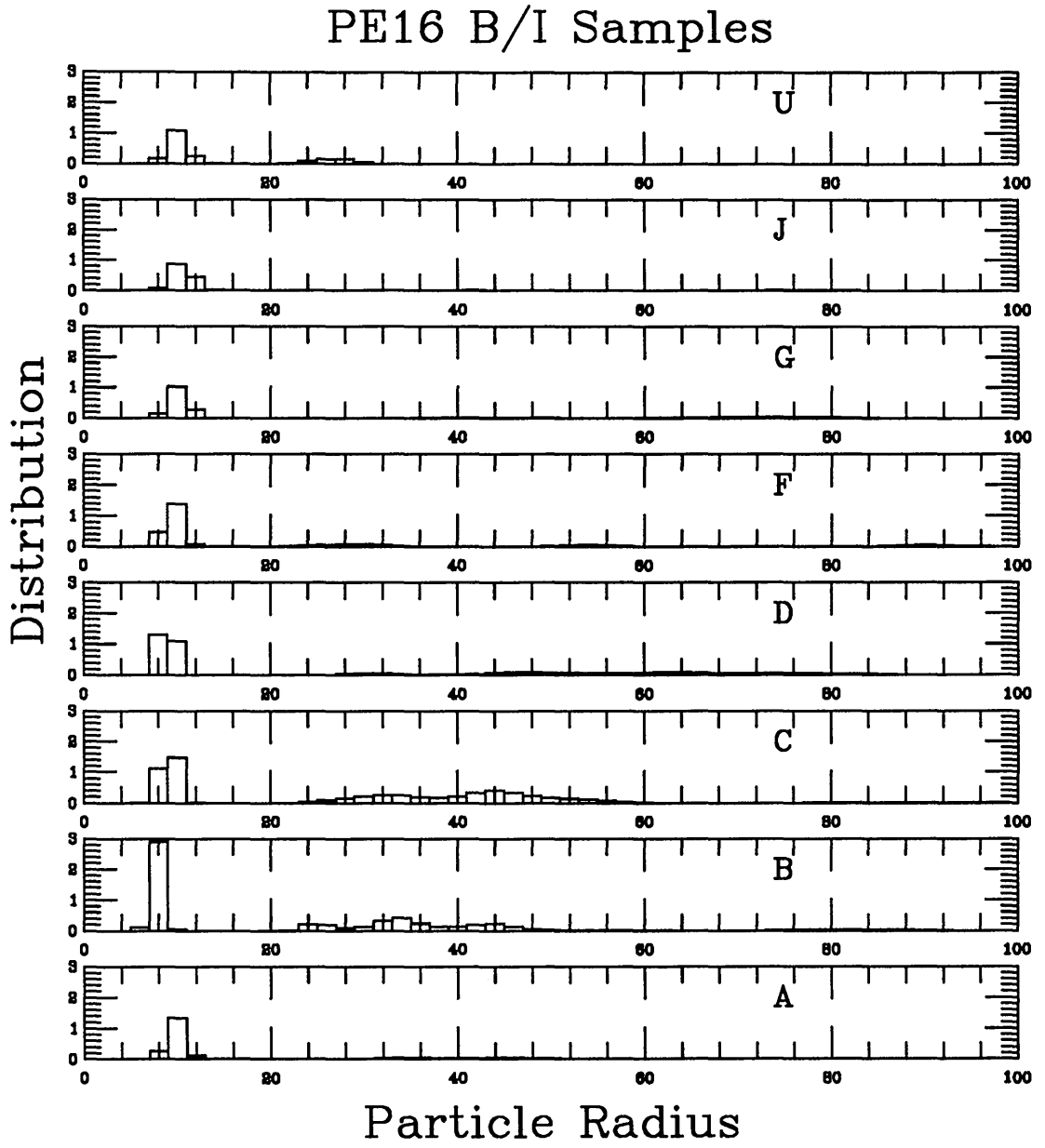

Figure 4.25: PE16 Heat treated samples, showing fitted size distribution of spherical scatters. The volume fractions are un-normalised with respect to the SANS contrast of the individual features. The group of peaks at around $25-50\mathring{A}$ radius is probably the γ' phase and the peak at around $12\mathring{A}$ radius, may be matrix voids of helium, for example. Larger features may be identified with weakly contrasting carbides in the alloy.

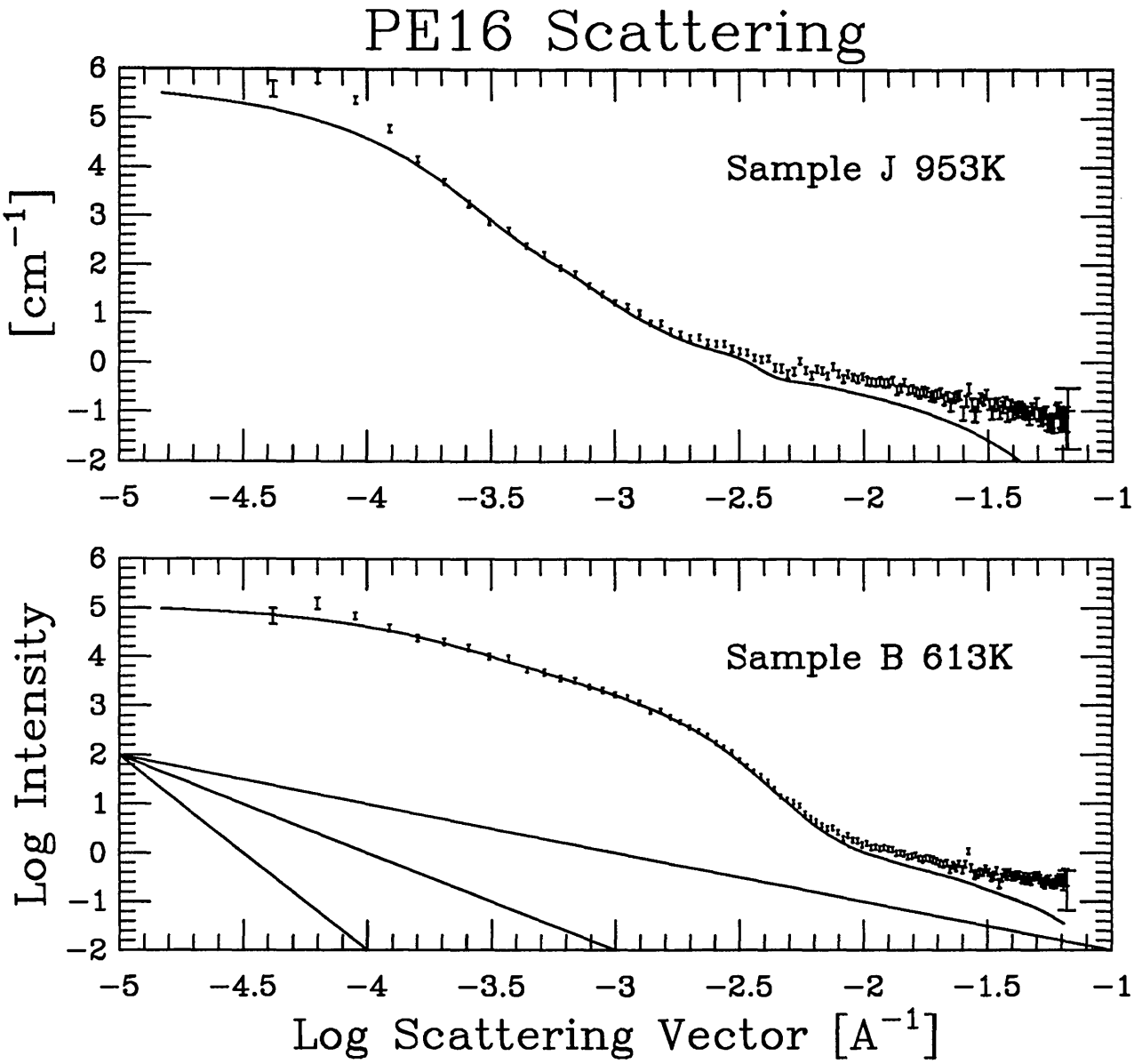

Figure 4.26: PE16 Heat treated samples B and J log-log plot of scattering intensity, measured in cm^{-1} as a function of scattering vector $|Q|$ measured in $\AA^{-1}$. The fitted continuous lines are from an assumption of a size distribution of scattering spheres. The straight lines are of slopes -4, -2 and -1 and illustrate the badly fitted region at high $|Q|$ values has slope -1 and might be expected to be associated with rod-like scattering features according to Porod's law.

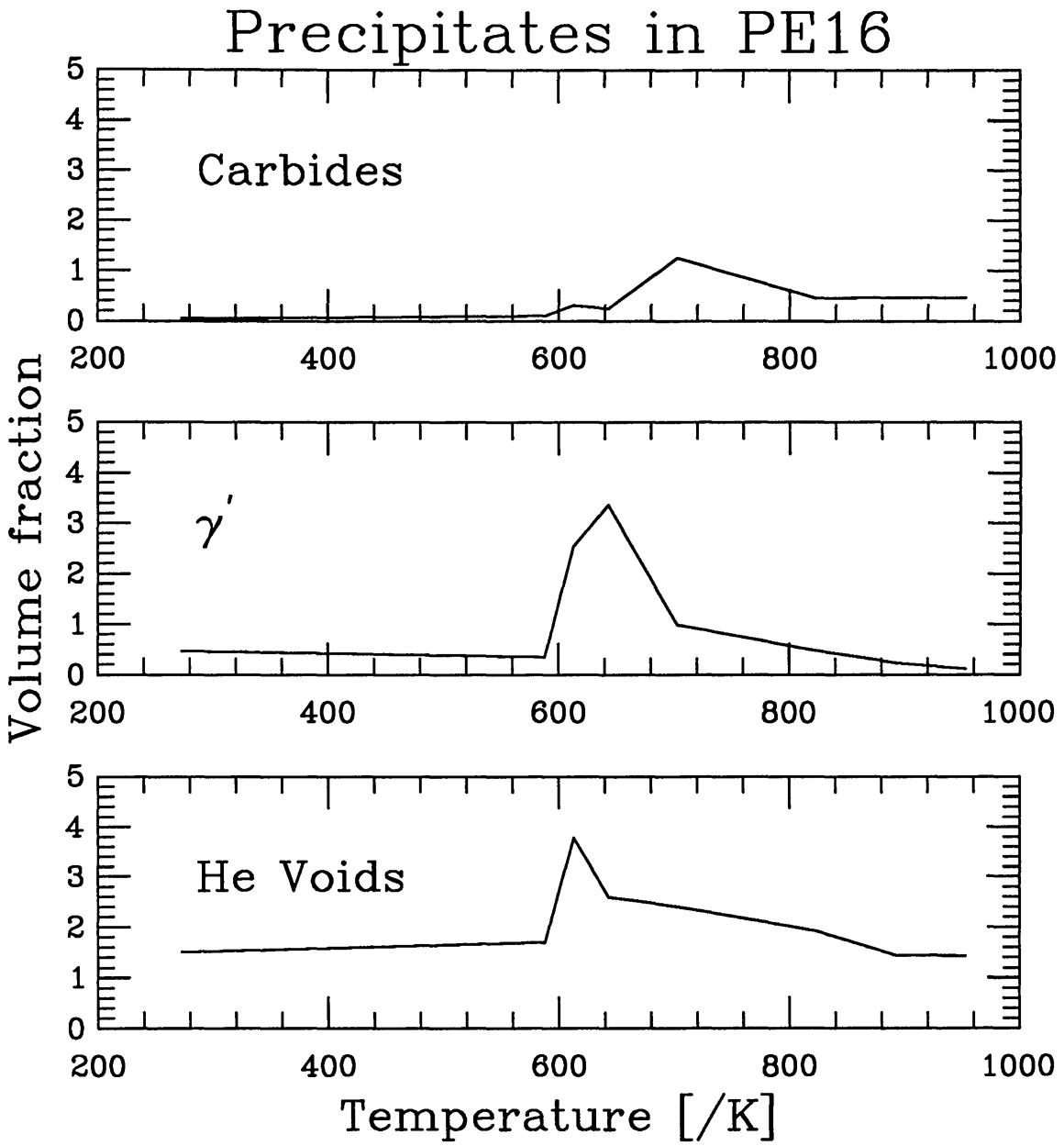

Figure 4.27: Volume fractions for the likely scattering features present in the heat treated PE16 samples. Only the γ' is correctly scaled as a percentage volume fraction. The carbides and voids have been treated numerically as additional γ' phase, but can be rescaled if values for their scattering length densities are known.

Chapter 5

Discussion

This chapter attempts to combine the results from the computer simulations, numerical integration of the Cahn-Hilliard-Cook equation and the small angle neutron scattering experiments together. Despite the disparity between the processes, real and idealised, in the real and and model alloys considered, there do appear to be universality classes for growth. These classes are distinguished not by details of the growth process itself, but by the type of order parameter and the dimensionality of the system under consideration.

The next section discusses scaling and the combination of the size scaling results. Section 5.2 considers some of the implications of fluctuations and noise in the numerical work, and finally the scope for future work on domain growth is discussed in section 5.3.

5.1 Scaling and Multi-scaling

5.1.1 Discussion of Scaling

The main idea behind dynamic scaling is that there is *one* length or size that is important in characterising the domain growth with time for a variety of complex systems. It is the functional dependence of measurable properties on this length

that categorises dynamic universality classes. The simplest theoretical prediction for the functional form of time-dependence of the dominant length is that of Lifshitz and Slyozov [13]. These authors considered a dynamic equilibrium process of diffusion in a dilute system of spherical particles. Their prediction was that:

$$R \approx At^n \tag{5.108}$$

Where the dynamic universality class is labelled by the value of the exponent $n = \frac{1}{3}$, and any system dependent details would be absorbed in the prefactor A, which would also absorb the time units and the system temperature.

This very simple law, was recently re-derived by Huse [11], who showed that its range of validity could also be extended to include non-dilute systems. Huse's law also describes the medium time coarsening mechanism whereby domains, having formed, would increase in size at the expense of smaller domains. The cost of this extension was a more complex dynamic exponent, given by the dominant value of $\frac{1}{3}$, for the alloy model with scalar concentration variables, but with corrective terms as follows:

$$3n_{\text{eff}} = 1 - \frac{R_0}{R(t)} + O\left(R^{-2}(t)\right) \tag{5.109}$$

where the effective exponent n_{eff} is controlled by a microscopic length R_0, which depends on the temperature T. This introduces an additional length into the theory.

It is also useful to consider the simple scaling ansatz for the time dependent pair correlation function $g(r,t)$, which is that:

$$g(r,t) \approx f(\frac{r}{R(t)}) \tag{5.110}$$

where f is a scaling function, and depends only on the scaled variable $\frac{r}{R(t)}$, with *all* the time dependence contained in $R(t)$. As Huse reports, this applies directly to the measured correlation function. The scattering intensity is just a Fourier transform of the pair-correlation function [1] so that given a suitable form for f, this allows the *scattering* curves obtained for different times to be collapsed onto one universal curve, independent of time. The consequences of transforming equation

[1] See appendix A

5.110 into reciprocal or wavevector space is that the function:

$$f^*(\frac{q}{Q(t)}) = \frac{Q^{\frac{1}{n}}(t)S(q,t)}{\int q^2 S(q,t)dq} \tag{5.111}$$

is independent of time, although it will be system specific and is not itself universal. The integrals reduce to summations for a discrete set of measured values.

This function f^* can readily be obtained from real or simulated scattering data, and it depends only on two parameters, the choice of dynamical exponent n, and the characteristic length R or wavevector Q. As discussed in previous chapters, there are a number of ways of extracting a characteristic length from a simulation, from which a characteristic wavevector can be obtained. There are other choices used by different authors. For example Marro and co-workers [51] used the first moment of the scattering intensity curve as defined by:

$$Q_1(t) = \frac{\int qS(q,t)dq}{\int S(q,t)dq} \tag{5.112}$$

A simpler approach [132] used the position of the peak in the scattering curve as a value for Q. This latter is employed in the next section to scale Monte-Carlo data, SANS data and integrated Cahn-Hilliard equation data to one curve.

It is a natural development of the scaling by one length to introduce other length scales for the additional corrective terms. This approach is know as multi-scaling and has been considered by [38] for the Monte-Carlo alloy model. At the time of writing there is insufficient numerical evidence to require multi-scaling for the short range interaction lattice models considered here. The real SANS data *does* however suggest that this may be useful in explaining the diversity of exponents found for the *Fe-Cr* and *Cu-Co* systems, simply because this theory allows more adjustable parameters. The accuracy of the SANS data presented here is such that it is adequate to use only scaling, and not to attempt a multi-scaling fit.

5.1.2 Fitted Data

This section presents a scaling analysis of some of the SANS and computer simulated data. These data can be combined if the model crystal is rescaled. This is

done crudely by setting the model crystal lattice length to the unit cell length of iron-chromium (~0.4nm). Figure 5.1 shows a comparison with 30at%Cr data and simulated data, with the scaling law of [51] applied. This scaling has also been successfully applied to SANS data from the *Fe-Cr-Ni* system [127]. The scaling law holds well over a wide q-range, in spite of the corrections involved in removing the magnetic scattering.

The time scale is also adjusted arbitrarily, to fit the SANS data. This crude comparison allows the computer simulation time to be calibrated in units of real time, for the particular system of iron chromium. It is found that one Monte-Carlo time step is approximately equivalent to two minutes of real time for *Fe-Cr(30at%)* at 515C. This numerical value is not interesting, but the fact that Monte-Carlo time *can* be related to real time *is*, and justifies the use of the lattice model.

Also shown on figure 5.1 is a solid line from re-scaled scattering intensity calculated for integrated solutions to the Cahn-Hillard-Cook equation. Twenty different starting configurations were used for this to reduce the statistical noise. The runs were for the symmetric case of 50% A-concentration, and this explains why the curve is too broad compared with the SANS data and Monte-Carlo data, which were for a concentration of 40%. This data does agree with the experimental data over some of the q range, and has the correct peak position. The behaviour of the Cahn-Hilliard equation solutions is qualitatively correct, although perhaps less impressive than that of the Monte-Carlo simulated data.

It is also useful to compare the relatively clean data obtained for various simulations. Consider the data shown in figure 5.2. It shows the measured characteristic size R_{max} for the spin-flip Ising model and the site-exchange Alloy model, for two and three dimensional lattices of 128^2 and 128^3 sites respectively.

The four curves represent an average over at least 10 independent runs at $\frac{T_c}{2}$, for times up 65,536 Monte-Carlo time steps. The R_{max} values were obtained from cluster radii of gyration at the earlier times and a peak fit to the numerical scattering at the later times. This diagram shows the two distinct dynamic universality classes with power law exponents $n \approx \frac{1}{3}$ for the Alloy model, and $n \approx \frac{1}{2}$ for the spin-flip model. There is also a distinct cross over to lower values for *both* models

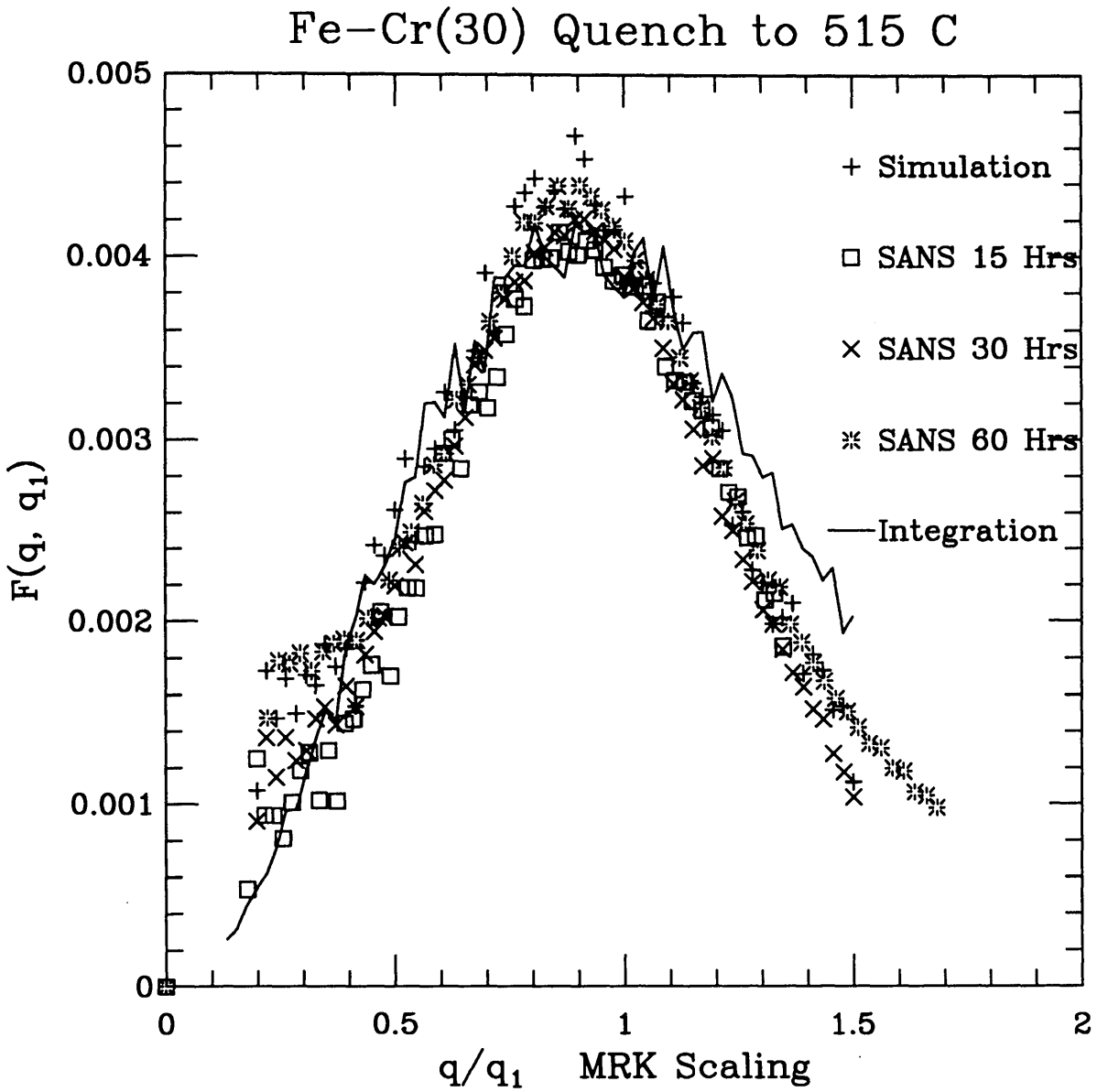

Figure 5.1: Scaled scattering data for Fe-Cr(30at%) after 15, 30 and 60 hours at 515°C, together with a scaled Monte-Carlo simulated structure factor after 512 time steps, and a time integrated solution to the Cahn-Hilliard equation for a total time of 10^5, following a quench from a random configuration.

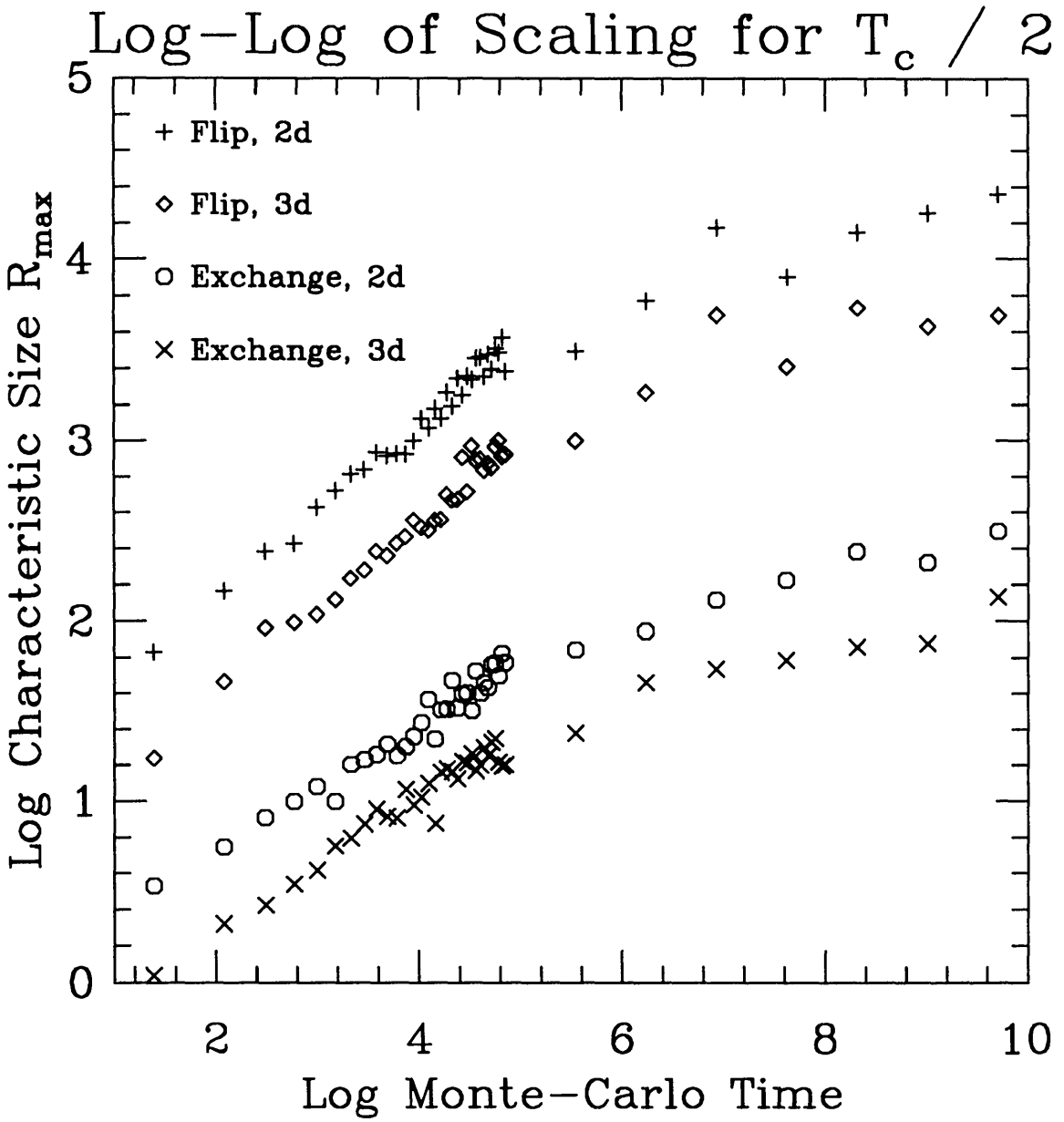

Figure 5.2: Universal scaling of the characteristic size for Alloy and Ising Models, showing the evolution of the characteristic length in simulations on a 128^2 and 128^3 site lattices for the spin-flip Ising and site-exchange alloy models. The quench was to $\frac{T_c}{2}$ using the Onsager or MCRG values for 2 and 3 dimensional lattices, respectively.

in the long time limit. This appears to confirm the need for Huse's exponent corrections.

Table 5.1 gives the least-squares best fitted values of the exponent n for the two models.

Model	Lattice	Short time exponent $t = 0 - 128$ steps	Long time exponent $t = 128 - 65536$ steps
Flip	Square	0.485 ± 0.01	0.19 ± 0.02
Flip	Cubic	0.480 ± 0.02	0.18 ± 0.02
Exchange	Square	0.365 ± 0.015	0.18 ± 0.02
Exchange	Cubic	0.360 ± 0.015	0.15 ± 0.02

Table 5.1: Power law exponents in the spin-flip and site exchange Ising models

In general the SANS experiments described in chapter 4 found a dominant exponent of $\frac{1}{3}$, although there is a shift to lower values after very long ageing times. An exception was the exponent of $\frac{1}{4}$, found for the *Cu-Co* system, which fit the SANS data over most of the later heat treatment time from 2 minutes to 128 minutes. A recent result by Bray [42] has postulated a value of $\frac{1}{4}$ for a vector order parameter, and it is an intriguing possibility that the magnetic ordering of the cobalt domains should also be taken into account in the growth process.

The following equation is perhaps the best empirical description of the findings of this thesis.

$$R(t) = B + At^n \tag{5.113}$$

with A absorbing the system specific details of time units and temperature, B a constant allowing for the finite particle size that would result from a random alloy at any finite temperature, even above the transition temperature, and $n = n(R)$, the dominant dynamical exponent, itself a function of the domain size.

The situation as regards measuring the dominant exponents is summarised in figure 5.3 which is a schematic of the characteristic size as it increases with time. The alloy is quenched from as high a temperature in as short a time as possible,

and domains are considered as starting to grow from that time. This is denoted by region 1 and is typically a few seconds. It is inaccessible to any experiment. This region is embodied by the constant term B in equation 5.113, whereby even above the transition temperature, there is a non zero characteristic length scale in the alloy.

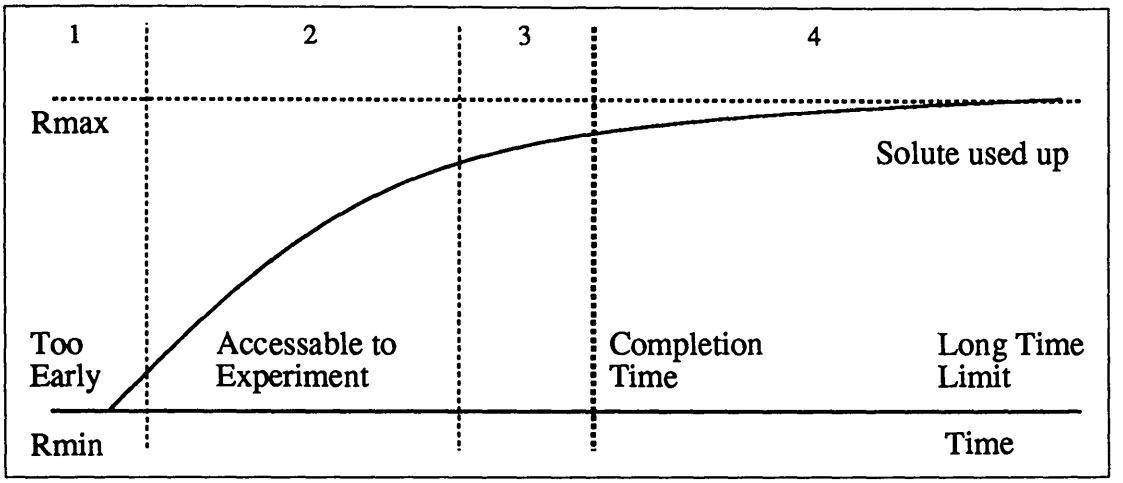

Figure 5.3: Power Law dependence of the characteristic size in a phase separating alloy.

Region 2 denotes the time scales that will typically be accessible to a real experiment, although for certain systems with high solute mobility, it may be possible to access regions 3 and 4. Binder has defined a completion time for phase separation, given by the time for the reaction to go halfway to completion [86]. This may not be easy to actually calculate for a real system where the reaction time is very long, such as several years in the case of the γ' formation in PE16. It does seem inevitable that the approximate laws of Lifshitz and Slyozov will fail at very long times for deep quenches, and the Huse law allows for this by incorporating an infinite series is corrections to the exponent n.

It is nevertheless, an interesting result that there does seem to be some degree of dynamic universality between the complicated growth processes taking place in alloys such as *Fe-Cr* and those occurring in the highly simplified Monte-Carlo model, and Cahn-Hilliard model. It seems that the growth of domains in alloys is best characterised by a power law such as that of Huse, and *not* as a logarithmic law as suggested by Mazenko and co-workers [12].

5.2 Fluctuations and Complexity

It seems appropriate to consider here the effect of fluctuations in the numerical work described in chapters 2 and 3. The Metropolis Monte-Carlo algorithm used in chapter 2 effectively couples a heat-bath or a source of thermal fluctuations to the ongoing simulated lattice. This is clearly important as stated, since without these fluctuations the cellular automaton algorithm rapidly becomes stuck, and no more domain growth can occur. This was in part alleviated by use of a very random initial configuration. The random start induces enough complexity that there is sufficient thermal activity to initiate the phase separation process.

It appears that a similar phenomena occurs during the numerical integration of the Cahn-Hilliard equation. The code for performing this integration bears a marked similarity to that of the Monte-Carlo simulation code. The evaluation of the $\nabla^4\phi$ term is numerically very similar to evaluating the short range pair-wise interactions in the lattice model, and in many aspects the Cahn-Hilliard equation is just a continuum limit of the lattice model. It has been reported in the literature [82] that the Cook noise term is unimportant in the numerical integration and that it does not affect the dynamics. However, as stated in chapter 3, the Cook term does speed up the dynamics, in the short time limit. Furthermore, the Cahn-Hilliard equation was found to be stable against any phase separation if the initial state was set to a uniform flat value of concentration, corresponding to perfectly mixed system. The fluctuations induced by using a random initial configuration were clearly important.

5.3 Future Work

There is still scope for considerable computer simulation work in the investigation of phase separative behaviour in alloys. This work suggests that dynamic universality classes do exist and furthermore can be distinguished in simulations of even the simplest models. There are a number of extensions and improvements to the model which could potentially result in a better understanding of the experimental data presently available.

One such extension is to accomodate a magnetic alloy component in the model. Most commercially useful alloys involve a ferromagnetic component such as iron, nickel or cobalt, and the influence of the magnetic interactions on the rate of domain growth is probably important. These interactions are usually *not* isotropic in nature and there are probably preferential directions on the lattice for growth to occur.

It would also be useful to consider the effect of a third component species in a model alloy. Some preliminary work by the author suggest that growth of one minority phase will probably be spatially correlated with that of the other. For example, one phase may form the nuclei around which the other forms. A suitable model for this is the logical extension of the binary alloy model to a site-exchange Potts model, where each site can have any of $q = 3$ states for a ternary alloy.

A very important addition to the model would be to take some account of defects, and non-uniformities such as grain boundaries. This can also be tackled within the framework of the lattice model by diluting the bonds, either randomly to simulate the effect of random defects, or in well defined patterns to simulate interaces. In addition, the bonds can vary in strength spatially, with weakly bonded regions having a higher effective temperature and hence atom mobility.

This work has not covered the possibility of anti-ferromagnetic coupling or longer range interactions with an alternating sign. These lead to the formation of more complex compound domains, and regions or long-range order. Such phenomena certainly occur in real alloys, and are worthy of simulation.

Appendix A

Parallel Computation

A great deal of the numerical work described in this thesis would have been impractical using conventional architecture computer technology [1]. The processing time would have been too great. It is therefore seems useful to discuss at some length the two principle super-computers which typify the class of machines used, some of the special parallel algorithms used and some possibilities for new computer systems only very recently available. It is difficult and uninteresting to discuss these machines and algorithms out of context of the physics work for which they were employed, so that in what follows, considerable reference is made to ideas discussed elsewhere in this thesis.

There are two major super-computers at Edinburgh which were heavily used in producing the work for this thesis, namely the Distributed Array Processors, DAP-510 and DAP-608, and the Edinburgh Concurrent Super-computer (ECS). Both these machines are manufactured in the UK, the DAPs by Active Memory Technology Ltd (AMT) and the ECS by Meiko Ltd. They are described below.

[1] Certainly at the time of writing

A.1 The Distributed Array Processor (DAP)

The DAP computer series is described in [133] and for the definitive description the reader should consult [134]. The following brief description covers the programming strategy necessary to make optimum use of this computer.

A.1.1 The Architecture

The hardware schematic is shown in figure A.1. An array of single-bit processors is controlled by a conventional microprocessor using broadcast instructions held in a separate code store. Each single-bit processing element (PE) has its own local memory and is capable of communicating directly with its 4 nearest neighbouring PEs on a square connected mesh. Combinations of single-bit operations are used to make up the conventional computer operations such as addition and multiplication of many-bit integer and floating-point numbers. A number of data storage modes make it easy to map arrays, vectors and scalars onto the processors in whatever way is most advantageous to the user's program [135]. The single-bit processors can only have their instructions broadcast to them one at a time and they are incapable of independent operation. For this reason the DAP is termed a single instruction multiple data-stream (SIMD) computer [136]. The DAP is essentially a single user machine, although a small number of users can share it using time-slicing techniques.

A.1.2 Programming Methodology

There are two stratagems for the efficient use of the DAP. Firstly, the data structures for the problem should be stored as efficiently as possible to cut down on the clock-cycles required for each operation. An obvious example is the single bit required to store an Ising spin or a binary alloy concentration variable. The DAP programming language allows this to be coded using a single physical bit of memory rather than the whole word required on some computers [137]. Secondly,

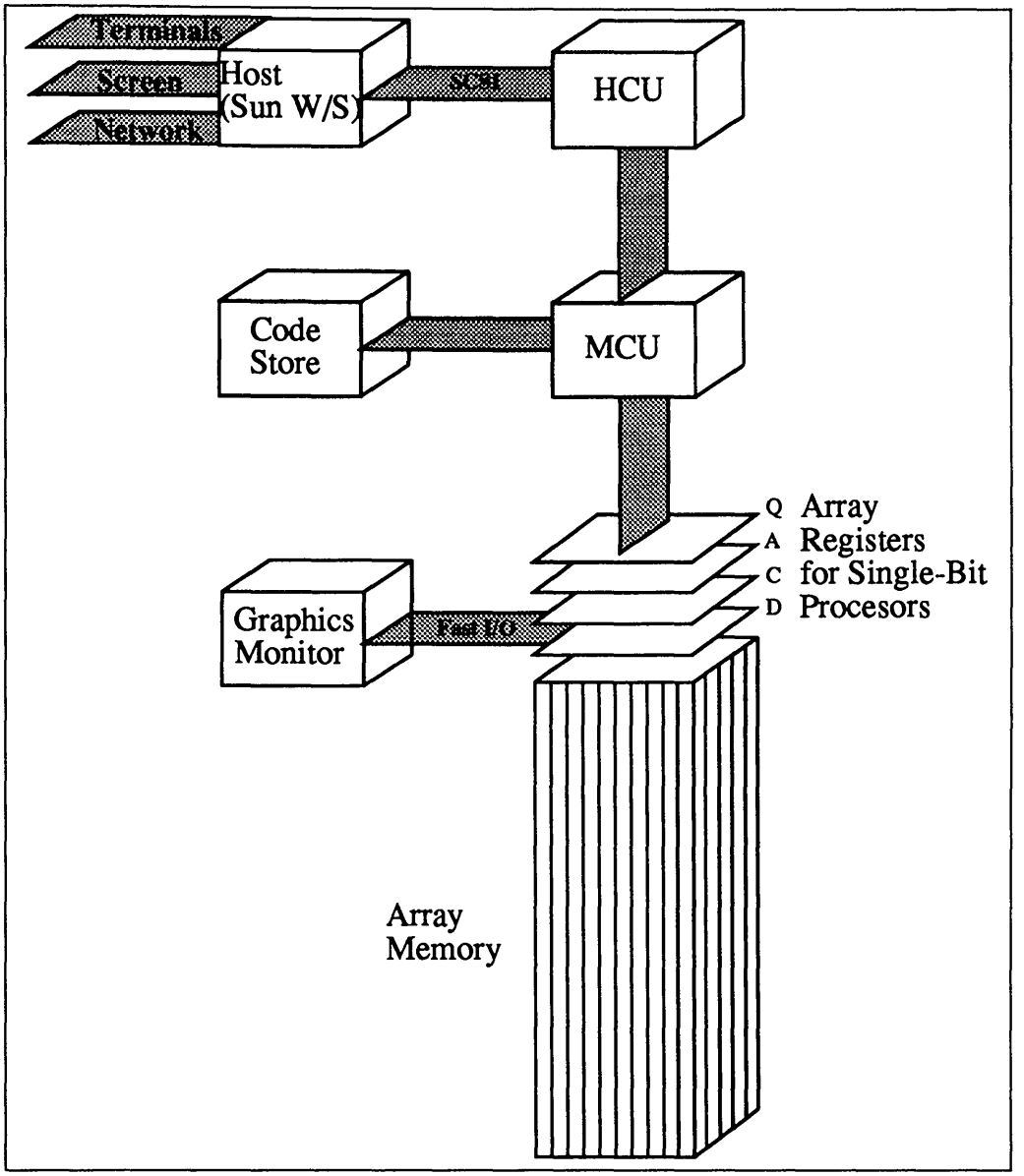

Figure A.1: Distributed Array Processor (DAP-600) schematic, showing normal host computer with terminals (TT), screen and networking facilities communicating with the host control unit (HCU). The master control unit (MCU), itself a conventional processor, controls the array processors, using the program stored in the code store. Each array processor can deal with a single bit at a time, through the use of activity masking (A), accumulator (Q), carry (C) and data transfer (D) registers. In addition, for the DAP-600, each processor has its own 64kb of memory, giving a total of 32 Mb of array memory.

the algorithm should be constructed to keep as many of the processing elements as busy as possible.

The DAP is well suited to the Monte-Carlo work described earlier in this work. The models used employ only one or two bits at each lattice site, so it is possible to code this very efficiently. Furthermore, the regular structure of the DAP processor grid maps well onto 2 and 3 dimensional lattices. In general it is most efficient if all the DAP processors are *all* kept busy so it is best to choose a lattice size that is some multiple of the DAP array size. Furthermore, since much of this work used fast Fourier transforms it was advantageous to restrict lattice sizes to powers of two [114]. Reasons for this are given in section A.8 below. Lattices bigger than the DAP array size are easily mapped onto the array by a memory folding technique known as crinkle-mapping [135], as described in section A.4.1 below. In addition, the 3rd dimension can also be folded up into the memory of the processors.

A.2 The ECS Meiko Computing Surface

The Edinburgh Concurrent Supercomputer (ECS) is at the present still the largest Meiko Computing Surface in the world. Meiko supply a number of transputer nodes, which can be linked together in several useful configurations. The word 'surface' is employed because each node has only four links with which it communicates with other processors, thus forming what is topologically a surface if all the links are used, and two links are needed for each dimension.

A.2.1 The Architecture

The ideas behind this machine are discussed in [138]. At the time of writing the ECS is built from Inmos transputer nodes each having at least 4Mb of local memory (see figure A.2). Unlike the DAP, these transputer nodes are powerful computers in their own right, each being the equivalent of a top-of-the-range PC. Linked together these provide a powerful and flexible computing resource. Figure

A.3 illustrates the general idea by showing one possible configuration of a small part of the ECS. The nodes are partitioned into domains of transputers, one user being given sole access to one or more domains on request.

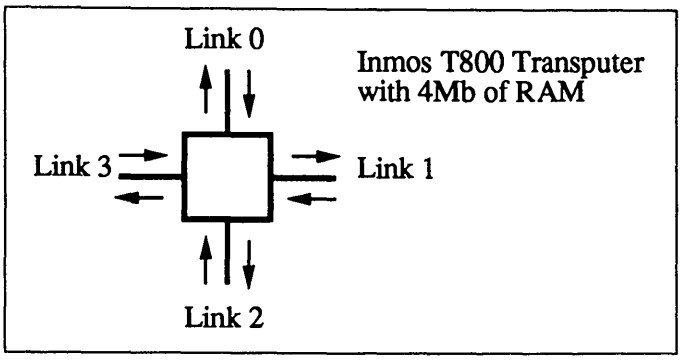

Figure A.2: An Inmos T800 Transputer showing the 4 bi-directional hardware links.

Unlike the DAP, the ECS is truly a multi-user computer, with different users effectively 'logged-on' to their own seat processors and controlling their own domain of processors, which they may reconfigure in software as they require. A number of node connection topologies have been experimented with at Edinburgh [139]. For the present work two simple structures, namely the ring and the torus, have been used. Figure A.4 shows how the physical lattice is mapped onto the transputer hardware.

The processors of the ECS are capable of completely independent operation and have their own separate or distributed memory. For these reasons the ECS is known as a multiple instruction multiple data-stream (MIMD) computer [136].

A.2.2 Programming Methodology

Meiko supply software modules for running code on each processor node, and for routing data between them. This package, now known as CS-Tools, has developed over some years using experience gathered from users at Edinburgh and elsewhere [140]. It is possible to write what are effectively serial code modules. These are run on separate processing nodes, or several virtual processes may be run on the one

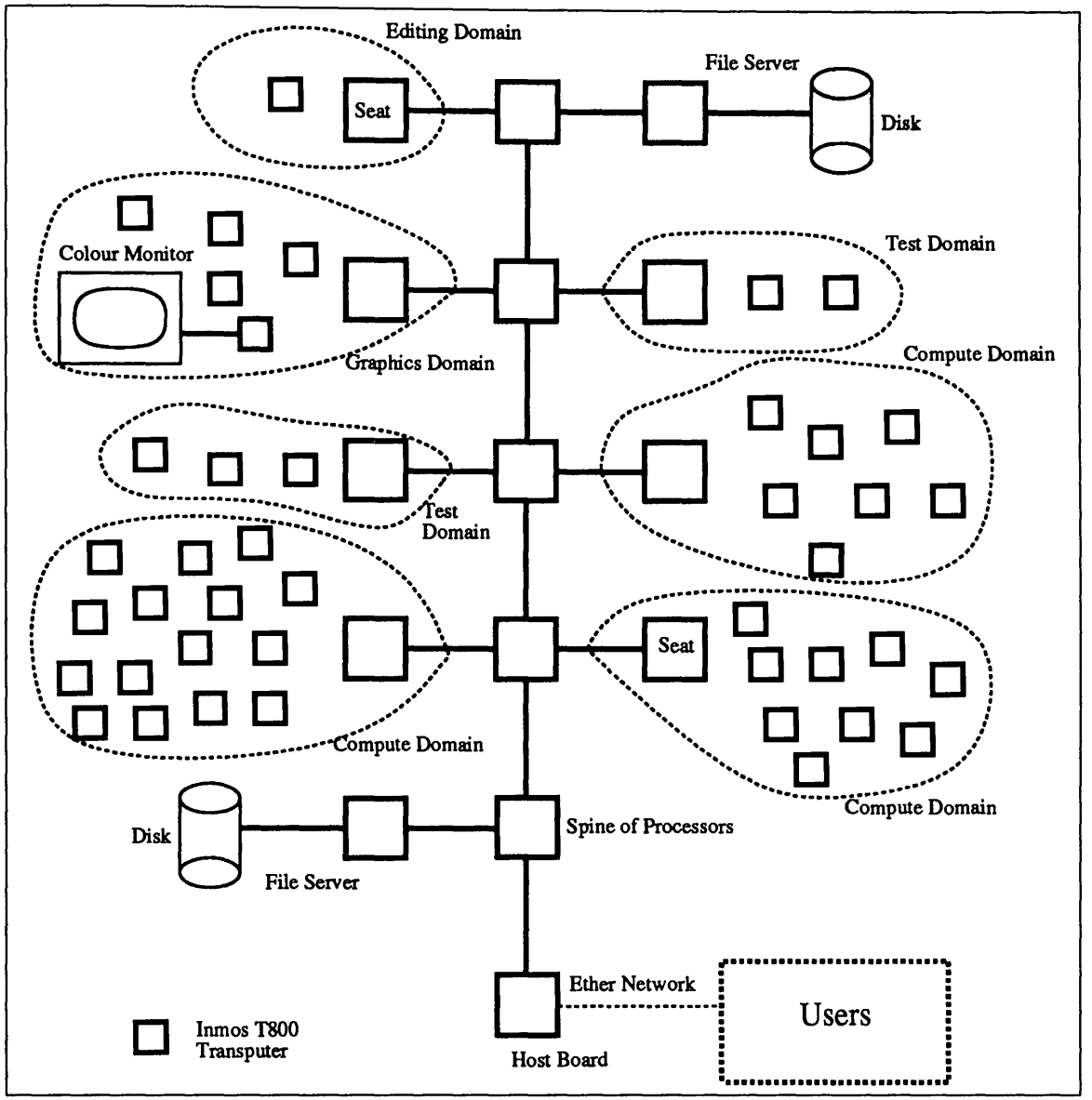

Figure A.3: Meiko Computing Surface schematic showing a possible configuration for the Edinburgh Concurrent Supercomputer. The machine is front-ended by a host transputer, which accesses a connecting spine of transputer nodes. Links leading off the spine access separate domains of user transputers, with the user effectively 'logged-on' to a seat transputer. Some domains may have special purpose hardware for handling graphics monitors or disk controllers. The connections within a domain are completely under the control of the user, and the whole machine may be reconfigured electronically at boot time.

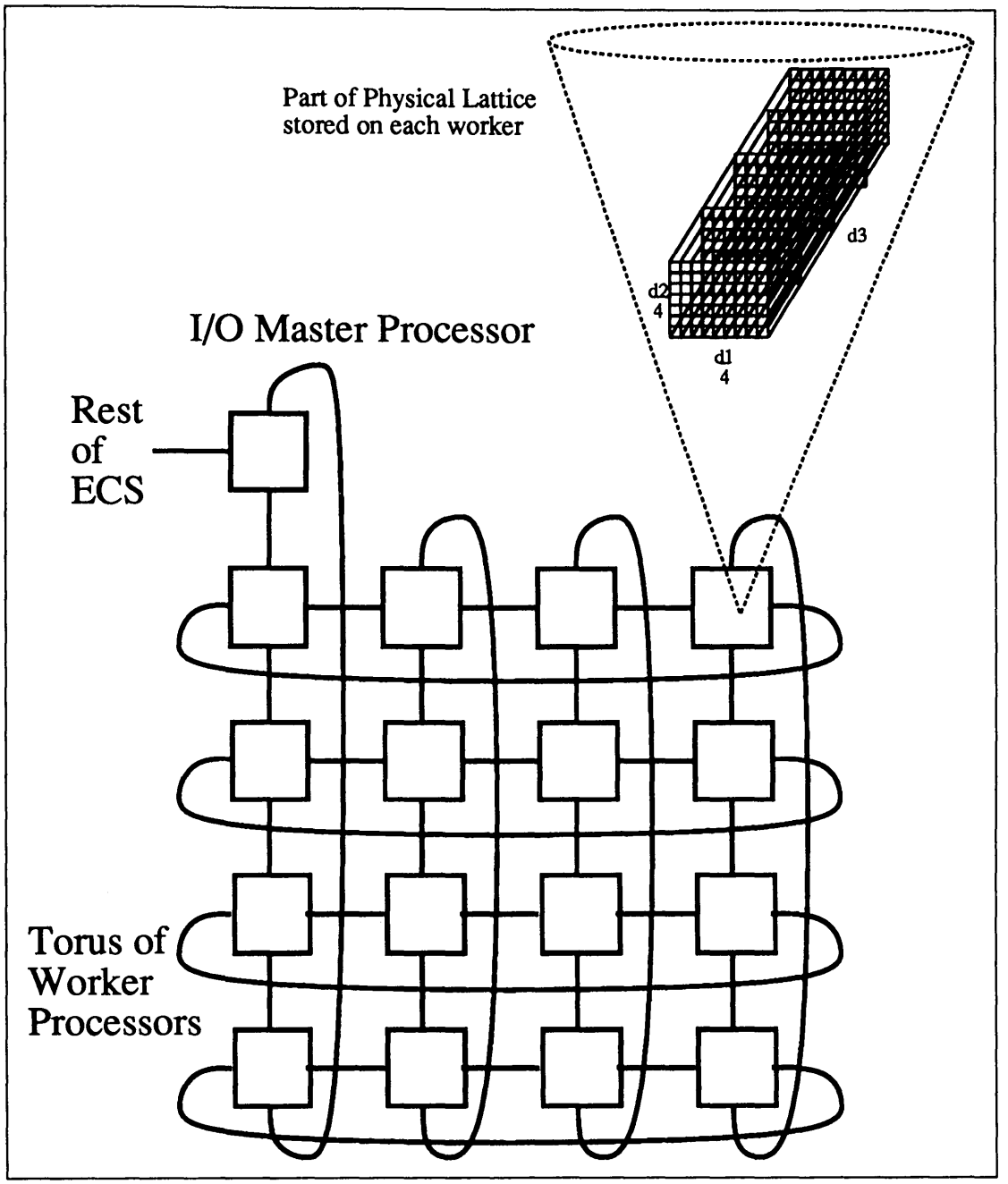

Figure A.4: 16 Transputer nodes configured in a torus with part of the physical lattice stored on each. Providing short range interactions are involved, the only communications required are one or at most two nodes distant, and the worker processors can operate in loose synchronisation. Note that an extra master processor is grafted into the torus to allow data to be fed in and out. This is done by having time-sliced parallel processes running on this processor. Each worker processor has $\frac{N}{P}$ lattice points stored in its own local memory, where N is the number of lattice points in the physical simulation, and P is the number of torus processors (16 as shown).

physical processor, to provide communications buffering for example. A harness program is generally written to encapsulate the applications code, and is roughly analogous to a customised parallel operating system.

The T800 processor nodes employed in this machine are suitable for floating-point calculations, being capable of approximately 1 million floating-point operations per second sustained performance. A typical domain might have 64 processing nodes making it suitable for solving a regular grid problem such as numerical integration of the Cahn-Hilliard equation. The method used in this work was to decompose the mesh geometrically, giving each processor a number of grid points to work on, and passing boundary information between processors at each time step. For numerical integration on a 3-dimensional grid, the 3rd dimension is conveniently folded up in the memory of the processing nodes, since there are only 4 links per node.

A.3 Other Super-Computers

The DAP typifies the class of SIMD machines, but a more recent development in this area is the Connection Machine 2 (CM2), manufactured by Thinking Machines Corporation [141]. Like the DAP the CM2 has many modes of programming conceptualisation, and can be considered as a hypercubic arrangement of some 65,536 single bit processors, with a floating-point processor shared amongst 32 of the single-bit PEs. This mode of operation would be appropriate for Monte-Carlo work on lattice gas models. The CM2 has a particular advantage over the DAP in that indirect addressing is supported for the single-bit processors through the use of a special chip. This allows the attractive possibility of using 'probability look-up tables' to speed up the Metropolis algorithm. See section A.4 below.

It is more common to use the CM2 as a DAP-like machine containing 2048 floating point processors. In this mode, the CM2 shows great promise for further numerical work on the Cahn-Hilliard equation, since it combines the floating-point speed of the ECS with the programming ease that comes with a grid-processor like the DAP. The latest generation of DAPs – the 'DAP series C' are to have an

additional 8-bit floating point co-processor attached to each single-bit processor. This 'floating-point DAP' will also be useful for solving field equations on regular grids.

The obvious directions for improvement of the MIMD class of machines, as typified by the Meiko ECS, are to employ more powerful processing nodes, to use nodes with greater connectivity (ie more links), and to use faster link hardware. Some of these directions have been taken in the form of the 'UK Grand Challenge Supercomputer', which is now installed at Edinburgh. This machine is essentially a 64 node Meiko Computing Surface with each node consisting of two T800 transputers and an Intel i860 vector processor. This combination, as shown in figure A.5 allows nodes to have 8 external links, by handling communications between the i860 and T800s using shared memory. The vector processor gives a considerable improvement in floating-point performance. This machine is already being

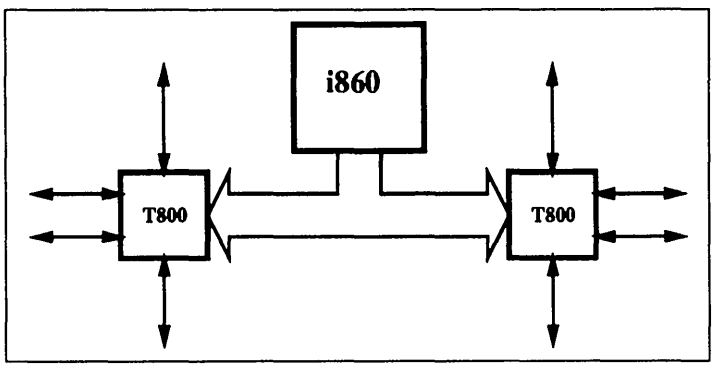

Figure A.5: The compound Intel i860 and Inmos transputer node used by Meiko in the 'UK Grand Challenge Super-Computer', indicating the 8 bi-directional external links, and the shared memory communications bus between the T800s and the i860.

used for, amongst other things, solving the Cahn-Hilliard equation in 3 and 4 dimensions.

A.4 Parallel Monte-Carlo Updating

It was thought until recently that many of the measured properties of Monte-Carlo simulated systems would be adversely effected by a failure to maintain strict de-

tailed balance as defined in [64]. In particular when using a parallel computer to do multiple updates to the simulated configuration, it was thought that this would only be valid if each of the simultaneous updates were at least an interaction length apart, so that in choosing the new configuration, the transition probablities could be properly computed [7]. The result was the so called checkerboard algorithm for the 2-d Ising model [142, 143], as described in section A.4.2 below. There is recent evidence to suggest that under certain conditions this may be over cautious. Landau and Stauffer [144] report no errors in using a simple-minded parallel updating scheme, up to values of the fourth cumulant near criticality, where it is generally believed that such effects would be most manifest.

This is still controversial, and all the Monte-Carlo work in this thesis has employed a conservative implementation of the checkerboard algorithm. Nevertheless it would aid simulation work considerably if this could be relaxed, particularly for simulating systems with long interaction lengths. At present the only solution is either to use the parallel computer slightly inefficiently, or to simulate a very much larger system than is actually required. This latter is particularly unhelpful when the physical system being simulated exhibits critical or hydrodynamic slowing-down effects. These effects typically worsen faster than the system size so that the relaxation time time τ required to achieve equilibrium is approximately given by:

$$\tau \sim N^x \tag{A.114}$$

where the exponent x is always greater than 1 and for many models is greater than 2 [7]. A simpler method, described below in section A.7, is to perform several independent simulations.

A.4.1 Crinkle and Sheet Mapping

Crinkle mapping is a way of mapping a simulated lattice onto the PEs of the DAP so as to optimise the update efficiency [135]. Consider the two-dimensional Ising model and a simulation of a lattice of $16 \times 16 = 256$ sites on a pseudo-DAP of $4 \times 4 = 16$ PEs. Figure A.6 shows two possible ways of mapping the lattice spins onto the memory of the PEs.

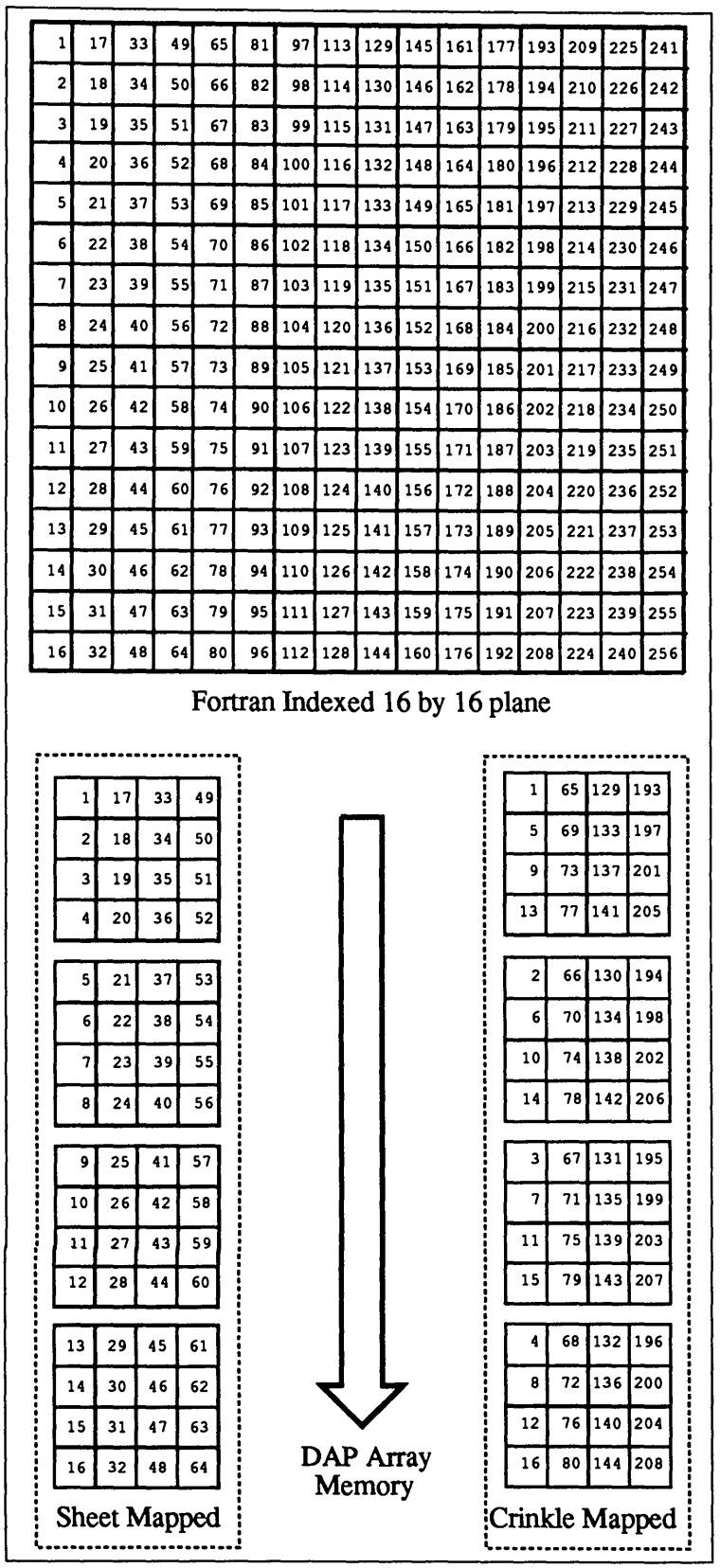

Figure A.6: Sheet and crinkle mapping of a 2d Ising lattice of size $16 \times 16 = 256$ sites onto a $4 \times 4 = 16$ processor pseudo-DAP.

The simplest case is to 'sheet' map the spins so that one DAP memory-plane is filled up at a time. It is easily seen from figure A.7, that due to the nearest neighbour interactions involved, using all the processors simultaneously would involve violating the detailed balance condition required by the Monte-Carlo algorithm [64] since 'hits' would involve transitions whose probabilities were no longer Boltzmann. If a site variable is updated, with a probability calculated on the basis of some other site variable which is itself changed simultaneously, then the probability was meaningless. Errors in the dynamics introduced by violation of detailed balance strongly manifest themselves near critical points [7].

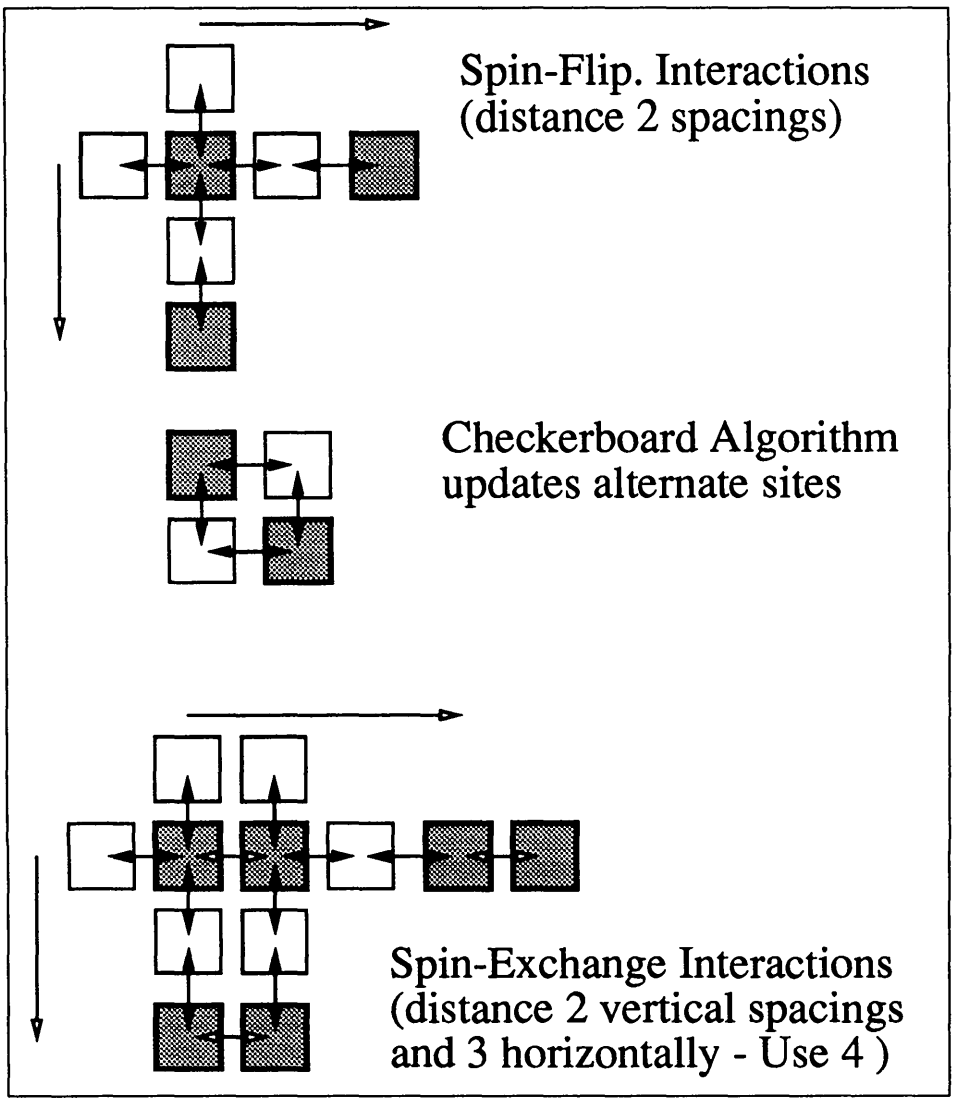

Figure A.7: Interaction radii for the spin-flip and spin-exchange models in 2d.

A better mapping is the 'crinkle' storage scheme, whereby whole 'tiles' of the lattice are stored on *one* PE, so that for the example shown, the first spin stored

on each PE is 4 lattice spacings distant from the corresponding spin on the next PE. This means that all PEs may be operated at once, without violation of the detailed balance condition. For the nearest neighbour Ising model, it is sufficient if the simulated lattice edge size is only twice the processor array edge size. Strictly speaking, in the case of the spin-flip model, it is possible to use the checkerboard algorithm as shown in figure A.7 where alternate sites are updated, although care must be taken at high temperatures to avoid 'marching effects' in which all the spins just flip up and down at once. For the alloy model however, *both* the exchanged sites must be outwith the interaction radius of independent 'hits' so that the lattice edge size should ideally be three times the processor array edge size. Three is not a convenient ratio when fast Fourier transforms are involved so four was used in most of this work.

If a 3-dimensional lattice is simulated, the third dimension can be folded or crinkled up alternately with the first two as regards array memory storage. It is then possible to avoid quite such large lattice edge sizes. This method also extends to the simulation of 4-dimensional lattices.

A.4.2 Super-decoding of the up-dating scheme

This is a highly specialised technique, only applicable to certain update algorithms and certain computers. Before explaining the technique, it should be stated what problem it solves.

Computers like the DAP suffer from the disadvantage that their processors operate in complete lockstep. For algorithms like that of Metropolis, a pseudo-random number is compared to a calculated probability for each hit. Random numbers are easily generated independently on each processing element (see section A.6 below) but it is undesirable to have to re-evaluate expressions like $e^{-d\mathcal{H}}$ for each hit. Since the two-dimensional spin-flip model has only 5 possible values for $d\mathcal{H}$ it is preferable to use a lookup table containing the pre-computed probabilities. (The spin-exchange model has a slightly larger but still small number of possible values). Unfortunately, the DAP hardware does not allow PEs to look at independent memory locations at once. They are effectively constrained to look at the address

broadcast to them by the MCU, so it would be necessary to loop over all entries to cover all possible options for all the PEs. The super-decode technique is a trick to exploit the fact that the DAP hardware can perform single-bit logical operations faster than it can loop over all entries in a look-up table and very much faster than it can perform floating-point operations like the *EXP* function.

The logical bit-representations of the desired look-up table entries are compared with the representations of the input values — 5 spins in the case of the 2-d spin-flip Ising model, and 8 spins for the spin-exchange model. After eliminating redundancies and with some manipulation it is possible to reduce the spin-flip look-up operation to 5 logical operations, and 7 for the spin-exchange model. Despite the difficulty in coding this, it is worthwhile, since it can yield more than an order of magnitude improvement in computational speed. Combined with a careful assembler coding of the random-number generator, this method makes very long simulation times possible [145].

A.5 Parallel Cluster labelling and Counting

In analysing the configurations simulated by Monte-Carlo methods, it is particularly useful to examine the cluster distributions. Clusters are defined here to be sites of the same spin (or concentration variable) which are connected together by the same connectivity as appears in the system's Hamiltonian (ie nearest neighbour connectivity for most of the systems described in this work). There are a number of numerical techniques for tackling this problem depending on whether it is sufficient merely to count the clusters, or if it is necessary to label them for later use, and whether computational speed or economy of memory is sought. Note that labelling is superior to counting since all the information is available for any distributions required in the labels. Table A.1 summarises the algorithms, which are described below.

In the descriptions that follows it is simplest to imagine a lattice of N sites referenced by a single index $i = 1, 2, ...N$, as shown in figure A.6. It is easy to generalise this to d-dimensional lattices, and even to continuous space if a 'con-

Algorithm (Originator)	Aim — Count or Labels	Speed	Memory Requirements	Comment
Ancestor (Eardley)	Labels	Slow	Medium	Serial
Ant (Toral and Wall)	Count	Fast	Low	DAP Specific
Hoshen and Kopelman (Themselves)	Labels	Medium	Huge	Serial
Colour Propagation (Baillie and Hawick)	Labels	Fast	Large	SIMD or MIMD
Colour Broadcast (Hawick / Parkinson)	Labels	Greased Lightening	Large	DAP Specific

Table A.1: Cluster counting and labelling algorithms.

nectivity function' can be defined to determine when two entities are part of the same cluster [146].

A.5.1 Ancestor Algorithm

This is the simplest and most efficient algorithm for cluster labelling on a *serial* computer. It is explained more fully in [147], but the principle is as follows:

1. Store an integer label L_i for each site i and initialise $L_i = i$
2. Sweep through the list noting local cluster connections and tracing them back to the earliest found connection or their greatest 'ancestor', thus re-assigning the labels L_i so that the member sites of each cluster have the same unique integer label.
3. Re-assign the cluster labels in ascending order from $j = 1...P$, so there are P clusters.

4. The labels can be histogrammed to determine the cluster size distribution, and any other moments of the distribution, since the original lattice is still intact and still indexed by i.

The tree-like sweeping that is necessary to trace all ancestor connections in step two above is time consuming and makes this algorithm of order N^2 in speed.

A.5.2 Ant Algorithm

This algorithm was first employed on the DAP [148], but can readily be adapted to other SIMD computers. This method is essentially a parallel adaptation of the ancestor algorithm. To save on memory, rather than store an integer label for each site, only a copy of the lattice is used (which will use fewer bits than an integer — typically a single-bit for Ising sites). The algorithm is as follows:

1. Find the first remaining occupied site in the lattice copy. This can be done very fast using the *FRST* function in the DAP Fortran language [137].
2. Release an 'ant' at this site and let it wander along all connected links of that site, recursively 'eating' the site variables until it can go no further and dies. The total number of site variables it has encountered is the cluster mass and it may be entered into the size distribution table.
3. Step 2 is repeated until the lattice is empty, and the number of 'ants' used is the total number of clusters.

A.5.3 Hoshen and Kopelman Algorithm

This method [149] is for *serial* computers only and while very fast is very expensive in terms of memory. It is a variation of the ancestor algorithm but rather than waste time tracing all the ancestor connections during each sweep of the lattice (as the ancestor algorithms does), this algorithm employs a working store of matching pairs of cluster labels. This store is then used to eliminate redundant cluster

numbers *once* outside the main sweep of the sites. Unfortunately, for an arbitrary configuration, the working table needs the same number of elements as the lattice, so that with the labels, there are two integers required for each lattice site, in addition to the site variables themselves. This method is very powerful for 'small' lattices (eg of less than say $16 \times 16 \times 16$ sites on today's technology).

A.5.4 Colour Propagation Algorithm

This method is an obvious extension to the ant algorithm (so obvious that it occurred independently to the author and to C.F.Baillie [70]). This method requires the storage of an integer label for each site. Some memory economy is possible on the DAP since it is possible to use 24-bit integers rather than 32-bit. The algorithm is:

1. Initialise the labels $L_i = i$ (imagining a different colour associated with each different label)
2. At each site set the label to the minimum (or maximum) of its current value and that of its *connected* neighbours.
3. Iterate step 2 until there are no more changes.

This is particularly fast on the DAP, since it is possible to program the algorithm as though you had a virtual DAP with the same number of processors as there are lattice sites (using the crinkle mapping technique described above), and a special DAP function *ANY* [137] indicates when the iteration should stop. An interesting visualisation of this algorithm is to map a colour to each integer value and watch the algorithm operate. The effect is one of colours diffusing out from their point of origin, as on chromatography paper, until all the clusters have one unique colour. For a dense percolated cluster of non-spiral topology, this algorithm will take at worst the number of iterations necessary to propagate one colour across the whole lattice. So for a 2-dimensional lattice of size $L \times L = N$ sites, it will take on average $L = \sqrt{N}$ iterations.

A.5.5 Colour Broadcast Algorithm

The colour propagation algorithm is easily programmed but can get stuck in very long iterations if a cluster has a spiral topology, since the algorithm uses only spatially local information and has no means of 'knowing' that it is chasing round a spiral. One method to avoid this trap is to incorporate a means of broadcasting the label of the dominant cluster to the whole lattice so that all intermediate labels are eliminated in one step rather than relying on the local propagation. I am grateful to D.Parkinson for a highly efficiently coded version of this algorithm for the DAP.

A.6 Parallel Pseudo-Random Number Generation

The importance of random number generators for quality Monte-Carlo work can hardly be over emphasised, and is discussed in [150]. It is not worth becoming embroiled in the argument over whether the random number generator (RNG) algorithms used on computers should be referred to as 'pseudo-random'. In this context, random simply means uncorrelated with the physical process being simulated, using any sensible definition. In particular the random number sequence should have a long period so that sequences are not repeated, and should not have any short length auto-correlations.

A.6.1 Random Number Algorithms

There are a number of review works on RNGs for serial computers [151, 152, 153, 154]. Considerably less has been written on suitable algorithms for the very fast parallel computers in use today, and less still on the problems associated with them. A fuller attempt to redress this balance is made in [155], and the following gives an overview. Random number generator algorithms used on computers must have the following properties.

1. The generator should provide a sequence of independent variates, being free from correlations.

2. The generated sequence should have a very long period so that even if very long sub-sequences are used, there is no possibility of repeating them.

3. The generator should be computationally efficient, probably requiring assembler coding, and should use as little memory as possible.

4. The sequence should be exactly repeatable, so that from a given point in the generated sequence, it is *always* possible to obtain the same sub-sequence.

5. The algorithm should be such that it can be implemented on a wide variety of computer architectures so that the same sub-sequence can be obtained (if desired) on any machine.

6. The variates produced must be homogeneous in nature, so that the machine representation of a variate will have all its bits equally random.

7. The algorithm should also be properly supported in terms of software interface, so that it can be easily incorporated in any application, without significant loss of speed.

In principle the ideal generator would produce a very long sequence of uncorrelated bits, from which any type of random variate can be constructed, ie integers, or floating-point numbers. The converse is not necessarily true; randomly generated machine representations of integers or floating-point numbers can not be taken apart to construct bit sequences. Algorithms are available which produce bit sequences (XOR-shift generators), integer sequences (linear congruential generators) [154] or hybrid algorithms such as that described below, which produce floating-point numbers. The list of desirable features described above are sometimes mutually exclusive, and the fastest algorithms are not always statistically reliable [155].

Many generator algorithms can be studied analytically and particularly bad ones can be avoided [154, 156]. However, it is useful to have a number of numerical tests which can be applied to generated sequences as additional re-assurance that Monte Carlo results are likely to be unbiased. A number of excellent stringent

tests are described in [153] and have been applied to the generarators in common use on the DAP [157] and ECS computers [155] with alarming results [2].

A.6.2 Marsaglia's Universal Generator

An algorithm known to satisfy the list of conditions above is described in [158] and was implemented on the DAP and ECS machines [155]. This 'universal generator' works by combining the sequences generated by two *different* Lagged-Fibonacci generators in a table of 97 values, and indexing randomly, using a third generator, into this table to produce each uniform variate in the sequence. This gives a sequence with a period of approximately 2^{144} which would take in excess of 10^{28} years to cycle through, assuming a very efficient computer with 10MHz clock speed. In addition, sub-sequences from this generator pass the statistical tests described in [153].

A.6.3 Problems in Parallel

There is a particular problem associated with operating a *single* random number generator on parallel computers. Not only must the sequence of variates produced on each processor be uncorrelated with itself, but it must also be independent of the sequences being generated on other processors. This is necessary for the bit-sequence generators used on DAP-like computers, where the bits are combined across the processor array to produce floating-point numbers, as well as on computers like the ECS where floating-point numbers are produced entirely on one processor. Clearly the seriousness of the problem depends on the way in which the variates are used, either on-processor or globally. The best solution is to ensure that the variates *are* completely independent across processors.

A method to do this is described in [155] and involves the initialisation of the sequences on each processor. It is usual for RNGs to be initialised in one of two

[2]The Manufacturer-supplied routines were found to be fast and of long period but with significantly poor short range correlations

ways:

1. The generator is always started from the same place in the sequence and the same sub-sequence is obtained. This is useful for test purposes but fairly useless for production Monte Carlo work.

2. The generator is initialised directly by input of one or more seed variables, and perhaps discarding some number of variates before use. As a caveat to this method, the seeds are sometimes obtained from the computer system clock, giving a different sequence each time the code is run.

The difficulty in the second way is that no information is generally available to say exactly what starting position in the sequence of variates a given combination of starting seeds will give. Indeed it is this non-trivial relation between the seeds and the sequence that endows the generator with its pseudo-random properties. The same seeds will produce the same sequence, but it is *not* necessarily the case that seeds differing by some amount will yield sequences a related distance apart. What is needed is a means of specifying that sub-sequences of variates generated on different processors will be a minimum distance apart in the total sequence. This would allow processors to be set up so that their sequences do not overlap, or if they do, they only do so a sufficient number of variates later that the inherent complexity of the application destroys any potential correlation. The 'Boost' procedure described in [155] allows the universal generator to be started on many processors a specified sub-sequence apart, by applying bit-matrix operations to a given start point and rapidly change it to a new distant start point.

A.7 Task Farming and Parameter Scanning

The apparently trivial use of parallel computers for task-farming deserves some discussion. While parallel computers are invaluable in performing simulations on large systems which would otherwise be intractable, it is also worthwhile to use them to perform multiple simulations on smaller systems. This mode of operation

can yield important information from the improved statistical accuracy when results from many smaller simulations are combined. The DAP has been used for this kind of work [41] where a number of 'smaller-than-DAP' sized lattices were simulated. This approach is even easier on the ECS. The limitations are mainly caused by problems with data management. Figure A.8 shows how the same serial program can be run on a tree of transputer nodes, each with its own access to a directory of files. The job scheduling and data management can then be done using existing tools available with the operating system [3].

The harness written to implement figure A.8 clearly has its limitations, since the number of file-access threads running to the root processor increases exponentially for binary and ternary trees. Nevertheless it was adequate to run 1+3+9+27 = 40 processes on a ternary tree, where the code running at each node, as shown in figure A.9, reads a control file, a configuration file, and runs overnight, before writing a new configuration. A serial code is run 'the morning after' to collate the night's work into one set of averaged results.

A.8 A Numerical Scattering Experiment

Equation 1.9 gives the structure factor $S(\mathbf{k}, t)$ for a simulated lattice and can be recast as:

$$S(\mathbf{q}, t) = \frac{1}{N} \sum_{\mathbf{r}} e^{i\mathbf{q}.\mathbf{r}} \sum_{i} \langle \tilde{c}(\mathbf{r}_i, t) \tilde{c}(\mathbf{r}_i + \mathbf{r}, t) \rangle \tag{A.115}$$

where the excess concentration field $\tilde{c}_i = c_i - \overline{c}$ can be obtained as a real (floating-point) quantity, using the average concentration $\overline{c}$. The structure factor for a given configuration is obtained by a numerical Fourier transform. There are a number of ways of implementing equation 1.9:

Equation A.115 can be rewritten as:

$$S(\mathbf{q}, t) = \left\langle \frac{1}{N} \sum_{\mathbf{r}} e^{i\mathbf{q}.\mathbf{r}} \tilde{g}(\mathbf{r}, t) \right\rangle \tag{A.116}$$

$$\tilde{g}(|\mathbf{r}|, t) = \sum_{i} \langle \tilde{c}(\mathbf{r}_i, t) \tilde{c}(\mathbf{r}_i + \mathbf{r}, t) \rangle \tag{A.117}$$

[3] UNIX

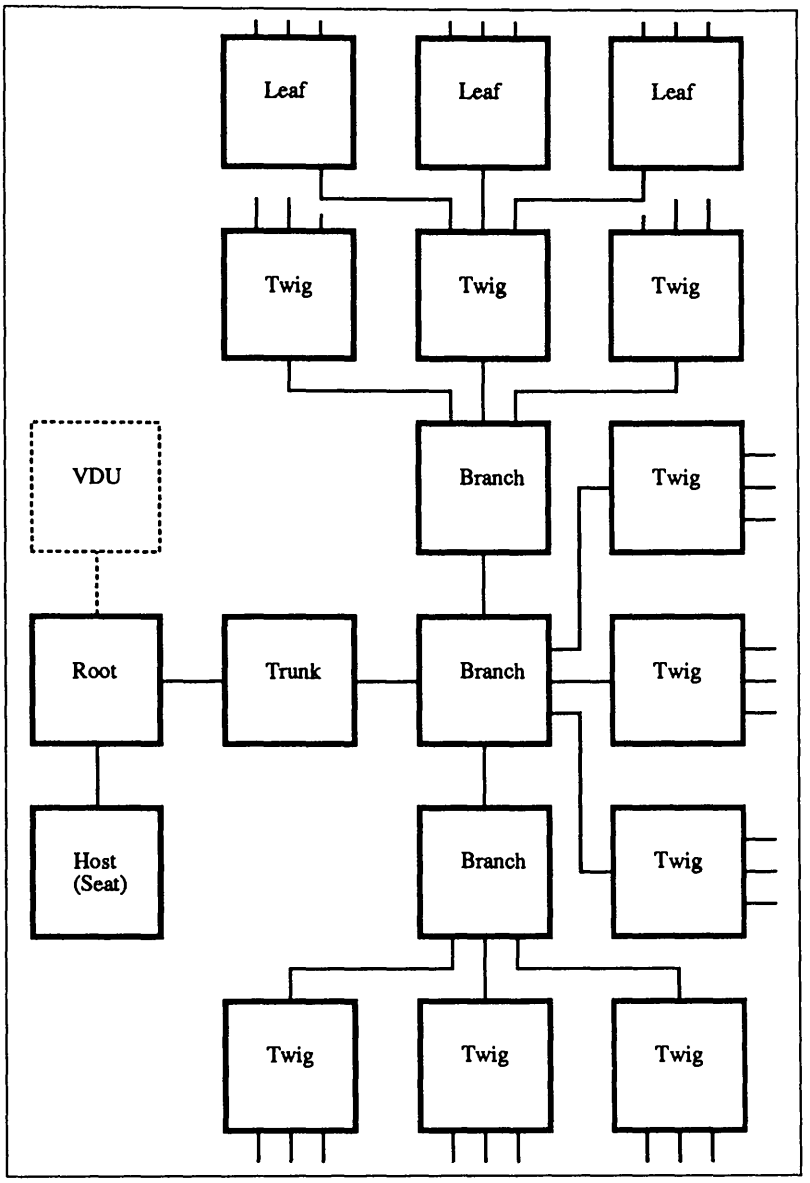

Figure A.8: A ternary tree of processing nodes, each running a copy of the same simulation code, but working within its own filing system directory, as well as passing filing system access threads to its branch processors. The root processor is grafted onto the rest of the ECS. There are: 1 (trunk) + 3 (branch) + 9 (twig) + 27 (leaf) processors in the tree. This gives a total of 40 copies of the applications code running simultaneously.

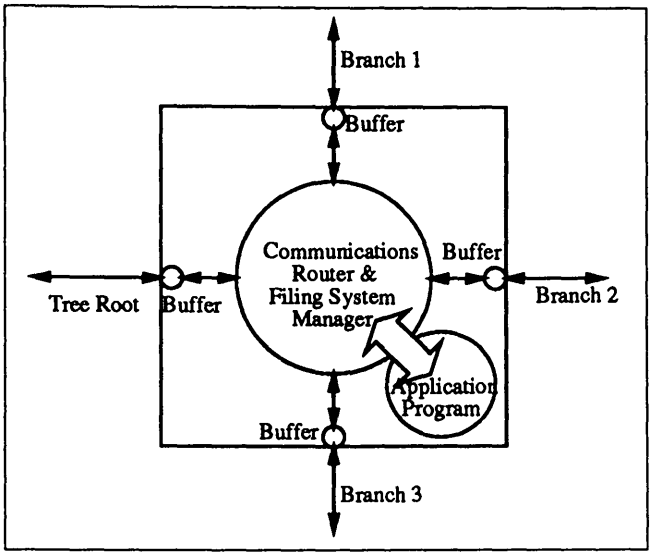

Figure A.9: The code run on each node of the tree. Each link has buffered I/O and is handled by the communications process, which supplies file access threads for its *own* applicatrion process as well as for the branch links. Providing the file access to compute ratio is low for the application process, this arrangement does not saturate until there are 30-40 such tree nodes from the one trunk.

Here, the *spherical* averaging process is applied to the configuration first, to define a correlation function $\tilde{g}(|\mathbf{r}|, t)$ which is a function of the radial correlation length $|\mathbf{r}|$. This can then be transformed directly using the sine transform:

$$S(q,t) = \frac{1}{N} \sum_{\mathbf{r}} \frac{\sin q.r}{q.r} \tilde{g}(r,t) \tag{A.118}$$

The correlation function $\tilde{g}(r,t)$ is not properly normalised, but is related to the proper correlation function $g(r,t)$ by:

$$g(r,t) = \frac{\tilde{g}(r,t)}{z(r)} \tag{A.119}$$

where $z(r)$ is the lattice multiplicity function [80]. Although this algorithm is of order N^2, it **is** computationally feasible since it is only one-dimensional and N is not too large (typically $N \lesssim 256$ for this work). Averaging over multiple configurations (to reduce statistical noise) is then a matter of collecting independent values of a *one-dimensional* function. This method is unfortunately highly susceptible to 'aliasing' problems as described in [114].

A better method is to perform d-dimensional Fourier transforms on each independent configuration, and average these *prior* to the *spherical* averaging process to

reduce the d-dimensional scattering to a one-dimensional structure factor. This method is much less prone to aliasing, and the high frequency random phase information from the details of individual configurations is convoluted or 'washed out' in the *configurational* averaging process. This leaves a less noisy scattering envelope.

Unfortunately, the computational effort involved in performing multi-dimensional Fourier transforms is considerable. The Fast-Fourier transform algorithm [114] can be applied to lattices which have edge sizes that are powers of two, and is an $N \log_2 N$ algorithm. In spite of this, this method pushes the present computational resources to their limits, in terms of speed *and* available memory. The FFT's *can* be coded for a serial computer using the subroutines given in [114]. However, these codes *cannot* be run for large lattices (eg $N \gtrsim 128 \times 128 \times 128$) due to limitations of speed *and* memory.

It is possible to perform very efficient Fast Fourier transforms (FFT) on the DAP, exploiting the single-bit processors in doing the 'butterfly bit reversal'. I am grateful to S.Sheard for codes which performed DAP-sized two-dimensional FFTs very efficiently [4]. These codes were modified for 'larger-than-DAP' sized arrays, and extra one-dimensional transforms over each index in the two-dimensional arrays, together with the greatest possible memory economy of using 24-bit floating point numbers, allowed three dimensional transforms to be performed in a tractable time [5].

A.9 Fourier Image Reconstruction

As has been described in chapter 4, a Small Angle Neutron Scattering detector is generally an array of detector elements in a regular mesh, of size 64×64 or 128×128 elements. It is possible to process the raw data using Fourier transforms to filter out the statistical noise present prior to normalisation and circular averaging. A

[4] These codes have been adopted by AMT and provide a *very* fast and efficient package for two dimensional FFTs

[5] ie overnight

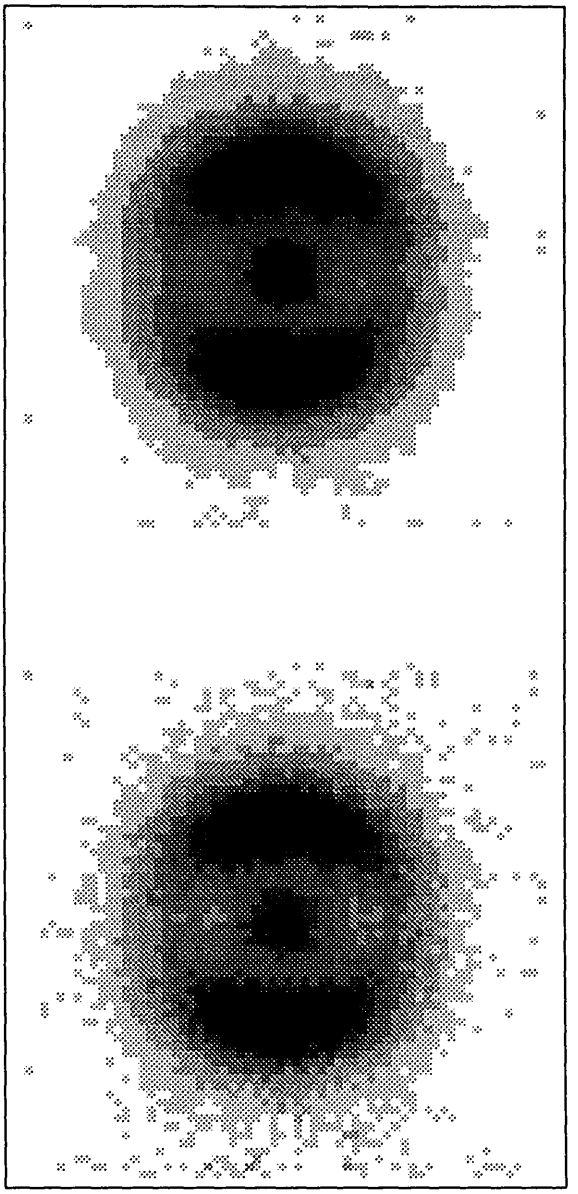

Figure A.10: Small Angle Scattering image from a polycrystalline *Fe-Cr* sample, showing the effect of the FFT smoothing algorithm. The anisotropic pattern comes from the sample being in a saturated magnetic field, applied in the horizontal direction.

two-dimensional Fast Fourier transform is applied to the data , and one of a choice of windowing functions is used to eliminate the high frequency components of the data before an inverse transform is applied. The scattering images so obtained can be considerably cleaner as is illustrated by the example of SANS data from a polycrystalline *Fe-Cr* sample shown in figure A.10

This computational process can be quite lengthy since several data collection runs are required to obtain the scattering intensity in standard units. The data array sizes are convenient multiples of the DAP array size, so codes were written to process the raw images in real time. This is useful as it allows interactive experimentation with different noise reduction windows as described in [114].

Appendix B

Maximum Entropy Fitting

B.1 Overview

This appendix is intended as a description of the method of non-linear parameter fitting that has become known as Maximum Entropy fitting, and how this method relates to fitting a particle size distribution to small angle scattering data.

The Maximum Entropy technique was pioneered by Gull and Skilling [159], and has been applied to particle size distributions by Potton and co-workers [160]. For commercial reasons, exact details of the iterative algorithms used by the above have not been forthcoming, although I am grateful to Dr. J.Potton for the prototype FORTRAN MAXE code she kindly supplied to the Materials Science and Metallurgy Division of AEA Harwell. The algorithm and code described below is a derivative of that work, with improved robustness, faster convergence, better numerical precision and a wider choice of fitted form factors. This code was written by the author during a stay at the Argonne National Laboratory, as a research visitor in 1989, and is described in [161].

The Maximum Entropy technique was originally employed by Gull and Skilling for noise reduction in astronomical images [162] and has recently been used for other two dimensional image work [163]. A general discussion of the use of the technique for reducing spurious signals in neutron scattering images is given in [164]. In what follows, the technique is applied to a positive set of numbers in the

form of a distribution function, rather than to an explicit image.

B.2 The Maximum Entropy Technique

Consider a set of experimental data values $d_j, j = 1 \ldots P$ which are measurements of some quantity y_j, and have estimated uncertainties of σ_j. Suppose that these y_j are linearly related to the N quantities $x_i, i = 1 \ldots N$ that we actually want to determine, by a relation like:

$$y_j = \sum_{i=1}^{N} \mathbf{O}_{j,i} x_i, \quad j = 1 \ldots P \tag{B.120}$$

This is quite general and states that the measured values y_j are a linear combination of the basis values x_i. The problem is known as a linear inverse one, where a unique solution does not exist if $N > P$ and even in the case where $N \leq P$ the solution may be unstable or the data inconsistent.

A commonly used technique for the case $N = P$ is the least squares minimisation method, whereby the x_i are chosen to exactly reproduce the data values d_j, with little account made of the experimental uncertainties, and with every fluctuation in the data contributing equally to the fit.

The maximum entropy criterion requires that the fitted values x_i contain only enough information consistent with the information content *supplied* in the form of the data d_j. A useful quantity to characterise the fitted values is the missing information function or the statistical entropy of the set of number x_i, defined as:

$$S = -\sum_{i=1}^{N} \log \frac{x_i}{b_i} \tag{B.121}$$

where the b_i are a set of base values which give a numerical meaning to the magnitude scale of the values x_i. The maximum entropy method is then to choose the solution $\{x_i\}$ to equation B.120 that maximises the entropy S, subject to the constraints of the available data $y_j = d_j \pm \sigma_j$.

Previous attempts to fit size distributions to scattering data have employed least squares minimisation techniques, with limited success [165]. These methods tend

to *overfit* to accommodate what can be substantial noise in the scattering signal from a weakly contrasting feature. In fact it is better *not* to constrain the fit too strongly. Since the measurements contain some errors, the solution set will contain features that are necessary only to accommodate these errors and it is better to allow some misfit between the d_j and the y_j. A sensible criterion for choosing the amount of misfit is the χ^2 statistic, computed here as:

$$\chi^2 = \sum_{j=1}^{P} \frac{(d_j - y_j)^2}{\sigma_j^2} \tag{B.122}$$

The mean value of χ^2 is P, and this gives a useful criterion for an iterative algorithm to maximise the entropy S, subject to the constraint $\chi^2 = P$.

Published literature on the Maximum Entropy technique tends to stop at this level of description, making no reference as to what numerical method should be used for the constrained maximisation.

There are a number of possible algorithms for the maximisation, including the downhill simplex algorithm, Powell's direction set method, and variations of the conjugate gradient method. These are all described in detail by [166], but the best algorithm for speed and range of convergence is the conjugate gradient algorithm. This is outlined briefly below.

B.3 Conjugate Gradient Minimisation

It is easiest to formulate the conjugate gradient algorithm as a minimisation process, rather than a maximisation. This presents no difficulty, as numerically it is feasible to minimise the negative of the entropy, hence maximising the entropy.

The problem can be stated as a requirement to minimise a function f which has a multi-dimensional argument $\mathbf{x}$. It is convenient to suppose that the function $f(\mathbf{x})$ can be approximated by the quadratic form:

$$f(\mathbf{x}) \simeq c - \mathbf{b}.\mathbf{x} + \frac{1}{2}\mathbf{x}.\mathbf{A}.\mathbf{x} + \cdots \tag{B.123}$$

where c is a constant, $\mathbf{b}$ a vector, and $\mathbf{A}$ the Hessian matrix. Suppose we start with some guessed starting point $\mathbf{P}_0$ in $\mathbf{x}$ space, and construct the following sequence of vectors in $\mathbf{x}$ space.

$$\begin{aligned} \mathbf{g}_{i+1} &= \mathbf{g}_i - \lambda_i \mathbf{A}.\mathbf{h}_i \\ \mathbf{h}_{i+1} &= \mathbf{g}_{i+1} + \gamma_i \mathbf{h}_i \end{aligned} \tag{B.124}$$

where λ_i, γ_i are chosen so that $\mathbf{g}_{i+1}.\mathbf{g}_i = 0$ and $\mathbf{h}_{i+1}.\mathbf{A}.\mathbf{h}_i = 0$ or:

$$\begin{aligned} \lambda_i &= \frac{\mathbf{g}_i.\mathbf{g}_i}{\mathbf{g}_i \mathbf{A} \mathbf{h}_i} \\ \gamma_i &= \frac{\mathbf{g}_{i+1}.\mathbf{A}\mathbf{h}_i}{\mathbf{h}_i \mathbf{A} \mathbf{h}_i} \end{aligned} \tag{B.125}$$

If the denominators are zero then λ_i, γ_i are taken as zero, so that in general:

$$\begin{aligned} \mathbf{g}_i.\mathbf{g}_j &= 0 \\ \mathbf{h}_i.\mathbf{A}\mathbf{h}_j &= 0 \quad \forall i \neq j \end{aligned} \tag{B.126}$$

This process is essentially a Gram-Schmidt orthogonalisation. A further rearrangement shows that:

$$\lambda_i = \frac{\mathbf{g}_i.\mathbf{h}_i}{\mathbf{h}_i.\mathbf{A}.\mathbf{h}_i} \tag{B.127}$$

and

$$\gamma_i = \frac{\mathbf{g}_{i+1}.\mathbf{g}_{i+1}}{\mathbf{g}_i.\mathbf{g}_i} \tag{B.128}$$

$$\gamma_i = \frac{(\mathbf{g}_{i+1} - \mathbf{g}_i).\mathbf{g}_{i+1}}{\mathbf{g}_i.\mathbf{g}_i} \tag{B.129}$$

Where equation B.128 is the basis for the Fletcher-Reeves version of the conjugate gradient algorithm and equation B.129 is used in the Polak-Ribiere version [1] [166].

At this stage, the *unknown* Hessian matrix $\mathbf{A}$ is still employed, but it can be eliminated from the calculation by the following procedure. Using the initial point $\mathbf{P}_i$, set $\mathbf{g}_i = -\nabla f(\mathbf{P}_i)$ and calculate $\mathbf{h}_i$ by taking the line minimum from $\mathbf{h}_i \nabla f = -\mathbf{h}_i.\mathbf{g}_{i+1}$. This can be shown to reproduce the sequence of vectors $\mathbf{h}_i, \mathbf{g}_i$ as above, *without* knowledge of the Hessian matrix $\mathbf{A}$, and hence the algorithm will converge for an arbitrary form of f, not necessarily quadratic as above.

[1] There appears to be little difference between the two algorithms, although the Polak-Ribiere algorithm is reputed to be more robust, and was used for the present Maximum Entropy work

For the problem of minimising the negative of the entropy, it is sufficient to follow the Polak-Ribiere conjugate gradient sequence until the condition $\chi^2 = P$ from above, is satisfied. Further iterations, make less use of the information content of the measured data. A good initial start point $\mathbf{P}_0$ is a small flat volume fraction value, essentially assuming no particles present and only a flat scattering background. Following the minimisation process reveals that the algorithm relaxes to fit the grosser scattering features first, and fits the details later.

B.4 Application to Particle Distributions

The inverse problem of interest in a small angle scattering experiment is to determine the volume fraction of particles of a given shape and size from the measured intensity as a function of scattering wavenumber. The intensity values then comprise the P data values d_j with estimated uncertainties σ_j, the fitted volume fractions are the N x_i parameters, and the operator $\mathbf{O}_{j,i}$ is determined by the form factor to be used. For example in the case of a distribution of spherical particles, $\mathbf{O}_{j,i}$ is chosen as:

$$\mathbf{O}_{j,i} = \frac{4}{3}\pi R_i^3 \ \triangle\rho^2 \ F^2(R_i Q_j) \tag{B.130}$$

where $\triangle\rho^2$ is the SANS contrast and $F^2(QR)$ is the Rayleigh form factor. The resulting solution is a volume weighted particle size distribution.

Note that is is necessary to choose the particle radius range $R_{\min} \ldots R_{\max}$ for fitting. This can usually be done, because the resolution limits of SANS instrument define the maximum and minimum particle sizes that will contribute to the measured intensity (typically $5 - 1000\mathring{A}$).

Other form factors can be employed if the sample is thought to contain particles of a different shape. Other experimental evidence is usually necessary if a combination of different form factors is used, since a combination of form factors greatly increases the size of parameter space in which to search for a best fit. For example, TEM micrographs may suggest the approximate particle dimension range to be fitted.

Appendix C

Spherical Particle Scattering

Textbooks on scattering invariably assume the Rayleigh formula for the scattering from a monodisperse system of spherical particles, employing the hideous phrase 'it can be shown that'. This appendix derives this formula starting from the equation relating the differential cross section to the squared modulus of the Fourier transform of the scattering length density function.

$$\frac{d\sigma}{d\Omega} = \frac{1}{V}\left|\int_V \rho(\mathbf{r}) e^{i\mathbf{Q}.\mathbf{r}} dr\right|^2 \tag{C.131}$$

V is the total sample volume and ρ is the scattering length density function.

The two phase approximation [98] is to assume that the scattering is from particles of some definite shape, size and volume V_p with scattering length density ρ_p suspended in a matrix phase of scattering length density ρ_m. If the volume density of such particles is low so that inter-particle interference effects can be ignored, then equation C.131 can be recast as:

$$\frac{d\sigma}{d\Omega} = \triangle\rho^2 \frac{1}{V} N_p \left|\int_{V_p} e^{i\mathbf{Q}.\mathbf{r}} dr\right|^2 \tag{C.132}$$

where $\triangle\rho^2 = (\rho_p - \rho_m)^2$ is the scattering contrast, and the integral is now over the volume of **one** particle. N_p is the number of particles present in the sample

volume V. It is convenient to rewrite this as:

$$\frac{d\sigma}{d\Omega} = \Delta\rho^2 V_f V_p |F(\mathbf{Q})|^2 \tag{C.133}$$

where the volume fraction $V_f = \frac{N_p V_p}{V}$ and the form particle factor F is defined as:

$$F(\mathbf{Q}) = \frac{1}{V_p}\int_{V_p} e^{i\mathbf{Q}.\mathbf{r}} dr \tag{C.134}$$

A particle structure factor $S(\mathbf{Q}$ is often defined as:

$$S(\mathbf{Q}) \equiv |F(\mathbf{Q})|^2 \tag{C.135}$$

Of particular interest is the simple case of a dilute distribution of randomly located compact spherical particles each of volume $V_p = \frac{4}{3}\pi R^3$. The Rayleigh scattering form factor for such particles can then be derived as follows:

$$F(\mathbf{Q}) = \frac{3}{4\pi R^3}\int_0^R \int_0^\pi \int_0^{2\pi} e^{i\mathbf{Q}.\mathbf{r}} r^2 dr \sin\theta d\theta d\phi \tag{C.136}$$

We are free to choose the orientation of the spherical polar co-ordinate system so that the angle θ is the angle between the scattering vector $\mathbf{Q}$ and the integration vector $\mathbf{r}$, and the dot product in the exponential can be made explicit by the spherical symmetry. The azimuthal integral is also easily separated out, to give:

$$F(\mathbf{Q}) = \frac{3}{2R^3}\int_0^R \int_0^\pi e^{iQr\cos\theta} r^2 dr \sin\theta d\theta \tag{C.137}$$

Employing the change of variables $x = -\cos\theta$ transforms this to:

$$F(\mathbf{Q}) = \frac{3}{2R^3}\int_0^R r^2 \int_{-1}^1 e^{-iQrx} dx dr \tag{C.138}$$

which evaluates to:

$$F(\mathbf{Q}) = \frac{3}{2R^3}\int_0^R r^2 \frac{e^{iQr} - e^{-iQr}}{iQr} dr \tag{C.139}$$

This is then:

$$F(\mathbf{Q}) = \frac{3}{R^3}\int_0^R r^2 \frac{\sin Qr}{Qr} dr \tag{C.140}$$

and by using $y = Qr$, we obtain:

$$F(\mathbf{Q}) = \frac{3}{(QR)^3}\left\{\left(\int_0^{QR}\cos y\,dy\right) - QR\cos QR\right\} \tag{C.141}$$

Which gives:

$$F(\mathbf{Q}) = \frac{3}{(QR)^3}\left\{\sin QR - QR\cos QR\right\} \tag{C.142}$$

This has the useful properties that it is dimensionless, and depends only on one characteristic of the particle, namely its radius R. It should be emphasised that this form does *not* take account of inter-particle interference effects. In addition, real particles precipitating out of solution, may not have such a sharp interface as is assumed in this model. This leads to some smearing out of the deep troughs in the scattering that are indicated by equation C.142

Bibliography

[1] J.D. Gunton, M. San Miguel, and P.S. Sahni. The dynamics of first order phase transitions. In C.Domb and J.L.Lebowitz, editors, *Phase transitions and critical phenomena*, chapter 3, pages 267–466. Academic Press, 1983. Volume 8.

[2] T. D. Lee and C. N. Yang. Statistical theory of equations of state and phase transitions. ii lattice gas and ising model. *Phys. Rev.*, 87(3):410–419, August 1952.

[3] W. L. Bragg and E. J. Williams. The effect of thermal agitation on atomic arrangement in alloys i. *Proc. Roy. Soc. A*, 145:699–730, 1934. Bakerian lecture 1934.

[4] F. Cernuschi and H. Eyring. An elementary theory of condensation. *J. Chem. Phys.*, 7:547–551, July 1939.

[5] K. Kawasaki. Diffusion constants near the critical point for time dependent ising model i. *Phys. Rev.*, 145(1):224–230, 1966.

[6] P.C.Hohenberg and B.I.Halperin. Theory of dynamic critical phenomena. *Rev.Mod.Phys.*, 49(2):435–479, April 1977.

[7] Kurt Binder, editor. *Monte Carlo Methods in Statistical Physics.* Topics in Current Physics. Springer-Verlag, 2 edition, 1986. Number 7.

[8] Kurt Binder, editor. *Applications of the Monte Carlo Method in Statistical Physics.* Topics in Current Physics. Springer-Verlag, 1987.

[9] A.Sadiq and K.Binder. Dynamics of the formation of two dimensional ordered structures. *J.Stat.Phys.*, 35(5):517–586, 1984.

[10] J. G. Amar, F. E. Sullivan, and R. D. Moutain. A monte carlo study of growth in the two dimensional spin-exchange ising model. *Physics Review B*, 37:196–200, 1988.

[11] David A. Huse. Corrections to late stage behaviour in spinodal decomposition: Lifshitz-slyozov scaling and monte-carlo simulations. *Phys. Rev. B*, 34(11):7845–7850, December 1986.

[12] G.F.Mazenko, O.T.Valls, and F.C.Zhang. Renormalisation group theory of spinodal decomposition. *Phys.Rev.B.*, 32(9):5807–5817, November 1985.

[13] I. M. Lifshitz and V. V. Slyozov. The kinetics of precipitation from supersaturated solid solutions. *J. Phys. Chem. Solids*, 19(1):35–50, 1961. Translated by R. D. Lowde.

[14] H. Eugene Stanley. *Introduction to phase transitions and critical phenomena.* Oxford Science Publications, 1987.

[15] Z.W.Lai, G.F.Mazenko, and Oriol T. Valls. Classes for growth kinetics at low temperatures. *Phys.Rev.B.*, 37(16):9481–9494, June 1988.

[16] J.D. Gunton. Some topics in the kinetics of first order phase transitions. In K.C.Bowler and A.J.McKane, editors, *Statistical and Particle Physics*, chapter 2, pages 101–153. Scottish Universities Summer School in Physics, University of Edinburgh, 1983.

[17] J.D. Gunton. Dynamics of topological defects in first order phase transitions. In L. Garrido, editor, *Fluctuations and stochastic phenomena in condensed matter*, chapter 2, pages 35–54. Springer-Verlag, 1987. Number 268.

[18] Farid F. Abraham. On the thermodynamics, structure and phase stability of the non-uniform fluid state. *Phys. Rep.*, 53(2):93–156, 1979.

[19] D. de Fontaine. Clustering effects in solid solutions. In N.B.Hannay, editor, *Treatise on Solid State Chemistry*, chapter 3, pages 129–178. Plenum press, 1975.

[20] J.W.Cahn and J.E.Hilliard. Free energy of a non-uniform system iii. nucleation in a two point compressible fluid. *J.Chem.Phys.*, 31:688–699, 1959.

[21] Kurt Binder. Mechanisms for the decay of unstable and metastable phases: Spinodal decomposition, nucleation and late-stage coarsening. In G. M. Stocks and A. Gonis, editors, *Alloy Phase Stability*, pages 233–262. Kluwer Academic, 1989.

[22] Ekhard Salje. Kinetic rate laws as derived from order parameter theory: I: Theoretical concepts. *Phys.Chem.Minerals*, 15:336–348, 1988.

[23] M.A.Carpenter and E.Salje. Time dependent landau theory for order / disorder processes in minerals. *Mineralogical Magazine*, 53:483–504, September 1989.

[24] H.E. Cook. Brownian motion in spinodal de-composition. *Acta.Met*, 18:297–306, March 1970.

[25] J.Marro and J.L.Valles. Relevance of the cahn-hilliard-cook theory at early times in spinodal decomposition. *Phys.Lett. A*, 95:443–446, 1983.

[26] J. S. Langer, M. Bar-on, and Harold D. Miller. New computational method in the theory of spinodal decomposition. *Phys. Rev. A*, 11(4):1417–1429, April 1975.

[27] Y. Saito. Anomalous fluctuation and mode selection in dynamics of spinodal decomposition. *J.Phys.Soc.Japan*, 41:1129–1136, 1976.

[28] Martin S. Grant, M. San Miguel, , J.Vinals, and J. D. Gunton. Theory for the early stages of phase separation: The long range force limit. *Phys. Rev. B*, 31(5):3027–3039, March 1985.

[29] C. Billotet and K. Binder. Nonlinear relaxation at first order phase transitions: A ginzberg-landau theory including fluctuations. *Z. Physik. B*, 32:195–213, 1979.

[30] Charles H. Bennett. Efficient estimation of free energy differences from monte-carlo data. *J. Comp. Phys.*, 22:245–268, 1976.

[31] K.Kaski, K.Binder, and J.D.Gunton. Study of cell distribution functions of the three-dimensional ising model. *Phys.Rev.B*, 29(7):3996–4009, 1984.

[32] R.Becker and W.Doring. Droplet theory. *Ann.Phys.*, 24:719, 1935.

[33] K. Binder and D. Stauffer. Statistical theory of nucleation, condensation and coagulation. *Adv. in Phys.*, 25(4):343–396, 1976.

[34] P. Mirold and K. Binder. Theory for the initial stages of grain growth and unmixing kinetics of binary alloys. *Acta.Met.*, 25:1435–1444, 1977.

[35] J. R. Henderson and P. Schofield. Statistical mechanics of a fluid drop. MPD/NBS/179 179, Harwell Laboratory, MPMD, Harwell Laboratory, Oxon. , UK., July 1981.

[36] K. W. Kehr, K. Binder, and S. M. Reulein. Mobility, interdiffusion, and tracer diffusion in lattice gas models of two-component alloys. *Phys. Rev. B*, 39(8):4891–4910, March 1989.

[37] D. Hayward, D. W. Heermann, and K. Binder. Dynamic percolation transition induced by phase separation: a monte carlo analysis. *J. Stat. Phys.*, 49:1053–1081, December 1987.

[38] Christopher Roland and Martin Grant. Lack of self-averaging, multiscaling, and 1/f noise in the kinetics of domain growth. *Phys. Rev. Lett.*, 63(5):551–554, July 1989.

[39] Scott F. Anderson, Gene F. Mazenko, and Oriol T. Valls. Generalized renormalization group treatment of the growth kinetics of unstable systems. *J. Stat. Phys.*, 41(1):17–36, 1985.

[40] M. Marder. Correlations and droplet growth. *Phys. Rev. Lett.*, 55(27):2953–2956, December 1985.

[41] G. S. Pawley, R. H. Swendsen, D. J. Wallace, and K. G. Wilson. Monte-carlo renormalization group calculations of critical behaviour in the simple cubic ising model. *Phys. Rev. B*, 29(7):4030–4040, April 1984.

[42] A. J. Bray. Exact renormalization-group results for domain-growth scaling in spinodal decomposition. *Phys. Rev. Lett.*, 62(24):2841–2844, June 1989.

[43] Amit Sur, Joel L. Lebowitz, J. Marro, and M. H. Kalos. Time evolution of a quenched binary alloy. iv. computer simulation of a three dimensional model system. *Phys. Rev. B.*, 15(6):3014–3026, March 1977.

[44] K. K. Mon and David Jasnow. Finite size scaling and critical nucleation. Centre for Simulational Physics, Georgia, Preprint, August 1987.

[45] W. L. Bragg and E. J. Williams. The effect of thermal agitation on atomic arrangement in alloys ii. *Proc. Roy. Soc. A*, 151:540–566, 1935.

[46] Lloyd D. Fosdick. Calculation of order parameters in a binary alloy by the monte carlo method. *Phys. Rev.*, 116(3):565–572, November 1959.

[47] U. D. Kulkarni, S. Muralidhar, and S. Banerjee. Computer simulation of the early stages of ordering in ni-mo alloys. *phys. stat. sol. (a)*, 110:331–345, 1988.

[48] A. B. Bortz, M. H. Kalos, J. L. Lebowitz, and M. A. Zendajas. Time evolution of a quenched binary alloy: Computer simulation of a two-dimensional model system. *Phys. Rev. B*, 10(2):535–541, July 1974.

[49] J. Marro, A. Bortz, M. H. Kalos, and J. L. Lebowitz. Time evolution of a quenched binary alloy. ii computer simulation of a three-dimensional model system. *Phys. Rev. B*, 12(6):2000–2011, September 1975.

[50] M. Rao, M. H. Kalos, J. L. Lebowitz, and J. Marro. Time evolution of a quenched binary alloy. iii computer simulation of a two dimensional model system. *Phys. Rev. B.*, 13(10):4328–4335, May 1976.

[51] J. Marro, Joel L. Lebowitz, and M. H. Kalos. Computer simulation of the time evolution of a quenched model alloy in the nucleation regime. *Phys. Rev. Lett.*, 43(4):282–285, July 1979.

[52] S. A. Safran, Paramdeep S. Sahni, and Gary S. Grest. Kinetics of ordering in two dimensions. i model systems. *Phys. Rev. B.*, 28(5):2693–2704, September 1983.

[53] J. M. Sanchez and D. de Fontaine. Ising model phase diagram calculations in the fcc lattice with first and second neighbour interactions. *Phys. Rev. B*, 25(3):1759–1765, February 1982.

[54] J. M. Sanchez and D . de Fontaine. Ordering in fcc lattices with first and second neighbour interactions. *Phys. Rev. B.*, 21(1):216–228, January 1980.

[55] C. G. Windsor, R. M. Barron, and J. R. Russell. Cluster shape changes during low temperature annealing. Private Communication, 1988.

[56] J. E. Epperson, P. Furnrohr, and C. Ortiz. The short-range-order structure of alpha-phase cu-al alloys. *Acta.Cryst.A*, 34:667–681, 1978.

[57] M. Furusaka, Y. Ishikawa, S. Yamaguchi, and Y. Fujino. Phase separation process in fecr alloys studied by neutron small angle scattering. *J. Phys. Soc. Japan*, 55(7):2253–2269, July 1985.

[58] J. E. Epperson, B. A. Loomis, J. Faber, J. S. Lin, and R. W. Hendricks. Phase separation in a ni-12. 7at. pct. al alloy at 550 c. *Metallurgical Transactions A*, 18:2027–2035, December 1987.

[59] J.E.Epperson, J.S.Lin, and P.D.Labarbe. Phase separation in an ni-al alloy at 575 k. *J.App.Cryst.*, 21(6):873–877, December 1988.

[60] M. Furusaka, Y. Ishikawa, and M. Mera. Early stage of phase-separation processes in fecr and alzn alloys. *Phys. Rev. Lett.*, 54(24):2611–2614, June 1985.

[61] Bjorn Jonsson. Interphase-reaction controlled growth and its application to the massive transformation in fe-ni alloys. *J. Appl. Phys.*, 67(3):1307–1311, February 1990.

[62] M.P. Allen and D.J. Tildesley. *Computer simulation of liquids.* Clarendon Press, 1987.

[63] G. S. Pawley. Molecuar dynamics and spectroscopy. In D. L. Price and K. Skold, editors, *Methods in experimental physics*, pages 441–519. Academic Press, 1986. Volume 23 Neutron Scattering Part A.

[64] Nicholas Metropolis, Arianna W. Rosenbluth, Marshall N. Rosenbluth, Augusta H. Teller, and Edward Teller. Equation of state calculations by fast computing machines. *J. Chem. Phys.*, 21(6):1087–1092, June 1953.

[65] R.J. Glauber. Time dependent statistics of the ising model. *J. Math. Phys.*, 4(2):294–307, 1963.

[66] H. Muller-Krumbhaar and K. Binder. Dynamic properties of the monte carlo method in statistical physics. *J. Stat. Phys.*, 8(1):1–24, 1973.

[67] A. B. Bortz, M. H. Kalos, and J. L. Lebowitz. A new algorithm for monte-carlo simulation of ising spin systems. *J. Comp. Phys.*, 17:10–18, 1975.

[68] Michael Creutz. Microcanonical monte carlo simulation. *Phys. Rev. Lett.*, 50(19):1411–1414, May 1983.

[69] Robert H. Swendsen and Jian-Sheng Wang. Nonuniversal critical dynamics in monte-carlo simulations. *Phys. Rev. Lett.*, 58(2):86–88, January 1987.

[70] Clive F. Baillie. Lattice spin models and new algorithms. Caltech Preprint C3P-777, May 1989.

[71] C.F.Baillie, R.Gupta, K.A.Hawick, and G.S.Pawley. Monte-carlo renormalisation group ising calculations. In preparation, 1991.

[72] Stephen Wolfram. Cellular automata as models of complexity. *Nature*, 311:419–424, October 1984.

[73] B. M. Boghosian, D. H. Rothman, and W.Taylor. A cellular automata simulation of two-phase flow on the cm-2 connection machine computer. Private Communication, March 1988.

[74] Bruce M. Boghosian, Washington Taylor IV, and Daniel H. Rothman. A cellular automata simulation of two-phase flow on the cm-2 connection machine computer. Thinking Machines, March 1988.

[75] Daniel H. Rothman and Jeffrey M. Keller. Immiscible cellular-automaton fields. *J.Stat.Phys.*, 52(3):1119–1127, 1988.

[76] William H. Press, Brian P. Flannery, Saul A. Teukolsky, and William T. Vetterling. *Numerical Recipies in C.* Cambridge University Press, 1988.

[77] Lars Onsager. Crystal statistics i. two-dimensional model with an order-disorder transition. *Phys.Rev.*, 65(3):117–149, February 1944.

[78] Dietrich Stauffer. *Introduction to percolation theory.* Taylor and Francis, 1985.

[79] K.A.Hawick, W. C-K. Poon, and G.J.Ackland. Relaxation in the dilute ising model. accepted for International Conference on Magnetism, Edinburgh 1991, 1991.

[80] C. G. Windsor, R. N. Sinclair, V. S. Rainey, B. Normand, and A. W. Bowen. Changing dimensionality in the early growth of clusters in an evaporated al-cr-fe alloy. *J. Phys. F:Met. Phys.*, 17:L229–235, 1987.

[81] J.A.Tuszynski, M.Skierski, and A.M.Grundland. Short-range induced critical phenomena in the landau-ginzburg model. *Can.J.Phys.*, 68:751–755, 1990.

[82] R. Toral, A. Chakrabarti, and J. D. Gunton. Numerical study of the cahn-hilliard equation in three dimensions. *Phys. Rev. Lett.*, 60(22):2311–2314, May 1988.

[83] B.L. Buzbee, G.H. Golub, and C.W. Nielson. On direct methods for solving poisson's equation. *SIAM J.Num.Analysis*, 7:627–656, 1970.

[84] A. Milchev, D. W. Heermann, and K. Binder. Monte-carlo simulation of the cahn-hilliard model of spinodal decomposition. *Acta. Metall.*, 36(2):377–383, 1988.

[85] W.H.Press, B.P.Flannery, S.A.Teukolsky, and W.T.Vetterling. *Numerical Recipes in C*, chapter 17, pages 636–688. Cambridge University Press, 1988. Partial Differential Equations.

[86] Kurt Binder. Theory of first order phase transitions. Mainz Preprint, March 1988.

[87] M.E.Fisher. The theory of equilibrium critical phenomena. *Rep.Prog.Phys.*, 30:615–730, 1967.

[88] Ya. B. Zeldovitch. Nucleation. *Acta Physicochim*, 18:1–9, 1943. USSR.

[89] Kurt Binder. Theory for the dynamics of clusters. ii critical diffusion in binary systems and the kinetics of phase separation. *Phys. Rev. B*, 15(9):4425–4447, May 1977.

[90] Stephen W. Lovesey. *Theory of Neutron Scattering from Condensed Matter.* Clarendon Press, Oxford, 1987. 2 Volumes.

[91] B.T.M. Willis, editor. *Chemical applications of thermal neutron scattering.* Harwell Series. Oxford University Press, 1973. Harwell Summer School 1972.

[92] D.L.Price and K.Skold, editors. *Methods in Experimental Physics: Neutron Scattering*, volume 23. Academic Press, 1986. Parts A, B and C.

[93] C.G.Windsor and K.A.Hawick. *The Evaluation of Neutron Scattering Experiments.* Oxford University Press, 1991. In Preparation.

[94] C. G. van Essen. Scanning electron microscopy. In J. A. Belk, editor, *Electron Microscopy and Microanalysis of Crystalline Materials*, pages 99–120. Applied Science Publishers, 1979.

[95] J. M. Titchmarsh, C. M. Sheperd, and I. A. Vatter. The measurement of chemical composition with high spatial resolution using a dedicated scanning transmission electron microscope. Aere r 12317 / hl87/1055(c14), Harwell Laboratory, Oxford OX11 ORA, UK, February 1987.

[96] C. G. Windsor, V. S. Rainey, P. K. Rose, and V. M. Callen. A study of gamma–prime particles in a nickel based superalloy. *J. Phys. F:Met. Phys.*, 14:1771–1787, 1984. Using TEM and SANS.

[97] Colin G. Windsor. Basic theory of thermal neutron scattering by condensed matter. In B. T. M. Willis, editor, *Chemical Applications of Thermal neutron Scattering*, pages 1–30, Harwell/Oxford, 1973. UKAERE, Oxford University Press. Harwell Series.

[98] C. G. Windsor. An introduction to small angle neutron scattering. *J. Appl. Cryst.*, 21:582–588, 1988.

[99] Varley F. Sears. Neutron scattering lengths and cross sections. In K. Skold and D. L. Price, editors, *Methods of Experimental Physics*, pages 521–550. Academic Press, 1986. Volume 23, Part A.

[100] Stephen Gasiorowicz. *Quantum Physics.* Wiley, 1974.

[101] Robert C. Weast, editor. *CRC handbook of Chemistry and Physics.* CRC Press, 1988. 1st Student Edition.

[102] D. I. Page. The structure of liquids by neutron scattering. In B. T. M. Willis, editor, *Chemical Applications of Thermal neutron Scattering*, pages 173–200, Harwell/Oxford, 1973. UKAERE, Oxford University Press. Harwell Series.

[103] J. E. Epperson and P. Thiyagarajan. Anomalous and resonance small angle scattering. *J. Appl. Cryst.*, 21:652–662, 1988.

[104] R.K.Crawford and J.M.Carpenter. Tailoring beams for small sngle neutron diffractometers. *J.App.Cryst.*, 21(6):589–601, 1988.

[105] Paul W. Schmidt. Collimation effects in small angle x-ray and neutron scattering. *J.App.Cryst.*, 21(6):602–612, 1988.

[106] Phil A. Seeger. Neutron detection systems for small angle scattering. *J.App.Cryst*, 21(6):613–617, 1988.

[107] D. I. Page. *Practical Guide to the PLUTO Small Angle Scattering Spectrometer.* UKAERE, Oxford OX11 ORA, UK, August 1980. HMSO AERE-R-9878.

[108] J. E. Epperson, P. Thiyagarajan, and T. E. Klippert. *Small Angle Diffractometer Users Manual.* IPNS ANL, Argonne National Laboratory, Chicago, Illinois USA, February 1987.

[109] N.F.Berk and K.A.Hardman-Rhyne. Analysis of sas data dominated by multiple scattering. *J.App.Cryst.*, 21(6):645–651, December 1988.

[110] T.P.Russel, J.S.Lin, S.Spooner, and G.D.Wignall. Intercalibration of small angle x-ray and neutron scattering data. *J.App.Cryst.*, 21(6):629–638, 1988.

[111] G.D.Wignall and F.S.Bates. unknown. *J.Appl.Cryst*, 20:28–40, 1987.

[112] P.Lindner. Fourier analysis of anisotropic scattering data. Private Communication, 1989.

[113] K.A.Hawick. Fourier decomposition of anisotropic small angle scattering data. ANLAN Program User Manual, 1989.

[114] W.H.Press, B.P.Flannery, S.A.Teukolsky, and W.T.Vetterling. *Numerical Recipes in C*, chapter 12, pages 398–470. Cambridge University Press, 1988. Fourier Transform Spectral Methods.

[115] Devinderjit Singh Sivia. Data analysis: Bayes' theorem, maximum entropy and deconvolution. Joint CNLS/Signal processing working group seminar, LANSCE, February 1989.

[116] Rex P. Hjelm Jr. The resolution of tof low-q diffractometers, instrumental, data acquisition and reduction factors. *J. Appl. Cryst.*, 21:618–628, 1988.

[117] M. Ernst, J. Schelten, and W. Schmatz. Small angle scattering of neutrons at single-domain precipitations in a cu-1 *Phys. Stat. Sol. (a)*, 7:469–476, 1971.

[118] L. A. Feigun and D. I. Svergun. *Structure Analysis by Small Angle X-Ray and Neutron Scattering.* Plenum Press, 1987.

[119] Irina S. Fedorova and Paul W. Schmidt. A general analytical method for calculating particle-dimension distributions from scattering data. *J. Appl. Cryst.*, 11:405–411, 1978.

[120] W.H.Press, B.P.Flannery, S.A.Teukolsky, and W.T.Vetterling. *Numerical Recipes in C*, chapter 6, pages 166–203. Cambridge University Press, 1988. Special Functions.

[121] Milton Abramowitz and Irene A. Stegun, editors. *Handbook of Methematical Functions.* Dover Pub. Inc., 1972.

[122] Kenneth A. Hawick, J. Ernest Epperson, Colin G. Windsor, and Vic. S. Rainey. Chemical phase separation in binary iron-chromium alloys. In *Proc. Materials Research Society Meeting*, Boston, USA, November 1990. Materials Research Society. Symposium F.

[123] Max Hansen. *Constitution of Binary Alloys.* Metallurgy and Metallurgical Engineering Series. McGraw-Hill Book Company, 2 edition, 1958.

[124] J.E.Epperson and K.A.Hawick. Research in progress. unpublished, 1991.

[125] J.E.Epperson, K.A.Hawick, C.G.Windsor, T.E.Klippert, D.G.Wozniak, and S.Spooner. Research in progress. unpublished, 1990.

[126] W.B.Pearson. *A Handbook of Lattice spacings and structures of metals and alloys.* Pergamon, 1965. NRC No 4303.

[127] J. Ernest Epperson, Kenneth A. Hawick, Colin G. Windsor, and Vic. S. Rainey. A small angle neutron scattering investigation of phase separation in an fe-cr-ni alloy. In *Proc. Materials Research Society Meeting*, Boston, USA, November 1990. Materials Research Society. Symposium F.

[128] A. D. Hardy and K. B. Smith. Examination of irradiated hinkley point pe16 tie bar samples by sans. Nd-m-2042(s):tbmsg/p35, UKAEA, Springfields Nuclear Power Development Laboratories, Salwick Preston PR4 ORR, April 1983.

[129] R. M. Boothby, G. C. Cattle, and T. L. Brydon. Precipitation in nimonic pe16. Gen/tbmsg/p(87)/6429/a/1, Materials Development Division AERE Harwell, Harwell Laboratory, Oxford OX11 ORA, October 1987.

[130] B. Reppich, W. Kuhlein, G. Meyer, D. Puppel, M. Schulz, and G. Schumann. Duplex gamma-prime particle hardening of the superalloy nimonic pe16. *Materials Science and Engineering*, 83:45–63, 1986.

[131] C.G.Windsor and K.A.Hawick. Research in progress. unpublished, 1991.

[132] H.Furukawa. Dynamical scaling of small angle scattering data. *Physica A*, 123:497–515, 1984.

[133] N. B. Wilding, A. S. Trew, K. A. Hawick, and G. S. Pawley. Scientific modelling on the dap. To appear in IEEE special issue, March 1990.

[134] AMT Ltd, 65 Suttons Park Avenue, Reading, RG6 1AZ. *DAP 600 APAL Language*, 1989.

[135] K.A.Hawick. Dap memory management. Technical Report ECSP-TN, Edinburgh Parallel Computing Centre, Edinburgh University, Mayfield Road, EH9 3JZ, UK, 1991.

[136] M.J.Flynn. Some computer organisations and their effectiveness. *IEEE Trans. on Computers. C*, 21:948–960, 1972.

[137] AMT Ltd, 65 Suttons Park Avenue, Reading, RG6 1AZ. *DAP Series FORTRAN PLUS Language (Enhanced)*, 1990.

[138] K.C. Bowler, R.D. Kenway, G.S. Pawley, and D. Roweth. *An introduction to Occam 2 programming.* Studentlitteratur. Chartwell-Bratt, 1987.

[139] EPCC. Project directory. Technical Report 3, Edinburgh Parallel Computing Centre, Edinburgh University, Mayfield Road, EH9 3JZ, 1990.

[140] Meiko Ltd, Southgate, Whitefriars, Lewins Mead, Bristol BS1 2NT. *Meiko CS-Tools User and Reference Manual*, 1990.

[141] W. Daniel Hillis. *The Connection Machine.* MIT Press, 1985.

[142] S. F. Reddaway, D. M. Scott, and K. A. Smith. A very high speed monte-carlo simulation on dap. *Comp. Phys. Comms.*, 37:351–356, 1985.

[143] G.S.Pawley and G.W.Thomas. The implementation of lattice calculations on the dap. *J.Comp.Phys.*, 47(2):165–178, August 1982.

[144] D.P.Landau and D. Stauffer. Test of parallel updating in ising model simulation. *Journal de Physique*, 50:509–512, March 1989.

[145] R.Toral and K.A.Hawick. A fast algorithm for kawasaki spin-exchange dynamics. In preparation, 1991.

[146] H.Muller-Krumbhaar. Simulation of small systems. In K.Binder, editor, *Monte Carlo methods in statistical physics*, Topics in Current Physics, chapter 5, pages 195–223. Springer-Verlag, 2 edition, 1986. Number 7.

[147] W.H.Press, B.P.Flannery, S.A.Teukolsky, and W.T.Vetterling. *Numerical Recipes in C*, chapter 12, pages 252–254. Cambridge University Press, 1988. Determination of Equivalence Classes.

[148] R. Toral and C. Wall. Finite size scaling study of the equilibrium cluster distribution of the two-dimensional ising model. *J.Phys.A*, 20:4949–4965, 1987.

[149] J. Hoshen and R. Kopelman. Percolation and cluster distribution 1. cluster multiple labeling technique and critical concentration algorithm. *Phys. Rev. B*, 14(8):3438–3445, October 1976.

[150] A. Milchev, K. Binder, and D. W. Heermann. Fluctuations and lack of self-averaging in the kinetics of domain growth. *Z. Phys. B.*, 63:521–535, 1986.

[151] B. D. Ripley. Computer generation of random variables: A tutorial. *Int. Statistical. Rev.*, 51:301–319, 1983.

[152] G. Marsaglia. Random number generation. Florida Preprint, 1983.

[153] George Marsaglia. A current view of random number generators. In *Computer science and statistics: 16th symposium on the interface*, Atlanta, March 1984. Keynote address.

[154] W.H.Press, B.P.Flannery, S.A.Teukolsky, and W.T.Vetterling. *Numerical Recipes in C*, chapter 7, pages 204–241. Cambridge University Press, 1988. Random Numbers.

[155] S.P. Booth and K.A. Hawick. Random number generators for super computers. Technical Report ECSP-TN, Edinburgh Parallel Computing Centre, Edinburgh University, Mayfield Road, EH9 3JZ, UK, 1991.

[156] George Marsaglia and Liang-Huei Tsay. Matrices and the structure of random number sequences. *Linear algebra and its applications*, 67:147–156, 1985.

[157] K. A. Smith, S. F. Reddaway, and D. M. Scott. Very high performance pseudo-random number generation on dap. *Comp. Phys. Comms.*, 37:239–244, 1985.

[158] George Marsaglia and Arif Zaman. Toward a universal random number generator. Florida State preprint, 1987.

[159] J. Skilling and S. F. Gull. Algorithms and applications. In C. Ray Smith and W. T. Grundy, editors, *Maximum Entropy and Bayesian Methods in Inverse Problems*, pages 83–132. Univ. Wyoming, D. Riedel Publishing Company, 1985.

[160] J. A. Potton, G. J. Daniell, and B. D. Rainford. Particle size distribution from sans data using the maximum entropy technique. *J. Appl. Cryst.*, 21:663–668, 1988.

[161] K.A.Hawick. Maximum entropy parameter fitting for small angle scattering data. MAXSANS Program User Manual, 1990.

[162] S. F. Gull and J. Skilling. Maximum entropy method in image processing. *IEEE proc.*, 131(6):646–659, October 1984.

[163] David M. Anderson, David C. Martin, and Edwin L. Thomas. Maximum entropy restoration using both real and fourier space analysis. University of Lund, Sweden - Preprint, March 1989.

[164] Devinderjit Singh Sivia. Applications of maximum entropy and bayesian methods in neutron scattering. In P. Fougere, editor, *9th Annual Workshop on Maximum Entropy and Bayesian Methods*, Dartmouth College, New Hampshire, USA., August 1989. Los Alomos National Laboratory, Kluwer Academic Publishers.

[165] C. G. Vonk. On two methods for determination of particle size distribution functions by means of small angle x-ray scattering. *J. Appl. Cryst.*, 9:433–440, 1976.

[166] W.H.Press, B.P.Flannery, S.A.Teukolsky, and W.T.Vetterling. *Numerical Recipes in C*, chapter 10, pages 290–352. Cambridge University Press, 1988. Minimization or Maximization of Functions.

This work made use of the DAP facilities in Edinburgh Parallel Computing Centre, which is supported by major grants from the Computer Board, The Department of Trade and Industry, the Science and Engineering Research Council, and Industry. Some of this work was performed under the auspices of the U.S. Department of Energy, Division of Materials Science, Office of Basic Energy Sciences, under contract W-31-109-ENG-38. It is also a pleasure to thank AEA Technology for financial support.

This page left deliberately blank